



Defense Nuclear Agency  
Alexandria, VA 22310-3398



DNA-TR-95-47

## Wave Propagation in Intact and Jointed Calcium Carbonate ( $\text{CaCO}_3$ ) Rock

Tarabay H. Antoun  
Donald R. Curran  
SRI International  
333 Ravenswood Avenue  
Menlo Park, CA 94025-3434

March 1996

Technical Report

CONTRACT No. DNA 001-92-C-0153

Approved for public release;  
distribution is unlimited.

19960320 025

DTIC QUALITY INSPECTED 1

Destroy this report when it is no longer needed. Do not return to sender.

PLEASE NOTIFY THE DEFENSE NUCLEAR AGENCY,  
ATTN: CSTI, 6801 TELEGRAPH ROAD, ALEXANDRIA, VA  
22310-3398, IF YOUR ADDRESS IS INCORRECT, IF YOU  
WISH IT DELETED FROM THE DISTRIBUTION LIST, OR  
IF THE ADDRESSEE IS NO LONGER EMPLOYED BY YOUR  
ORGANIZATION.



## DISTRIBUTION LIST UPDATE

This mailer is provided to enable DNA to maintain current distribution lists for reports. (We would appreciate your providing the requested information.)

- Add the individual listed to your distribution list.
- Delete the cited organization/individual.
- Change of address.

**NOTE:**

Please return the mailing label from the document so that any additions, changes, corrections or deletions can be made easily. For distribution cancellation or more information call DNA/IMAS (703) 325-1036.

NAME: \_\_\_\_\_

ORGANIZATION: \_\_\_\_\_

**OLD ADDRESS**

**CURRENT ADDRESS**

---

---

---

---

---

---

TELEPHONE NUMBER: ( ) \_\_\_\_\_

**DNA PUBLICATION NUMBER/TITLE**

**CHANGES/DELETIONS/ADDITIONS, etc.)**

*(Attach Sheet if more Space is Required)*

---

---

---

---

---

---

DNA OR OTHER GOVERNMENT CONTRACT NUMBER: \_\_\_\_\_

CERTIFICATION OF NEED-TO-KNOW BY GOVERNMENT SPONSOR (if other than DNA):

SPONSORING ORGANIZATION: \_\_\_\_\_

CONTRACTING OFFICER OR REPRESENTATIVE: \_\_\_\_\_

SIGNATURE: \_\_\_\_\_

CUT HERE AND RETURN



**DEFENSE NUCLEAR AGENCY  
ATTN: TITL  
6801 TELEGRAPH ROAD  
ALEXANDRIA, VA 22310-3398**

**DEFENSE NUCLEAR AGENCY  
ATTN: TITL  
6801 TELEGRAPH ROAD  
ALEXANDRIA, VA 22310-3398**

# REPORT DOCUMENTATION PAGE

*Form Approved  
OMB No. 0704-0188*

Public reporting burden for this collection of information is estimated to average 1 hour per response including the time for reviewing instructions, searching existing data sources, gathering and maintaining the data needed, and completing and reviewing the collection of information. Send comments regarding this burden estimate or any other aspect of this collection of information, including suggestions for reducing this burden, to Washington Headquarters Services Directorate for Information Operations and Reports, 1215 Jefferson Davis Highway, Suite 1204, Arlington, VA 22202-4302, and to the Office of Management and Budget, Paperwork Reduction Project (0704-0188), Washington, DC 20503.

1. AGENCY USE ONLY (Leave blank)			2. REPORT DATE 960301		3. REPORT TYPE AND DATES COVERED Technical 920805 – 950430		
4. TITLE AND SUBTITLE  Wave Propagation in Intact and Jointed Calcium Carbonate ( $\text{CaCO}_3$ ) Rock			5. FUNDING NUMBERS C - DNA 001-92-C-0153 PE - 63711H PR - AE TA - CE WU - DH600050				
6. AUTHOR(S)  Tarabay H. Antoun and Donald R. Curran			8. PERFORMING ORGANIZATION REPORT NUMBER  PYU-3822				
7. PERFORMING ORGANIZATION NAME(S) AND ADDRESS(ES)  SRI International 333 Ravenswood Avenue Menlo Park, CA 94025-3434			10. SPONSORING/MONITORING AGENCY REPORT NUMBER  DNA-TR-95-47				
9. SPONSORING/MONITORING AGENCY NAME(S) AND ADDRESS(ES)  Defense Nuclear Agency 6801 Telegraph Road Alexandria, VA 22310-3398 FCTT\Rinehart							
11. SUPPLEMENTARY NOTES  This work was sponsored by the Defense Nuclear Agency under RDT&E RMC Code T4613D AE CE 60005 5900A 25904D.							
12a. DISTRIBUTION/AVAILABILITY STATEMENT  Approved for public release; distribution is unlimited.				12b. DISTRIBUTION CODE			
13. ABSTRACT (Maximum 200 words)  In support of the Defense Nuclear Agency's HYDRO PLUS program, SRI performed a series of uniaxial strain experiments using in-contact explosive techniques to investigate the effects of in situ and artificial joints on wave propagation in calcium carbonate ( $\text{CaCO}_3$ ) rock. The in situ joints investigated were healed, calcite-filled fissures in a nonporous limestone matrix. These joints did not have a significant effect on the observed response. On the other hand, artificial, sand-filled joints in marble caused an increase in the peak particle velocity upstream from the joint and a delayed time of arrival (TOA) of the wave at the gage downstream from the joint. Both peak particle velocity and TOA are used within the framework of the HYDRO PLUS yield estimation methodology.  A spherical wave experiment was also conducted on a sample of intact Danby marble to complement the uniaxial strain experiments and to provide data that can be used to validate and/or calibrate constitutive models for use in finite element and finite difference hydrocodes. The results of this experiment indicate that the occurrence of cracking can have a significant effect on the observed response if measurements are made in the strength-dominated region.							
14. SUBJECT TERMS  Phase Transition      Joints      Precursor Wave Propagation      Marble      Limestone Calcium Carbonate      Plane Waves      Spherical Waves					15. NUMBER OF PAGES 230		
					16. PRICE CODE		
17. SECURITY CLASSIFICATION OF REPORT UNCLASSIFIED		18. SECURITY CLASSIFICATION OF THIS PAGE UNCLASSIFIED		19. SECURITY CLASSIFICATION OF ABSTRACT UNCLASSIFIED		20. LIMITATION OF ABSTRACT SAR	

**UNCLASSIFIED**

SECURITY CLASSIFICATION OF THIS PAGE

CLASSIFIED BY:

N/A since Unclassified.

DECLASSIFY ON:

N/A since Unclassified.

## EXECUTIVE SUMMARY

The present investigation was undertaken as part of the HYDRO PLUS program to gain an improved knowledge of the material behavior parameters and thus increase confidence in the HYDRO PLUS yield estimation methodology. For this purpose, a series of uniaxial strain experiments were performed using in-contact explosive techniques to investigate the effect of *in situ* and artificial joints on wave propagation in calcium carbonate ( $\text{CaCO}_3$ ) rock. A spherical wave experiment was also conducted on a sample of intact Danby marble to complement the uniaxial strain experiments and provide data that can be used to validate and/or calibrate constitutive models for use in finite element and finite difference hydrocodes. Hydrocode simulations were used to aid in the interpretation of the experimental data. The uniaxial strain experiments were simulated using the one-dimensional finite difference code SRI PUFF, and the spherical wave experiment was simulated in the finite element code DYNA2D using a multiplane cracking model.

The *in situ* joints investigated were healed, calcite-filled fissures in a limestone matrix, Utah Test and Training Range (UTTR) limestone, composed primarily of calcite (62%) and quartz (31%) with traces of dolomite (2%), K-feldspar (2%), illite (2%), and pyrite (1%). These *in situ* joints did not have a significant effect on the observed response.

The artificial joints were embedded in Danby marble specimens. The joint parameters varied during our investigation included surface texture (smooth versus rough), thickness (closed versus sand-filled), number (single versus triple), and orientation (normal versus inclined with respect to the direction of shock propagation). Intact marble specimens were also tested to provide baseline data for comparison with data from the jointed samples.

Closed joints did not have a measurable effect on the behavior of the rock, nor did the surface texture of the joint. However, significant effects were produced when a sand-filled joint was introduced into the sample. Upstream from the joint, a temporary increase in the magnitude of the particle velocity profiles was observed. Downstream from the joint, the effect of the joint was manifested as a delayed time of arrival (TOA) of the wave at the gage plane. The perturbations to the free field were greatest for the triple normal joint configuration and smaller for the single inclined joint configuration, while the single normal joint configuration had the smallest measurable effect.

From these results, we conclude that the presence of sand-filled joints can have a significant effect on the HYDRO PLUS yield estimation methodology, because sand-filled joints perturb the free-field motion in a manner that causes an increase in the peak particle velocity upstream from the joint and a

delayed TOA downstream from the joint. Both peak particle velocity and TOA are used within the framework of the HYDRO PLUS yield estimation methodology.

In addition to the effects of joints on wave propagation described above, the results of the uniaxial strain experiments yielded information regarding the precursor and a high pressure phase transformation in CaCO<sub>3</sub> rock. The precursor was observed both during loading and unloading and was most likely associated with the I-II and II-III phase transitions in calcite. Based on the loading data, the magnitude of the precursor was estimated to be between 16 and 19 kbar in marble and 14.3 kbar in UTTR limestone. The high pressure phase transition was observed in the marble experiments. The stress level associated with this transition was about 118 kbar.

In the spherical wave experiment on Danby marble, extensive radial and circumferential crack networks were observed in the specimen after the test. The circumferential crack patterns were asymmetric and led to load-induced anisotropy in the late-time response of the sample, as indicated by the systematic differences between the particle velocity histories recorded on diametrically opposite sides of the explosive charge. Since the initial loading was spherically symmetric, the lack of symmetry in the late-time particle velocity histories was attributed to asymmetric cracking. Code simulation results indicated that close to the charge cavity the behavior of the rock was dominated by porous compaction, whereas away from the charge the behavior was dominated by crack propagation.

Accurate modeling of the cracking process thus appears to be necessary to allow assessment of the potential impact of cracking on the HYDRO PLUS yield estimation methodology if measurements are made in the strength-dominated region.

## PREFACE

This project was supported by the Defense Nuclear Agency (DNA) and conducted in the Poulter Laboratory of SRI International under the general supervision of James D. Colton, Laboratory Director. Robert Reinke was the DNA Contract Monitor. His support and active participation throughout the project are greatly appreciated.

The authors also express their appreciation to Audrey Martinez, DNA, who assisted in planning the study, and to the following SRI personnel who contributed to the success of the investigation: Paul S. DeCarli for expert advice and moral support; Douglas K. Keough for consultation on particle velocity measurements; Lynn Seaman and Michael Cowperthwaite for help with the Lagrangian analysis; Alexander L. Florence and Paul R. Gefken for participation in the design and execution of the spherical wave experiment; Daniel F. Walter, Michael A. Merritt, Michael Misner, and Patricia Whitney for the electronic measurements of particle velocity; Thomas Gaines for fielding and firing the explosives; Mario Oyola, Jerry Mattson, Timothy Mattson, and Galen Chaney for mechanical support; John Stotts for assembling the specimens; Terri Lopez for clerical support and for typing the manuscript, Marjorie Saunders for editing the manuscript, and Joyce Berry and Lee Gerrans for assisting with the illustrations.

## CONVERSION TABLE

Conversion factors for U. S. Customary to metric (SI) units of measurement  
 MULTIPLY  $\xrightarrow{\text{BY}}$  TO GET  
 TO GET  $\xleftarrow{\text{BY}}$  DIVIDE

angstrom	1.000 000	X E -10	meters (m)
atmosphere (normal)	1.013 25	X E +2	kilo pascal (kPa)
bar	1.000 000	X E +2	kilo pascal (kPa)
barn	1.000 000	X E -28	meter <sup>2</sup> (m <sup>2</sup> )
British thermal unit (thermochemical)	1.054 350	X E +3	joule (J)
calorie (thermochemical)	4.184 000	X E -2	joule (J)
cal (thermochemical)/cm <sup>2</sup>	4.184 000	X E +1	mega joule/m <sup>2</sup> (MJ/m <sup>2</sup> )
curie	3.700 000	X E -2	*giga becquerel (GBq)
degree (angle)	1.745 329	X E -2	radian (rad)
degree Fahrenheit	T <sub>K</sub> = (T °F + 459.67)/1.8		degree kelvin (K)
electron volt	1.602 19	X E -19	joule (J)
erg	1.000 000	X E -7	joule (J)
erg/second	1.000 000	X E -7	watt (W)
foot	3.048 000	X E -1	meter (m)
foot-pound-force	1.355 818		joule (J)
gallon (U.S. liquid)	3.785 412	X E -3	meter <sup>3</sup> (m <sup>3</sup> )
inch	2.540 000	X E -2	meter (m)
jerk	1.000 000	X E +9	joule (J)
joule/kilogram (J/kg) (radiation dose absorbed)	1.000 000		Gray (Gy)
kilotons	4.183		terajoules
kip (1000 lbf)	4.448 222	X E +3	newton (N)
kip/inch <sup>2</sup> (ksi)	6.894 757	X E +3	kilo pascal (kPa)
ktap	1.000 000	X E +2	newton-second/m <sup>2</sup> (N·s/m <sup>2</sup> )
micron	1.000 000	X E -6	meter (m)
mil	2.540 000	X E -5	meter (m)
mile (international)	1.609 344	X E +3	meter (m)
ounce	2.834 952	X E -2	kilogram (kg)
pound-force (lbs avoirdupois)	4.448 222		newton (N)
pound-force inch	1.129 848	X E -1	newton-meter (N · m)
pound-force/inch	1.751 268	X E +2	newton-meter (N/m)
pound-force/foot <sup>2</sup>	4.788 026	X E -2	kilo pascal (kPa)
pound-force/inch <sup>2</sup> (psi)	6.894 757		kilo pascal (kPa)
pound-mass (lbm avoirdupois)	4.535 924	X E -1	kilogram (kg)
pound-mass-foot <sup>2</sup> (moment of inertia)	4.214 011	X E -2	kilogram·meter <sup>2</sup> (kg·m <sup>2</sup> )
pound-mass-foot <sup>3</sup>	1.601 846	X E +1	kilogram/meter <sup>3</sup> (kg/m <sup>3</sup> )
rad (radiation dose absorbed)	1.000 000	X E -2	**Gray (Gy)
roentgen	2.579 760	X E -4	coulomb/kilogram (C/kg)
shake	1.000 000	X E -8	second (s)
slug	1.459 390	X E +1	kilogram (kg)
torr (mm Hg, 0° C)	1.333 22	X E -1	kilo pascal (kPa)

\*The becquerel (Bq) is the SI unit of radioactivity; 1 Bq = 1 event/s.

\*\*The Gray (Gy) is the SI unit of absorbed radiation.

## TABLE OF CONTENTS

Section	Page
SUMMARY .....	iii
PREFACE .....	v
CONVERSION TABLE .....	vi
FIGURES .....	ix
TABLES.....	xx
<b>1 INTRODUCTION .....</b>	<b>1</b>
<b>1.1 BACKGROUND AND OBJECTIVES .....</b>	<b>1</b>
<b>1.2 SUMMARY .....</b>	<b>3</b>
<b>1.2.1 Literature Review .....</b>	<b>3</b>
<b>1.2.2 Uniaxial Strain Experiments .....</b>	<b>7</b>
<b>1.2.3 Spherical Wave Experiment.....</b>	<b>15</b>
<b>1.3 REPORT ORGANIZATION .....</b>	<b>23</b>
<b>2 LITERATURE REVIEW OF THE SHOCK RESPONSE OF CALCITE .....</b>	<b>24</b>
<b>2.1 PHASE TRANSITIONS.....</b>	<b>24</b>
<b>2.2 LOADING HUGONIOT .....</b>	<b>36</b>
<b>2.3 UNLOADING ADIABAT .....</b>	<b>42</b>
<b>2.4 EFFECT OF JOINTS ON WAVE PROPAGATION .....</b>	<b>44</b>
<b>2.5 SYNOPSIS .....</b>	<b>47</b>
<b>3 UNIAXIAL STRAIN EXPERIMENTS .....</b>	<b>49</b>
<b>3.1 MOTIVATIONS AND OBJECTIVES .....</b>	<b>49</b>
<b>3.2 EXPERIMENTAL TECHNIQUES .....</b>	<b>49</b>
<b>3.2.1 Materials.....</b>	<b>49</b>
<b>3.2.2 Specimen Configurations and Assembly .....</b>	<b>51</b>
<b>3.2.3 Instrumentation .....</b>	<b>54</b>
<b>3.3 EXPERIMENTAL RESULTS .....</b>	<b>59</b>
<b>3.4 LAGRANGIAN ANALYSIS .....</b>	<b>64</b>

## TABLE OF CONTENTS (Continued)

Section		Page
3.5	CODE SIMULATIONS.....	65
3.6	DISCUSSION .....	69
	3.6.1 Hugoniot Elastic Limit and Phase Transitions.....	69
	3.6.2 Effect of Joints on Wave Propagation.....	71
4	SPHERICAL WAVE EXPERIMENT.....	81
4.1	MOTIVATIONS AND OBJECTIVES.....	81
4.2	EXPERIMENTAL TECHNIQUES .....	81
4.3	EXPERIMENTAL RESULTS AND DISCUSSION .....	83
4.4	CODE SIMULATIONS.....	98
	4.4.1 Description of the Model .....	98
	4.4.2 Simulation Results .....	99
5	REFERENCES.....	101
APPENDICES		
A	RISE TIME OF IN-MATERIAL GAGES.....	A-1
B	SUMMARY OF THE EXPERIMENTAL RESULTS OF THE UNIAXIAL STRAIN, IN-CONTACT EXPLOSIVE EXPERIMENTS .....	B-1
C	MODEL SOLUTIONS FOR THE INTERACTION OF STEADY-STATE COMPRESSION WAVES WITH A BOUNDARY .....	C-1

## FIGURES

Figure		Page
1-1	A collection of Hugoniot data for nonporous (less than 0.5% porosity) calcium carbonate ( $\text{CaCO}_3$ ) rock in the stress-volumetric strain plane .....	6
1-2	Configurations of the uniaxial strain experiments .....	8
1-3	Simulated particle velocity histories for a typical experiment on intact marble .....	10
1-4	Simulated particle velocity histories at the first gage plane .....	11
1-5	Simulated particle velocity histories at the second gage plane .....	11
1-6	Effect of a single sand-filled joint on wave propagation .....	13
1-7	Effect of a triple sand-filled joint on wave propagation .....	14
1-8	Overall configuration of the spherical wave experiment in Danby marble .....	16
1-9	Layout of the particle velocity gages in the spherical wave experiments .....	17
1-10	Summary of the particle velocity histories recorded during the spherical wave experiment in Danby marble .....	18
1-11	Experimentally observed crack patterns in the spherical wave experiment on Danby marble (the markings on the left half of the specimen are the grooves for the particle velocity gages and their leads .....	20
1-12	Comparison between simulated and experimentally observed crack patterns in the spherical wave experiment on Danby marble .....	22
2-1	Phase diagram for $\text{CaCO}_3$ including metastable phases II, III, and IV .....	26
2-2	Pressure-volume relationship showing the various low pressure phase transformations in calcite rock .....	28
2-3	Compressional wave velocity as a function of pressure for several calcite rocks. The sharp drop in velocity at a pressure of about 15 kbar is associated with the calcite I - calcite II transition .....	29
2-4	Wave velocity as a function of pressure for Solenhofen limestone in three mutually perpendicular directions .....	31
2-5	Compressional and shear wave velocities as a function of pressure for Oak Hall quarry limestone .....	32

## FIGURES (Continued)

Figure		Page
2-6	Compressional wave velocity as a function of pressure for Danby marble, depicting the dependence of calcite I-calcite II phase transition pressure on temperature.....	33
2-7	Calcite I-calcite II and calcite II-calcite III phase boundaries in pressure-temperature space for calcite rock .....	34
2-8	A collection of Hugoniot data for calcium carbonate ( $\text{CaCO}_3$ ) rock in the stress-volumetric strain plane.....	38
2-9	A collection of Hugoniot data for nonporous (less than 0.5% porosity) calcium carbonate ( $\text{CaCO}_3$ ) rock in the stress-volumetric strain plane .....	39
2-10	Comparison of the loading Hugoniots of dry and saturated nonporous calcium carbonate ( $\text{CaCO}_3$ ) rock.....	40
2-11	Comparison of the loading Hugoniots of dry, saturated, and saturated-frozen porous calcium carbonate ( $\text{CaCO}_3$ ) rock .....	41
2-12	A collection of Hugoniot data for calcium carbonate ( $\text{CaCO}_3$ ) rock in the stress-specific volume plane .....	43
2-13	Hugoniot and release data for dry Indiana limestone .....	45
2-14	Hugoniot and release data for water-saturated Indiana limestone .....	46
3-1	Configurations of the uniaxial strain experiments .....	52
3-2	Geometry of the surfaces of a rough joint.....	53
3-3	Specimen configuration and dimensions for HPEOS Experiment 1 in UTTR limestone .....	55
3-4	Schematic diagram of a typical uniaxial strain experiment instrumented with particle velocity gages.....	57
3-5	Engineering drawing showing the specifications and dimensions of a prefabricated particle velocity gage .....	58
3-6	Manganin gage record in HPEOS Experiment 1 .....	60
3-7	Stress history at the gage plane in HPEOS Experiment 1 .....	61
3-8	Wave reverberations due to impedance mismatch between the test medium and the free surface velocity gage (pressure is positive in compression) .....	63
3-9	Comparison between the equation of state used in the PUFF simulations and experimental data for nonporous calcite .....	67

## FIGURES (Continued)

Figure		Page
3-10	Target configuration and dimensions for Murri Experiment 1883-53 on Linden Hall limestone .....	68
3-11	Comparison of experimental and calculated particle velocity histories for Murri Experiment 1883-53 .....	70
3-12	Average particle velocity history at the second gage plane of HPEOS Experiment 2 showing the prominent features of the experimental data for intact marble .....	72
3-13	Simulated particle velocity histories for a typical experiment on intact marble .....	74
3-14	Simulated particle velocity histories at the first gage plane .....	75
3-15	Simulated particle velocity histories at the second gage plane .....	75
3-16	Simulated particle velocity histories at the third gage plane .....	76
3-17	Simulated particle velocity histories at the fourth gage plane .....	76
3-18	Effect of a single sand-filled joint on wave propagation .....	78
3-19	Effect of a triple sand-filled joint on wave propagation .....	79
4-1	Overall configuration of the spherical wave experiment in Danby marble .....	82
4-2	Details of the charge cavity and the detonating fuze used in the spherical wave experiment .....	84
4-3	Layout of the particle velocity gages in the spherical wave experiments .....	85
4-4	Particle velocity histories at the 1.0-cm range in the spherical wave experiment on Danby marble .....	86
4-5	Particle velocity histories at the 1.5-cm range in the spherical wave experiment on Danby marble .....	86
4-6	Particle velocity histories at the 2.0-cm range in the spherical wave experiment on Danby marble .....	87
4-7	Particle velocity histories at the 2.5-cm range in the spherical wave experiment on Danby marble .....	87
4-8	Particle velocity histories at the 3.0-cm range in the spherical wave experiment on Danby marble .....	88
4-9	Particle velocity histories at the 3.5-cm range in the spherical wave experiment on Danby marble .....	88

## FIGURES (Continued)

<b>Figure</b>		<b>Page</b>
4-10	Particle velocity histories at the 4.0-cm range in the spherical wave experiment on Danby marble .....	89
4-11	Particle velocity histories at the 5.0-cm range in the spherical wave experiment on Danby marble .....	89
4-12	Experimentally observed crack patterns in the spherical wave experiment on Danby marble .....	91
4-13	Distance-time of arrival data for determining the wave velocity in the spherical wave experiment .....	93
4-14	Displacement histories at the 1.0-cm range in the spherical wave experiment on Danby marble .....	94
4-15	Displacement histories at the 1.5-cm range in the spherical wave experiment on Danby marble .....	94
4-16	Displacement histories at the 2.0-cm range in the spherical wave experiment on Danby marble .....	95
4-17	Displacement histories at the 2.5-cm range in the spherical wave experiment on Danby marble .....	95
4-18	Displacement histories at the 3.0-cm range in the spherical wave experiment on Danby marble .....	96
4-19	Displacement histories at the 3.5-cm range in the spherical wave experiment on Danby marble .....	96
4-20	Displacement histories at the 4.0-cm range in the spherical wave experiment on Danby marble .....	97
4-21	Displacement histories at the 5.0-cm range in the spherical wave experiment on Danby marble .....	97
4-22	Comparison between simulated and experimentally observed crack patterns in the spherical wave experiment on Danby marble .....	100
A-1	Wave interactions between the test medium and the gage package (compressive waves are shown positive .....	A-2
A-2	Wave reverberations due to impedance mismatch between the test medium and the gage plane .....	A-4
A-3	Relative pressure and corresponding rise time for a typical gage plane .....	A-7
B-1	Specimen configuration and dimensions for HPEOS Experiment 1 (UTTR limestone) .....	B-3

## FIGURES (Continued)

<b>Figure</b>		<b>Page</b>
B-2	Manganin gage record in HPEOS Experiment 1 .....	B-4
B-3	Stress history at the gage plane in HPEOS Experiment 1.....	B-5
B-4	Specimen configuration and dimensions for HPEOS Experiment 2 (marble).....	B-6
B-5	Summary of the output of all particle velocity gages in HPEOS Experiment 2 .....	B-7
B-6	Output of particle velocity gages at the first gage plane of HPEOS Experiment 2 .....	B-8
B-7	Output of particle velocity gages at the second gage plane of HPEOS Experiment 2 .....	B-8
B-8	Output of particle velocity gages at the third gage plane of HPEOS Experiment 2 .....	B-9
B-9	Output of particle velocity gages at the fourth gage plane of HPEOS Experiment 2 .....	B-9
B-10	Output of the particle velocity gages at the fifth gage plane (free surface) of HPEOS Experiment 2 .....	B-10
B-11	Particle velocity histories at the first gage plane of HPEOS Experiment 2 .....	B-11
B-12	Particle velocity histories at the second gage plane of HPEOS Experiment 2 .....	B-11
B-13	Particle velocity histories at the third gage plane of HPEOS Experiment 2 .....	B-12
B-14	Particle velocity histories at the fourth gage plane of HPEOS Experiment 2 .....	B-12
B-15	Particle velocity histories at the fifth gage plane (free surface) of HPEOS Experiment 2 .....	B-13
B-16	Specimen configuration and dimensions for HPEOS Experiment 4 (marble).....	B-14
B-17	Summary of the output of all particle velocity gages in HPEOS Experiment 4 .....	B-15
B-18	Output of the particle velocity gages at the first gage plane of HPEOS Experiment 4 .....	B-16
B-19	Output of the particle velocity gages at the second gage plane of HPEOS Experiment 4 .....	B-16
B-20	Output of the particle velocity gages at the third gage plane of HPEOS Experiment 4 .....	B-17
B-21	Output of the particle velocity gages at the fourth gage plane of HPEOS Experiment 4 .....	B-17

## FIGURES (Continued)

<b>Figure</b>		<b>Page</b>
B-22	Specimen configuration and dimensions for HPEOS Experiment 5 (marble).....	B-18
B-23	Summary of the output of all particle velocity gages in HPEOS Experiment 5 .....	B-19
B-24	Output of the particle velocity gages at the first gage plane of HPEOS Experiment 5 .....	B-20
B-25	Output of the particle velocity gages at the second gage plane of HPEOS Experiment 5 .....	B-20
B-26	Output of the particle velocity gages at the third gage plane of HPEOS Experiment 5 .....	B-21
B-27	Output of the particle velocity gages at the fourth gage plane of HPEOS Experiment 5 .....	B-21
B-28	Specimen configuration and dimensions for HPEOS Experiment 6 (marble).....	B-22
B-29	Summary of the output of all particle velocity gages in HPEOS Experiment 6 .....	B-23
B-30	Output of prefabricated particle velocity gages at the first gage plane of HPEOS Experiment 6 .....	B-24
B-31	Output of SRI-manufactured particle velocity gages at the first gage plane of HPEOS Experiment 6 .....	B-24
B-32	Output of SRI-manufactured particle velocity gages at the second gage plane of HPEOS Experiment 6 .....	B-25
B-33	Output of SRI-manufactured particle velocity gages at the third gage plane of HPEOS Experiment 6 .....	B-25
B-34	Output of SRI-manufactured particle velocity gages at the fourth gage plane of HPEOS Experiment 6 .....	B-26
B-35	Comparison of the output of prefabricated and SRI-manufactured particle velocity gages in HPEOS Experiment 6 (data for the first gage plane).....	B-27
B-36	Particle velocity histories at the first gage plane of HPEOS Experiment 6 (prefabricated gages).....	B-28
B-37	Particle velocity histories at the first gage plane of HPEOS Experiment 6 (SRI-manufactured gages) .....	B-28
B-38	Particle velocity histories at the second gage plane of HPEOS Experiment 6 (SRI-manufactured gages) .....	B-29
B-39	Particle velocity histories at the third gage plane of HPEOS Experiment 6 (SRI-manufactured gages) .....	B-29

## FIGURES (Continued)

<b>Figure</b>		<b>Page</b>
B-40	Particle velocity histories at the fourth gage plane of HPEOS Experiment 6 (SRI-manufactured gages) .....	B-30
B-41	Specimen configuration and dimensions for HPEOS Experiment 7 (marble).....	B-31
B-42	Summary of the output of all particle velocity gages in HPEOS Experiment 7 .....	B-32
B-43	Output of prefabricated particle velocity gages at the first gage plane of HPEOS Experiment 7 .....	B-33
B-44	Output of SRI-manufactured particle velocity gages at the first gage plane of HPEOS Experiment 7 .....	B-33
B-45	Output of SRI-manufactured particle velocity gages at the second gage plane of HPEOS Experiment 7 .....	B-34
B-46	Output of SRI-manufactured particle velocity gages at the third gage plane of HPEOS Experiment 7 .....	B-34
B-47	Output of SRI-manufactured particle velocity gages at the fourth gage plane of HPEOS Experiment 7 .....	B-35
B-48	Comparison of the output of prefabricated and SRI-manufactured particle velocity gages in HPEOS Experiment 7 (data for the first gage plane).....	B-36
B-49	Particle velocity histories at the first gage plane of HPEOS Experiment 7 (prefabricated gages).....	B-37
B-50	Particle velocity histories at the first gage plane of HPEOS Experiment 7 (SRI-manufactured gages) .....	B-37
B-51	Particle velocity histories at the second gage plane of HPEOS Experiment 7 (SRI-manufactured gages) .....	B-38
B-52	Particle velocity histories at the third gage plane of HPEOS Experiment 7 (SRI-manufactured gages) .....	B-38
B-53	Particle velocity histories at the fourth gage plane of HPEOS Experiment 7 (SRI-manufactured gages) .....	B-39
B-54	Specimen configuration and dimensions for HPEOS Experiment 8 (marble).....	B-40
B-55	Summary of the output of all particle velocity gages in HPEOS Experiment 8 .....	B-41
B-56	Output of the particle velocity gages at the first gage plane of HPEOS Experiment 8 .....	B-42
B-57	Output of the particle velocity gages at the second gage plane of HPEOS Experiment 8 .....	B-42

## FIGURES (Continued)

<b>Figure</b>		<b>Page</b>
B-58	Output of the particle velocity gages at the third gage plane of HPEOS Experiment 8 .....	B-43
B-59	Output of the particle velocity gages at the fourth gage plane of HPEOS Experiment 8 .....	B-43
B-60	Particle velocity histories at the first gage plane of HPEOS Experiment 8 .....	B-44
B-61	Particle velocity histories at the second gage plane of HPEOS Experiment 8 .....	B-44
B-62	Particle velocity histories at the third gage plane of HPEOS Experiment 8 .....	B-45
B-63	Particle velocity histories at the fourth gage plane of HPEOS Experiment 8.....	B-45
B-64	Specimen configuration and dimensions for HPEOS Experiment 10 (marble).....	B-46
B-65	Summary of the output of all particle velocity gages in HPEOS Experiment 10.....	B-47
B-66	Output of the particle velocity gages at the first gage plane of HPEOS Experiment 10 .....	B-48
B-67	Output of the particle velocity gages at the second gage plane of HPEOS Experiment 10 .....	B-48
B-68	Output of the particle velocity gages at the third gage plane of HPEOS Experiment 10 .....	B-49
B-69	Output of the particle velocity gages at the fourth gage plane of HPEOS Experiment 10 .....	B-49
B-70	Particle velocity histories at the first gage plane of HPEOS Experiment 10 .....	B-50
B-71	Particle velocity histories at the second gage plane of HPEOS Experiment 10 .....	B-50
B-72	Particle velocity histories at the third gage plane of HPEOS Experiment 10.....	B-51
B-73	Particle velocity histories at the fourth gage plane of HPEOS Experiment 10.....	B-51
B-74	Specimen configuration and dimensions for HPEOS Experiment 11 (marble).....	B-52
B-75	Summary of the output of all particle velocity gages in HPEOS Experiment 11 .....	B-53
B-76	Output of the particle velocity gages at the first gage plane of HPEOS Experiment 11 .....	B-54
B-77	Output of the particle velocity gages at the second gage plane of HPEOS Experiment 11 .....	B-54

## FIGURES (Continued)

<b>Figure</b>		<b>Page</b>
B-78	Output of the particle velocity gages at the third gage plane of HPEOS Experiment 11 .....	B-55
B-79	Output of the particle velocity gages at the fourth gage plane of HPEOS Experiment 11 .....	B-55
B-80	Particle velocity histories at the first gage plane of HPEOS Experiment 11 .....	B-56
B-81	Particle velocity histories at the second gage plane of HPEOS Experiment 11 .....	B-56
B-82	Particle velocity histories at the third gage plane of HPEOS Experiment 11 .....	B-57
B-83	Particle velocity histories at the fourth gage plane of HPEOS Experiment 11.....	B-57
B-84	Specimen configuration and dimensions for HPEOS Experiment 12 (marble).....	B-58
B-85	Summary of the output of all particle velocity gages in HPEOS Experiment 12 .....	B-59
B-86	Output of the particle velocity gages at the first gage plane of HPEOS Experiment 12 .....	B-60
B-87	Output of the particle velocity gages at the second gage plane of HPEOS Experiment 12 .....	B-60
B-88	Output of the particle velocity gages at the third gage plane of HPEOS Experiment 12 .....	B-61
B-89	Output of the particle velocity gages at the fourth gage plane of HPEOS Experiment 12 .....	B-61
B-90	Particle velocity histories at the first gage plane of HPEOS Experiment 12 .....	B-62
B-91	Particle velocity histories at the second gage plane of HPEOS Experiment 12 .....	B-62
B-92	Particle velocity histories at the third gage plane of HPEOS Experiment 12 .....	B-63
B-93	Particle velocity histories at the fourth gage plane of HPEOS Experiment 12.....	B-63
B-94	Specimen configuration and dimensions for HPEOS Experiment 13 (marble).....	B-64
B-95	Summary of the output of all particle velocity gages in HPEOS Experiment 13 .....	B-65
B-96	Output of the particle velocity gages at the first gage plane of HPEOS Experiment 13 .....	B-66
B-97	Output of the particle velocity gages at the second gage plane of HPEOS Experiment 13 .....	B-66

## FIGURES (Continued)

Figure		Page
B-98	Output of the particle velocity gages at the third gage plane of HPEOS Experiment 13 .....	B-67
B-99	Output of the particle velocity gages at the fourth gage plane of HPEOS Experiment 13 .....	B-67
B-100	Particle velocity histories at the first gage plane of HPEOS Experiment 13 .....	B-68
B-101	Particle velocity histories at the second gage plane of HPEOS Experiment 13 .....	B-68
B-102	Particle velocity histories at the third gage plane of HPEOS Experiment 13 .....	B-69
B-103	Particle velocity histories at the fourth gage plane of HPEOS Experiment 13 .....	B-69
B-104	Specimen configuration and dimensions for HPEOS Experiment 14 (marble).....	B-70
B-105	Summary of the output of all particle velocity gages in HPEOS Experiment 14 .....	B-71
B-106	Output of the particle velocity gages at the first gage plane of HPEOS Experiment 14 .....	B-72
B-107	Output of the particle velocity gages at the second gage plane of HPEOS Experiment 14 .....	B-72
B-108	Output of the particle velocity gages at the third gage plane of HPEOS Experiment 14 .....	B-73
B-109	Output of the particle velocity gages at the fourth gage plane of HPEOS Experiment 14 .....	B-73
B-110	Particle velocity histories at the first gage plane of HPEOS Experiment 14 .....	B-74
B-111	Particle velocity histories at the second gage plane of HPEOS Experiment 14 .....	B-74
B-112	Particle velocity histories at the third gage plane of HPEOS Experiment 14 .....	B-75
B-113	Particle velocity histories at the fourth gage plane of HPEOS Experiment 14.....	B-75
B-114	Specimen configuration and dimensions for HPEOS experiment 16 (UTR limestone) .....	B-76
B-115	Summary of the output of all particle velocity gages in HPEOS Experiment 16 .....	B-77
B-116	Output of the particle velocity gages at the first gage plane of HPEOS Experiment 16 .....	B-78
B-117	Output of the particle velocity gages at the second gage plane of HPEOS Experiment 16 .....	B-78

## FIGURES (Continued)

Figure		Page
B-118	Output of the particle velocity gages at the third gage plane of HPEOS Experiment 16 .....	B-79
B-119	Output of the particle velocity gages at the fourth gage plane of HPEOS Experiment 16 .....	B-79
B-120	Particle velocity histories at the first gage plane of HPEOS Experiment 16 .....	B-80
B-121	Particle velocity histories at the second gage plane of HPEOS Experiment 16 .....	B-80
B-122	Particle velocity histories at the third gage plane of HPEOS Experiment 16 .....	B-81
B-123	Particle velocity histories at the fourth gage plane of HPEOS Experiment 16.....	B-81
C-1	A nondimensional Lagrange distance-time diagram for the flow produced by the reflection of a steady-state compression wave from a boundary with a higher shock impedance when the material supporting the incident wave and the bounding material (BM) have linear stress ( $\sigma$ ) - particle velocity (u) relationships .....	C-4
C-2	A set of nondimensional Lagrange particle velocity ( $u/\ell_0$ ) - time ( $t/T$ ) profiles recorded in the flow produced when a steady-state compression wave propagating in a material with a linear stress ( $\sigma$ ) - particle velocity (u) relationship is reflected from a free surface .....	C-11
C-3	A nondimensional Lagrange distance-time diagram showing the stress ( $\sigma$ ) and particle velocity (u) contours in an incident nonlinear steady-state compression wave and in the flow produced by its reflection from a free surface .....	C-12

## TABLES

Table		Page
1-1	Summary of the wave propagation experiments .....	2
1-2	Static experimental measurements of the pressures and volume changes associated with the various calcite phase transitions .....	4
1-3	Dynamic experimental measurements of the pressures associated with the various calcite phase transitions .....	5
2-1	Static experimental measurements of the pressures and volume changes associated with the various calcite phase transitions .....	27
2-2	Dynamic experimental measurements of the pressures associated with the various calcite phase transitions .....	35
2-3	Summary of experimental studies investigating the behavior of calcite rock under impact loading conditions .....	37
3-1	Parameters used to describe the behavior of marble in the PUFF finite difference simulations .....	66
A-1	Computed relative pressures and equilibrium times for an epoxy gage plane embedded in limestone .....	A-6
B-1	Summary of the configurations and dimensions of the uniaxial strain experiments .....	B-2

## **SECTION 1**

### **OVERVIEW**

#### **1.1 BACKGROUND AND OBJECTIVES.**

The present investigation was undertaken as part of the HYDRO PLUS program to gain an improved knowledge of the material behavior parameters and thus increase confidence in the HYDRO PLUS yield estimation methodology. With this methodology, the yield of a large, nonstandard, underground nuclear event is estimated based on a combination of experimental measurements of the shock wave parameters (stress, particle velocity, shock velocity) near the source and computational predictions of the close-in ground motion as a function of the yield of the nuclear event. The reliability of the estimated yield is therefore closely related to the quality of the experimental ground shock data and the accuracy of the constitutive model used in the numerical simulations.

During the early stages of the investigation, SRI performed a literature review to identify regions of the high pressure equation of state of rock that are of interest to the HYDRO PLUS program and have not been explored experimentally. The material behavior parameters emphasized in this review were the loading Hugoniot, the unloading adiabat, phase transitions, and the effect of joints on wave propagation. Our findings, which are detailed in a later section, revealed that the effect of joints on wave propagation is the least investigated aspect of the behavior of rock. For this reason, investigating the effect of joints on wave propagation became the primary objective of the present investigation. Calcite (calcium carbonate, chemical formula  $\text{CaCO}_3$ ) was chosen for this study; partly because it is one of the most abundant carbonate mineral types in the crust of the earth and partly because of DNA's ongoing interest in obtaining statistical variations in material properties for jointed limestone (a calcite rock) and in developing techniques for including the observed effects in material models for ground shock.

The experiments performed during the study are summarized in Table 1-1. As indicated, all but one of the experiments were performed under uniaxial strain loading conditions. Three of the uniaxial strain experiments were performed on UTTR limestone samples with naturally occurring, *in situ* joints. Danby (Vermont) marble was used in all the remaining experiments. Well characterized artificial joints of various configurations were introduced into the marble specimens to investigate the effect of joints on wave propagation. A spherical wave experiment was also conducted on a sample of intact Danby marble to complement the uniaxial strain experiments and to provide data that can be used to validate and/or calibrate constitutive models for use in finite element and finite difference hydrocodes.

**Table 1-1. Summary of the wave propagation experiments.**

Rock type	Loading Condition	Stress Range (kbar)	No. of Experiments	Measured Variable	Purpose of Experiment
UTTR limestone	Uniaxial strain (in-contact explosives)	250	1	Stress	<ul style="list-style-type: none"> <li>• Feasibility of measurement</li> <li>• Signal-to-noise ratio</li> </ul>
UTTR limestone	Uniaxial strain (in-contact explosives)	100 -150	2	Particle velocity	<ul style="list-style-type: none"> <li>• Effect of <i>in situ</i> joints</li> <li>• Loading/unloading data</li> </ul>
Danby marble	Uniaxial strain (in-contact explosives)	100 -150	13	Particle velocity	<ul style="list-style-type: none"> <li>• Effect of joints</li> <li>• Loading/unloading data</li> </ul>
Danby marble	Spherical wave (spherical charge)	<100	1	Radial particle velocity	<ul style="list-style-type: none"> <li>• Complement 1-D strain data</li> <li>• Constitutive model validation</li> </ul>

## **1.2 SUMMARY.**

### **1.2.1 Literature Review.**

Numerous studies have been conducted over the past 30 years to characterize the behavior of calcium carbonate rock under dynamic loadings. Many of the early dynamic wave propagation studies emphasized the characteristics of the loading Hugoniot and, to a lesser extent, the unloading adiabat and the effects of strength, porosity, and phase transformations on the material behavior.

Static high pressure studies played a significant role in furthering our understanding of the behavior of calcium carbonate rock. The pressure and volume change associated with the calcite I - calcite II and calcite II - calcite III phase transitions were first measured accurately in static experiments. These transitions have since been observed in shock wave propagation experiments and are now known to affect the shape of both the loading Hugoniot and the unloading adiabat of calcite rock in a predictable fashion. The loading and unloading behaviors of calcite rock are also affected by another phase transformation - the calcite III - calcite IV transition. This transition occurs at stresses in excess of 100 kbar and has only been observed in dynamic wave propagation experiments. Summaries of static and dynamic phase transformation measurements in calcium carbonate rock are provided in Tables 1-2 and 1-3, respectively.

The Hugoniot of calcium carbonate rock has been investigated for stresses up to about 500 kbar. For nonporous rock, the Hugoniot is well characterized and results from numerous investigations are very reproducible, as depicted in Figure 1-1. The Hugoniot elastic limit (HEL) of calcite occurs in the stress range from 10 to 20 kbar and depends on the porosity and graininess of the sample. The HEL is associated with the first two polymorphic calcite transitions (I - II and II - III).

The unloading adiabat is not too far removed from the loading Hugoniot, partly because of the fully reversible nature of the calcite phase transitions. In nonporous calcite, little hysteresis is observed upon complete unloading from a shock-loaded state. As one might expect, hysteresis increases with increasing porosity.

The effect of joints on material response is the least investigated aspect of the behavior of calcite rock. Our literature review unveiled only two studies aimed at investigating the effect of joints on wave propagation. These studies showed drastic differences between the responses of intact and jointed samples. This discovery, combined with DNA's interest in obtaining statistical variations in material properties for jointed limestone and developing techniques for including the observed effects in material models for ground shock, led to the consensus that the experiments to be conducted in this study should emphasize the effect of joints on material behavior.

**Table 1-2. Static experimental measurements of the pressures and volume changes associated with the various calcite phase transitions.**

Reference	Testing Method	Observed Transition	Pressure (kbar)	$\Delta V$ (cm <sup>3</sup> /g)
Bridgman (1939)	Hydrostatic compression	Calcite I $\rightarrow$ Calcite II Calcite II $\rightarrow$ Calcite III	14.7 17.7	0.00135 0.00956
Adadurov et al. (1960)	Hydrostatic compression	Calcite I $\rightarrow$ Calcite II Calcite II $\rightarrow$ Calcite III	11.21 16.32 22.43	0.00656 0.00293 0.01033
Vaidya et al. (1973)	Hydrostatic compression	Calcite II $\rightarrow$ Calcite III	17.1±0.4	0.04
Singh and Kennedy (1974)	Hydrostatic compression	Calcite I $\rightarrow$ Calcite II Calcite II $\rightarrow$ Calcite III	14.5 17.4	0.00483 0.01291
Wang (1966)	Ultrasonic measurements	Calcite I $\rightarrow$ Calcite II	15.5±0.5	
Wang and Meltzer (1973)	Ultrasonic measurements	Calcite I $\rightarrow$ Calcite II Calcite II $\rightarrow$ Calcite III	15.5 23.0	

**Table 1-3. Dynamic experimental measurements of the pressures associated with the various calcite phase transitions.**

Reference	Material	Initial Density (g/cm <sup>3</sup> )	Observed Transition	Transition Pressure (kbar)
Adadurov et al. (1960)	Icelandic spar	2.70	Calcite III → Calcite IV	153
Ahrens and Gregson (1964)	Yule and Vermont marbles and Solenhofen and Indiana limestones	2.38 - 2.70	Calcite I → Calcite II Calcite II → Calcite III Calcite III → Calcite IV	22 40 95
Murri et al. (1975)	Linden Hall limestone	2.70	Calcite I → Calcite II Calcite II → Calcite III Calcite III → Calcite IV	15 20 - 56 149±20
Grady et al. (1978)	Solenhofen and Oak Hall limestones and Vermont marble	2.61 - 2.71	Calcite I → Calcite II Calcite II → Calcite III	6, 10, 12* 24
Grady (1986)	Icelandic spar single crystal (z-axis)	2.71	Calcite III → Calcite IV	120 - 140
Stapleton and Gupta (1992)	Icelandic spar single crystal (c-axis)	2.71	Calcite I → Calcite II	17.6±0.4

\*6 kbar for Solenhofen limestone, 10 kbar for Oak Hall limestone, and 12 kbar for Vermont marble.

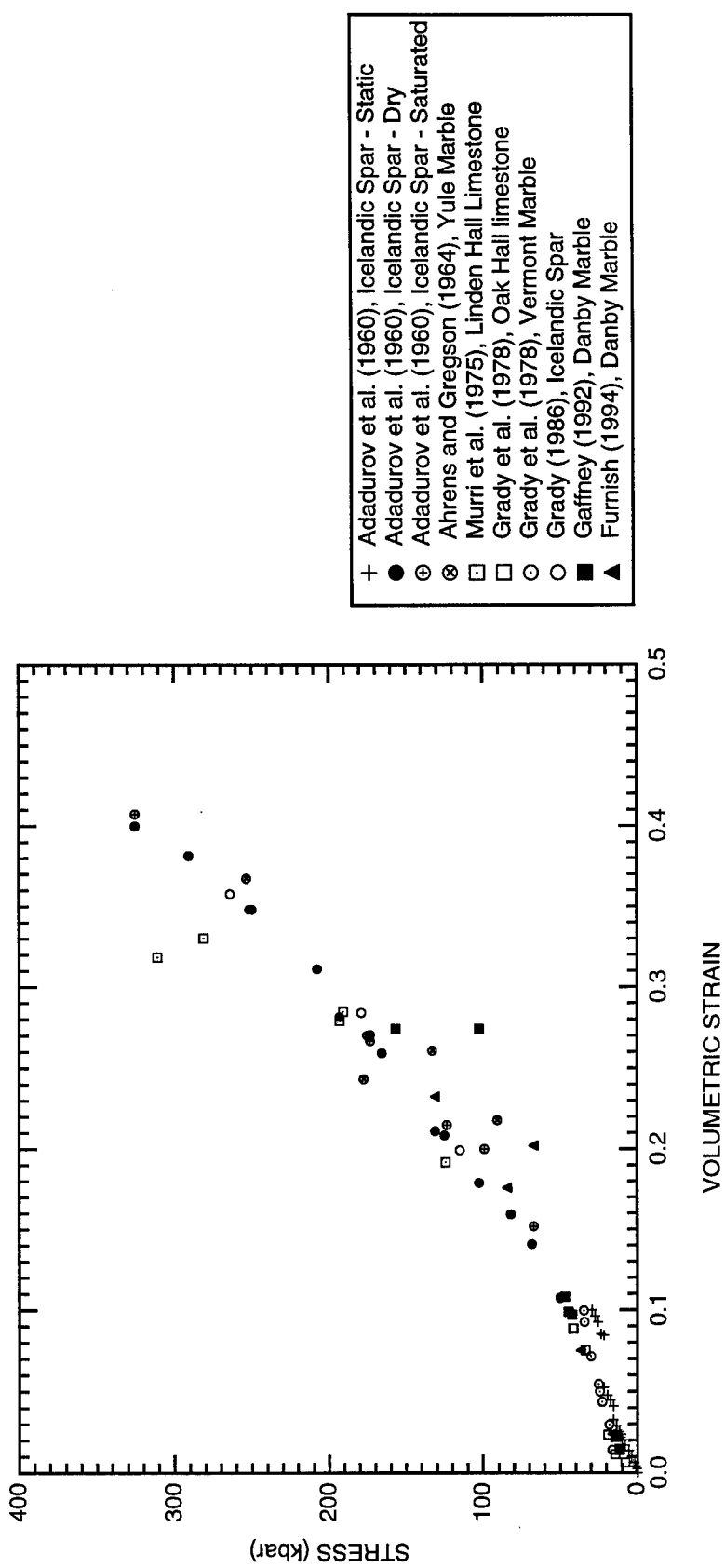


Figure 1-1. A collection of Hugoniot data for nonporous (less than 0.5% porosity) calcium carbonate ( $\text{CaCO}_3$ ) rock in the stress-volumetric strain plane.

## **1.2.2 Uniaxial Strain Experiments.**

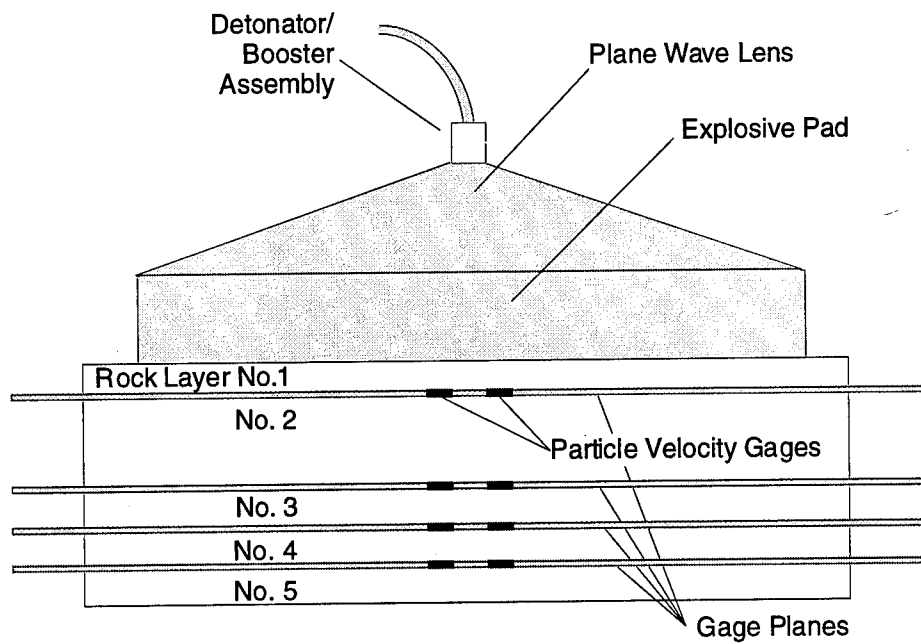
A series of uniaxial strain experiments was performed using in-contact explosive techniques to investigate the effect of *in situ* and artificial joints on wave propagation in calcium carbonate ( $\text{CaCO}_3$ ) rock. The experiments were motivated by a lack of experimental data on wave propagation in jointed rock and were aimed at providing results that will further our understanding of the effect of joints on wave propagation and provide a consistent set of results that can be used to develop, calibrate, or validate constitutive models suitable for use in hydrocode calculations.

The study consisted of experimental and analytical investigations. Experimentally, uniaxial strain experiments were conducted on both intact and jointed calcite rock samples. The experimental configurations investigated are shown in Figure 1-2. In the experiments, in-contact explosives initiated using 15.24-cm-diameter (6.0 in.) plane wave lenses were used to provide shock loadings in the rock samples. Several specimen designs incorporating different joint configurations were investigated. Experimental diagnostics consisted of in-material Lagrangian particle velocity gages embedded between rock layers at several serial locations within the specimen. Duplicate particle velocity measurements were obtained on each of four gage planes. The particle velocity gages on the first gage plane (nearest to the explosives) were used to record the oncoming stress wave generated by the explosives and thereby provide a basis for comparing the results of different experiments with different joint configurations. The remaining gages recorded the wave profile after passage of the wave through the jointed section of the specimen.

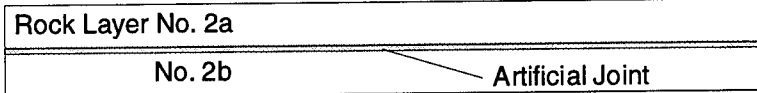
Analytically, Lagrangian finite difference hydrocode simulations were carried out to help in the interpretation of experimental results and provide added insight into the effect of joints on the response of calcium carbonate rock.

**1.2.2.1 Effect of Joints on Wave Propagation.** Two types of joints were investigated: *in situ* joints in UTTR limestone, and artificial joints in Danby (Vermont) marble. The *in situ* joints investigated were healed, calcite-filled fissures in a UTTR limestone matrix composed of calcite (62%) and quartz (31%) with traces of dolomite (2%), K-feldspar (2%), illite (2%), and pyrite (1%). Our limited results from the UTTR limestone experiments indicated that the *in situ* joints did not have a significant effect on the observed response.

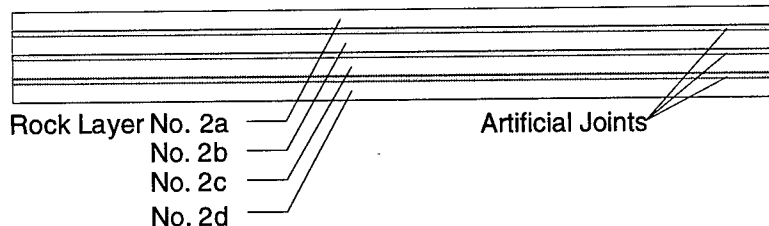
The artificial joints were embedded in Danby marble specimens. The joint parameters that were varied included surface texture (smooth versus rough), thickness (closed versus 2-mm-thick sand-filled), number (single versus triple), and orientation (normal versus inclined with respect to the direction of shock propagation). Intact marble specimens were also tested to provide baseline data for comparison with data for the jointed sample.



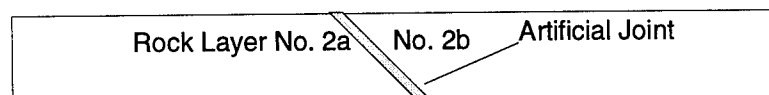
**(a)** Configuration for experiments on intact rock (basic configuration).



**(b)** Modification of the basic configuration to include a single, normal joint.



**(c)** Modification of the basic configuration to include a triple, normal joint.



**(d)** Modification of the basic configuration to include a single, inclined joint.

Figure 1-2. Configurations of the uniaxial strain experiments.

Closed joints did not have a measurable effect on the behavior of the rock, nor did the surface texture of the joint. However, significant effects were produced when a sand-filled joint was introduced into the sample. The perturbations to the free field were greatest for the triple normal joint configuration and smaller for the single inclined joint configuration, while the single normal joint configuration had the smallest measurable effect.

To better understand the effect of artificial joints on wave propagation, we performed a series of hydrocode simulations using the finite difference, wave propagation hydrocode SRI PUFF (Seaman and Curran, 1978). First, we simulated the response of an intact marble specimen having the configuration shown in Figure 1-2(a). We then simulated the response of jointed specimens having the configurations shown in Figures 1-2(b) (single joint) and 1-2(c) (triple joint). The effect of joints was established by comparing the results of the benchmark simulation in intact marble with the results of simulations in jointed marble.

Figure 1-3 shows the simulated particle velocity histories at each of the gage planes and at the free surface of the intact marble experiment. The first peak in the particle velocity histories corresponds to peak stress, and it is the same on all the gage planes. This peak, which also corresponds to the Chapman-Jouguet (C-J) pressure of the explosives, is followed by a gentle unloading wave that causes a gradual decrease in the particle velocity profiles. This is the Taylor unloading wave, which originates in the explosive gases. The second plateau in the particle velocity records is associated with the stress-free state in the specimen. It is carried through the specimen by a backward-travelling release wave that originates at the back surface of the specimen.

To gain insight into the effect of joints on wave propagation, the two experimental configurations with normally oriented artificial joints, shown in Figure 1-2(b) and 1-2(c), were also simulated. The resulting particle velocity histories at the first and second gage planes are compared with the results of the intact marble simulation in Figures 1-4 and 1-5, respectively. Two features associated with the effect of joints on the simulated particle velocity profiles are readily apparent. The first of these features is depicted in Figure 1-4: The particle velocity profiles on the first gage plane (ahead of the joint) are modified by spikes—one spike for the single joint configuration and three spikes for the triple joint configuration. These spikes, and the corresponding decrease in stress, result from wave reflections at the rock/joint interfaces. Interestingly, these spikes are not quite as apparent on the gage planes located behind the joint, although on the second gage plane the velocity history associated with the triple joint configuration shows characteristics similar to those observed on the first gage plane. The second feature associated with the effect of joints on the simulated particle velocity profiles is the delayed time of arrival (TOA) of the wave at the gage planes behind the joint. This delayed TOA is barely perceptible for the single joint configuration but more pronounced for the triple joint configuration. The TOA delay can be related to the number of reverberations required to bring the joint to pressure and particle velocity

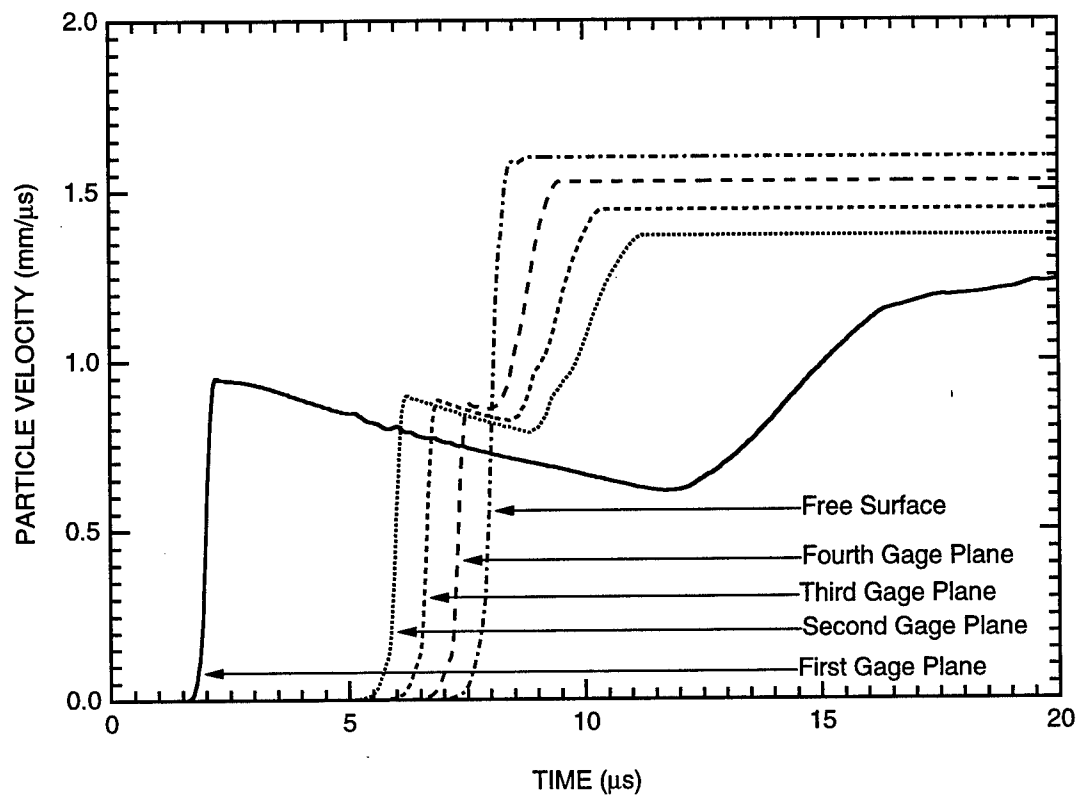


Figure 1-3. Simulated particle velocity histories for a typical experiment on intact marble.

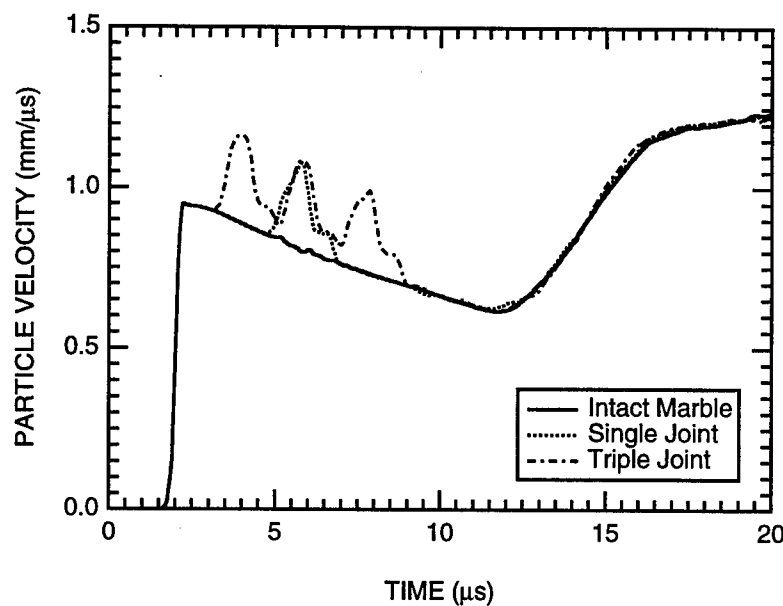


Figure 1-4. Simulated particle velocity histories at the first gage plane.

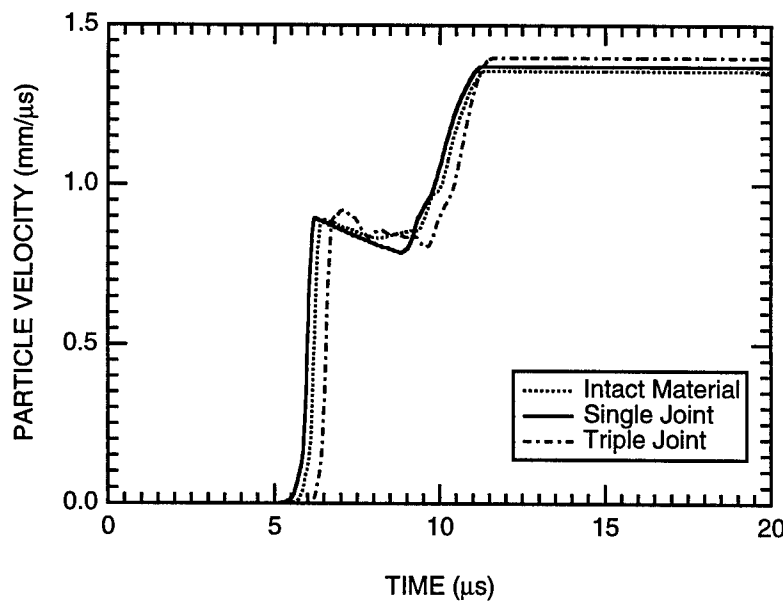


Figure 1-5. Simulated particle velocity histories at the second gage plane.

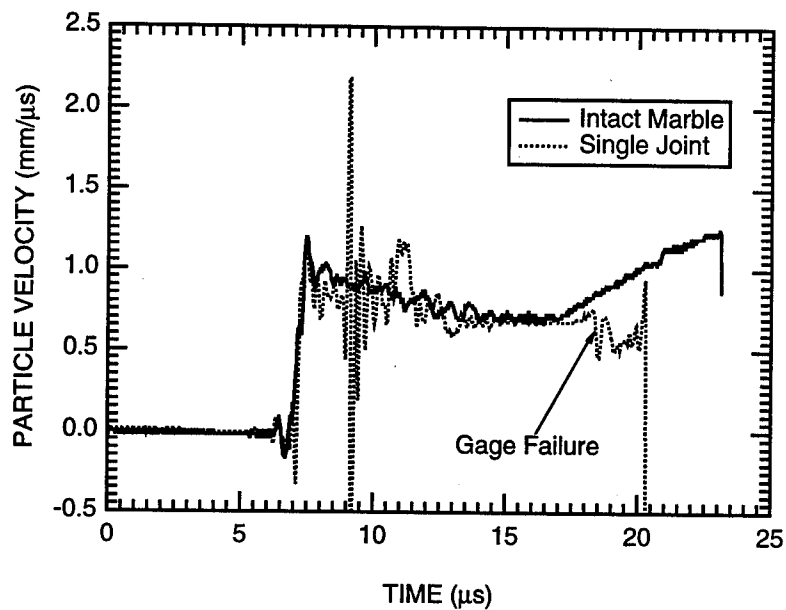
equilibrium with the test medium. It is not surprising, therefore, that the TOA delay associated with the triple joint is approximately three times that associated with the single joint.

The same effects observed in the PUFF simulations can also be observed in the experimental data, as illustrated in Figures 1-6 and 1-7 for the single joint and triple joint configurations, respectively. In each figure, the results from an experiment on intact marble are superimposed onto the results of an experiment on jointed marble. Part (a) in each figure corresponds to the gage location in front of the jointed section of the specimen, whereas part (b) corresponds to the gage location behind the jointed section. The narrow, large amplitude spikes at  $t = 8 \mu\text{s}$  in Figure 1-6(a) and at  $t = 11 \mu\text{s}$  in Figure 1-7(a) are most likely due to an air gap at the interface between the joint and the rock. This explanation is plausible because the spike is not observed at any of the gage planes behind the joint; and also because the spike reaches the gage before the expected reflection from the joint, a result indicating that the source of the spike is located at the interface between the gage plane and the joint.

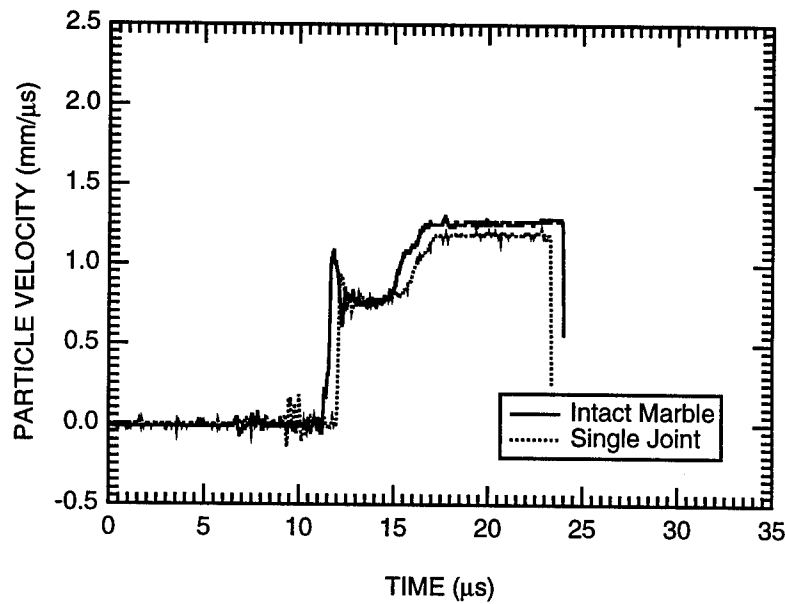
**1.2.2.2 Implications of the Results on the HYDRO PLUS Program.** The HYDRO PLUS methodology estimates the yield of a nuclear event on the basis of a combination of experimental measurements of the shock wave parameters near the source and computational predictions of the close-in ground motion. The methodology relies on measurements of peak stress, peak particle velocity, and shock TOA (and hence shock velocity) at different radii from the charge. The presence of joints was observed to have a wide range of effects on the magnitude of the particle velocity and the TOA measured in our uniaxial strain experiments. On one hand, negligible effects were observed when the joint was either closed or filled with a material that has an impedance similar to that of the host medium (i.e., calcite-filled joints in UTTR limestone). On the other hand, significant effects were observed when the joint was filled with a material that has an impedance substantially different from that of the host medium (i.e., sand-filled joints in marble).

Figures 1-4, 1-6, and 1-7 showed that a sand-filled joint causes a temporary increase in the magnitude of the particle velocity upstream from the joint. The TOA of the joint signature at the gage plane depends on the distance separating the joint from the gage. If this distance is small, the joint signature could affect the peak of the particle velocity profile, which in turn may lead to an erroneous HYDRO PLUS yield estimate. It is possible to recognize the signature of a joint by a careful, systematic analysis of the recorded data (DeCarli, 1993), but it is not easy to determine the free field velocity from the joint-affected, measured velocity. This difficulty may have an adverse effect on the overall precision of the yield estimated using the HYDRO PLUS methodology.

Downstream from the joint, the only significant effect observed in our uniaxial strain experiments was delayed TOA of the shock wave at the gage plane. The measured peak particle velocity (and the simulated peak stress) was not influenced by the joint. Thus, the presence of a joint upstream from the gage would only have a significant effect on the HYDRO PLUS yield estimation methodology if the

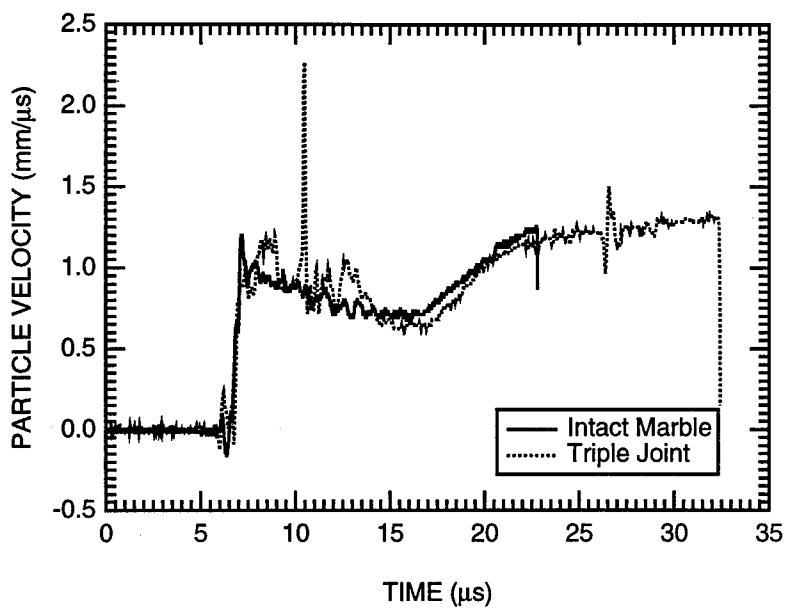


(a) Particle velocity histories at the first gage plane.

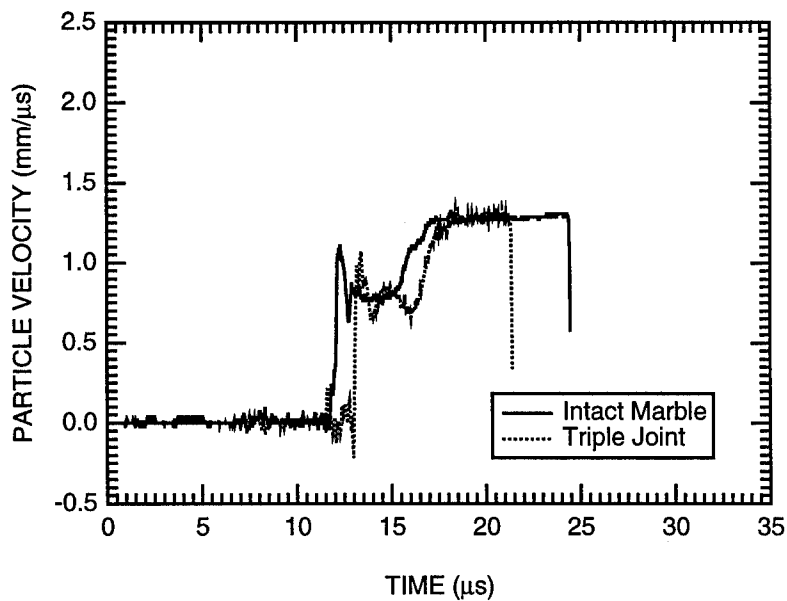


(b) Particle velocity histories at the second gage plane.

Figure 1-6. Effect of a single sand-filled joint on wave propagation.



(a) Particle velocity histories at the first gage plane.



(b) Particle velocity histories at the second gage plane.

Figure 1-7. Effect of a triple sand-filled joint on wave propagation.

shock velocity calculated based on TOA measurements is used to estimate the yield. It is worth noting that this effect becomes more significant with decreasing distance between TOA recording stations.

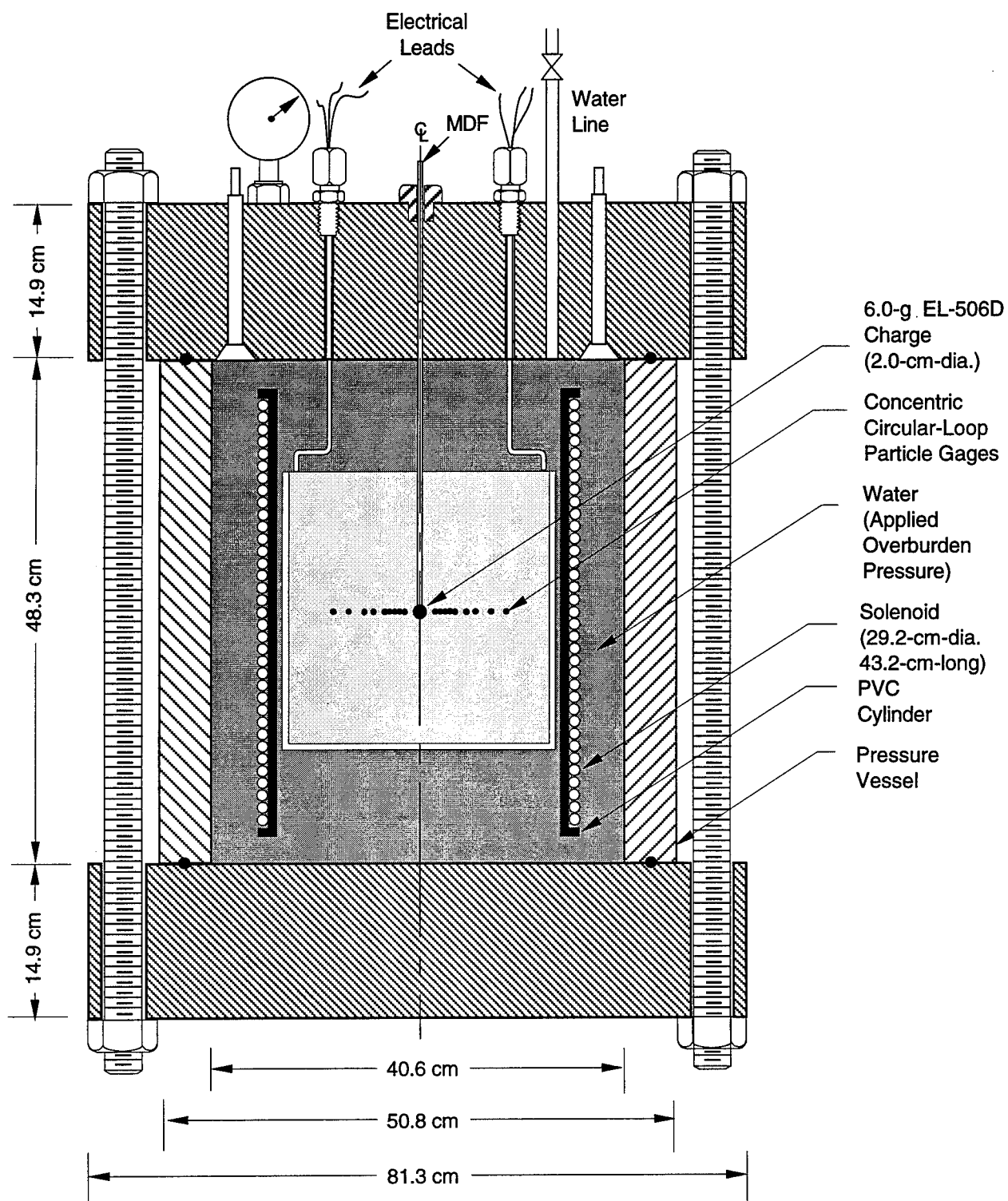
**1.2.2.3 Hugoniot and Phase Transitions.** In addition to the effects of joints on wave propagation described above, the results of the uniaxial strain experiments yielded information regarding the precursor and a high pressure phase transformation in  $\text{CaCO}_3$  rock. The precursor was observed during both loading and unloading and was most likely associated with the I-II and II-III phase transitions in calcite. Based on the loading data, the magnitude of the precursor was estimated to be between 16 and 19 kbar in marble and 14.3 kbar in UTTR limestone. The high pressure phase transition was observed in the marble experiments. The stress level associated with this transition was about 118 kbar.

### 1.2.3 Spherical Wave Experiment.

A spherical wave experiment was conducted on a sample of intact Danby marble to complement the uniaxial strain experiments and provide data that can be used to validate and/or calibrate constitutive models for use in finite element and finite difference hydrocodes. In the experiment, a 2-cm-diameter, 6-g EL-506D (Detasheet) explosive charge was detonated at the center of a 27-cm-diameter, 27-cm-long cylindrical block of marble as shown in Figure 1-8. The specimen assembly was placed inside a pressure vessel and surrounded by a solenoid that applied a constant, vertically oriented magnetic field through the particle velocity gage planes. A 6.9 MPa static overburden pressure was applied to the specimen during the experiment.

Particle velocity histories at several radii from the charge were measured by monitoring the motion of embedded wire gages through the externally applied magnetic field. The particle velocity gages consisted of strips of copper wire mounted into concentric, precision-machined grooves in the specimen. As shown in Figure 1-9, two diametrically opposite gages were used at each of eight radii starting at the charge boundary and extending outward to a radius of 5.0 cm. In most applications, the active element of each gage would cover the full circumference of one of the concentric circles shown in the figure. However, in the present study a different approach was taken to ensure that the direction along which the particle velocity histories were measured coincided with the direction of wave propagation in the uniaxial strain experiments. This arrangement allows for a direct comparison between the results of the uniaxial strain experiments and the results of the spherical wave experiment even if the rock behaves in an anisotropic fashion.

The particle velocity histories measured in the experiment on Danby marble are shown in Figure 1-10. Each of Figures 1-10(a) through 1-10(h) shows the two particle velocity histories measured at a given range. The letters 'a' and 'b' (following the gage number) in Figure 1-10 designate the two gage arrays



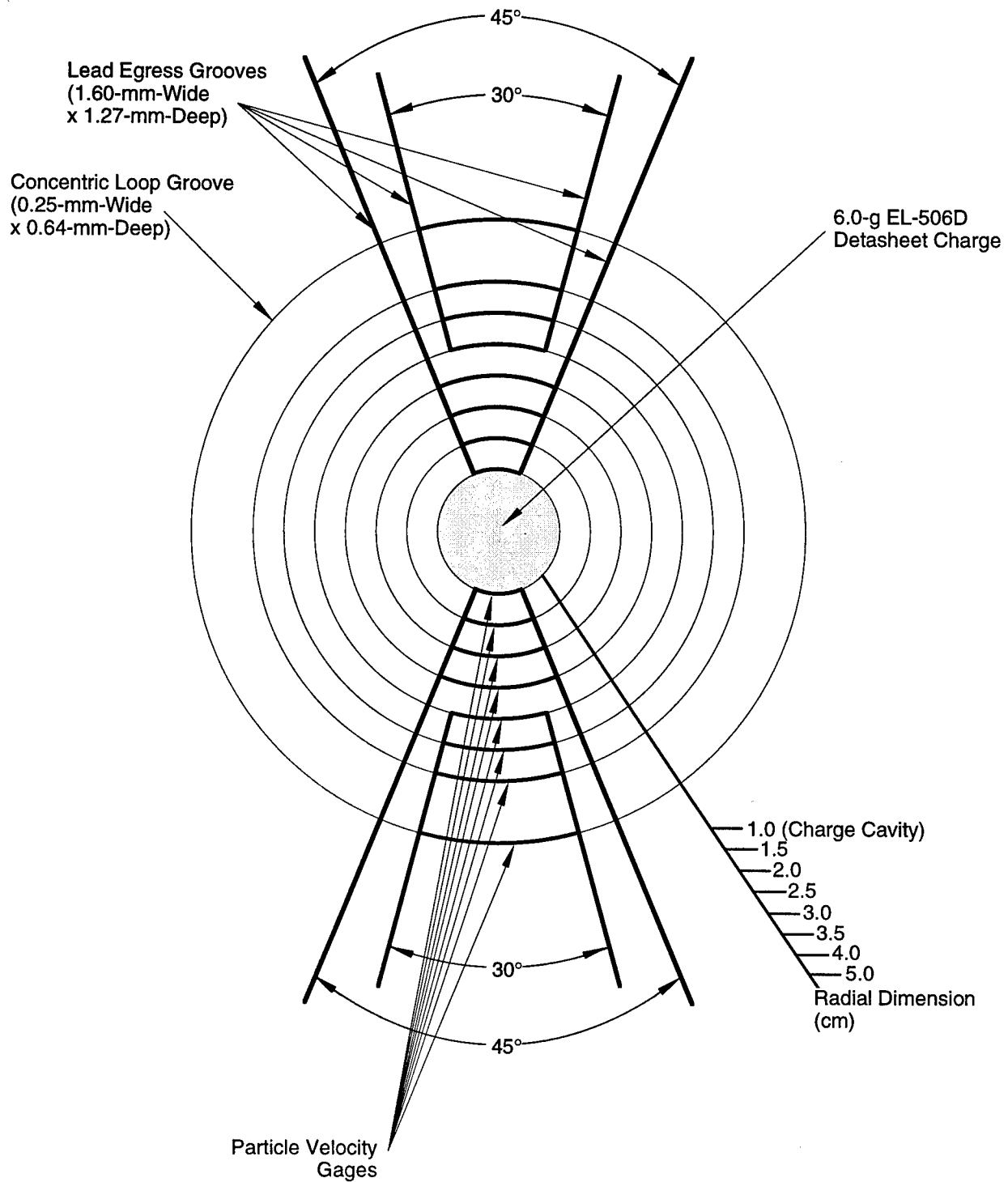


Figure 1-9. Layout of the particle velocity gages in the spherical wave experiments.

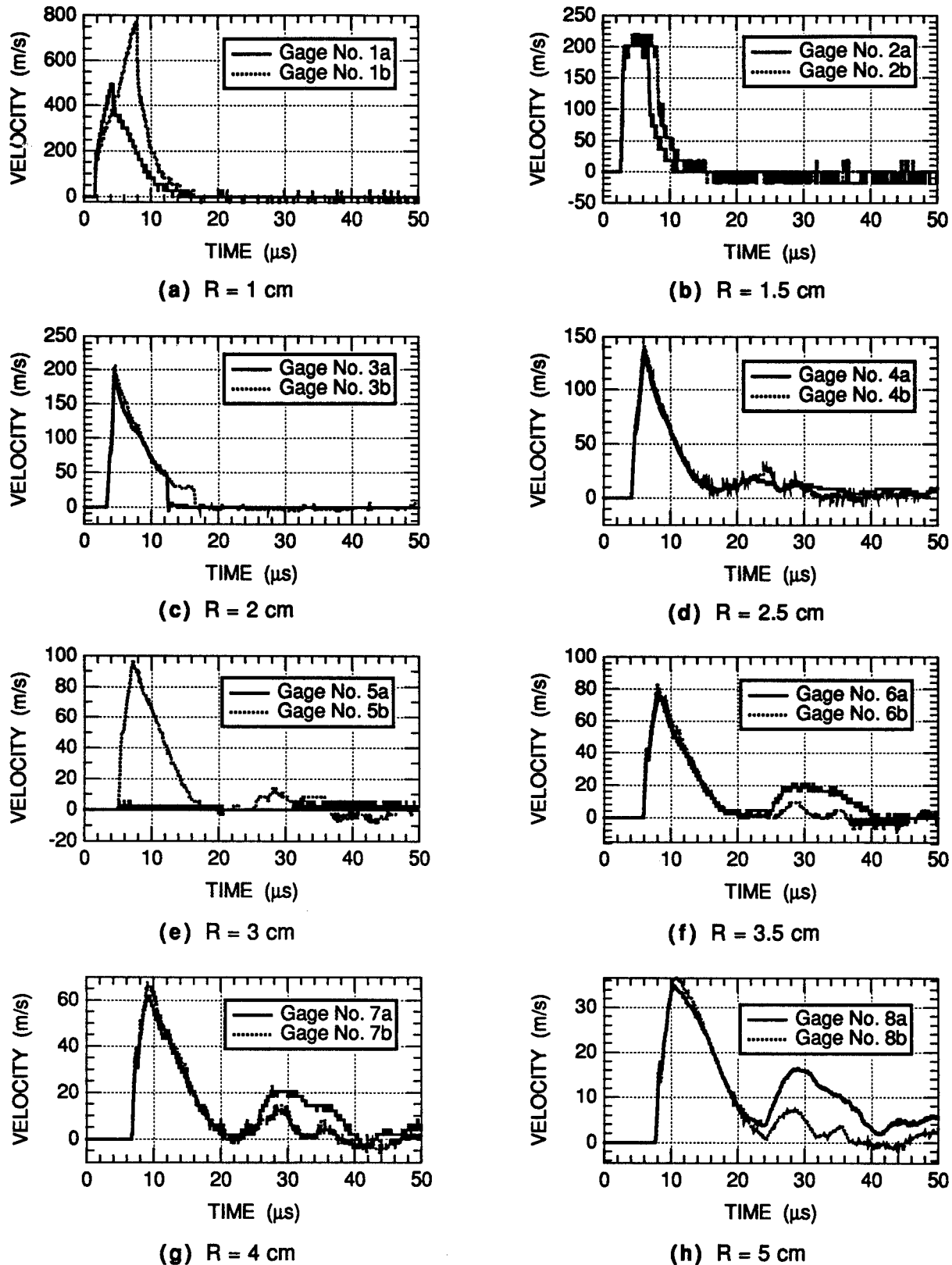


Figure 1-10. Summary of the particle velocity histories recorded during the spherical wave experiment in Danby marble.

on diametrically opposite sides of the charge. The particle velocity histories at the two ranges closest to the charge show characteristics that are different from the remainder of the data. We believe this is the result of premature gage failure due to the high stresses generated by the explosive charge.

The particle velocity gages at the 2.0-cm range [Figure 1-10(c)] captured the early-time response of the rock but failed to record the subsequent rebound signal. At ranges of 2.5 cm or larger, the particle velocity histories in the specimen were recorded for the duration of the experiment. At early times, these histories are characterized by a sharp rise to peak followed by an outward motion that lasts for about 10  $\mu$ s. This early-time response of the rock is very reproducible, as indicated by the nearly identical responses of the gage arrays on either side of the explosive charge [Figures 1-10(c) through 1-10(h)].

The outward expansion phase is followed by a rebound phase. In previous experiments on nonporous rock (Miller and Florence, 1990) and on porous CaCO<sub>3</sub> rock (Gefken and Florence, 1992), the rebound signal caused an inward contraction in the motion of the rock sample that was manifested by a reversal of the sign of the particle velocity histories. In the present experiment, the particle velocities recorded at all ranges remained positive throughout the rebound phase of the signal. This difference between the rebound signals measured in the present experiment and those measured in other investigations can be related to cracking of the rock sample. Extensive cracking was not observed in either of the two studies cited above. In contrast, the Danby marble specimen of the present study was severely cracked, as shown in Figure 1-11. Two distinct networks of cracks can be seen in each half of the specimen. The first network consists of numerous cracks emanating from the charge boundary and extending radially outward toward the free surface of the specimen. These radial cracks extend throughout the gaged region of the specimen, and a few cracks propagate all the way to the free surface. The second network of cracks consists primarily of circumferential cracks and does not appear to be symmetric with respect to the center of the explosive charge. An additional crack that does not appear to be associated with either of the crack networks mentioned so far can be observed spanning the whole specimen surface. This crack follows the path of a pre-existing *in situ* joint in the rock.

We believe that the extensive cracking in the Danby marble specimen caused degradation of the material properties and reduced the stiffness of the rock. For this reason, the specimen unloaded along a “damaged” modulus that was substantially lower than the intact modulus. Consequently, much of the early-time deformation was not recovered during the contraction, or rebound, phase.

The results of the spherical wave experiment also show evidence of load-induced anisotropy, a response mode usually associated with cracking in brittle materials. This anisotropy is manifested as a difference in the recorded particle velocity histories along the two different gage arrays of the spherical wave

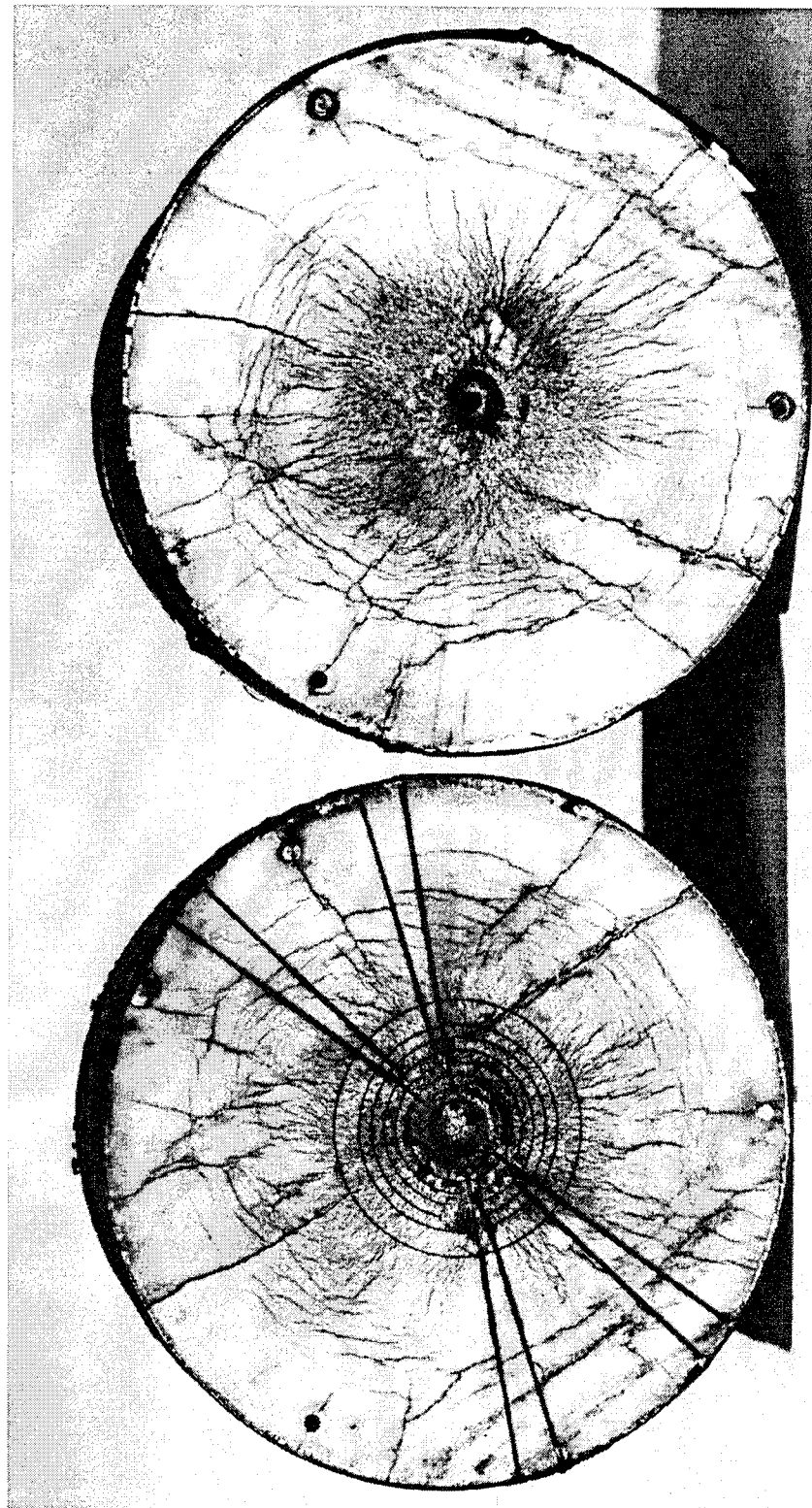


Figure 1-11. Experimentally observed crack patterns in the spherical wave experiment on Danby marble (the markings on the left half of the specimen are the grooves for the particle velocity gages and their leads).

experiment. This occurs during the rebound phase of the response and can be seen in the results shown in Figures 1-10(f) through 1-10(h). A careful comparison of the results shown in these figures reveals a systematic difference between the late-time particle velocity histories recorded by gages in the 'a' array and those recorded by gages in the 'b' array. A single rebound signal with a duration of about 15-17  $\mu$ s is observed on the 'a' side of the specimen. In contrast, a two-spike rebound signal is observed on the 'b' side of the specimen. The first spike has a larger amplitude and longer duration than the second spike, but when the two spikes on the 'b' side of the specimen are combined, they have the same duration as the single spike on the 'a' side. We believe that these systematic differences are closely related to the effects of cracks on wave propagation. Specifically, the lack of symmetry in the cracking patterns caused the stress wave to become asymmetric, and thus gages located in different regions of the specimen recorded different motions.

Code simulations were performed to aid in interpretation of the results of the spherical wave experiment. The simulations were performed in DYNA2D (Whirley and Engelmann, 1992) using a newly developed, computationally oriented constitutive model based on the evolution of damage by crack propagation (Simons et al., 1995).

After choosing reasonable values for the material parameters in the model on the basis of published data for marble and similar geologic materials, we attempted to simulate the spherical wave experiment. However, with the cracking model alone, we were unable to obtain a good qualitative agreement between the measured and calculated particle velocity histories. To obtain such agreement, we found it necessary to use a porous compaction model to represent the material behavior in the vicinity of the charge cavity (within a diameter of 3.5 cm).

The simulated crack patterns in the spherical wave experiment are shown in Figure 1-12 along with the experimentally observed crack patterns. The model reproduced the radial and circumferential crack networks observed in the experiment. The crack observed experimentally along the path of the *in situ* joint in the rock was not reproduced in the simulation because the joint itself was not modeled (i.e., initially isotropic behavior was assumed in the calculations).

The model was not quantitatively calibrated to reproduce all the details of the experimental data. The objective of the simulations was to try to provide a better understanding of the mechanisms that contributed to the observed response. To this end, our results indicate that close to the charge cavity, the behavior of the rock is dominated by porous compaction, whereas away from the charge, the behavior is dominated by crack propagation.

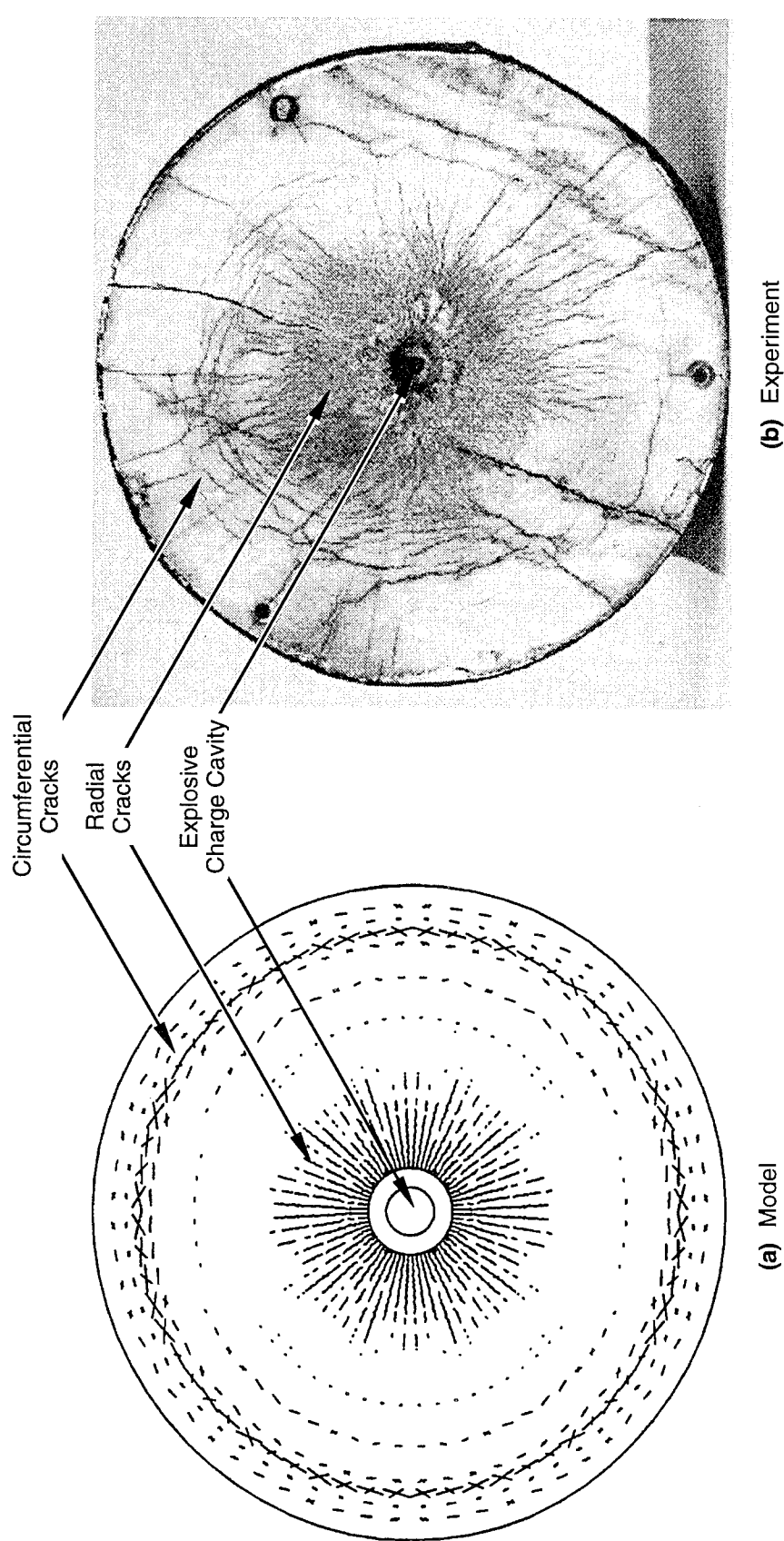


Figure 1-12. Comparison between simulated and experimentally observed crack patterns in the spherical wave experiment on Danby marble.

### **1.3 REPORT ORGANIZATION.**

The literature review is presented in Section 2, the uniaxial strain experiments in Section 3, and the spherical wave experiment in Section 4. The report also includes three self-contained appendices. The first, Appendix A, describes a simple analysis for calculating the rise time of in-material gages; the second, Appendix B, summarizes the experimental data from all the uniaxial strain experiments performed during the study; and the third, Appendix C, describes an analytical solution for the flow field produced by the reflection of compression waves at impedance mismatched boundaries. This solution was derived by M. Cowperthwaite (1995) of Poulter Laboratory.

## SECTION 2

### LITERATURE REVIEW OF THE SHOCK RESPONSE OF CALCITE

Investigations of the high pressure behavior of geologic materials under static loading conditions can be traced back to the 1920s (Adams and Williamson, 1923). These early efforts focused primarily on measuring the compressibility of minerals of various compositions. Not until the pioneering work of Bridgman (1939) were phase transformations in geologic materials investigated. The use of shock wave experiments to study the high pressure behavior of geologic media dates back to the 1960s. The early work was motivated in part by interest in investigating reactions and processes in the earth's mantle that occur at a combination of pressures and temperatures unattainable in static experiments (Ringwood, 1962; Ahrens and Gregson, 1964). Since calcite rocks such as marble and limestone are among the most abundant carbonate mineralogies in the crust of the earth, many investigations have been performed to characterize their behavior under conditions of high pressure and temperature.

This section presents the findings of a critical review of existing studies concerned with the behavior of calcite and calcite-based geologic materials under high pressure and temperature. The material behavior parameters emphasized during this review were

- Phase transitions
- Loading Hugoniot
- Unloading adiabat
- Effect of joints on wave propagation.

Although the review was not exhaustive, it allows us to present here a fairly accurate account of the state of the art of existing knowledge regarding the behavior of calcite and calcite-based minerals, especially with regard to the material behavior parameters enumerated above.

#### **2.1 PHASE TRANSITIONS.**

Several calcite polymorphs have been identified in the literature. Calcite I is the stable phase under conditions of ambient pressure and temperature. It has a rhombohedral structure and a crystal density of 2.71 g/cm<sup>3</sup>. Aragonite becomes the stable phase under high pressure. It has an orthorhombic structure and a crystal density of 2.93 g/cm<sup>3</sup> (Kerley, 1989). The phase diagram of calcium carbonate rocks is further complicated by the appearance of the calcite II and calcite III intermediate, high pressure phases in the pressure range from 10 to 25 kbar (Bridgman, 1939, 1948). At even higher pressures, calcite is

known to undergo yet another phase transition (Adadurov et al., 1960; Murri et al., 1975; Grady, 1986); this high pressure phase, known as calcite IV, occurs at pressures in excess of 100 kbar and is usually observed in impact experiments in the form of a somewhat anomalous rarefaction shock. None of the intermediate phases of calcite has a field of stability under equilibrium conditions.

Kerley (1989) developed a theoretical model for the equation of state of  $\text{CaCO}_3$  that includes phase transitions and melting. For the solid phases, the model combines the contributions from the cold compression curve and lattice vibrations, and for the liquid phase, the model is constructed using fluid perturbation theory. The phase diagram calculated using this model is shown in Figure 2-1. As noted, calcite IV is assumed to have the same properties as aragonite except for a shift in the energy.

The calcite II and calcite III polymorphs of  $\text{CaCO}_3$  were first observed experimentally by Bridgman (1939) at pressure levels of 14.7 and 17.7 kbar, respectively. Subsequent static measurements performed by other investigators yielded similar results. The results of these static studies are summarized in Table 2-1. As indicated in the table, the transition pressures and associated changes in specific volume measured by the various investigators are in reasonable agreement. A noteworthy exception is the study performed by Adadurov et al. (1960), who identified three transitions, instead of two, in the stress range between 0 and 30 kbar. The results of this study are shown in Figure 2-2, along with similar data obtained by Singh and Kennedy (1973). As shown, the second and third transitions in the Adadurov et al. (1960) data agree favorably with the calcite I - calcite II and calcite II - calcite III transitions measured by Singh and Kennedy (1973). It is not likely that the first transition identified by Adadurov et al. (1960) is a new transition, different from the two identified by other investigators. It is possible that the first discontinuity observed by Adadurov et al. (1960) signifies the initiation of the calcite I - calcite II transition in small portions of the specimen where local stress concentrations lead to stresses that are higher than the remote continuum stresses. The second discontinuity would then signify the completion of the phase transformation.

In some respects, this explanation is consistent with the results of the ultrasonic wave measurements performed by Wang (1966). Wang's results are shown in Figure 2-3. The initiation of the phase transition (at a microscopic level) is signified in this figure by the drop in compressional wave velocity as a function of increasing pressure. The completion of the transition corresponds to the pressure level where the wave velocity attains its minimum value. Figure 2-2 indicates that, for all the calcite rocks investigated, completion of the transition occurs within a narrow pressure range ( $15.5 \pm 0.5$  kbar). However, the transformation initiates at different pressures and proceeds at different rates depending on the morphology of the rock. In coarse-grained rock (e.g., Solnhofen limestone), the transformation begins sooner and proceeds slower than in fine-grained rock (e.g., Danby marble). In a single crystal, the transition begins and ends abruptly within a narrow band of 0.5 kbar. This trend can be explained in terms of local stress fluctuations. With increasing grain size, the material behaves less and less like a

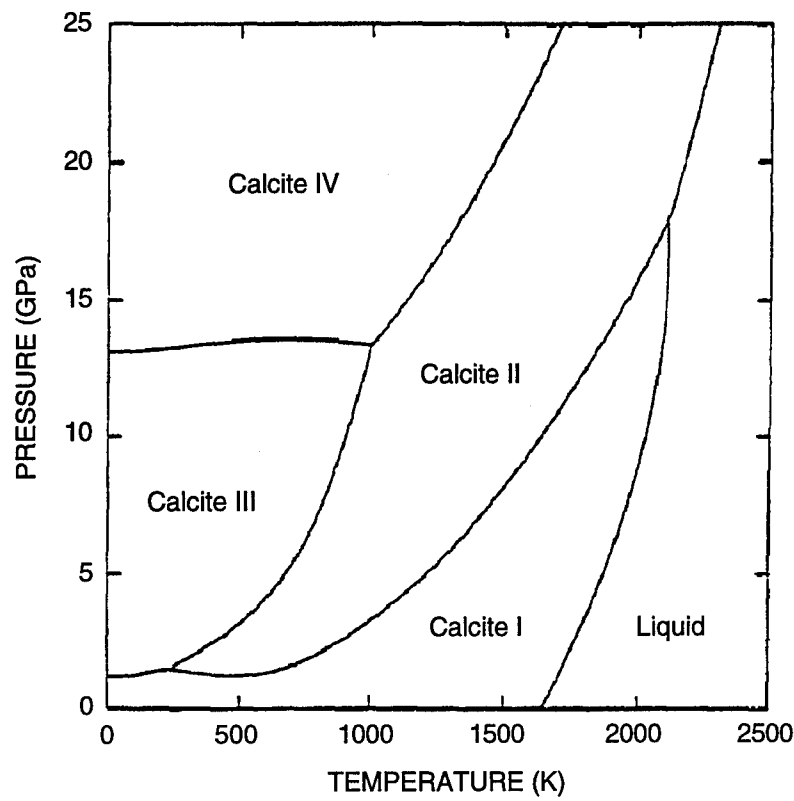


Figure 2-1. Phase diagram for  $\text{CaCO}_3$  including metastable phases II, III, and IV. The calcite IV properties are the same as for aragonite, except for a shift in the energy (after Kerley, 1989).

**Table 2-1.** Static experimental measurements of the pressures and volume changes associated with the various calcite phase transitions.

Reference	Testing Method	Observed Transition	Pressure (kbar)	$\Delta V$ (cm <sup>3</sup> /g)
Bridgman (1939)	Hydrostatic compression	Calcite I → Calcite II Calcite II → Calcite III	14.7 17.7	0.00135 0.00956
Adadurov et al. (1960)	Hydrostatic compression	Calcite I → Calcite II Calcite II → Calcite III	11.21 16.32 22.43	0.00656 0.00293 0.01033
Vaidya et al. (1973)	Hydrostatic compression	Calcite II → Calcite III	17.1±0.4	0.04
Singh and Kennedy (1974)	Hydrostatic compression	Calcite I → Calcite II Calcite II → Calcite III	14.5 17.4	0.00483 0.01291
Wang (1966)	Ultrasonic measurements	Calcite I → Calcite II	15.5±0.5	
Wang and Meltzer (1973)	Ultrasonic measurements	Calcite I → Calcite II Calcite II → Calcite III	15.5 23.0	

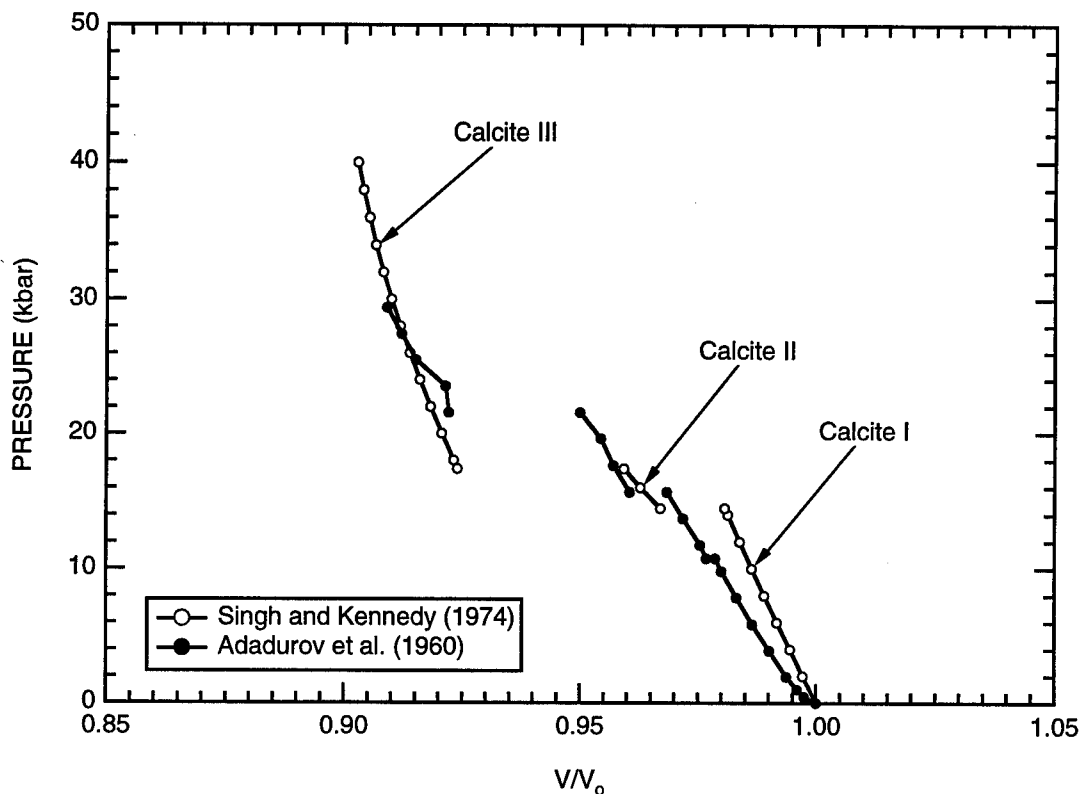


Figure 2-2. Pressure-volume relationship showing the various low pressure phase transformations in calcite rock.

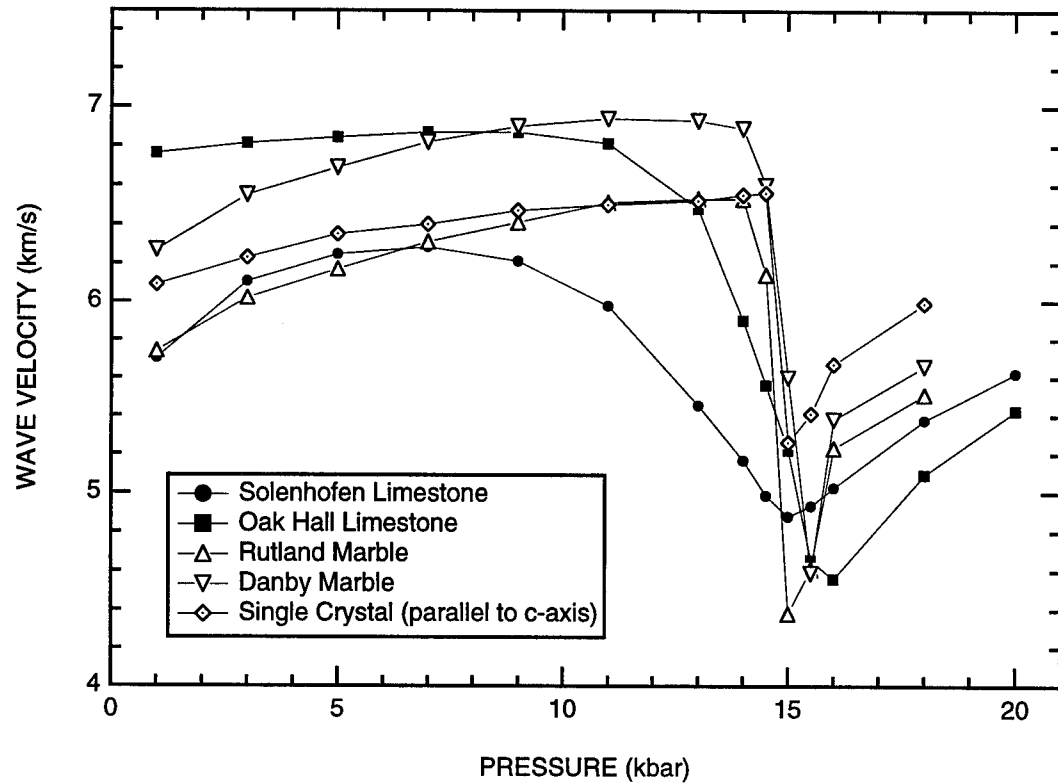


Figure 2-3. Compressional wave velocity as a function of pressure for several calcite rocks. The sharp drop in velocity at a pressure of about 15 kbar is associated with the calcite I - calcite II transition (Wang, 1966).

continuum; local stress gradients develop that lead to localized regions of high stress concentrations. These regions of high stress concentrations transform before the rest of the specimen and lead to the gradual decrease in velocity observed in Figure 2-3.

Measurements such as those shown in Figure 2-3 may be significantly influenced by anisotropy. This is illustrated in Figure 2-4, where the wave velocity is displayed as a function of pressure for three mutually perpendicular directions in Solenhofen limestone. As shown, the pressure that corresponds to the initial drop in velocity varies from one orientation to the next by as much as 5 kbar. The pressure that corresponds to minimum velocity varies between 14 and 15 kbar. Such variations contribute to some of the scatter in the results presented in Table 2-1.

The results shown in Figures 2-3 and 2-4 correspond to pressures between 1 and 20 kbar. In this pressure range, Wang (1966) observed only the calcite I - calcite II transition. Wang and Meltzer (1973) extended the pressure range by a few kilobars and were able to detect the calcite II - calcite III transition at a pressure of about 23 kbar, as shown in Figure 2-5. The first transition shown in this figure is in good agreement with the earlier results of Wang (1966), shown in Figure 2-3.

It has already been shown that the phase boundaries among the various polymorphs of calcite are affected by temperature (see Figure 2-1). Experimental measurements that verify this phenomenon are shown in Figures 2-6 and 2-7. Figure 2-6 illustrates this behavior in terms of the shift in the pressure that corresponds to minimum compressional wave velocity. These results are combined with Bridgman's (1939) data in Figure 2-7. The trends exhibited by the two sets of data are very similar. Quantitative differences are small enough to be attributed to possible variations between the rock specimens used in the two different investigations. The results shown in Figure 2-7 are in good agreement with Kerley's analytically derived phase diagram shown in Figure 2-1.

Our discussion has so far been limited to static data, but many wave propagation studies have been undertaken to investigate the calcite phase transformations under dynamic conditions. Several of these investigations are summarized in Table 2-2. The dynamic data in this table differ from their static counterparts in that the combination of high pressure and high temperature environments achievable dynamically are not easily attainable using conventional static testing techniques. For this reason, the calcite III - calcite IV transition observed in many wave propagation experiments was not detected in the static tests. This transition occurs in the pressure range between 95 and 170 kbar. The transition pressure of 95 kbar reported by Ahrens and Gregson (1964) has not been independently verified by other investigators and appears to be too low compared with other measurements.

Another difference between the static and dynamic data is the generally higher calcite II - calcite III transition pressures recorded in impact experiments. This difference may be due to the higher temperatures usually attained in dynamic experiments. According to the pressure-temperature relations

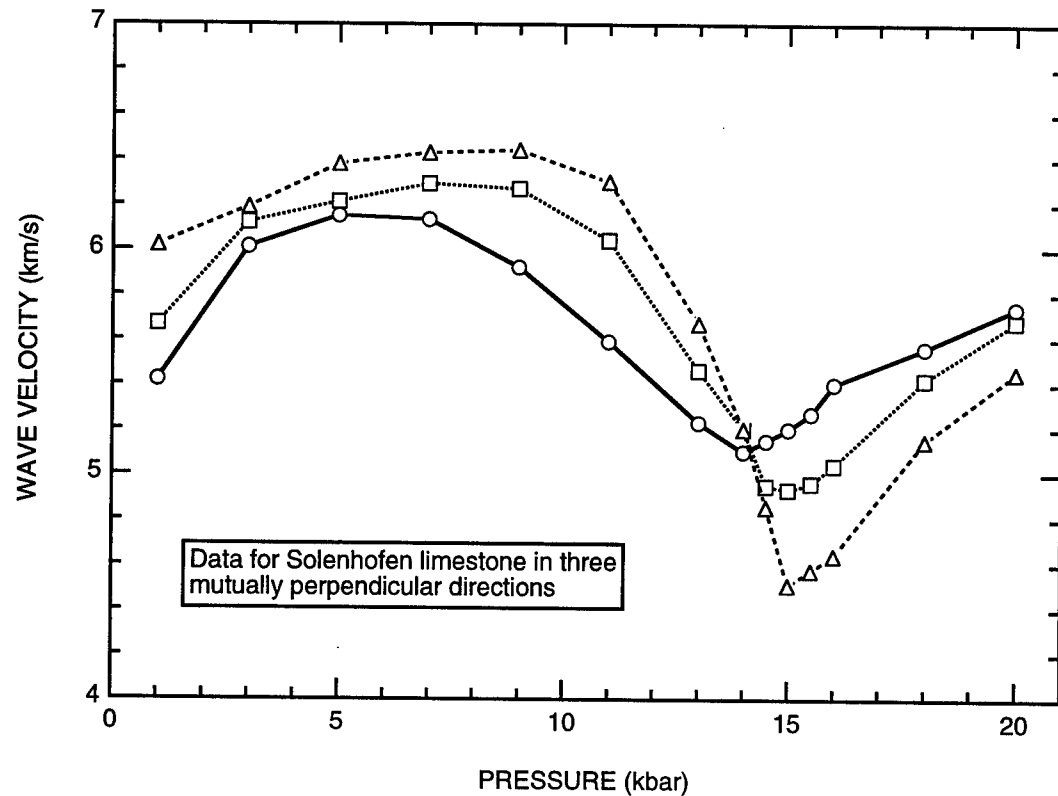


Figure 2-4. Wave velocity as a function of pressure for Solenhofen limestone in three mutually perpendicular directions (Wang, 1966).

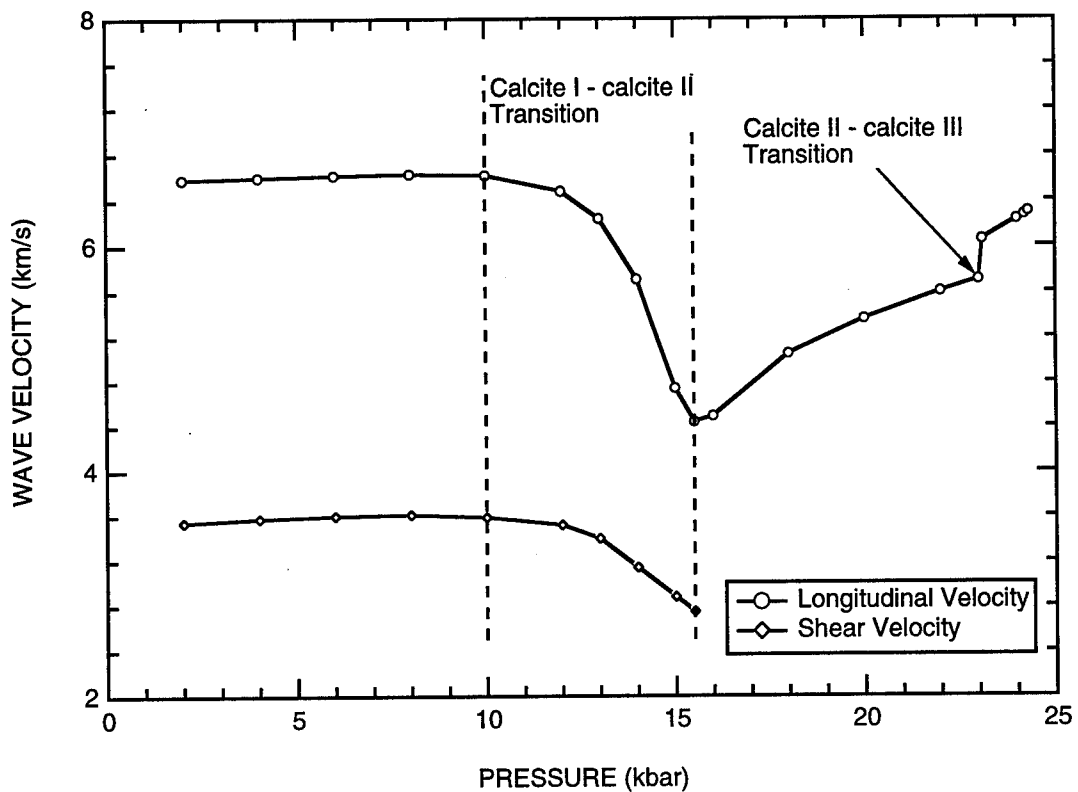


Figure 2-5. Compressional and shear wave velocities as a function of pressure for Oak Hall quarry limestone (Wang and Meltzer, 1973).

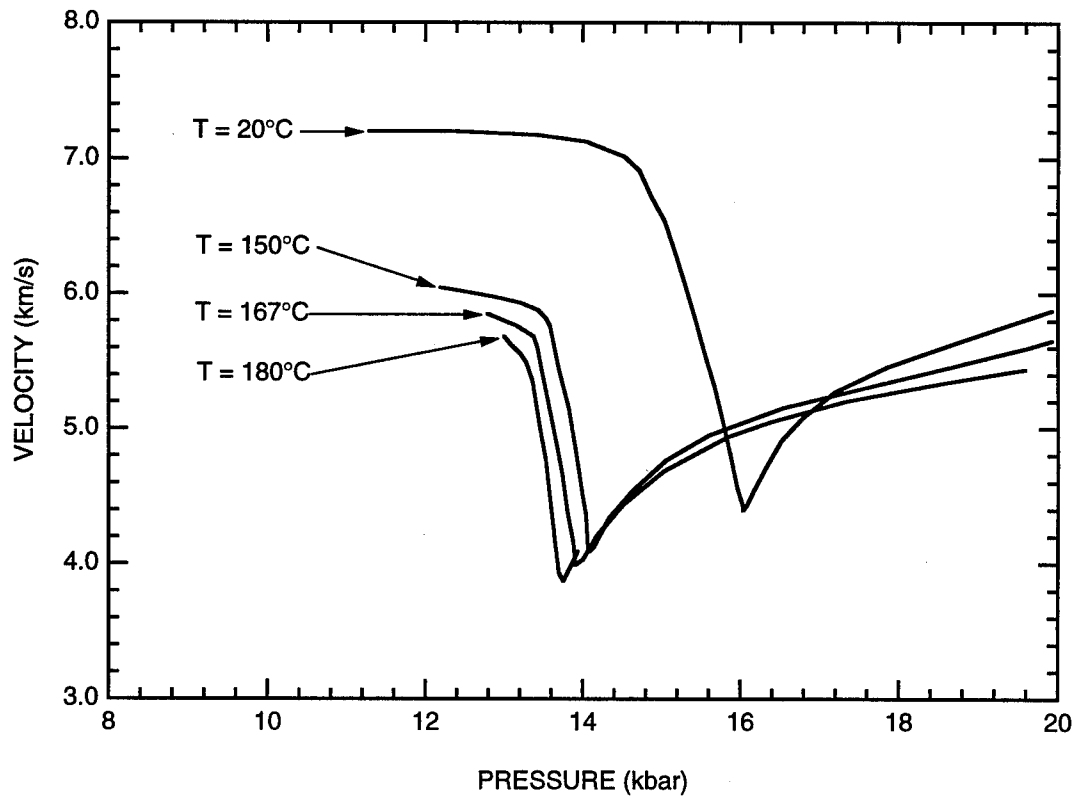


Figure 2-6. Compressional wave velocity as a function of pressure for Danby marble depicting the dependence of calcite I - calcite II phase transition pressure on temperature (Wang, 1968).

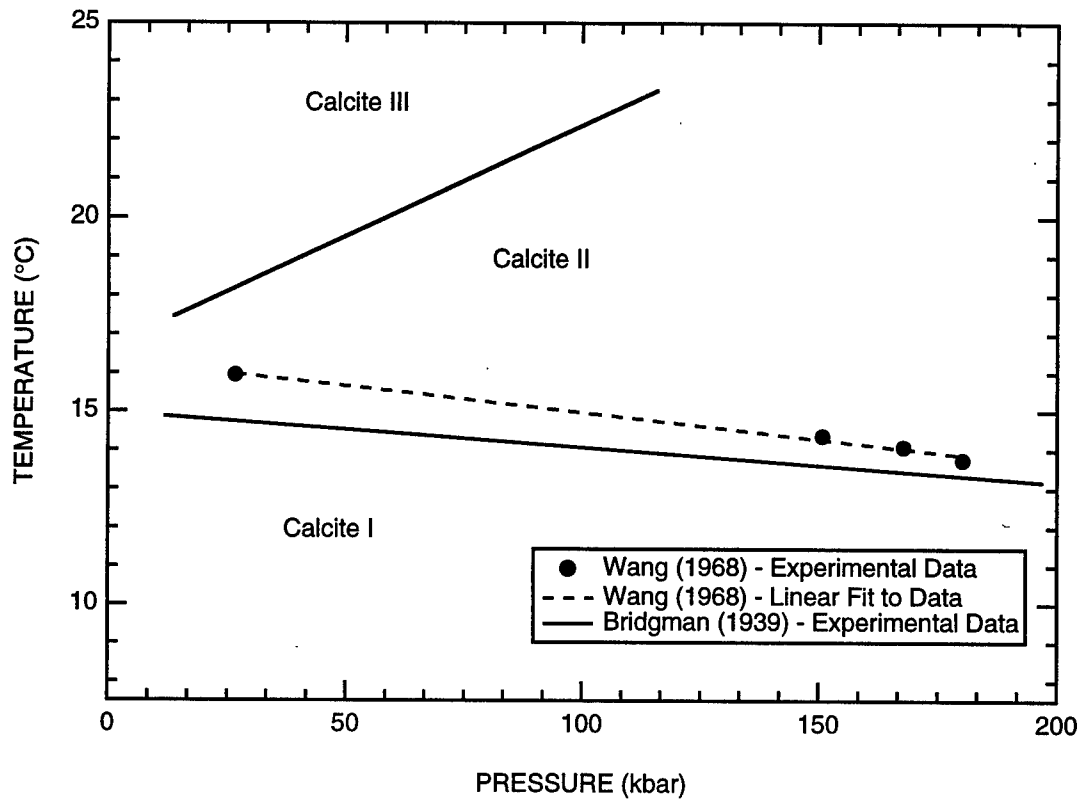


Figure 2-7. Calcite I - calcite II and calcite II - calcite III phase boundaries in pressure-temperature space for calcite rock.

**Table 2-2. Dynamic experimental measurements of the pressures associated with the various calcite phase transitions.**

Reference	Material	Initial Density (g/cm <sup>3</sup> )	Observed Transition	Transition Pressure (kbar)
Adadurov et al. (1960)	Icelandic spar	2.70	Calcite III → Calcite IV	153
Ahrens and Gregson (1964)	Yule and Vermont marbles and Solenhofen and Indiana limestones	2.38 - 2.70	Calcite I → Calcite II Calcite II → Calcite III Calcite III → Calcite IV	22 40 95
Muri et al. (1975)	Linden Hall limestone	2.70	Calcite I → Calcite II Calcite II → Calcite III Calcite III → Calcite IV	15 20 - 56 $149 \pm 20$
Grady et al. (1978)	Solenhofen and Oak Hall limestones and Vermont marble	2.61 - 2.71	Calcite I → Calcite II Calcite II → Calcite III	6, 10, 12* 24
Grady (1986)	Icelandic spar single crystal (z-axis)	2.71	Calcite III → Calcite IV	120 - 140
Stapleton and Gupta (1992)	Icelandic spar single crystal (c-axis)	2.71	Calcite I → Calcite II	$17.6 \pm 0.4$

\*6 kbar for Solenhofen limestone, 10 kbar for Oak Hall limestone, and 12 kbar for Vermont marble.

depicted in Figures 2-1 and 2-7, the calcite II - calcite III transition pressure increases with increasing temperature. Furthermore, the phase transition in dynamic experiments is usually observed during unloading (i.e., *reverse* transition), which means that the specimen would have reached its maximum temperature before the transition pressure was measured. If the peak pressure is high and/or the specimen is porous, temperatures on the order of few hundred degrees are easily attainable in an impact experiment, which in turn leads to the upward displacement, in pressure, of the phase boundary. A similar trend is not expected for the calcite I - calcite II transition, simply because the slope of the phase boundary in the pressure-temperature space is essentially flat in the temperature range of interest.

## 2.2 LOADING HUGONIOT.

Impact experiments at pressures ranging from a few kilobars to several hundred kilobars have been performed to characterize the loading Hugoniot of calcium carbonate rock and to determine the effects of porosity, saturation, freezing, phase transformations, and anisotropy on the dynamic material behavior. Several such investigations pertinent to the present study are summarized in Table 2-3. The Hugoniot data from these investigations are shown in Figure 2-8 in terms of stress versus volumetric strain. In this figure, the hollow symbols represent data for calcite in the porous state, the solid symbols represent data for calcite in the nonporous state (porosity less than 0.5%) and the composite symbols (e.g., crossed hollow circle) represent data for saturated and/or frozen calcite. Scatter in the data is evident. However, if the data are separated into classes based on porosity and saturation, a pattern begins to emerge. This observation is illustrated in Figures 2-9 through 2-11. Figure 2-9 shows the data for nonporous calcium carbonate rock. The very good correlation observed between the data from different investigations indicates that the high pressure equation of state representing the loading Hugoniot of nonporous calcium carbonate rock is predictable with good accuracy.

Figure 2-10 shows the results of a study that investigated the effect of saturation on the behavior of Icelandic spar, a nonporous, single crystal calcite rock. As shown, the effect of saturation on the behavior of the rock is barely perceptible. In a similar fashion, Furnish (1994), who tested frozen and saturated low porosity Louisville and Jacksonville limestones, observed no systematic differences between the behaviors of the saturated and the frozen samples. The results of these two studies collectively indicate that, when the rock is nonporous, saturation and freezing have little effect on the Hugoniot.

Figure 2-11 shows the results of several studies that investigated the effects of saturation and freezing on the behavior of porous calcite rock. For each study represented in the figure, the data for the dry rock are shown with hollow symbols, the data for the saturated rock are shown with solid symbols, and the data for frozen samples are shown with composite symbols (crossed hollow circle). As expected, a marked difference can be observed between the Hugoniot of the dry samples and that of the saturated

**Table 2-3. Summary of experimental studies investigating the behavior of calcite rock under impact loading conditions.**

Reference	Material	Initial Density (g/cm <sup>3</sup> )	Testing Conditions	Pressure (kbar)
Furnish (1994)	Marble Louisville limestone Jeffersonville limestone Indiana limestone	2.63 - 2.70 2.77 - 2.79 2.71 - 2.74 2.19 - 2.21	Dry Saturated - frozen Saturated - frozen Dry - saturated	15 - 130 75 - 200 40 - 110 10 - 125
Keough et al. (1993)	Danby marble*	2.69 - 2.73	Dry	60 - 170
Gaffney and Smith (1994)	Danby marble Salern limestone	2.70 - 2.72 2.29	Dry Dry - saturated - frozen	10 - 150 5 - 50
Grady (1986)	Icelandic spar (single crystal)	2.71	Dry	100 - 250
Larson and Anderson (1979)	Indiana limestone	2.28	Dry - saturated	5 - 50
Grady et al. (1978)	Solenhofen limestone Oak Hall limestone Vermont marble	2.61 2.70 2.71	Dry Dry Dry	0 - 50 0 - 50 0 - 50
Murri et al. (1975)	Indiana limestone Linden Hall limestone	2.31 2.70	Dry - saturated Dry	100 - 300 100 - 300
Ahrens and Gregson (1964)	Icelandic spar (single crystal) Yule marble Vermont marble Solenhofen limestone Spergen limestone	2.71 2.70 2.69 2.58 2.38	Dry Dry Dry Dry Dry	4 - 250 4 - 250 4 - 50 4 - 100 4 - 250
Adadurov et al. (1960)	Icelandic spar (single crystal)	2.70	Dry - saturated	50 - 500

\*The Danby (Vermont) marble used in the present investigation is the same as that used in the large scale experiments of Keough et al. (1993).

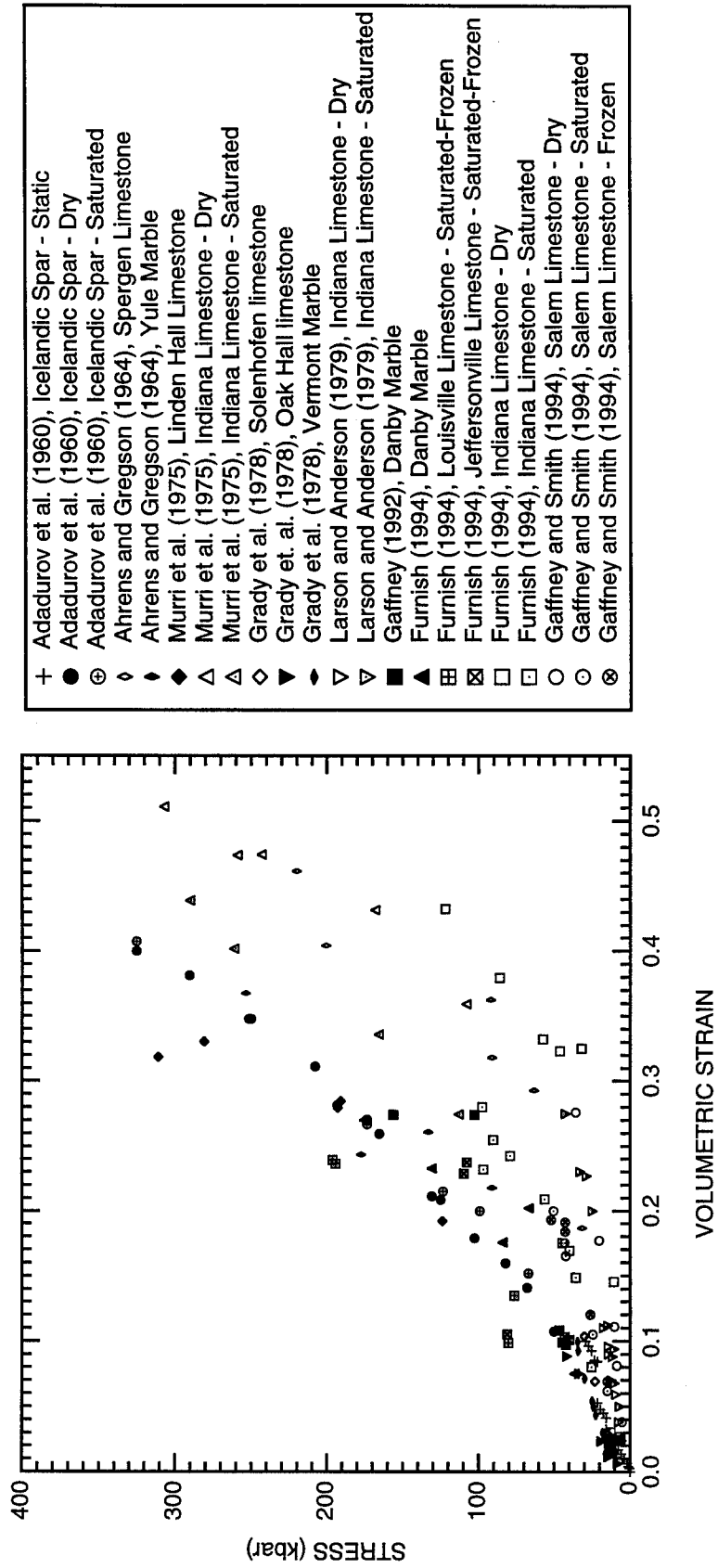


Figure 2-8. A collection of Hugoniot data for calcium carbonate (CaCO<sub>3</sub>) rock in the stress-volumetric strain plane.

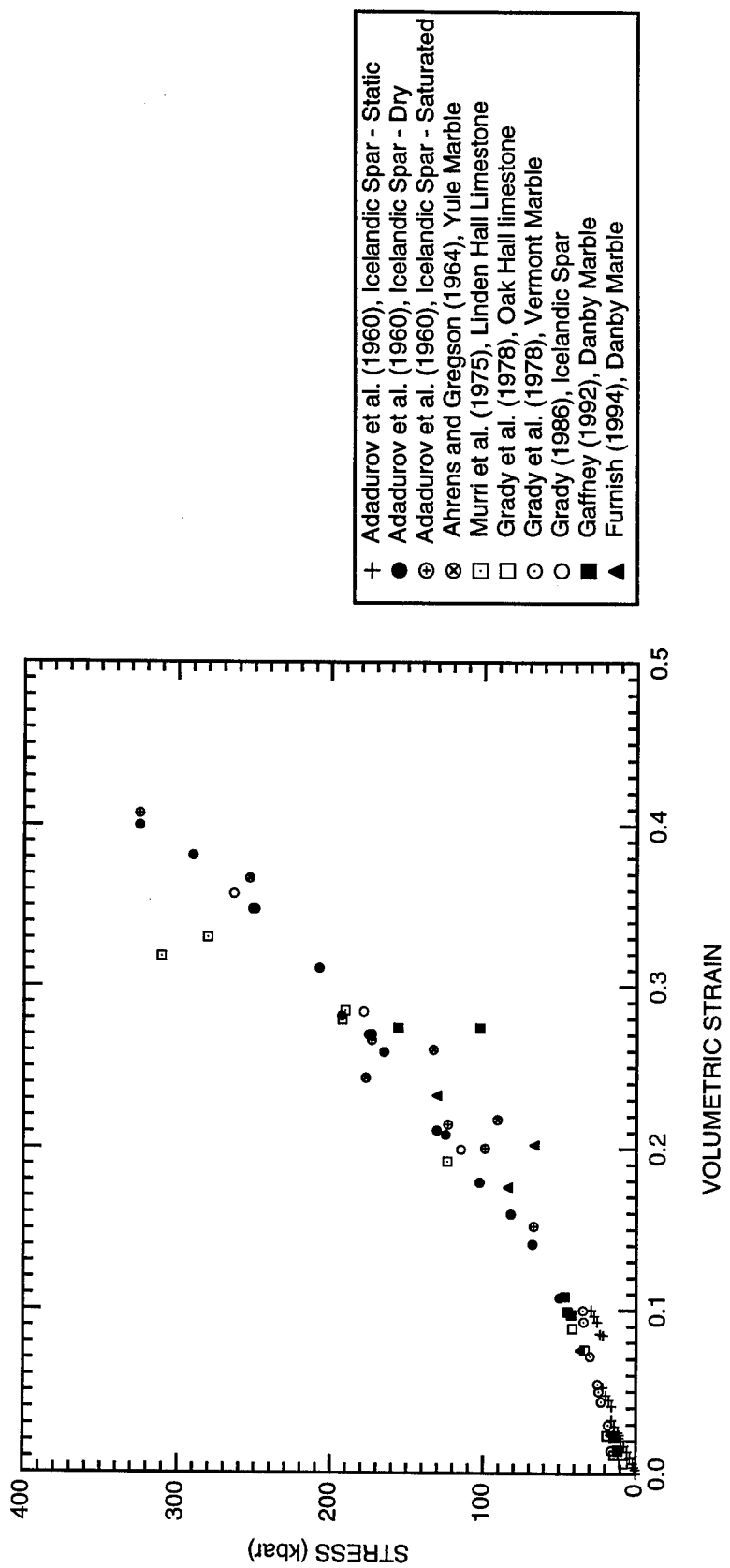


Figure 2-9. A collection of Hugoniot data for nonporous (less than 0.5% porosity) calcium carbonate ( $\text{CaCO}_3$ ) rock in the stress-volumetric strain plane.

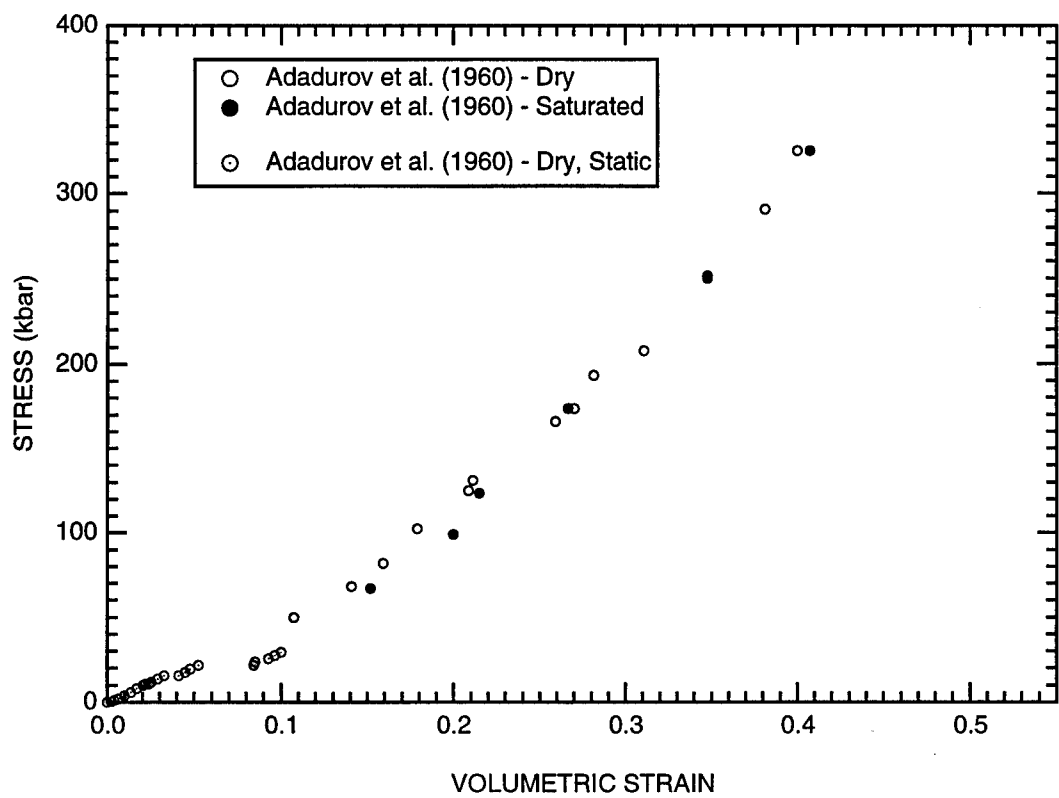


Figure 2-10. Comparison of the loading Hugoniots of dry and saturated nonporous calcium carbonate ( $\text{CaCO}_3$ ) rock.

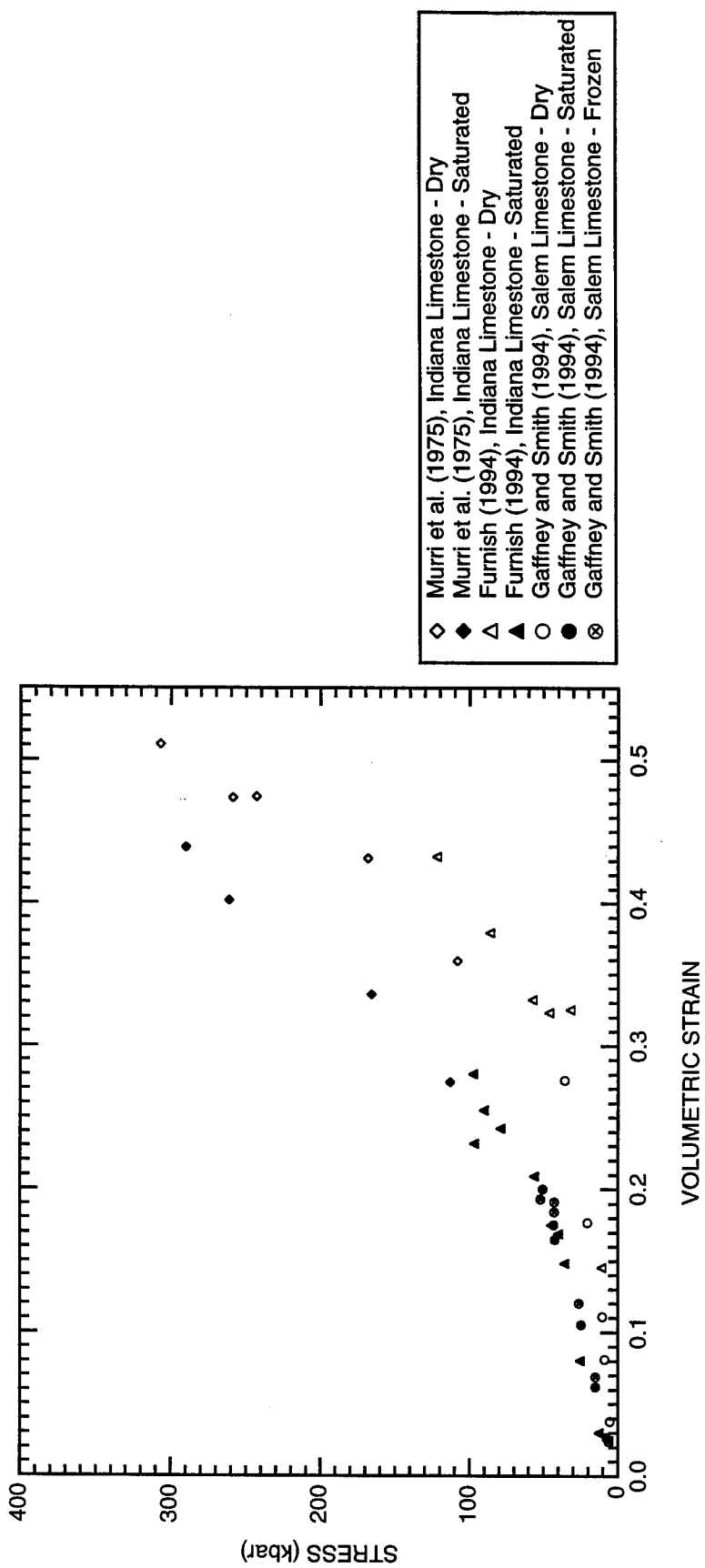


Figure 2-11. Comparison of the loading Hugoniots of dry, saturated, and saturated-frozen porous calcium carbonate ( $\text{CaCO}_3$ ) rock.

(and saturated-frozen) samples. Hydration reactions in saturated calcite, leading to the formation of ikaite ( $\text{CaCO}_3 \cdot 6\text{H}_2\text{O}$ ) as suggested by Furnish (1994), may be a contributing factor to the observed differences.

Figure 2-11 also shows that the Hugoniot data for the dry samples from the various investigations fall essentially on the same curve as do the data for the saturated and frozen samples. This is because the data shown in the figure correspond to rock samples of similar composition (nearly pure  $\text{CaCO}_3$ ) and porosity (between 14% and 18%). An interesting observation based on the data shown in Figure 2-11 is that freezing had no detectable effect on the loading Hugoniot of porous, saturated calcite rock.

Another useful representation of the data shown in Figures 2-8 through 2-11 is in the stress-volume plane, as shown in Figure 2-12. In this figure, as in Figure 2-8, the hollow symbols represent data for calcite in the porous state, the solid symbols represent data for calcite in the nonporous state (porosity less than 0.5%), and the composite symbols (e.g., crossed hollow circle) represent data for saturated and/or frozen calcite. The figure shows that, at low pressures (less than about 50 kbar), significant differences exist between the behaviors of rock of different porosities. With increasing pressure, the data for both porous and nonporous rocks converge to the same Hugoniot curve, which represents the high pressure solid equation of state of calcite IV - the high pressure polymorph of calcium carbonate rock.

As in the static case, dynamic data are influenced by anisotropy. Ahrens and Gregson (1964) performed plane wave experiments on Icelandic spar single crystal specimens. The samples were oriented so that the plane of the shock was perpendicular to the x-axis, y-axis, z-axis, and c-axis of the crystal. Their results show a distinct difference in behavior among the crystals of different orientations up to a stress of 100 kbar. The Hugoniot elastic limits (HEL) measured for the various crystal orientations ranged from 18.5 kbar (c-axis) to 23.7 kbar (y-axis).

## 2.3 UNLOADING ADIABAT.

Generally speaking, the unloading behavior of calcium carbonate rock has been less investigated than the loading behavior. The recent study performed by Furnish (1994) (see Table 2-3) is the most extensive investigation to date of the unloading behavior of calcite rocks. Another significant study investigating the unloading behavior of calcium carbonate rock was performed by Murri et al. (1975). Most of the information provided in this section is derived from the results of these two studies.

Murri et al. (1975) performed plane wave experiments on Linden Hall limestone and on dry and saturated Indiana limestone at peak stresses ranging between 100 and 300 kbar. In all cases, rarefaction shocks associated with the calcite IV - calcite III, calcite III - calcite II, and calcite II - calcite I

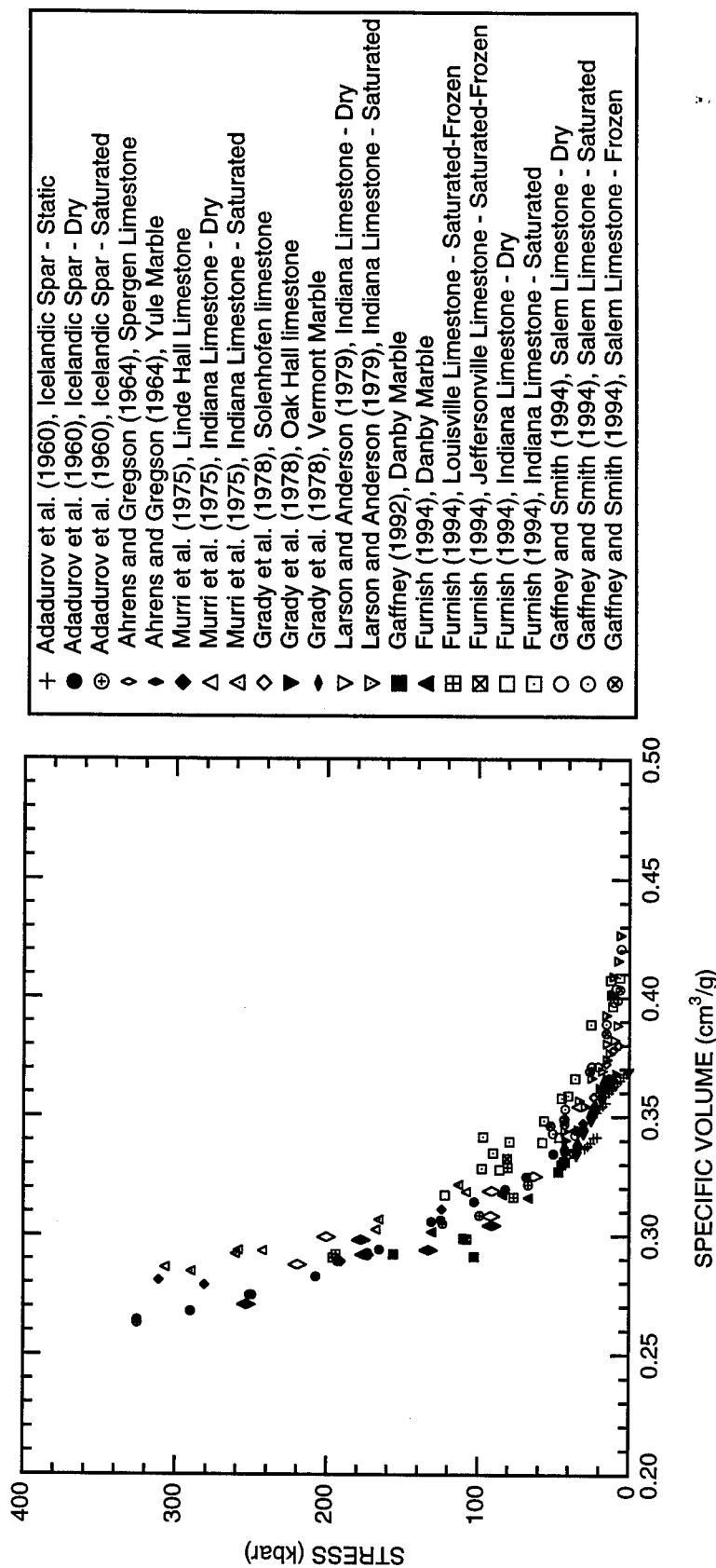


Figure 2-12. A collection of Hugoniot data for calcium carbonate ( $\text{CaCO}_3$ ) rock in the stress-specific volume plane.

transformations were observed in the experimental records during unloading. Not all of these transformations were observed during loading. The calcite I - calcite II transition, for example, was only observed during loading in the experiments on nonporous limestone, so in the porous case the transition may have been obscured by processes associated with the compaction of the pores. It is also noteworthy that the calcite II - calcite III transition was not observed during loading in any of the experiments conducted by Murri et al. (1975), which led them to conclude that the kinetics of the calcite II - calcite III transformation were too slow for the transition to be observed in a shock wave experiment. The reverse transformation, however, occurred fast enough for detection. Porosity and water content did not seem to greatly affect the stress at which the rarefaction shocks associated with the reverse phase transformations in calcite occurred.

Murri et al. (1975) observed little hysteresis in the unloading behavior of nonporous limestone. Porous limestone, on the other hand, exhibited some hysteresis upon unloading, in part because of shock heating. Water-saturated, porous limestone was intermediate between solid and dry porous limestone. This behavior is illustrated in Figures 2-13 and 2-14, which show the unloading paths for dry and water-saturated Indiana limestone, respectively.

Furnish (1994), who also calculated the unloading paths for porous (Indiana limestone) and nonporous (Danby marble) calcite up to stresses of about 130 kbar, observed more hysteresis in the behavior of the nonporous samples than that of the porous samples.

#### **2.4 EFFECT OF JOINTS ON WAVE PROPAGATION.**

The effect of joints on wave propagation in geologic material has not been extensively studied experimentally. The two known studies were performed by Gaffney (1992) and by Gefken and Florence (1993).

Gaffney (1992) studied wave propagation in marble specimens containing 1-mm-thick water-filled and ice-filled artificial joints under uniaxial strain conditions at stresses of 10 and 50 kbar. The investigation was aimed at determining the transition pressure at which the effect of freezing vanishes (i.e., the pressure beyond which water-filled and ice-filled joints have the same effect on wave propagation). Results in the form of stress history measurements behind the jointed region of the specimen indicated that at 10 kbar ice-filled and water-filled joints attenuated the stress pulse by 78% and 60%, respectively, and at 50 kbar ice-filled and water-filled joints attenuated the stress pulse by 40% and 24%, respectively. These results indicate that the transition pressure under the conditions investigated in this study is higher than 50 kbar.

The second investigation of the effect of joints on wave propagation in geological materials is that of Gefken and Florence (1993), who used the spherical wave experimental technique to measure

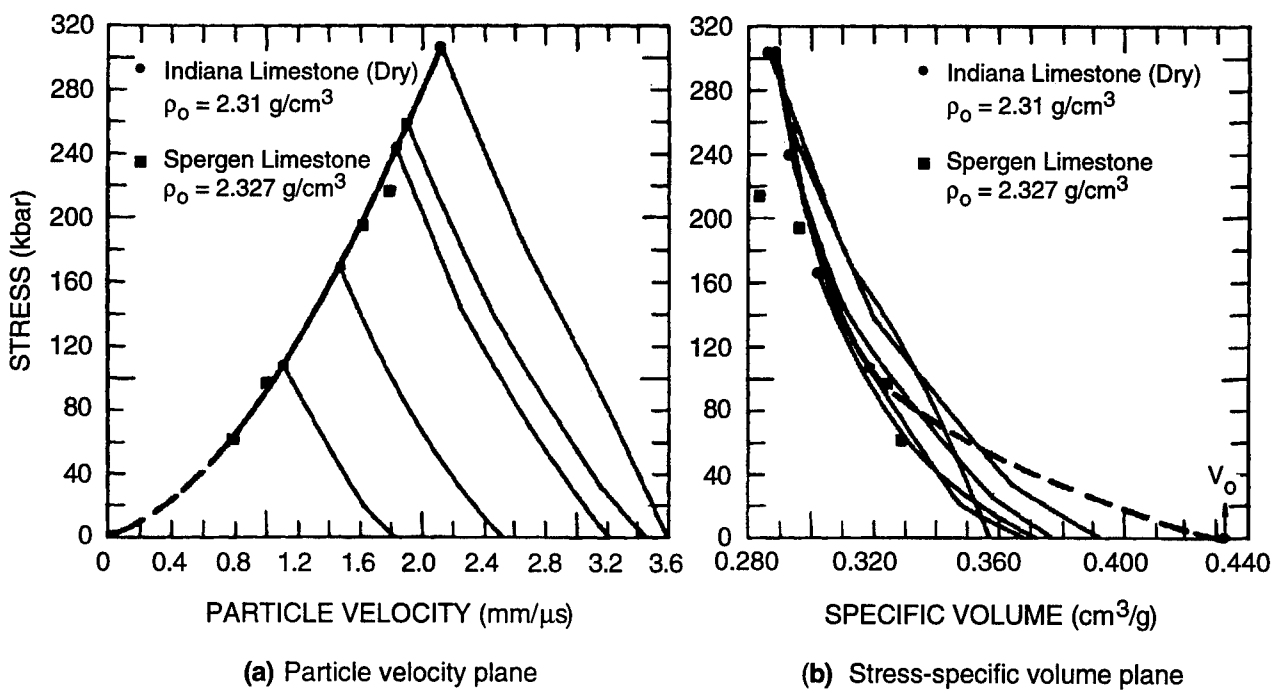


Figure 2-13. Hugoniot and release data for dry Indiana limestone.

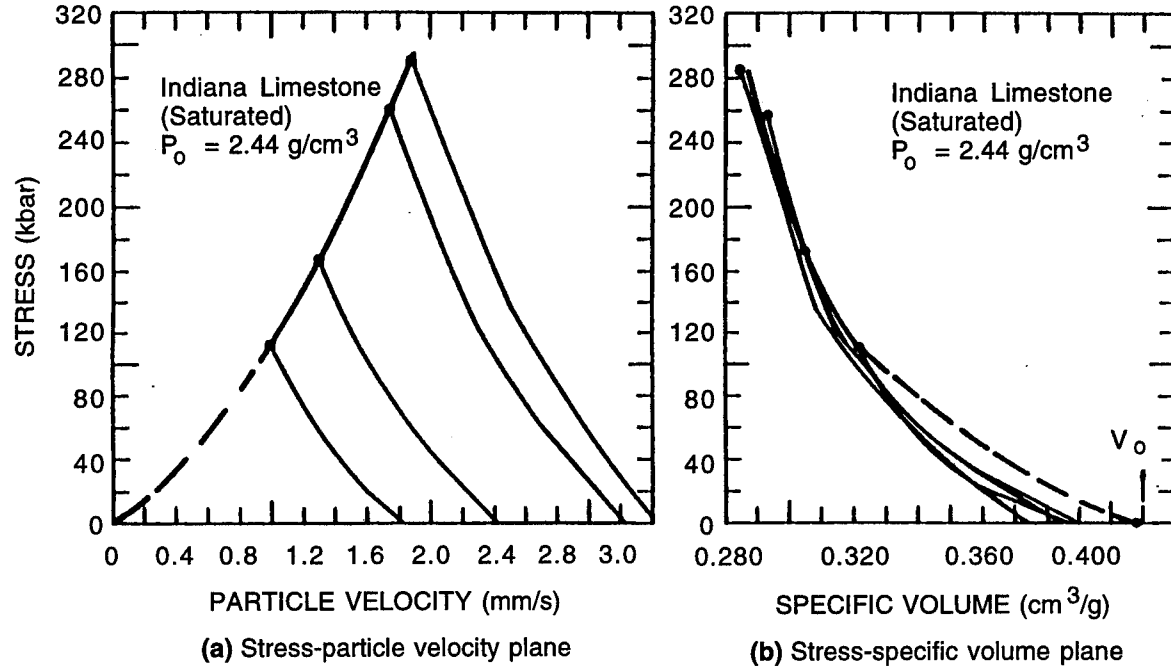


Figure 2-14. Hugoniot and release data for water-saturated Indiana limestone.

Heavy line is Hugoniot and light lines are release paths determined from experiment.

attenuation characteristics of particle motion across smooth (polished) and rough (sand-filled) artificial joints in Indiana limestone. The study included axial and radial velocity measurements in both dry and saturated samples.

Polished joints in dry limestone showed no indication of radial slip during the passage of the initial compression wave. Late time slip was observed across the joint. Polished joints in saturated limestone showed evidence of instantaneous slip as well as late time separation of the two joint surfaces. A polished joint in dry limestone produced more transmitted radial motion than a similar joint in saturated limestone or a rough, sand-filled joint in either dry or saturated limestone.

## 2.5 SYNOPSIS.

Many studies have been conducted over the past 30 years to characterize the behavior of calcium carbonate rock under dynamic loadings. Many of the early dynamic wave propagation studies emphasized the characteristics of the loading Hugoniot and to a lesser extent, the effects of strength, porosity, and phase transformations on the material behavior.

Static high pressure studies played a significant role in furthering our understanding of the behavior of calcium carbonate rock. The pressure and volume changes associated with the calcite I - calcite II and calcite II - calcite III phase transitions have been measured accurately in static experiments. These transitions have since been observed in shock wave propagation experiments and are now known to affect the shape of both the loading Hugoniot and the unloading adiabat of calcite rock in a predictable fashion. The loading and unloading behaviors of calcite rock are also affected by another phase transformation: the calcite III - calcite IV transition, which occurs at stresses in excess of 100 kbar and has only been observed in dynamic wave propagation experiments.

The Hugoniot of calcium carbonate rock has been investigated for stresses up to about 500 kbar. For nonporous rock, the Hugoniot is well characterized and results from numerous investigations are very reproducible. The Hugoniot elastic limit (HEL) of calcite occurs in the stress range from 10 to 20 kbar depending, on the porosity and graininess of the sample. The HEL is associated with the first two polymorphic calcite transitions (I - II and II - III).

The unloading adiabat is not too far removed from the loading Hugoniot, partly because of the fully reversible nature of the calcite phase transitions. Little hysteresis has been observed upon complete unloading from a shock-loaded state.

The effect of joints on material response is the least investigated aspect of the behavior of calcite rock. Our literature review unveiled only two studies aimed at investigating the effect of joints on wave propagation. These studies showed drastic differences between the response of intact and jointed samples. This information, combined with DNA's interest in obtaining statistical variations in material

properties for jointed limestone and developing techniques for including the observed effects in material models for ground shock, led to the consensus that the experiments to be conducted during the course of the present study should emphasize the effect of joints on material behavior.

## SECTION 3

### UNIAXIAL STRAIN EXPERIMENTS

#### **3.1 MOTIVATIONS AND OBJECTIVES.**

Fracture-free rock formations are rare in nature. For this reason, constitutive models for predicting ground motion in the vicinity of a large explosion, such as are required for the HYDRO PLUS methodology, must include the effect of joints and inhomogeneities on the material response. The experiments described in this section were motivated by a lack of experimental data on wave propagation in jointed rock. The experiments aimed to provide results that will further our understanding of the effect of joints on wave propagation and provide a consistent set of results that can be used to develop, calibrate, or validate constitutive models suitable for use in hydrocode calculations.

The study consisted of experimental and analytical investigations. Experimentally, uniaxial strain experiments were conducted on both intact and jointed calcite rock samples. In the experiments, in-contact explosives, initiated using 15.24-cm-diameter (6.0 inch) plane wave lenses, were used to provide shock loadings in the rock samples. Several specimen designs incorporating different joint configurations were investigated. Experimental diagnostics consisted of in-material Lagrangian particle velocity gages embedded between rock layers at several serial locations within the specimen. Analytically, Lagrangian finite difference hydrocode simulations were carried out to help in the interpretation of experimental results and provide added insight into the behavior of jointed calcium carbonate rock.

#### **3.2 EXPERIMENTAL TECHNIQUES.**

This section describes the experimental techniques used to carry out the uniaxial strain experiments on intact and jointed calcite rock samples. The two geologic materials used in the experiments are described first, then the procedures used to assemble and instrument the specimens, and finally details of the experiments themselves.

##### **3.2.1 Materials.**

Two materials, UTTR (Utah Test Training Range) limestone and Danby (Vermont) marble, were selected for use in this investigation. The UTTR limestone was selected because it contains *in situ* calcite-filled fractures that are representative of naturally occurring joints. Danby marble was selected

because it is a well characterized calcite rock with predictable behavior in the stress range of interest, so that when artificial joints are introduced into a specimen, it will be possible to isolate the effect of joints on the observed behavior.

**3.2.1.1. Danby Marble.** The Danby marble (trade name “Montclaire” marble) used in the present study was obtained from the marble quarry in Danby, Vermont. This crack- and foliation-free marble was used in several other investigations connected with the DISTANT MOUNTAIN test series (Furnish, 1994; Gaffney and Smith, 1994; Keough et al., 1993). This Danby marble has a very low porosity and is composed of nearly pure calcite. It has a density of  $2.71 \pm 0.9\% \text{ g/cm}^3$ , which is essentially the same as the  $2.71 \text{ g/cm}^3$  ideal crystal density of pure calcite.

Slabs of Danby marble were rough-cut from a stock with cross sectional dimensions of 30.5 cm (12 in.) by 20.3 cm (8 in.). The slabs were then precision-ground flat to within a 0.05-mm (0.002-in.) tolerance over the entire surface of the slab.

**3.2.1.2. UTTR Limestone.** As its name indicates, the UTTR limestone is native to the Utah Test and Training Range. It was obtained from vertical drill holes near Candy Mountain at UTTR. It is composed primarily of calcite, quartz, and dolomite and contains traces of other minerals, including K-feldspar, pyrite and apatite (Martin and Felice, 1992). The exact mineralogical composition varies with depth. The material used in our investigation was obtained from depth intervals ranging between 24 and 38 m. From the depth data and the results of the Martin and Felice (1992) study, the following mineralogical and physical properties were obtained. The UTTR specimen used in HPEOS (high pressure equation of state) Experiment 1 was composed of 62% calcite, 31% quartz, 2% dolomite, 2% feldspar, 2% illite, and 1% pyrite. The remainder of the UTTR specimens used in our investigation were composed of approximately 66% calcite, 28% quartz, 4% dolomite, 1% feldspar, and 1% illite. The material has a density of  $2.70 \text{ g/cm}^3$ , a grain density of  $2.71 \text{ g/cm}^3$ , and a porosity of 0.4%. The UTTR rock contains *in situ* calcite-filled fractures/joints ranging in thickness from less than 0.02 mm to a few millimeters. The samples used in the present study contained a random distribution of these *in situ* joints. The joints in our samples were less than 1 mm thick.

The UTTR limestone was supplied to SRI in the form of 15.24-cm-diameter (6.0-in.) cores obtained from a bore hole at the Utah Test and Training Range. Slabs were cut from the limestone cores at an angle of  $42^\circ$  with respect to the axis of the core. This procedure resulted in ellipse-shaped slabs with dimensions of 30.5 and 20.3 cm along the major and minor axes, respectively. The 20.3-cm dimension was the same as the diameter of the explosives. The 30.5-cm dimension was larger than the diameter of the explosives and provided the shielding necessary to protect the particle velocity gages from the blast generated by the explosives. The slabs were precision-ground flat to within a 0.05-mm (0.002-in.) tolerance over the entire surface of the slab.

### **3.2.2 Specimen Configurations and Assembly.**

The specimen configurations investigated during this study are shown in Figure 3-1. They included

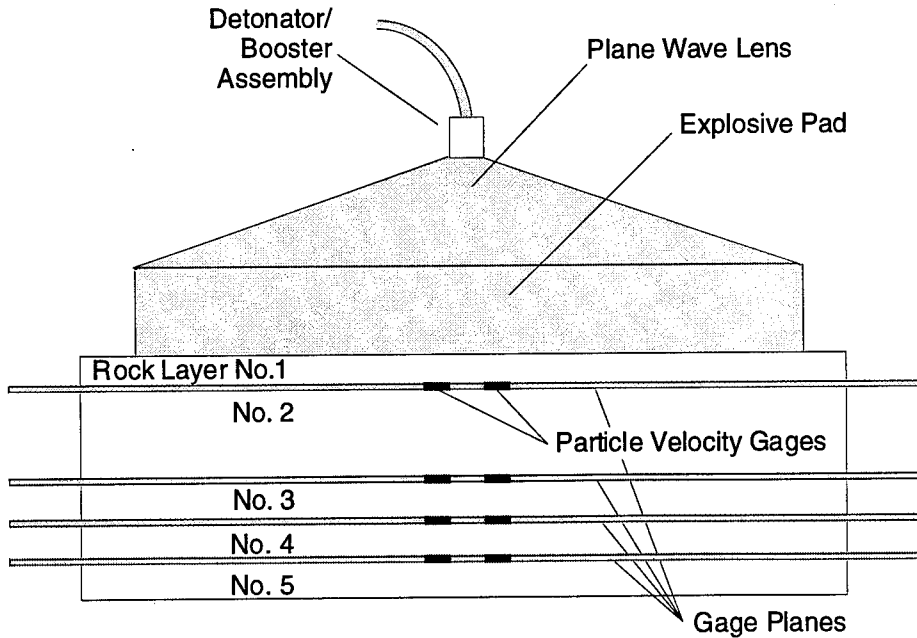
- Intact Danby marble specimens with no joints
- Artificially jointed Danby marble specimens
- UTTR limestone specimens with *in situ* joints.

The same basic experimental design shown in Figure 3-1 was used in all the uniaxial strain experiments except HPEOS Experiment 1, which is described in a later section. As shown in Figure 3-1(a), two particle velocity gages on each of four gage planes were embedded within the specimen. The gages on the first gage plane (closest to the top surface of the specimen) were used to record the oncoming stress wave generated by the explosives and thereby provide a basis for comparing the results of different experiments with different joint configurations. In experiments on jointed rock samples, this gage was also used to record the reflected stress pulse from the rock-joint interface. The remaining gages were used to record the stress wave profile after the wave propagated through the jointed section of the specimen. The results from several experiments were compared to determine the effect of joints of various configurations on the propagation of stress waves in rock.

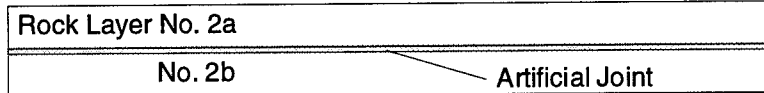
Most experiments were conducted at a peak stress of about 120 kbar. In each experiment, the shock loading was provided using a 15.24-cm-diameter (6.0-in.) plane wave lens and an explosive pad of a type and thickness appropriate to achieve the required loading conditions for the experiment (a 5.08-cm-thick BARATOL pad was used in most experiments).

**3.2.2.1. Artificial Joints.** Several artificial joint configurations were investigated during this study. These configurations included variations of surface texture (smooth versus rough), thickness (closed versus sand-filled), number (single versus triple), and orientation (normal versus inclined with respect to the direction of shock propagation). The smooth joint surfaces were precision ground as described above. The rough joint surfaces were prepared by first grinding the surfaces flat, then inscribing them with regularly spaced grooves as shown in Figure 3-2. As indicated in the figure, rough joints were filled with a 2-mm-thick layer of Reid-Bedford sand, the properties of which are described by Phillips (1986a, 1986b). Some sand-filled smooth joints were also investigated during the present study.

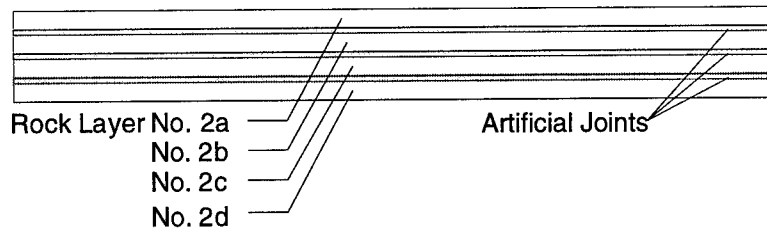
Specimens with sand-filled joints were constructed as follows. First, the specimen was assembled with 2.0-mm-thick shims around the periphery of the joint surface. After the specimen construction was complete and the gages were properly wired, sand was pored into the joint(s) through egress holes along the side of the specimen. The sand was compacted by repeated tamping of the specimen. Once the sand could no longer be compacted using this method, the egress holes were sealed with epoxy.



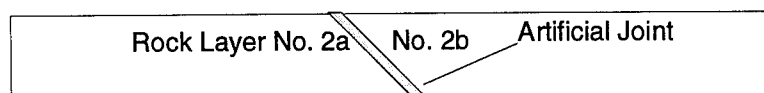
**(a)** Configuration for experiments on intact rock (basic configuration).



**(b)** Modification of the basic configuration to include a single, normal joint.



**(c)** Modification of the basic configuration to include a triple, normal joint.



**(d)** Modification of the basic configuration to include a single, inclined joint.

Figure 3-1. Configurations of the uniaxial strain experiments.

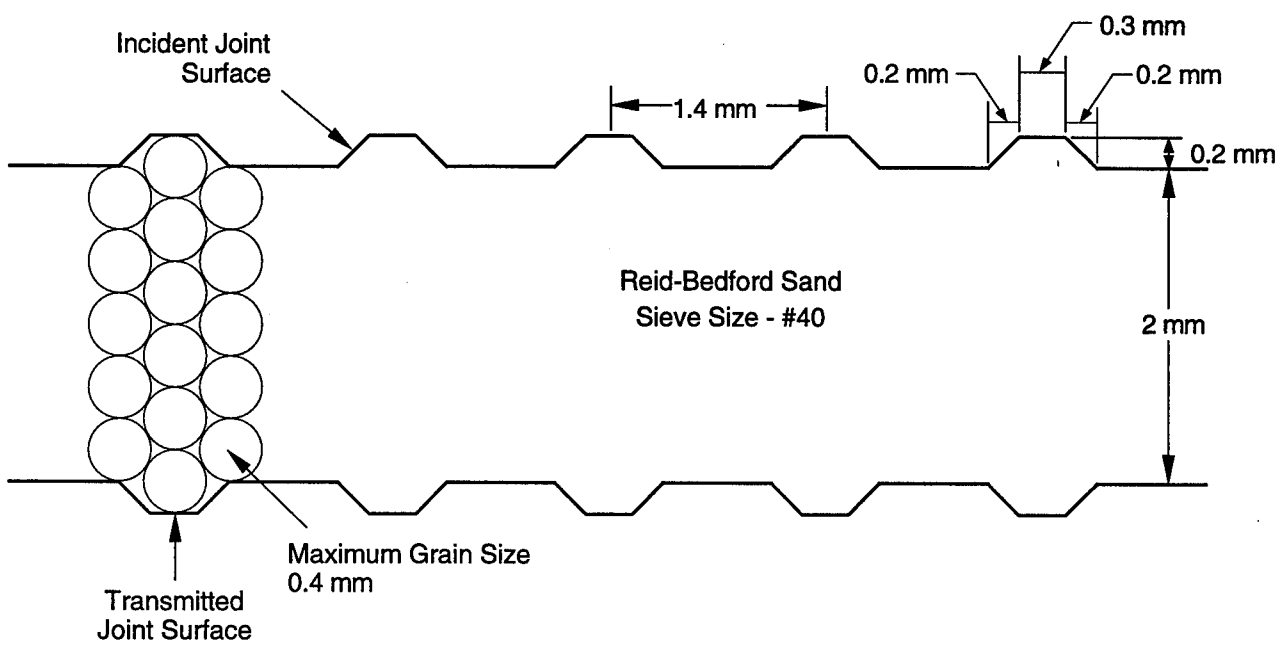


Figure 3-2. Geometry of the surfaces of a rough joint.

### 3.2.3 Instrumentation.

Two types of in-material Lagrangian gage systems were used to record either stress or particle velocity histories in the impacted geological specimens. Ideally, a Lagrangian gage monitors and records the flow field at some location within the specimen without perturbing the motion of the specimen. In practice, however, this is not the case. Because of the finite thickness of the gage package and the impedance mismatch between the specimen material and the gage plane, the flow field in the vicinity of the gage is disturbed, and a finite rise time is required to establish a state of equilibrium at the specimen-gage interface. An analytical method was devised during this study to estimate the rise time of in-material Lagrangian gages. This method, which is described in Appendix A, shows that the rise time of the gages used in our investigation is less than 50 ns. This is well within the resolution for the measurement.

**3.2.3.1. Stress Gage System.** The stress gage system was used only in HPEOS Experiment 1, which was a relatively simple experiment designed primarily to investigate the effect of quartz content in the UTTR rock on the signal-to-noise ratio of transient measurements made using in-material stress or particle velocity gages. The configuration for this experiment is shown in Figure 3-3. As shown, the specimen consists of a four-terminal manganin gage sandwiched between two slabs of UTTR limestone. The gage leads exit the specimen at a 45° angle so that they are shielded from the blast generated by the explosives and a longer recording time is ensured. The explosives used in this experiment consisted of a 10.2-cm-diameter (4-in.) plane wave lens and a 5.08-cm-thick (2-in.) pad of the high explosive PBX. The four-lead manganin gage grid shown in Figure 3-3 was photo-etched from a 0.05-mm-thick manganin foil. This type of stress gage is based on the principle of piezoresistance. The resistance of the gage, initially about  $0.1 \Omega$ , changes predictably when a pressure disturbance like a stress wave passes through the gage element. The voltage associated with this change in resistance is recorded using a digital oscilloscope and is then converted to stress using well established calibration relationships.

In reducing the voltage data, it is assumed that

$$\frac{\Delta R}{R_0} = \frac{\Delta V}{V_0} \quad (3-1)$$

where  $R_0$  is the initial resistance of the gage,  $\Delta R$  is the change in resistance,  $V_0$  is the initial voltage, and  $\Delta V$  is the change in voltage. This assumption carries the implication that the effects of changes in the resistance of the gage element and leads and decay of the capacitor voltage (power supply) are negligible. In reality, these effects account for 1%, or less, of the recorded signal.

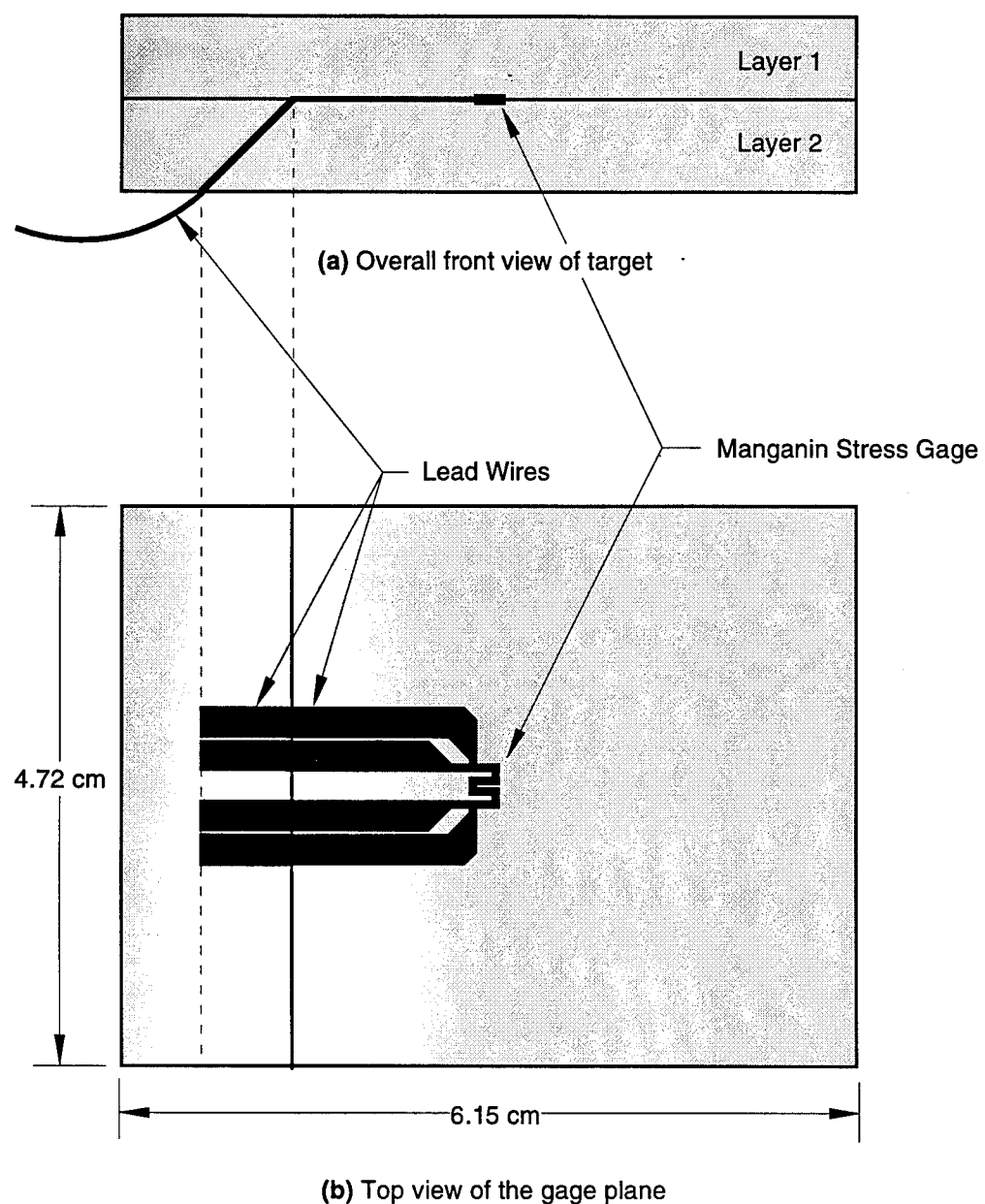


Figure 3-3. Specimen configuration and dimensions for HPEOS Experiment 1 in UTTR limestone.

In the stress range of interest here, and assuming uniaxial strain behavior, the relationship between the change in resistance (or voltage) and the stress in the manganin gage is given by the equation

$$\sigma \text{ (kbar)} = \alpha \left( \frac{\Delta R (\Omega)}{R_0 (\Omega)} \right) \quad (3-2)$$

where  $\sigma$  is the stress and  $\alpha$  is an experimentally determined proportionality constant with a value of 350 kbar/ $\Omega/\Omega$  (DeCarli, 1976).

**3.2.3.2. Particle Velocity Gage System.** The magnetic particle velocity gages used throughout this study are based on the principle that a conductor (the particle velocity gage) moving in the direction normal to a uniform quasi-static magnetic field generates a voltage proportional to its length and velocity and the strength of the magnetic field. Mathematically, this proportionality is expressed through the relation

$$u(t) = \frac{V(t)}{\ell B} \times 10^4 \quad (3-3)$$

where  $t$  is time,  $u(t)$  is particle velocity in millimeters per microsecond,  $V(t)$  is gage voltage in volts,  $\ell$  is the center-to-center active gage length in millimeters, and  $B$  is the magnetic field strength in gauss.

The uniform magnetic field was provided using Helmholtz coils. A schematic representation of a specimen situated within a Helmholtz coil assembly is shown in Figure 3-4. Each coil consisted of 40 circular turns of No. 8 copper wire. The coil radius, which was equal to the separation distance between the coils, was about 45.72-cm (18-in.). The coil assembly was pulsed with a constant current of about 350 amperes a few hundred microseconds before the experiment. The current in the coils was measured using a pulse current transformer (Pearson Electronics, Inc., Palo Alto, CA 94303). The magnitude of the uniform magnetic field was calculated from the relation

$$B = 0.286 \frac{\pi NI}{r} \quad (3-4)$$

where  $B$  is the field strength in gauss,  $N$  is the number of turns in one coil,  $I$  is the current through the coils in amperes, and  $r$  is the coil radius in centimeters.

Two types of particle velocity gages were used in this investigation: SRI-manufactured gages and prefabricated gages manufactured by TAYCO Engineering (P.O. Box 6034, Cypress, CA 90630). A detailed engineering drawing of the TAYCO particle velocity gages is shown in Figure 3-5. As shown, the gages were fabricated in pairs, with one gage made of copper and the other of Inconel. The gages were laid out on a 0.05-mm-thick Teflon backing. A gage package such as the one shown in

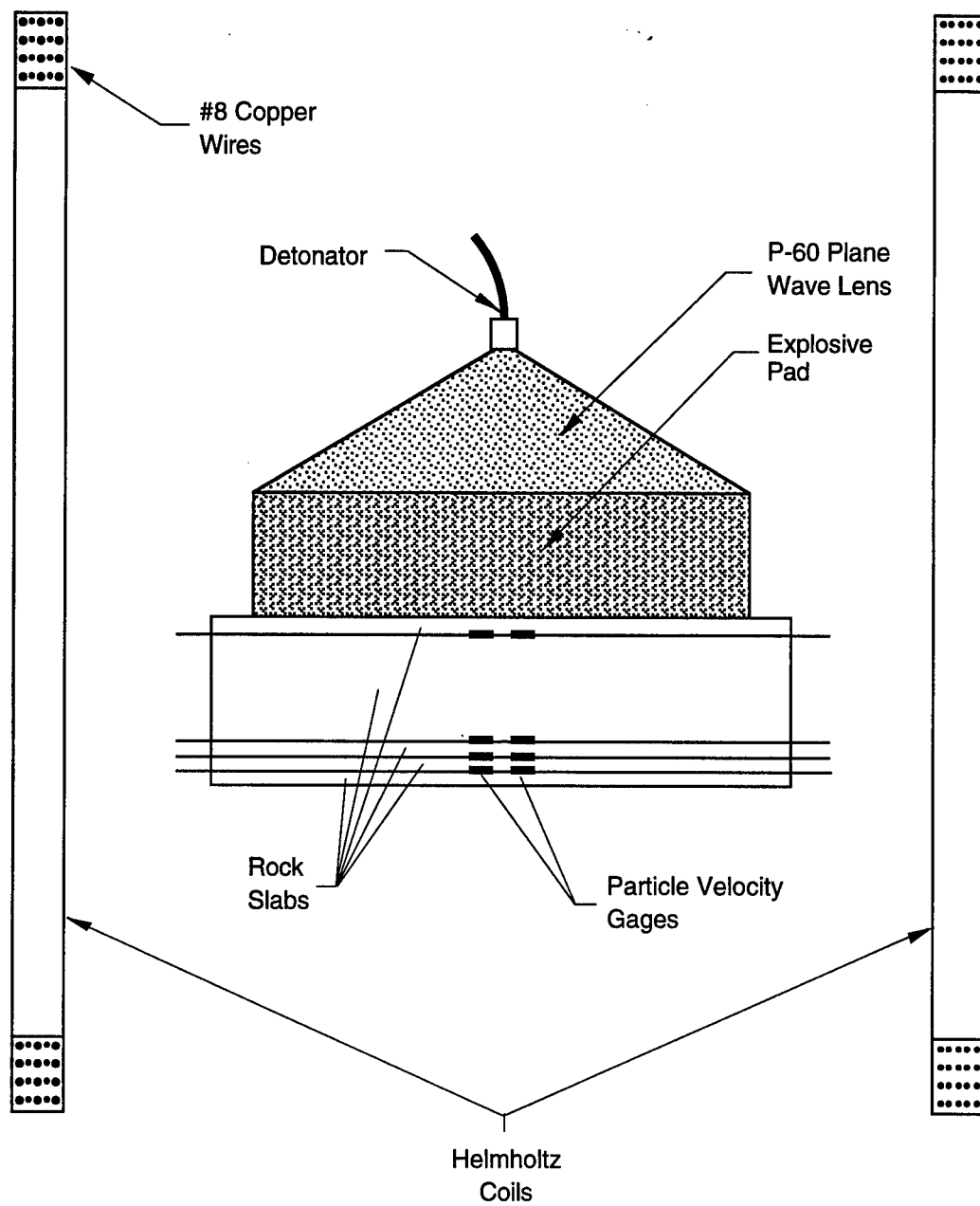


Figure 3-4. Schematic diagram of a typical uniaxial strain experiment instrumented with particle velocity gages.

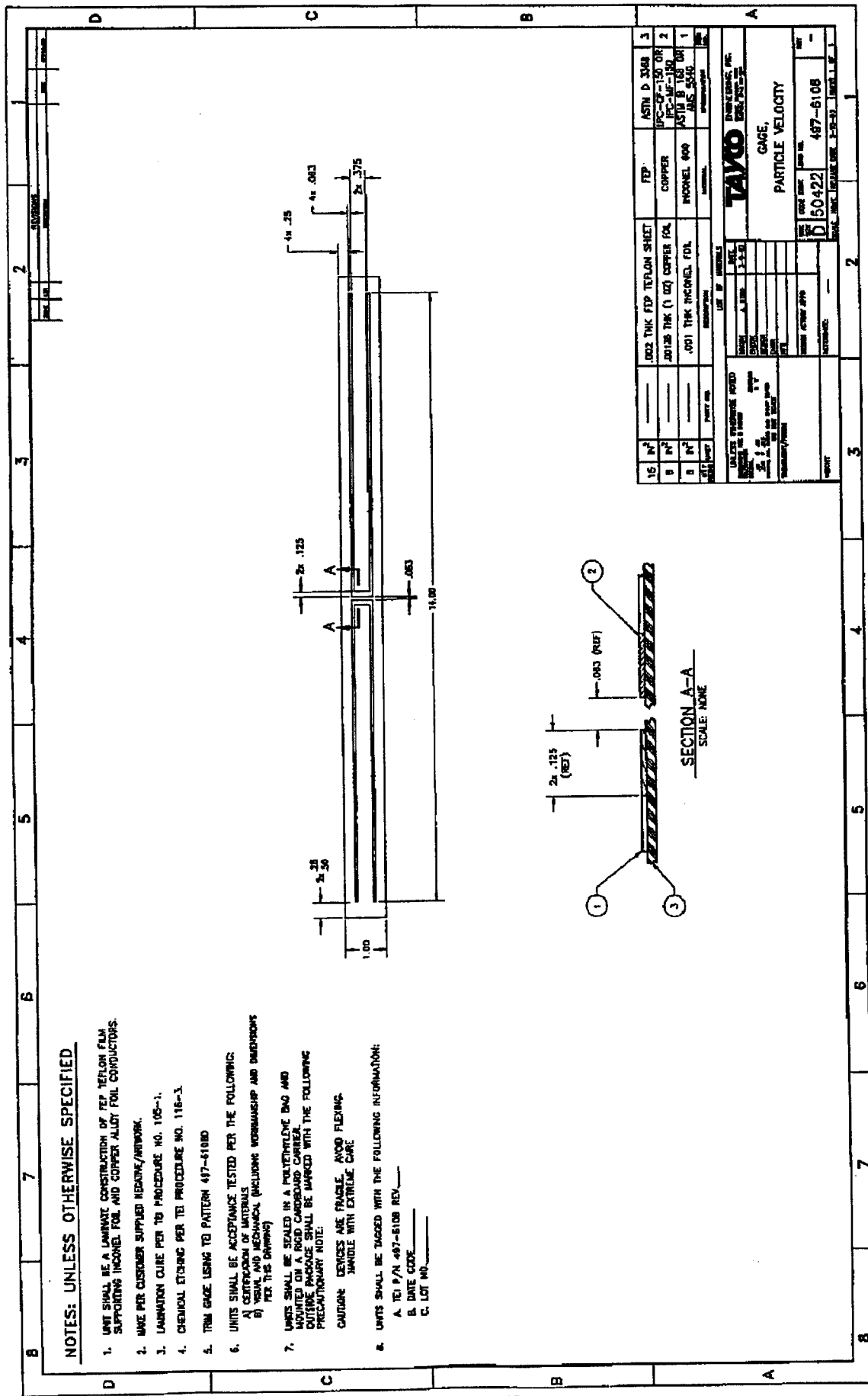


Figure 3-5. Engineering drawing showing the specifications and dimensions of a prefabricated particle velocity gage.

Figure 3-5 was embedded in each gage plane to provide a duplicate recording of the particle velocity at the gage plane. The active elements of the prefabricated gages each had an area of 12.7 by 3.18 mm. The SRI gages had the same dimensions as the prefabricated gages and had Inconel active elements connected to copper leads. Unlike the prefabricated gages, the SRI gages were laid out directly on the specimen without any backing materials.

### 3.3 EXPERIMENTAL RESULTS.

The measurements from the uniaxial strain, in-contact explosive experiments are presented in Appendix B. The appendix describes the experimental conditions and specimen geometries and summarizes the raw data and reduced experimental results. For easy reference, Appendix B includes a tabular summary of all the uniaxial strain experiments (Table B-1).

In general, the experimental results were self-consistent and revealed important information about phase transformations in calcium carbonate rock as well as the effect of joints on wave propagation. The results were repeatable. In each of the uniaxial strain experiments, two gages were used to provide duplicate measurements of the particle velocity histories at each gage plane. In general, the agreement between the gages on a given gage plane was excellent, as can be seen by a close examination of the experimental records in Appendix B.

Two types of gages were used to measure particle velocity histories: SRI-manufactured gages and prefabricated gages. To ensure that both types of gages yielded identical results, duplicate measurements were taken during two experiments (HPEOS Experiments 6 and 7) and the measured histories were compared. The two types of gages yielded identical results.

HPEOS Experiment 1 was conducted to determine the effect of the quartz content of the UTTR limestone on the signal-to-noise ratio in the recorded data. The results of this experiment (shown in Figures 3-6 and 3-7) indicate that quartz content has little effect on the recorded signal. Figure 3-6 shows the voltage history recorded during the experiment. The voltage in the gage element is zero initially, but increases to about 1 V at  $t \approx 0.5 \mu s$ . This is the exitation voltage, and it is provided using a constant current power supply. The voltage in the gage remains constant until the arrival of the stress wave at the gage plane approximately 20  $\mu s$  after the gage is pulsed.

The voltage history shown in Figure 3-6 was converted to a stress history by using Equation (3-2), and the results are plotted in Figure 3-7. The origin of the time axis in this figure is chosen arbitrarily and has no bearing on the results. The wave structure depicted in the figure is relatively simple: a compressional loading wave that shocks the material up to a peak stress of 260 kbar, a gentle unloading wave that causes a 50-kbar decrease in peak stress, and a main release wave that unloads the rock to a stress-free state. The initial shock wave originates in the explosive as does the gentle, Taylor unloading

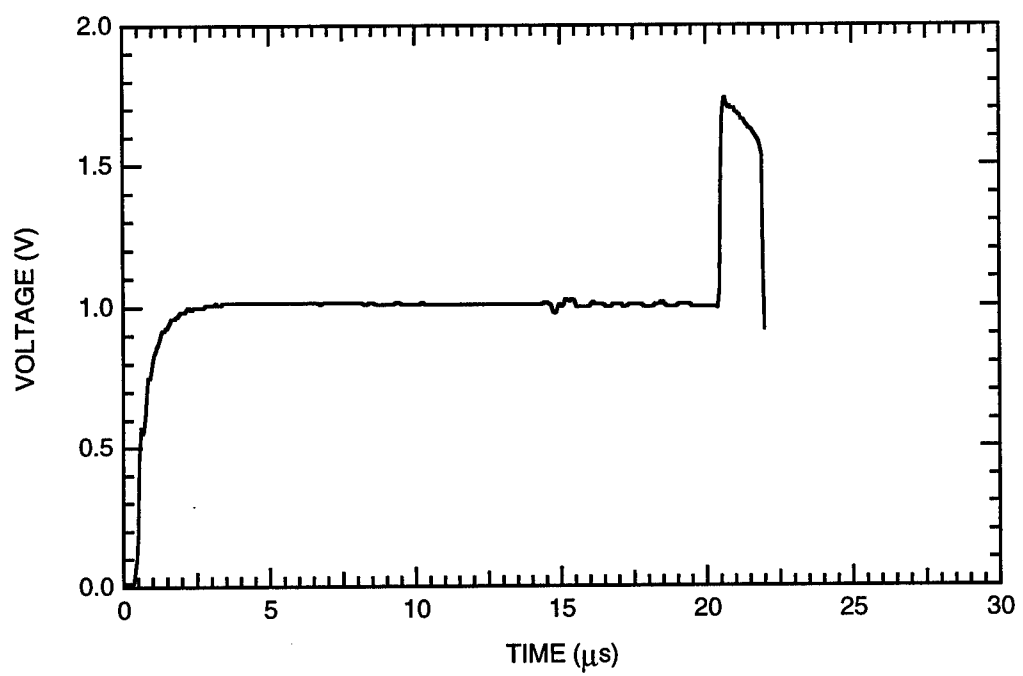


Figure 3-6. Manganin gage record in HPEOS Experiment 1.

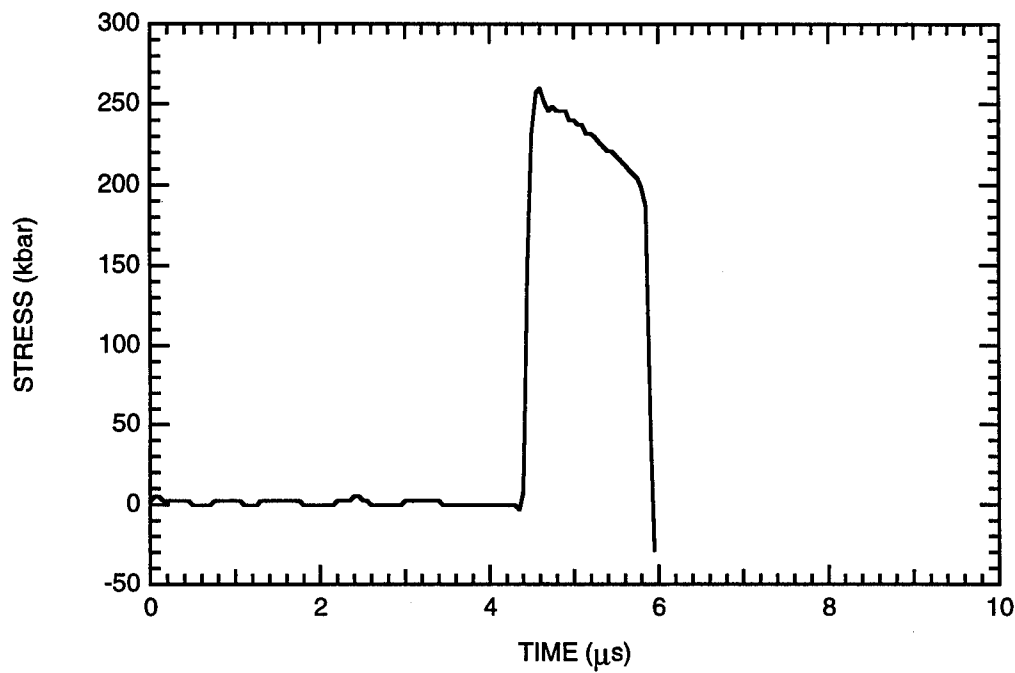
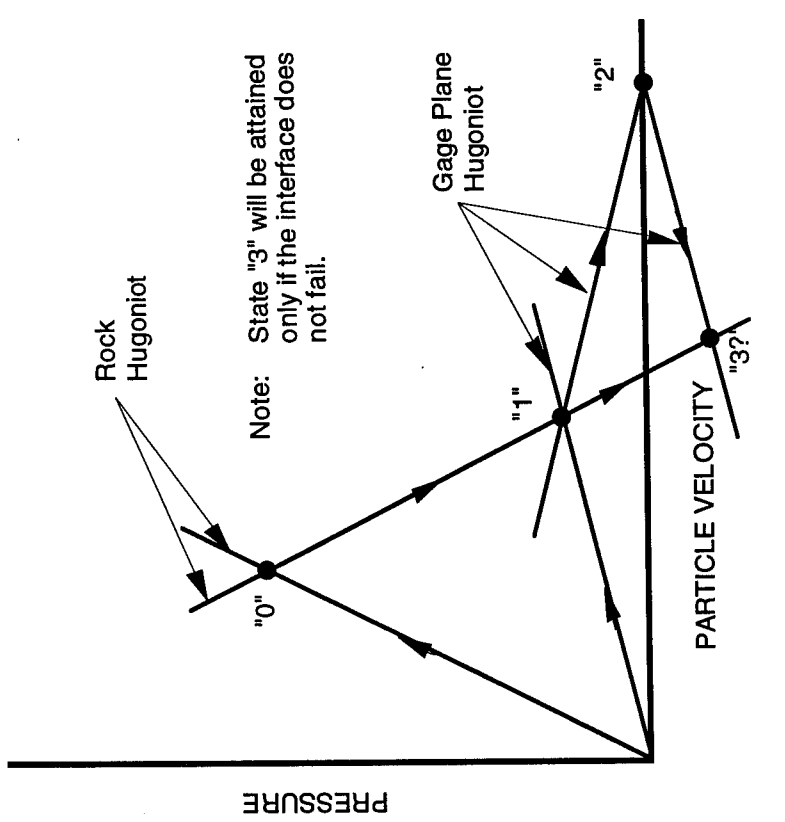


Figure 3-7. Stress history at the gage plane in HPEOS Experiment 1.

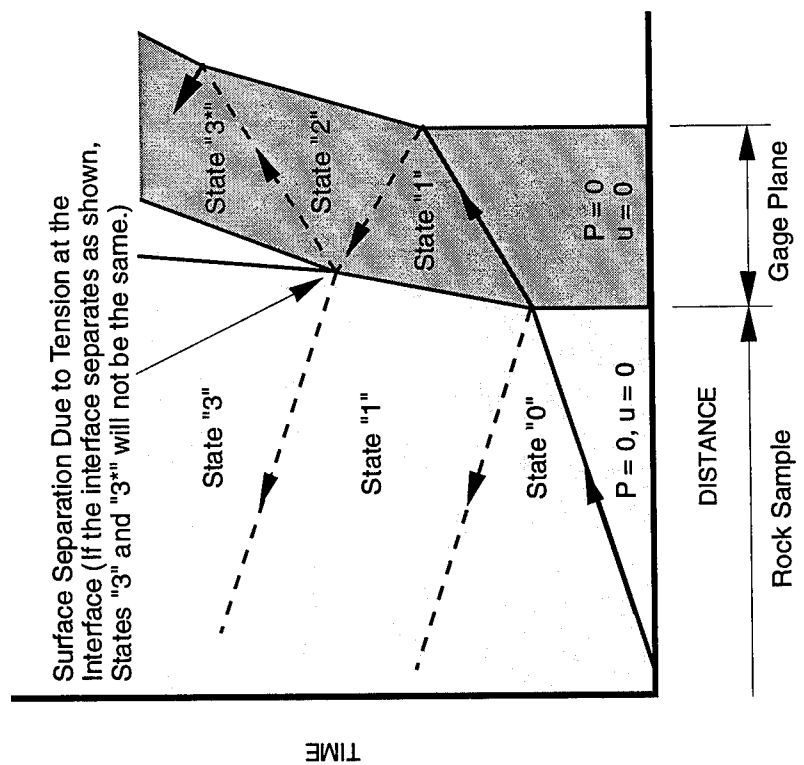
wave. The main release wave is a backward facing wave that originates at the back free surface of the specimen. The pulse duration of 1.8  $\mu$ s is equivalent to the time required for the stress wave to propagate from the gage plane to the back surface of the specimen and back again to the gage plane. This time interval is less than the time required for the release waves from the lateral specimen boundaries to reach the gage plane (approximately 3  $\mu$ s), and thus a uniaxial strain state is ensured in the specimen for the duration of the experiment.

HPEOS Experiment 2 was instrumented as shown in Figure 3-1. In addition, a particle velocity gage was installed at the back surface of the specimen to attempt to measure the free surface velocity of the sample. We believe that the data recorded by this gage do not reflect the real free surface velocity of the specimen, for reasons illustrated in Figure 3-8. The figure shows a distance-time diagram and a pressure-particle velocity diagram for the first few wave reverberations resulting from the interaction between the free surface of the specimen and the gage package. Solid lines in Figure 3-8(a) represent compression waves, whereas dashed lines represent rarefaction waves. In reality, each of the dashed lines represents the "toe" of a dispersive rarefaction fan, the remainder of which is omitted from the figure for clarity. Figure 3-8 shows three stress states in the gage package. State "1" is a compressive stress state that results from the interaction of the main pressure wave with the gage/specimen interface. State "2" is a stress-free state created by the reflection of the stress wave from the free surface of the gage package. State "3" is a tensile stress state due to the second interaction between the specimen and the gage package. It is this latter stress state that causes the free surface velocity measurement to be erroneous. Because of the tensile stress generated at the gage/sample interface, the gage separates from the back surface of the specimen and moves at a velocity higher than the velocity of the specimen. This observation is supported by the experimental data of HPEOS Experiment 2, which show the peak velocity recorded by the free surface gage to be more than 50% larger than the velocity recorded 3.3-mm away in the interior of the sample. Ideally, these two gages should reach approximately the same velocity. Owing to the failure at the gage/sample interface, the free surface gage was omitted from later experiments.

The voltage output of the particle velocity gages in HPEOS Experiments 3 and 4 could not be converted to particle velocity histories because of failure of the pulse current transformer. This failure was corrected and did not affect subsequent experiments. Given the consistency and good reproducibility of the results, and the fact that most of the uniaxial strain experiments were conducted under the same boundary and loading conditions, the particle velocity histories for Experiments 3 and 4 can be calculated with reasonable accuracy ( $\pm 5\%$ ) by using the calibration values of other similar experiments. However, such calculations were not attempted.



(b)  $P-u$  diagram showing the gage plane equilibrium gage process



(a)  $x-t$  diagram showing wave reverberations in gage plane

Figure 3-8. Wave reverberations due to impedance mismatch between the test medium and the free surface velocity gage.  
(pressure is positive in compression).

### **3.4 LAGRANGIAN ANALYSIS.**

Since its introduction by Fowles and Williams (1970), the Lagrangian analysis method has had a long history of improvements (Cowperthwaite and Williams, 1971; Grady, 1973), which culminated in the development of the GUINSY computer code developed by Seaman (1987) in our laboratory and considered to be the industry standard.

Originally, we had intended to use the Lagrangian analysis code GUINSY to obtain loading and unloading paths for the rock samples investigated during our study. However, this analysis could not be performed owing to inherent deficiencies in the present version of GUINSY in handling wave interactions resulting from reflections from impedance-mismatched boundaries, as discussed below.

In the uniaxial strain experiments, the compressive wave generated by the explosive travels through the gaged region of the specimen, reaches the free surface, then reflects back into the specimen as a release wave that unloads the specimen to a stress-free state. The forward-traveling compression wave and the backward-traveling release wave interact near the free surface of the specimen to create a region of mixed flow. Wave interactions in this region require the use of complicated algorithms different from the ones used in routine GUINSY applications. A method of analysis incorporating these algorithms was programmed into GUINSY and tested on our data. Because of the complex nature of this method, it had been speculated when the method was developed that further developments might be required before it could be used reliably (see Seaman, 1987, p. 12-14).

When an attempt was made to use GUINSY to analyze the data from the present experiments, deficiencies were indeed discovered in the code's ability to handle wave interactions. Several steps have since been taken to fix the problem. First, the old GUINSY algorithms have been revised and new algorithms have been added to the code. Second, a closed-form analytic solution of a problem that involves wave reflections from an impedance-mismatched boundary was obtained to be used as a test case of the new code to ensure proper operations within the code. This analytic solution is described in detail by Cowperthwaite (1995) in the technical paper included in Appendix C.

We are currently debugging the new algorithms, and at the time this report was prepared the GUINSY code was not robust enough to be used reliably in the analysis of the experimental data. Instead, numerical simulations of the experiments were performed using the Lagrangian finite difference hydrocode PUFF (Seaman and Curran, 1978). These simulations are described below.

### 3.5 CODE SIMULATIONS.

Numerical simulations were carried out using the finite difference code PUFF to help in the interpretation of experimental results and provide added insight into the behavior of jointed calcium carbonate rock. This section describes the constitutive models used in the simulations. It also shows a verification analysis in which PUFF was used to simulate an experiment similar to the ones performed during the present investigation. Simulation results for jointed samples will be described and compared with experimental data as appropriate in a later section.

In the simulations, the rock behavior was described using a rate-independent, elastic-plastic model for deviatoric stress calculations and a Mie-Grüneisen equation of state for pressure calculations. In PUFF, the Mie-Grüneisen equation takes the following form:

$$P = (C\mu + D\mu^2 + S\mu^3) \left( 1 - \frac{\Gamma\mu}{2} \right) + \Gamma\rho E \quad (3-5)$$

where  $P$  is the pressure,  $\Gamma$  is the Grüneisen coefficient,  $\rho$  is the density,  $E$  is the internal energy,  $(C\mu + D\mu^2 + S\mu^3)$  is the Hugoniot pressure,  $C$ ,  $D$  and  $S$  are coefficients with moduli units, and  $\mu$  is the volumetric strain given by the relation

$$\mu = \frac{\rho}{\rho_0} - 1 \quad (3-6)$$

where  $\rho_0$  is the initial density. The model parameters were determined from the collection of existing data for nonporous calcite rock encountered in the literature review. These parameters are summarized in Table 3-1, and a comparison between experimental data for nonporous calcite and the Hugoniot equation of state used in the code calculations is shown in Figure 3-9.

When the response of a specimen with a sand-filled joint was simulated, the behavior of the sand was modeled using a porous equation of state. The sand was assumed to have an initial density of 1.74 g/cm<sup>3</sup>, an initial bulk modulus of 28 kbar, and a shear modulus of 10 kbar and to reach its solid density at a pressure of 20 kbar and thereafter behave like solid quartz.

Before we simulated the experiments of the present investigation, we carried out a verification analysis in which an experiment similar to the ones described here was simulated and the results compared to experimental data [Murri et al. (1975), Experiment 1883-53]. The experimental configuration is shown in Figure 3-10. The material used in the experiment was Linden Hall limestone (<0.5% porosity). The in-contact explosives used for loading consisted of a 20.32-cm-diameter (8 in.) plane wave lens and a 15.24-cm-thick (6-in.) pad of Baratol explosives [see Murri et al. (1975) for more details].

**Table 3-1. Parameters used to describe the behavior  
of marble in the PUFF finite difference  
simulations.**

Parameter	Value	Units
Initial density	2.7	g/cm <sup>3</sup>
Yield stress	10.0	kbar
Shear modulus	400.0	kbar
Hugoniot parameters		
C (bulk modulus)	191.7	kbar
D	1732.0	kbar
S	-742.5	kbar
Grüneisen coefficient	1.59	

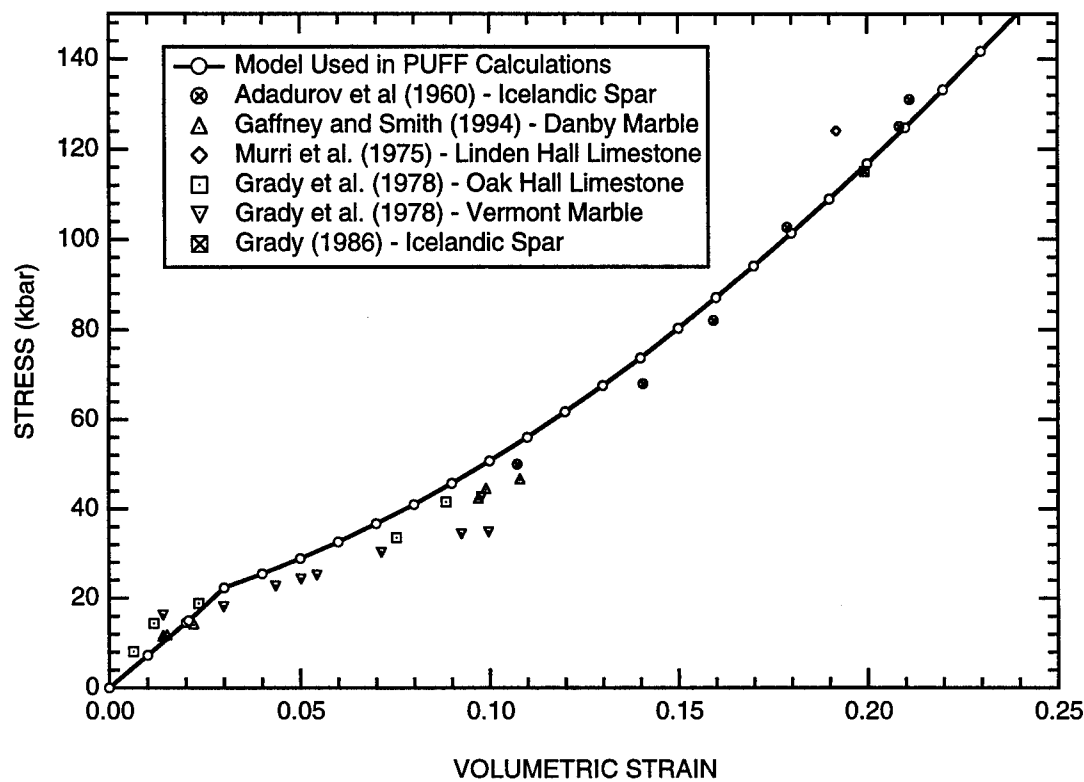


Figure 3-9. Comparison between the equation of state used in the PUFF simulations and experimental data for nonporous calcite.

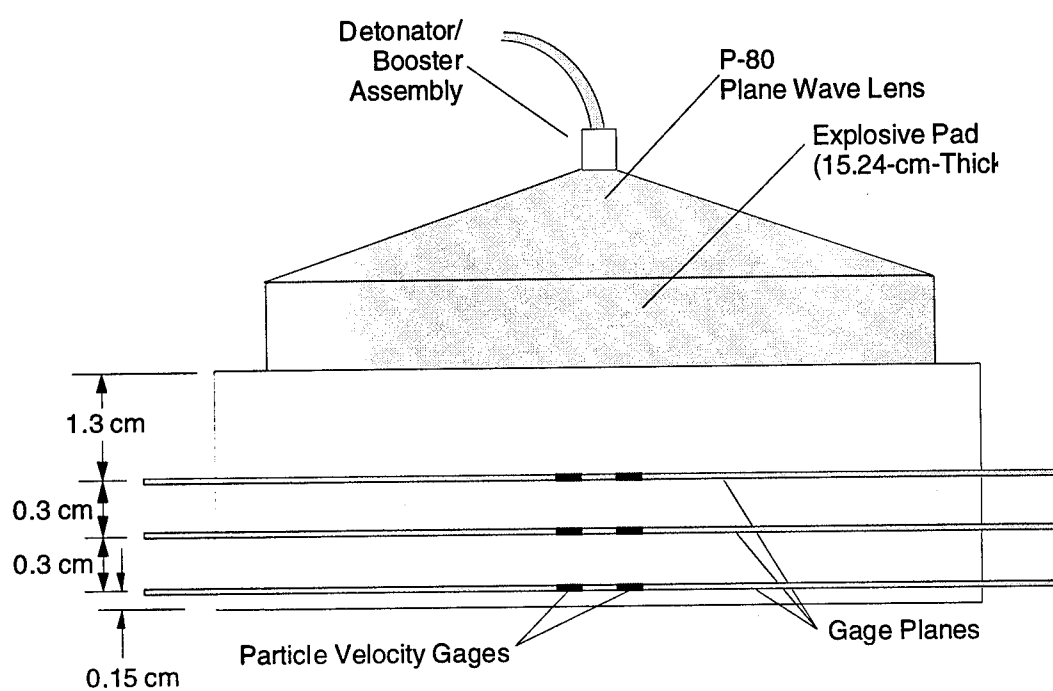


Figure 3-10. Target configuration and dimensions for experiment 1883-53 on Linden Hall limestone (Murri et al., 1975.)

The experimental and simulated particle velocity histories are compared in Figure 3-11. The correlation between the experimental and calculated records is rather close. The overall shape, first particle velocity plateau (corresponding to peak stress), and peak particle velocities (corresponding approximately to the free surface velocity) are all reproduced by the code calculations. The "kink" in each of the experimental velocity histories just prior to the peak velocity plateau is associated with a reverse phase transformation. This feature was not reproduced in the code calculations because phase transitions were not incorporated in the material description in the hydrocode.

The close correlation between the simulated velocity histories and the experimental data in the example tested lends credence to the simulation results and justifies the use of PUFF to help in the interpretation of experimental results and to provide added insight into the effect of joints on wave propagation.

### 3.6 DISCUSSION.

#### 3.6.1 Hugoniot Elastic Limit and Phase Transitions.

A precursor to the main compression wave was observed in the uniaxial strain experiments on both Danby marble and UTTR limestone. The magnitude of the precursor was determined for HPEOS Experiments 2, 6, 7, 8, and 16 by using the conservation of momentum equation across the shock front, namely,

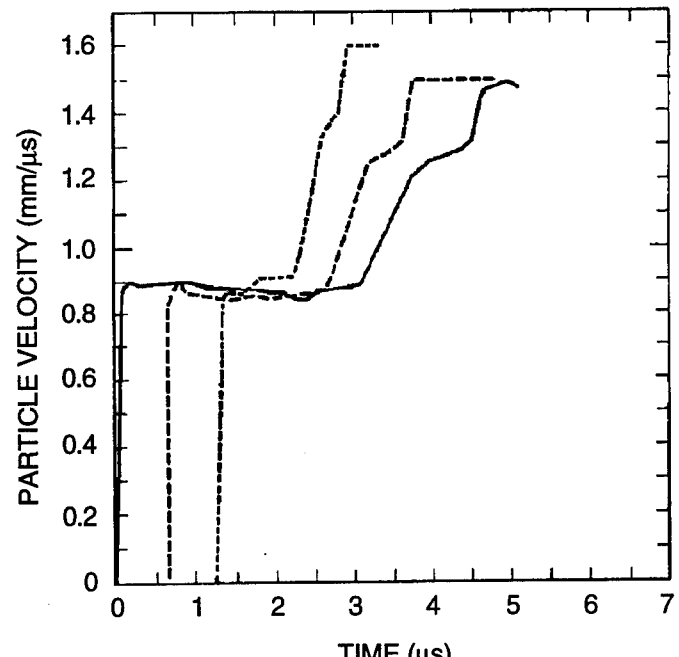
$$\sigma - \sigma_0 = \rho_0 (U - u_0)(u - u_0) \quad (3-7)$$

where  $\sigma$  and  $u$  are the stress and particle velocity behind the shock front;  $\rho_0$ ,  $\sigma_0$ , and  $u_0$  are the density, stress, and particle velocity ahead of the shock front; and  $U$  is the shock velocity. Ahead of the precursor, both  $\sigma_0$  and  $u_0$  are zero, and Equation (3-7) reduces to

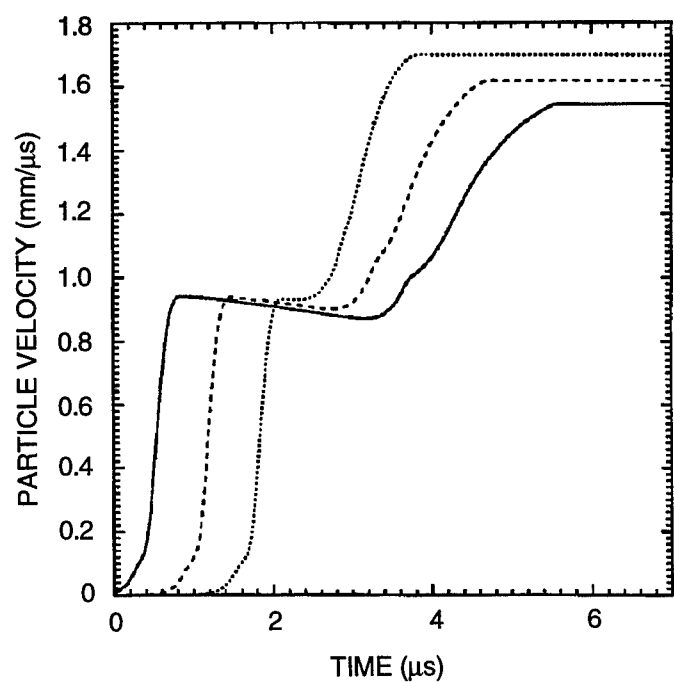
$$\sigma = \rho_0 U u. \quad (3-8)$$

Equation (3-8) was used to determine the precursor stress for Danby marble and UTTR limestone by using the experimentally recorded values of particle velocity and shock velocity. The particle velocity along the precursor was obtained directly from the experimental records. The precursor wave velocity was determined based on the time of arrival of the elastic wave at two subsequent gage locations and the separation distance between the gage planes.

The average precursor stress for Danby marble was 17.1 kbar, based on calculated values of 16.8, 16.3, 19.0, and 16.2 kbar for HPEOS Experiments 2, 6, 7 and 8, respectively. These results are in good



(a) Experimental data



(b) PUFF simulation

Figure 3-11. Comparison of experimental and calculated particle velocity histories for Murri et al. (1975) Experiment 1883-53.

agreement with the Danby marble results of Keough et al. (1993), who reported precursor stress values between 14 and 16 kbar; Furnish (1994), who reported precursor stress values between 13 and 15 kbar; and Gaffney et al. (1994), who reported precursor stress values between 14 and 16 kbar.

The precursor stress for UTTR limestone was 14.3 kbar, which was calculated based on the results of HPEOS Experiment 16. This stress is slightly higher than the 11-14 kbar precursor stresses reported by Furnish (1994) for UTTR limestone.

Figure 3-12 shows an average of the two particle velocity histories recorded at the second gage plane of HPEOS Experiment 2. The prominent features of the experimental data for intact marble are indicated in the figure by the letters A, A', B and B'. The precursor observed in our experiments and indicated by Point A in Figure 3-12 is most likely the result of processes associated with the calcite I - calcite II and calcite II - calcite III transitions, not plastic yielding. This observation is supported by our unloading data. If the precursor were due to yielding, reverse yielding would be expected to occur early during unloading (for elastic/perfectly plastic materials, reverse yielding occurs when the stress reaches a value equal to the peak stress minus twice the yield stress). However, this is not observed in our results. Instead, the signature of a reverse phase transition is observed in the form of a rarefaction shock that occurs late during unloading, at a stress level approximately equal to the precursor stress. This feature (Point A' in Figure 3-10) indicates that the precursor observed in our experiments is associated with the calcite phase transformations.

Another interesting feature of the particle velocity history shown in Figure 3-12 is an apparent high-pressure phase transition at Point B and a corresponding reverse phase transition at Point B'. Assuming a two wave structure, and making use of Equation (3-7) and the mass conservation equation across a shock front,

$$\frac{\rho}{\rho_0} = 1 - \frac{u - u_0}{U - u_0} \quad (3-9)$$

the pressure at Point B can be calculated. For HPEOS Experiment 2, this pressure is 118.3 kbar. High pressure phase transitions in calcium carbonate rocks have been observed in this pressure range by Murri et al. (1975), Ahrens and Gregson (1964), and Adadurov et al. (1960) (see Table 2-2), findings providing further evidence that the wave structure at points B and B' is associated with this high pressure phase transition in calcite rock.

### **3.6.2 Effect of Joints on Wave Propagation.**

Experiments were performed to determine the effects of *in situ* and artificial joints on wave propagation in CaCO<sub>3</sub> rock. The *in situ* joints in UTTR limestone did not have a measurable effect, as evidenced by

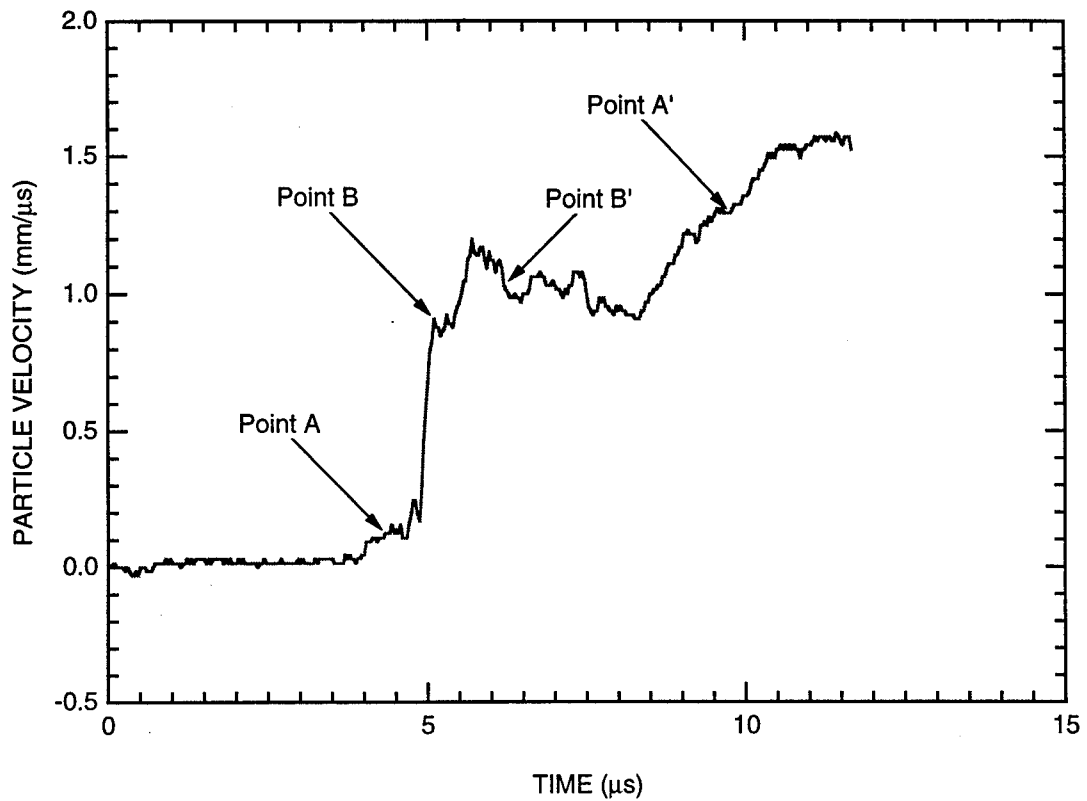


Figure 3-12. Average particle velocity history at the second gage plane of HPEOS Experiment 2 showing the prominent features of the experimental data for intact marble.

the similarity between the particle velocity histories recorded in the UTTR limestone experiment (HPEOS Experiment 16) and their counterparts in the intact marble experiments (HPEOS Experiments 2, 6, and 7). On the other hand, artificial joints in marble had a significant effect on the observed response. To better understand the effect of artificial joints on wave propagation, we performed a series of hydrocode simulations using the finite difference wave propagation hydrocode SRI PUFF (Seaman and Curran, 1978). First, we simulated the response of an intact marble specimen having the configuration shown in Figure 3-1(a) and the same dimensions as HPEOS Experiment 2. We then simulated the response of jointed specimens having the configurations shown in Figures 3-1(b) (single joint) and 3-1(c) (triple joint). The effect of joints was established by comparing the results of the benchmark simulation in intact marble with the results of simulations in jointed marble.

Figure 3-13 shows the simulated particle velocity histories at each of the gage planes and at the free surface of the intact marble experiment shown in Figure 3-1(a). The first peak in the particle velocity histories corresponds to peak stress, and it is approximately the same on all the gage planes. This peak, which also corresponds to the Chapman-Jouguet (C-J) pressure of the explosives, is followed by a gentle unloading wave that causes a gradual decrease in the particle velocity profiles. This is the Taylor unloading wave, which originates in the explosive gases. The second plateau in the particle velocity records is associated with the stress-free state in the specimen. It is carried through the specimen by a backward-traveling release wave that originates at the back surface of the specimen.

To gain insight into the effect of joints on wave propagation, the two experimental configurations with normally oriented artificial joints, shown in Figure 3-1(b) and 3-1(c), were also simulated. The resulting particle velocity histories at the first through the fourth gage planes are compared with the results of the intact marble simulation in Figures 3-14 through 3-17. Two features associated with the effect of joints on the simulated particle velocity profiles are readily apparent. The first of these features is depicted in Figure 3-14. The particle velocity profiles on the first gage plane (ahead of the joint) are modified by spikes—one spike for the single joint configuration, and three spikes for the triple joint configuration. These spikes, and the corresponding decrease in stress, result from wave reflections at the rock/joint interfaces. Interestingly, these spikes are not quite as apparent on any of the gage planes located behind the joint (Figures 3-15 through 3-17), although on the second gage plane the velocity history associated with the triple joint configuration shows characteristics similar to those observed on the first gage plane. The second feature associated with the effect of joints on the simulated particle velocity profiles is the delayed time-of-arrival (TOA) of the wave at the second, third, and fourth gage planes (all located behind the joint). This delayed TOA is barely perceptible for the single joint configuration but more pronounced for the triple joint configuration. The TOA delay can be related to the number of reverberations required to bring the joint to pressure and particle velocity equilibrium with the test

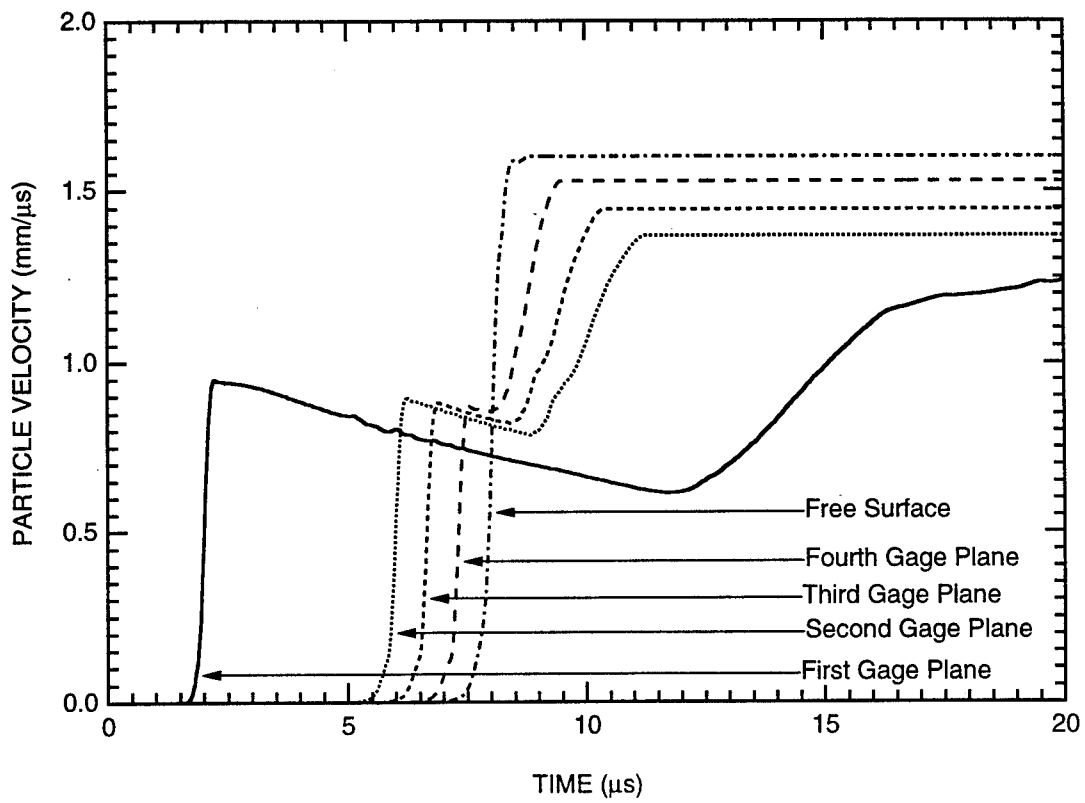


Figure 3-13. Simulated particle velocity histories for a typical experiment on intact marble.

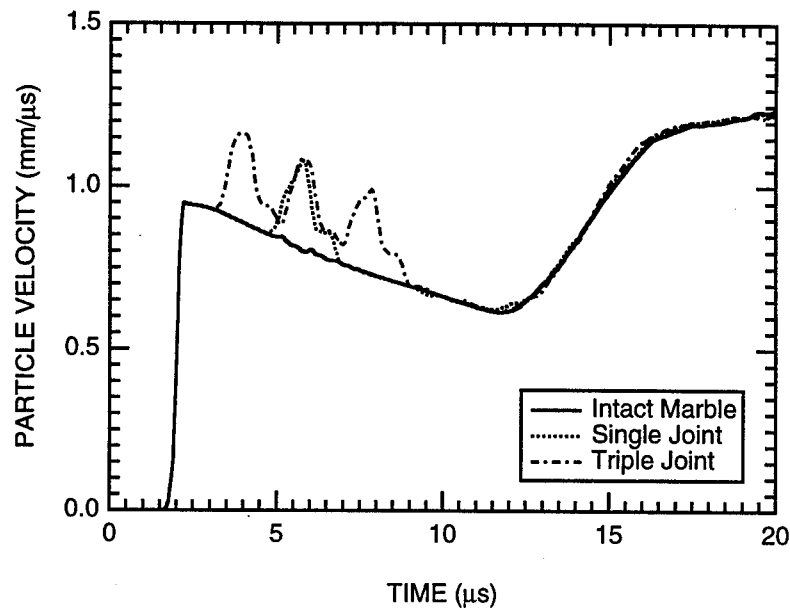


Figure 3-14. Simulated particle velocity histories at the first gage plane.

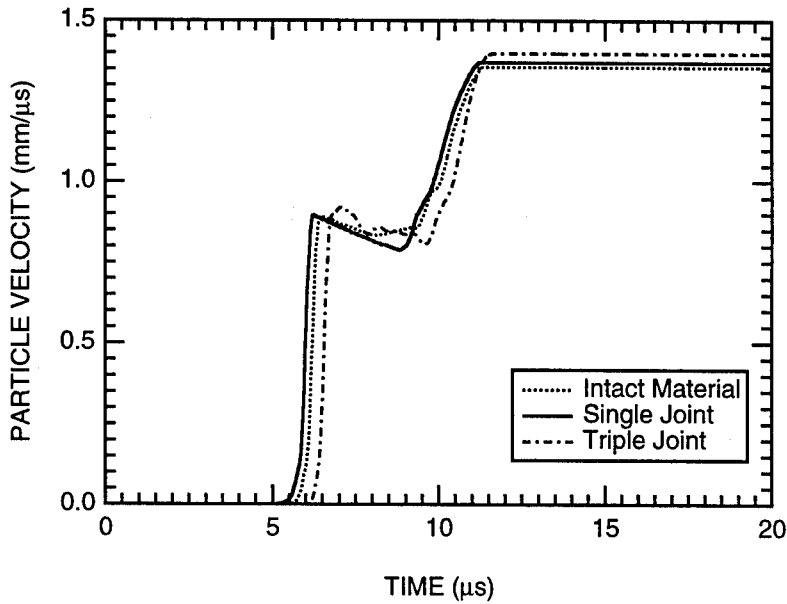


Figure 3-15. Simulated particle velocity histories at the second gage plane.

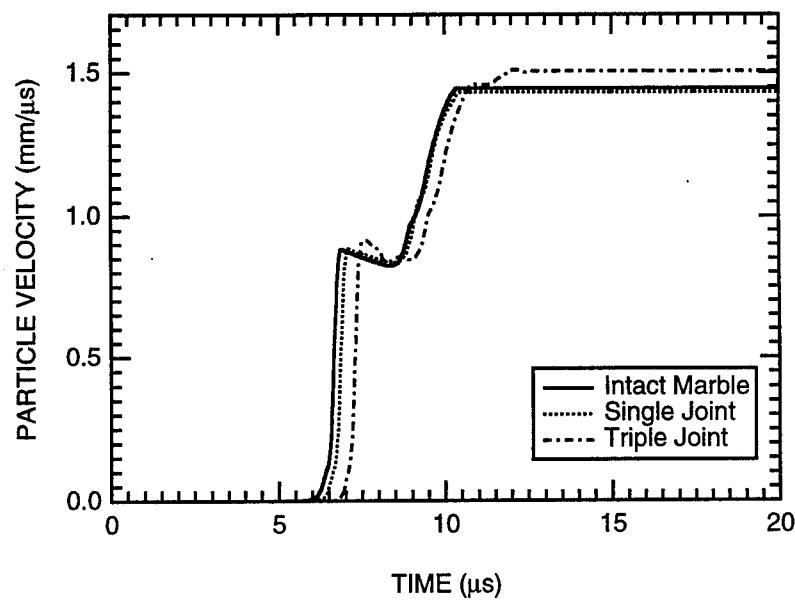


Figure 3-16. Simulated particle velocity histories at the third gage plane.

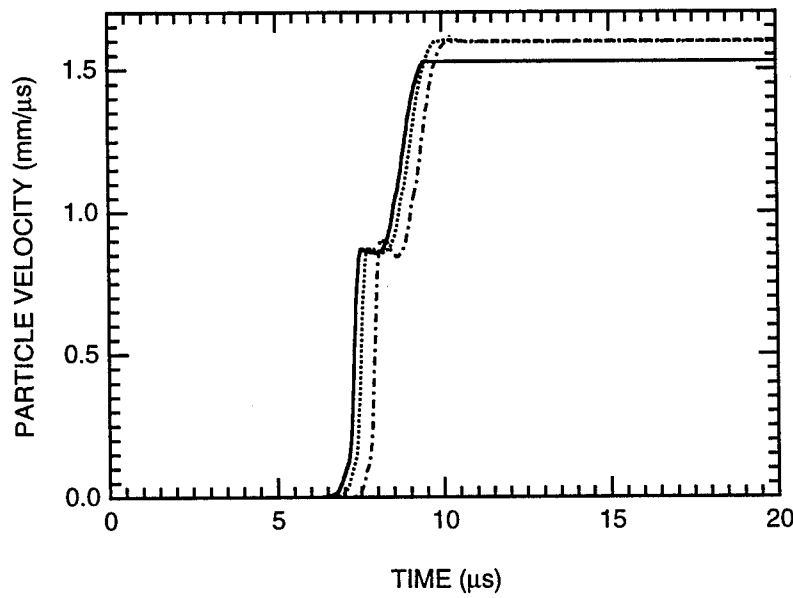


Figure 3-17. Simulated particle velocity histories at the fourth gage plane.

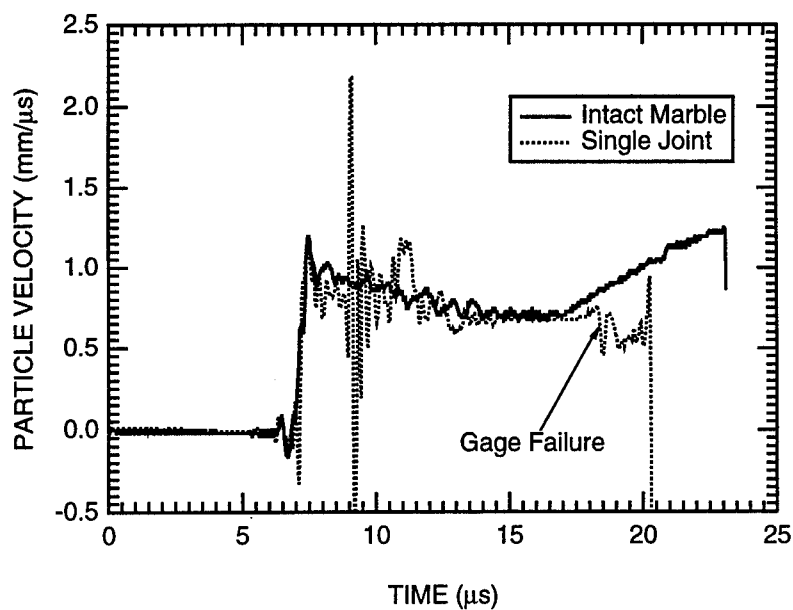
medium. It is not surprising, therefore, that the TOA delay associated with the triple joint is approximately three times the TOA delay associated with the single joint.

The same effects observed in the PUFF simulations can also be observed in the experimental data, as illustrated in Figures 3-18 and 3-19 for the single joint and triple joint configurations, respectively. In each figure, the results from an experiment on intact marble (HPEOS Experiments 6 and 7) are superimposed onto the results of an experiment on jointed marble (HPEOS Experiment 10 for the single joint and HPEOS Experiment 12 for the triple joint). Part (a) in each figure corresponds to the gage location in front of the jointed section of the specimen, whereas part (b) corresponds to the gage location behind the jointed section. The narrow, large amplitude spikes at  $t = 8 \mu\text{s}$  in Figure 3-18(a) and at  $t = 11 \mu\text{s}$  in Figure 3-19(a) are most likely due to an air gap at the interface between the joint and the rock. This explanation is plausible because the spike is not observed at any of the gage planes behind the joint and also because the spike reaches the gage before the expected reflection from the joint, an indication that the source of the spike is located at the interface between the gage plane and the joint.

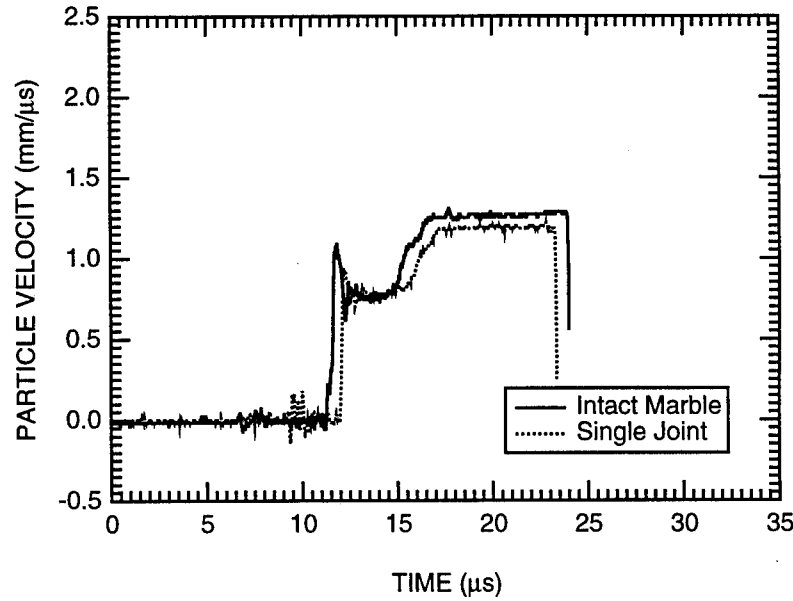
The two features that are associated with the effect of joints on wave propagation in the simulated particle velocity histories can also be observed in the experimental records. On the first gage plane, the particle velocity history is modified by the appearance of spikes—one spike for the single joint configuration and three spikes for the triple joint configuration. On the second gage plane, the effect of joints is observed primarily in the form of a delayed TOA of the wave at the gage plane. For the triple joint configuration, a slight perturbation to the particle velocity history at the second gage plane can also be observed. The larger than expected delay in the TOA of the wave at the second gage plane for the experiment with a single joint is due to the presence of an air gap at the rock-joint interface and, to a lesser extent, to slight geometrical differences between the intact and jointed samples.

The results presented so far pertain to the effect of sand-filled normal joints with rough surfaces. Similar effects were observed for sand-filled normal joints with smooth surfaces. A comparison of the results of HPEOS Experiment 13 (smooth triple joint) with the results of HPEOS Experiment 12 (rough triple joint) reveals no detectable differences in the response of smooth and rough triple joints. The same can be said of the response of smooth and rough single joints, except that the particle velocity gages on the first gage plane of HPEOS Experiment 11 (smooth single joint) failed before the arrival of the reflection from the joint at the gage plane.

Joint inclination appears to have had a significant effect on the observed behavior. Only inclined single joints were investigated. The joint was oriented at an angle of  $45^\circ$  with respect to the direction of wave propagation. Two experiments, one with a rough joint (Experiment 9) and one with a smooth joint (Experiment 14), were conducted, but a failure in the data acquisition system resulted in no data being recorded in HPEOS Experiment 9. The data on the first gage plane of HPEOS Experiment 14 were polluted by high amplitude spikes believed to be due to an air gap at the rock-joint interface. However,

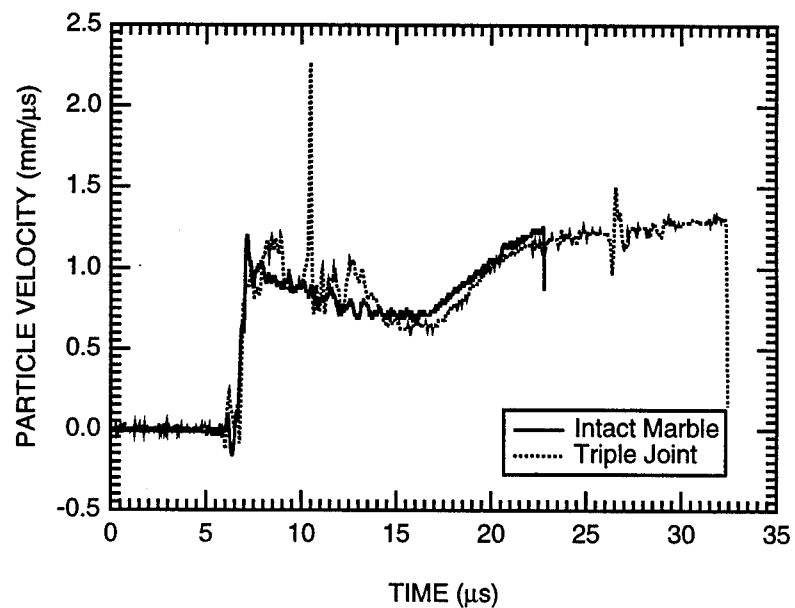


(a) Particle velocity histories at the first gage plane.

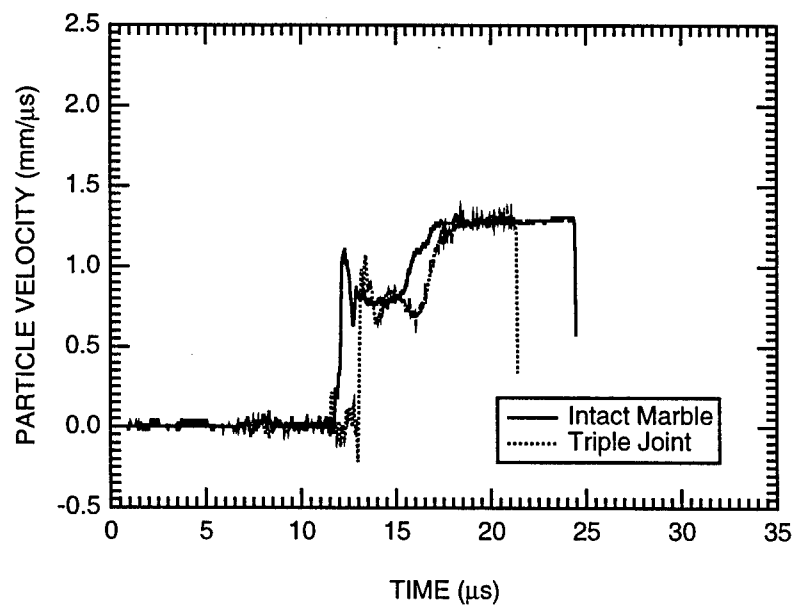


(b) Particle velocity histories at the second gage plane.

Figure 3-18. Effect of a single sand-filled joint on wave propagation.



(a) Particle velocity histories at the first gage plane.



(b) Particle velocity histories at the second gage plane.

Figure 3-19. Effect of a triple sand-filled joint on wave propagation.

the particle velocity histories on this gage plane indicate that the inclined single joint has the same signature as the normal joint, but with a prolonged duration. The signature of the inclined joint at the second gage plane resembles that of a triple normal joint more than that of a single normal joint. Both these observations point to the inclined joint as having more effect on wave propagation than a normal joint, all other parameters being equal. This is not surprising. From Figure 3-1, it can be seen that a plane wave propagating through the jointed section of a specimen with a single normal joint, interacts with the joint only as it propagates through the joint itself, and thus the effective thickness of the joint is the same as its actual thickness. On the other hand, a single inclined joint interacts with the plane wave throughout the time it takes for the wave to propagate through the whole jointed layer; thereby making the effective thickness of the joint equal to the thickness of the layer, not the thickness of the joint. In the present study the jointed layer was about 13 mm thick, compared with a joint thickness of 2 mm.

The final joint parameter varied in this study was joint thickness. HPEOS Experiment 8 was conducted with a single smooth inclined joint. The joint was closed, i.e., the two joint surfaces were in contact. The results of this experiment do not differ from the results of the experiments on intact marble, an indication that closed joints have no effect on compressive wave propagation.

## SECTION 4

### SPHERICAL WAVE EXPERIMENT

#### **4.1 MOTIVATIONS AND OBJECTIVES.**

Over the past several years, DNA has sponsored experimental programs that provided high stress, dynamic material property data for Danby marble. These programs include the large scale DISTANT MOUNTAIN test series that provided data for Danby marble up to stresses of about 100 kbar (Keough et al., 1993). The in-contact explosive experiments described in Section 3 of this report also provide data for Danby marble at stresses in excess of 100 kbar, but at a smaller scale than that of the DISTANT MOUNTAIN experiments. Still more experiments on Danby marble were performed by Furnish (1994) and Gaffney and Smith (1994), and numerous other investigations were found in the literature. This data bank provides a wealth of information about the behavior of marble under dynamic loading, including precursor and precursor decay, attenuation, unloading, and phase transitions. However, all these data were obtained under one-dimensional strain loading conditions. The spherical wave experiment described in this section supplements the existing data by providing results for marble in a comparable stress range (~100 kbar) but under spherical loading conditions. Furthermore, the experimental results can be used to validate and/or calibrate constitutive models for use in finite element and finite difference hydrocodes.

#### **4.2 EXPERIMENTAL TECHNIQUES.**

In the spherical wave experiment, a small explosive charge is detonated at the center of a 27-cm-diameter, 27-cm-long cylindrical block of marble. The motion of embedded wire gages through an externally applied magnetic field measures the velocity histories at several radii from the charge (Florence et al., 1993; Gefken and Florence, 1993). The specimen was prepared from a core obtained from the same stock used in the DISTANT MOUNTAIN test series as well as for the uniaxial strain experiments of the present study.

The overall configuration of the experiment is shown in Figure 4-1. The specimen assembly was placed inside a pressure vessel and surrounded by a solenoid that applied a constant, vertically oriented magnetic field through the particle velocity gage planes. A 6.9-MPa static overburden pressure was applied to the specimen during the experiment. Beforehand, the specimen was treated with a waterproofing agent to ensure that it remains dry during the experiment.

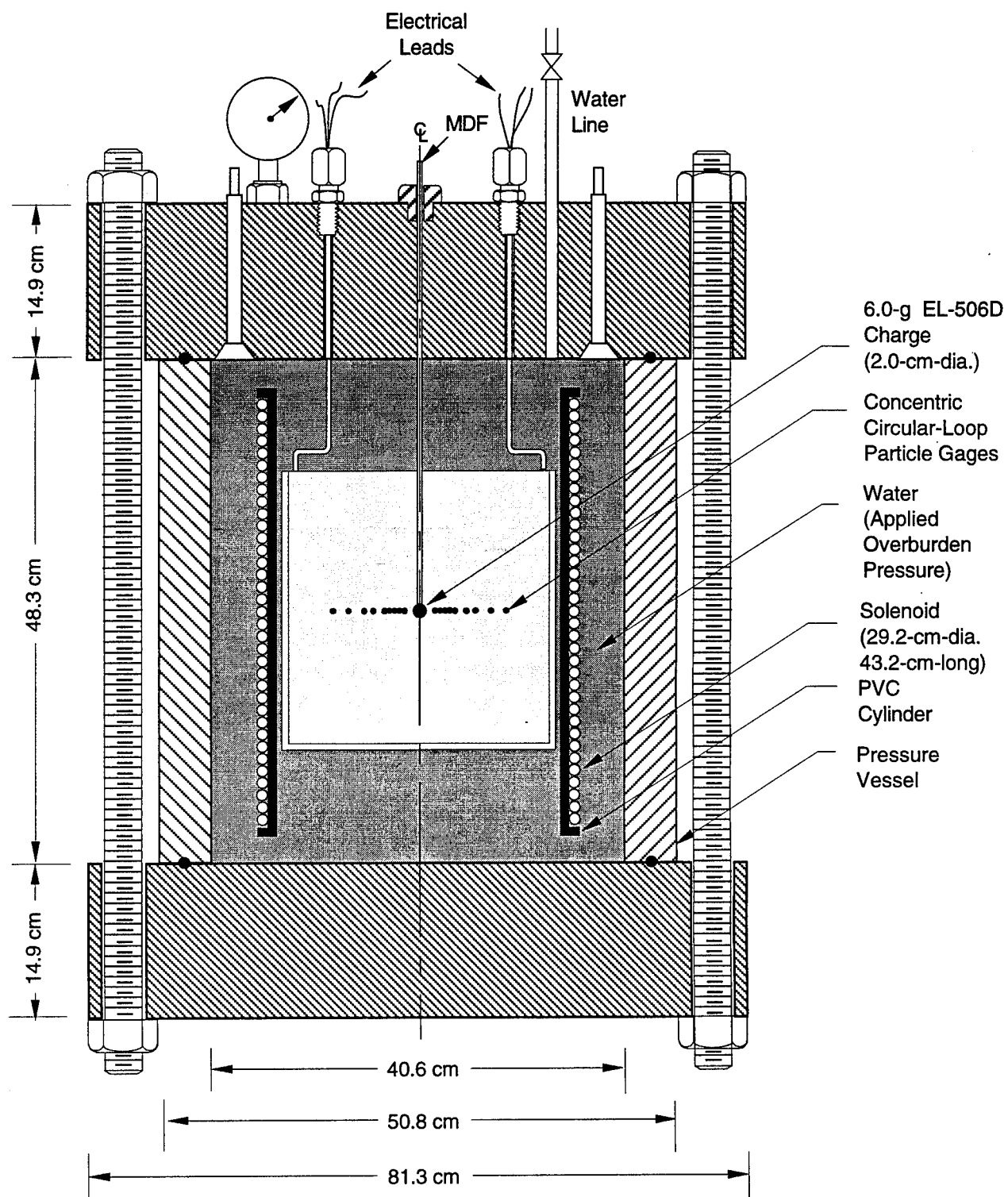


Figure 4-1. Overall configuration of the spherical wave experiment in Danby marble.

A 6.0-g EL506D (Detasheet) charge, detonated using a mild detonating fuse (MDF), was used to provide the loading in the spherical wave experiment. Details of the charge cavity are shown in Figure 4-2. As shown, the EL506D charge was contained within a Lexan casing, and the MDF fuze within a stainless steel tube. The charge was detonated at its center to produce as symmetric a spherical wave as possible in the rock sample.

The particle velocity gages operated on the same principle as their counterpart in the uniaxial strain experiments. The motion of a gage element of length  $\ell$ , moving through a magnetic field of strength  $B$ , generates an electromagnetic force  $\epsilon$ , which can be related to the velocity by Faraday's law,

$$u = \frac{\epsilon}{B\ell} \quad (4-1)$$

In this experiment, eight gages were used to record the radial particle velocity of the rock sample at several radii from the charge. The particle velocity gages consisted of strips of copper wire mounted into precision-machined grooves in the specimen. As shown in Figure 4-3, two diametrically opposite gages were used at each of eight radii starting at the charge boundary and extending outward to a radius of 5.0 cm. In most applications, the active element of each gage would cover the full circumference of one of the concentric circles shown in the figure. However, in the present study a different approach was taken to ensure that the direction along which the particle velocity histories were measured coincided with the direction of wave propagation in the uniaxial strain experiments. This arrangement allows for a direct comparison between the results of the uniaxial strain experiments and the results of the spherical wave experiment even if the rock behaves in an anisotropic fashion.

#### 4.3 EXPERIMENTAL RESULTS AND DISCUSSION.

The particle velocity histories measured in the spherical wave experiment on Danby marble are shown in Figures 4-4 through 4-11. Each of these figures shows the two particle velocity histories measured at a given range. As was shown in Figure 4-3, two colinear gage arrays, one on either side of the high-explosive charge, were used to measure the particle velocity histories. These gage arrays are designated by the letters 'a' and 'b' in Figures 4-4 through 4-11. The particle velocity histories at the two ranges closest to the charge show characteristics that are different from the remainder of the data. This difference may be related to premature gage failure due to the high stresses generated by the explosive charge, or it may be related to a transition from a compaction-dominated behavior near the charge cavity to a crack propagation-dominated behavior further away from the charge. The diameter of the charge cavity increased by more than 25% (from an initial value of 2.0 cm before the experiment to a final value of 2.55 cm after the experiment), indicating significant compaction near the charge cavity.

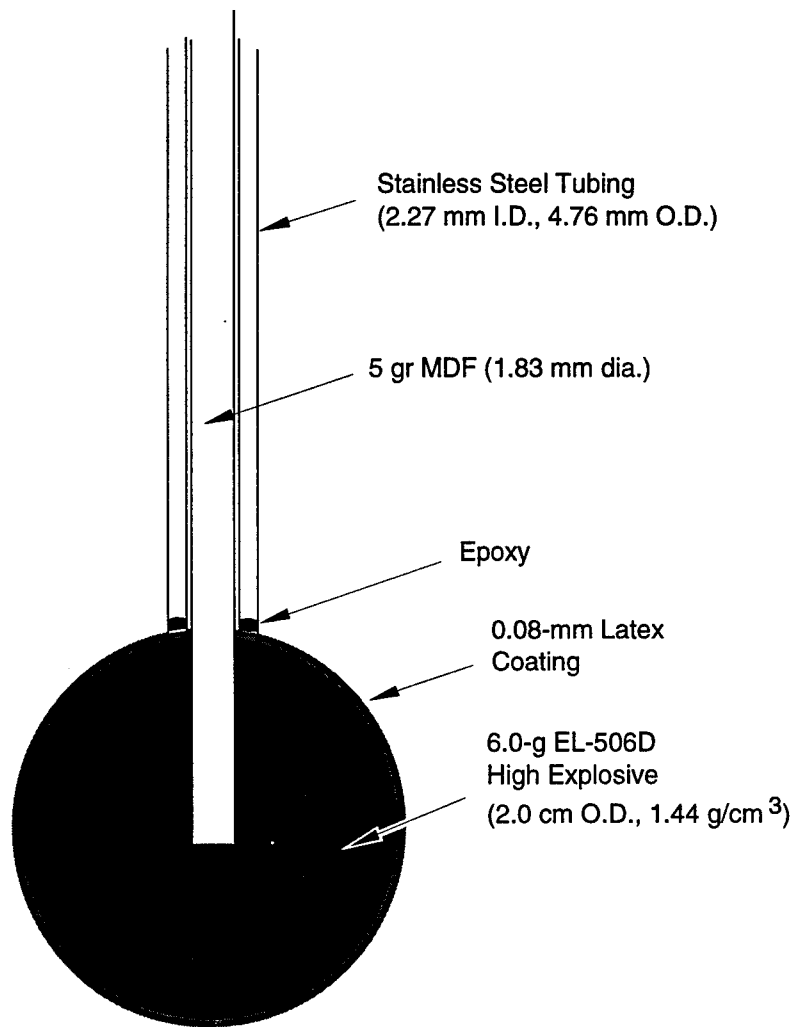


Figure 4-2. Details of the charge cavity and the detonating fuze used in the spherical wave experiment.

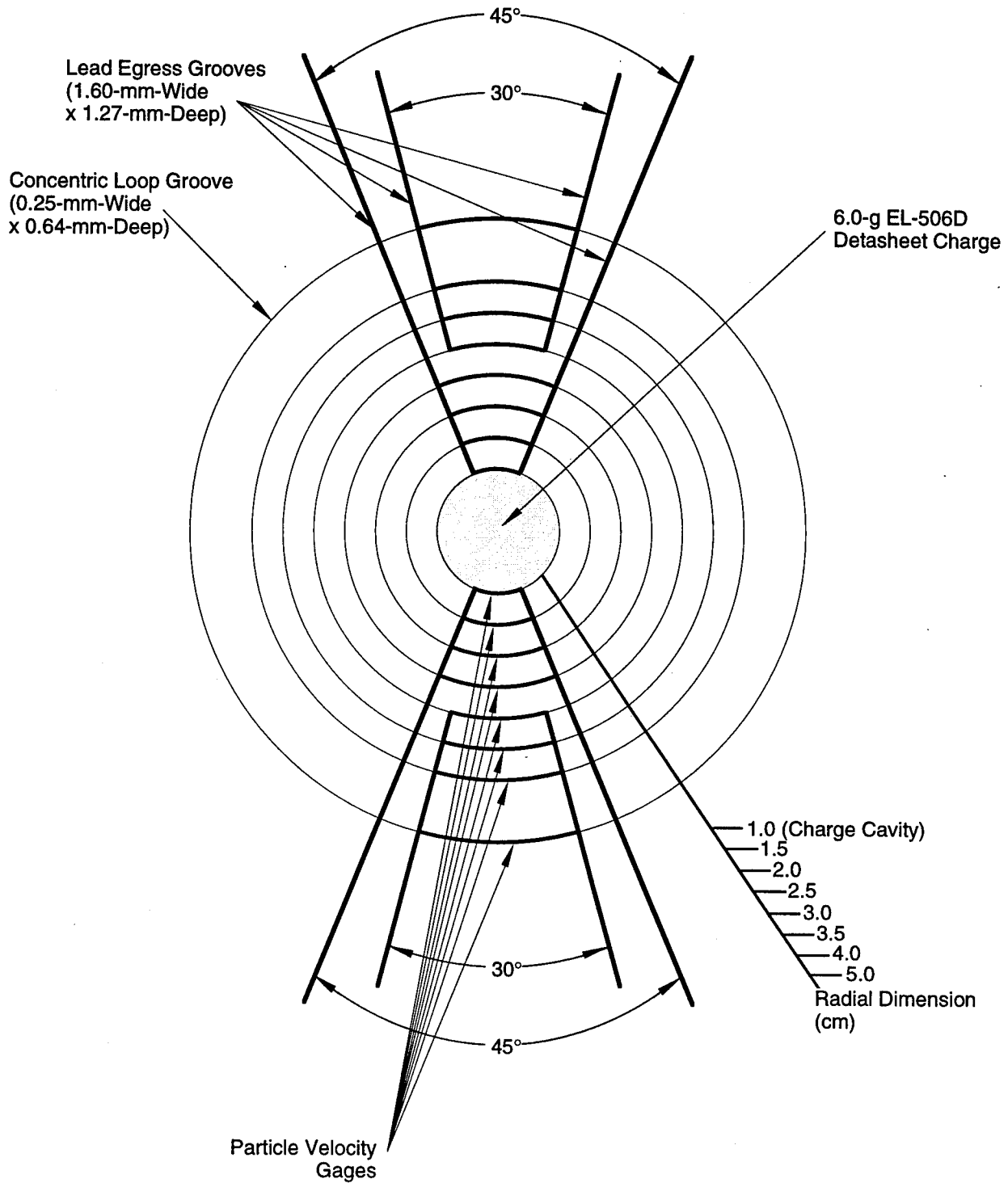
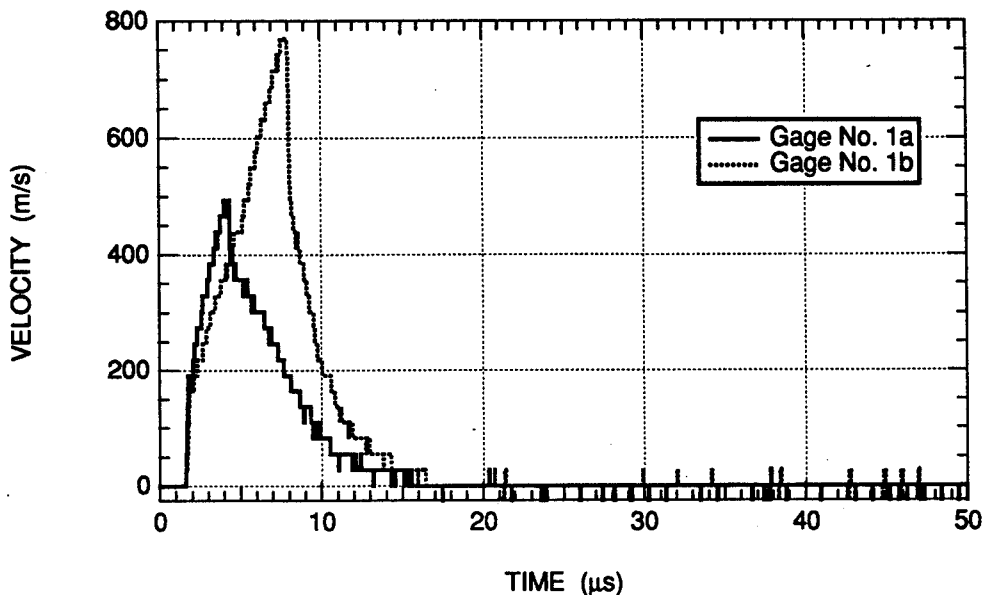
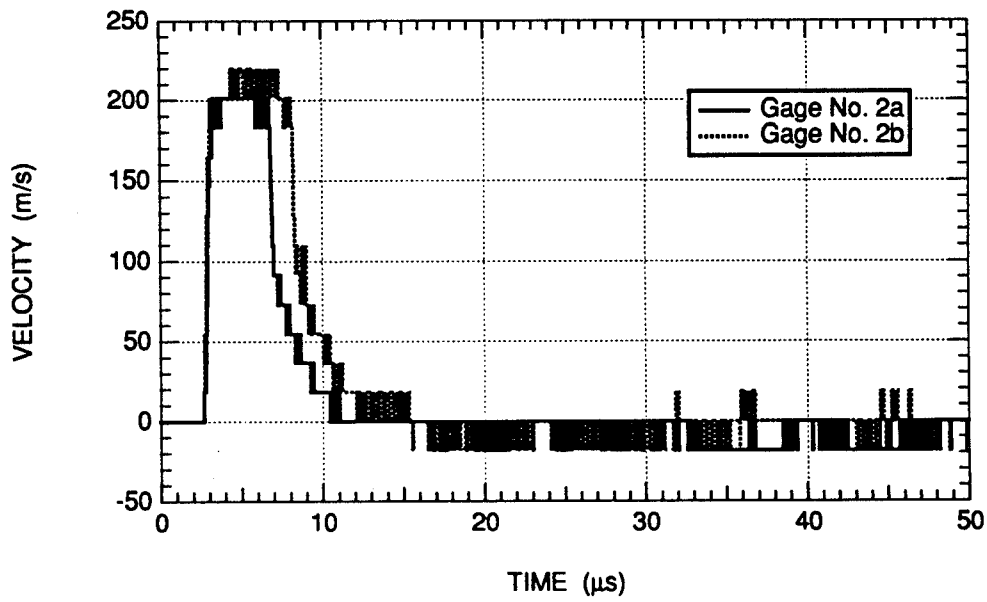


Figure 4-3. Layout of the particle velocity gages in the spherical wave experiments.



**Figure 4-4.** Particle velocity histories at the 1.0-cm range in the spherical wave experiment on Danby marble.



**Figure 4-5.** Particle velocity histories at the 1.5-cm range in the spherical wave experiment on Danby marble.

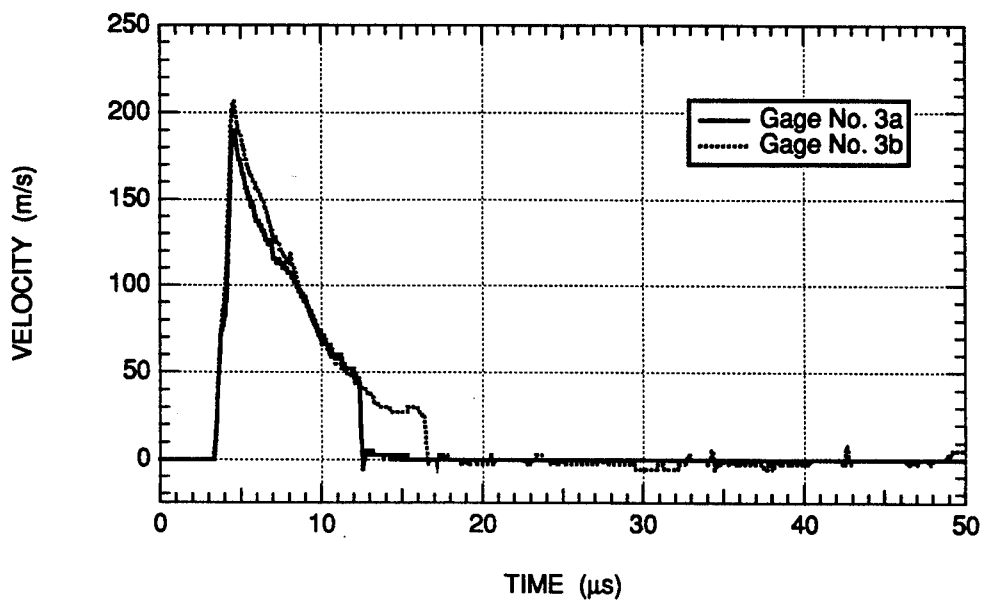


**Figure 4-6.** Particle velocity histories at the 2.0-cm range in the spherical wave experiment on Danby marble.

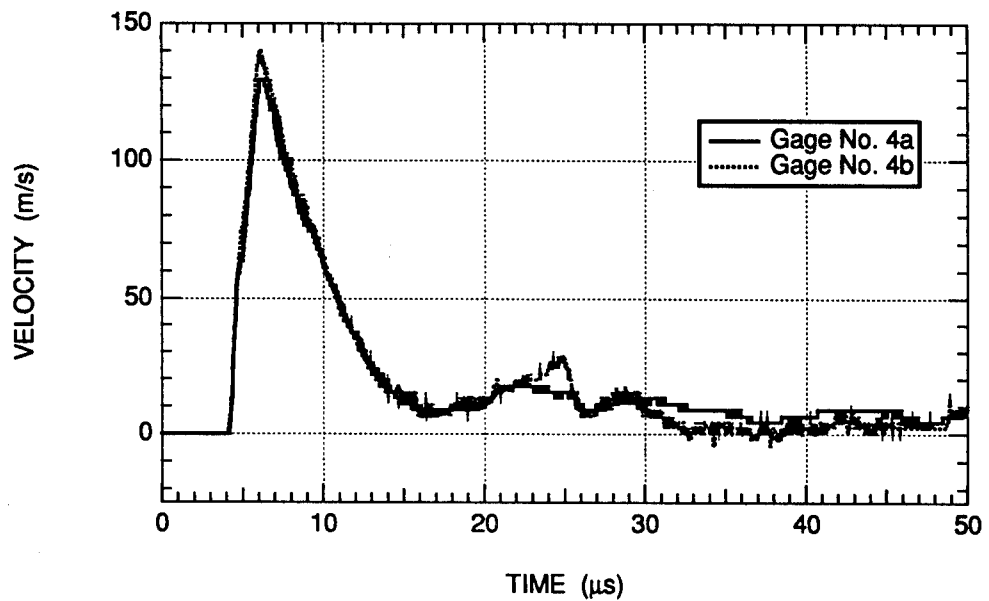


**Figure 4-7.** Particle velocity histories at the 2.5-cm range in the spherical wave experiment on Danby marble.

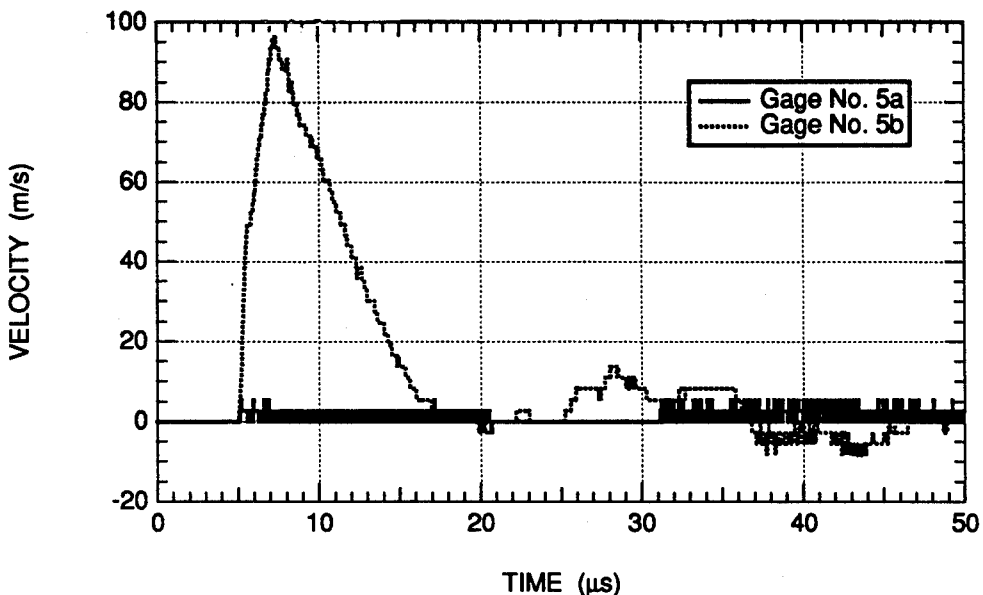


Figure 4-8. Particle velocity histories at the 3.0-cm range in the spherical wave experiment on Danby marble.

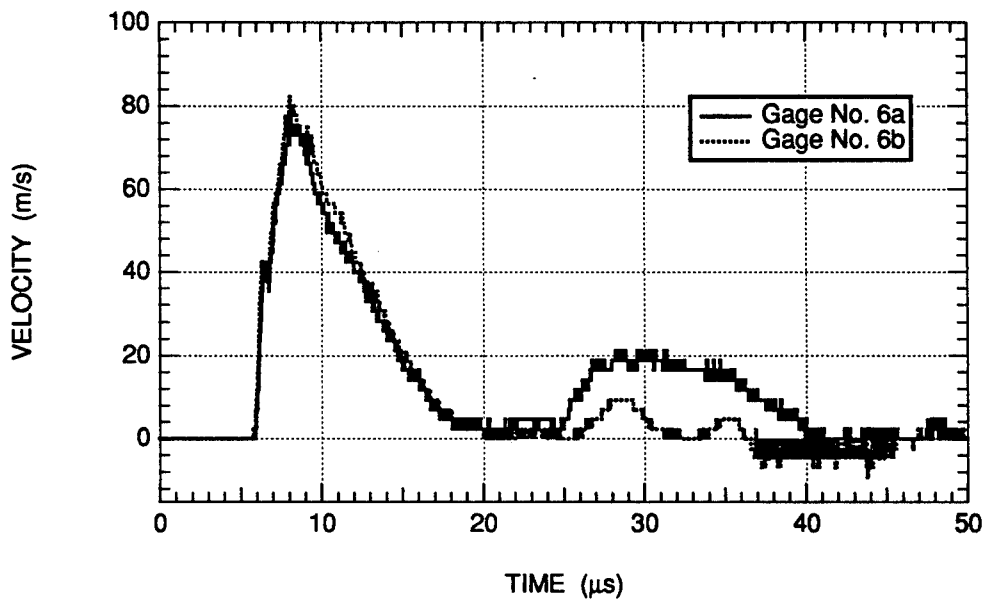


Figure 4-9. Particle velocity histories at the 3.5-cm range in the spherical wave experiment on Danby marble.

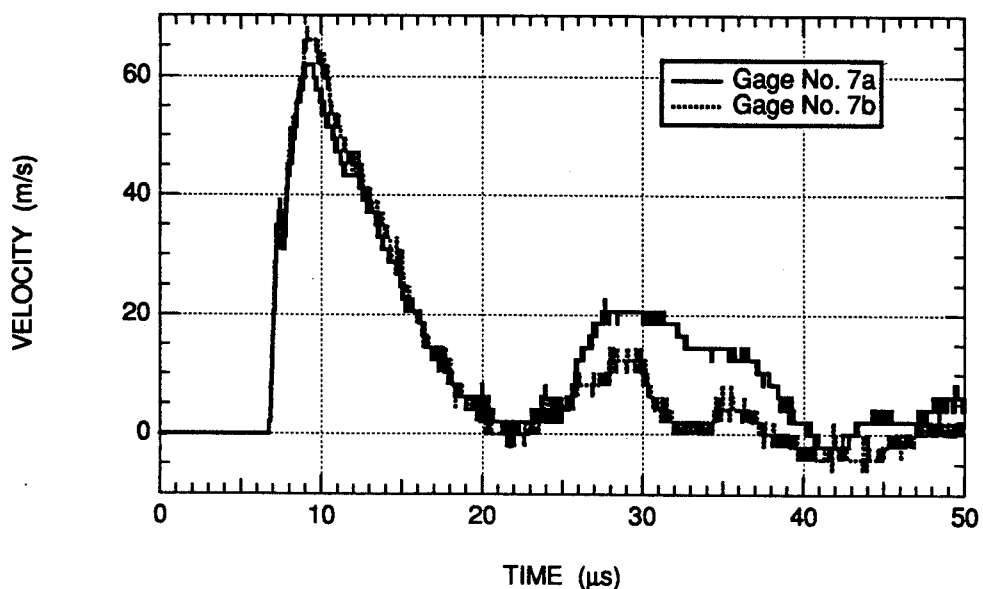


Figure 4-10. Particle velocity histories at the 4.0-cm range in the spherical wave experiment on Danby marble.

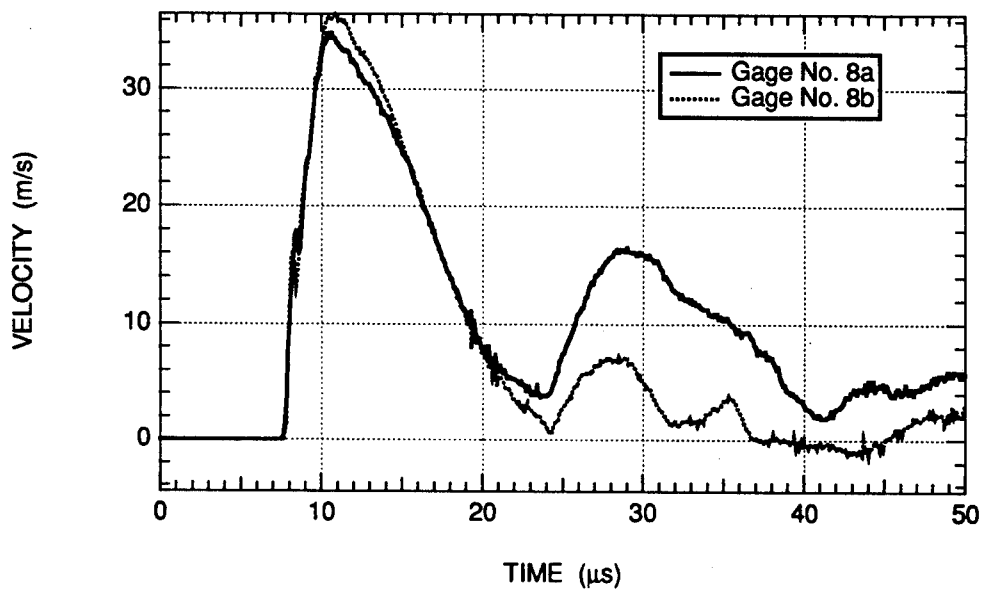


Figure 4-11. Particle velocity histories at the 5.0-cm range in the spherical wave experiment on Danby marble.

The particle velocity gages at the 2.0-cm range captured the early time response of the rock but failed to record the subsequent rebound signal. The late time failure of the gages at this range is a strong indication that the gages at the 1.0-cm and the 1.5-cm ranges are likely to have failed during the experiment, and that the signals recorded by these gages are not a reliable indication of the actual response of the rock.

At ranges of 2.5 cm or more, the particle velocity histories in the specimen were recorded for the duration of the experiment. At early times, these histories are characterized by a sharp rise to peak followed by an outward motion that lasted for about 10  $\mu$ s. This portion of the velocity records is associated with the outward-traveling wave that originates in the explosives. This early-time response of the rock is very reproducible, as indicated by the nearly identical responses of the gage arrays on either side of the explosive charge (see Figures 4-6 through 4-11).

The outward expansion phase was followed by a rebound phase. In previous experiments on nonporous rock (Miller and Florence, 1990) and on porous CaCO<sub>3</sub> rock (Gefken and Florence, 1992), the rebound signal caused an inward contraction in the motion of the rock sample that was manifested by a reversal of the sign of the particle velocity histories. In the present experiment, the particle velocities recorded at all ranges remained positive throughout the rebound phase of the signal. No specimen contraction was observed.

This important difference between the rebound signals measured in the present experiment and those measured in other investigations can be related to cracking of the rock sample. In the Miller and Florence (1990) study, the explosive consisted of a 3/8-g PETN charge, as opposed to the more powerful 6-g Datasheet charge of the present investigation. In the Gefken and Florence (1992) study, the same 6-g Datasheet charge was used, but the limestone tested was approximately 15% porous. Extensive cracking was not observed in either of the two earlier studies. In contrast, the Danby marble specimen of the present study was severely cracked, as shown in Figure 4-12. Two distinct networks of cracks can be seen in each half of the specimen. The first network consists of numerous cracks emanating from the charge boundary and extending radially outward toward the free surface of the specimen. These radial cracks extend throughout the gaged region of the specimen, with a few cracks propagating all the way to the free surface. The second network of cracks consists primarily of circumferential cracks and does not appear to be symmetric with respect to the center of the explosive charge. An additional crack that does not appear to be associated with either of the crack networks mentioned so far can be observed spanning the whole specimen surface. This crack follows the path of a preexisting *in situ* joint in the rock.

We believe that the extensive cracking in the Danby marble specimen caused degradation of the material properties and reduced the stiffness of the rock. For this reason, the specimen unloaded along a

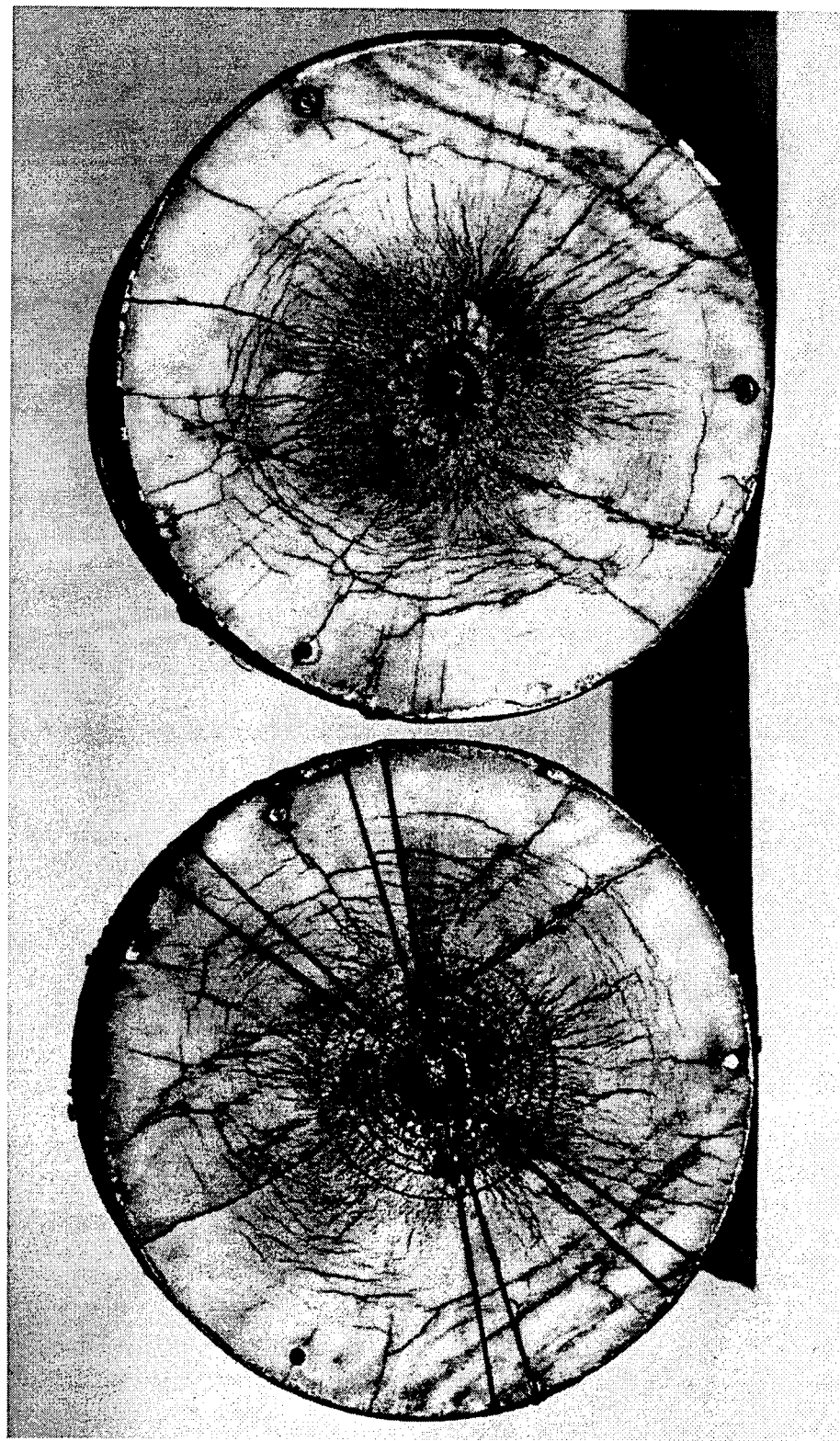


Figure 4-12. Experimentally observed crack patterns in the spherical wave experiment on Danby marble (the markings on the left half of the specimen are the grooves for the particle velocity gages and their leads).

"damaged" modulus that was substantially lower than the intact modulus. Consequently, much of the early time deformation was not recovered during the contraction, or rebound, phase.

The results of the spherical wave experiment also show evidence of load-induced anisotropy, a response mode usually associated with cracking in brittle materials. This anisotropy is manifested as a difference in the recorded particle velocity histories along the two different gage arrays of the spherical wave experiment. This occurred during the rebound phase of the response and can be seen in the results shown in Figures 4-8 through 4-11. A careful comparison of the results presented in these figures shows a systematic difference between the late-time particle velocity histories recorded by gages in the 'a' array and those recorded by gages in the 'b' array: a single rebound signal with a duration of about 15-17  $\mu$ s is observed on the 'a' side of the specimen. In contrast, a two-spike rebound signal is observed on the 'b' side of the specimen; the first spike has a larger amplitude and a longer duration than the second spike, but when the two spikes on the 'b' side of the specimen are combined, they have the same duration as the single spike on the 'a' side. We believe that these systematic differences are closely related to the effects of cracks on wave propagation. Specifically, the lack of symmetry in the cracking patterns caused the stress wave to become nonsymmetric, and therefore gages located in different regions of the specimen recorded different motions.

The time of arrival of the initial disturbance at the successive particle velocity gages, combined with the known location of the gages, was used to determine the initial wave propagation velocity in the Danby marble specimen. A least squares linear fit of the results indicated that the wave velocity was 6.46 mm/ $\mu$ s. This fit is compared with the experimental TOA data in Figure 4-13.

Radial particle displacement histories were obtained by temporal integration of the velocity histories. The results are shown in Figures 4-14 through 4-21. Figure 4-14 indicates that the average maximum displacement at a 1.0-cm range (i.e., the charge boundary) was 2.92 mm. On the other hand, the post-test measured displacement at the cavity wall was 2.75 mm. It may be argued that the reasonably close agreement between the two independent measurements lends credibility to the particle velocity history measurement at the charge boundary. The good agreement does not, however, explain the large differences in the peak particle velocities recorded at gage locations 1a and 1b.

The displacement histories can be used to determine the spatial deformation gradient in the specimen, which, with appropriate assumptions, can be used to compute the strain paths during the test. However, because of extensive cracking, the relationship between the radial motion (measured) and the circumferential motion of the specimen is not obvious. An alternative approach would be to combine the experimental data with a physically based constitutive model to analyze the response of the rock and characterize the strain field in the specimen. Initial steps toward this type of analysis were taken during our investigation. The results of this effort are described in the next section.

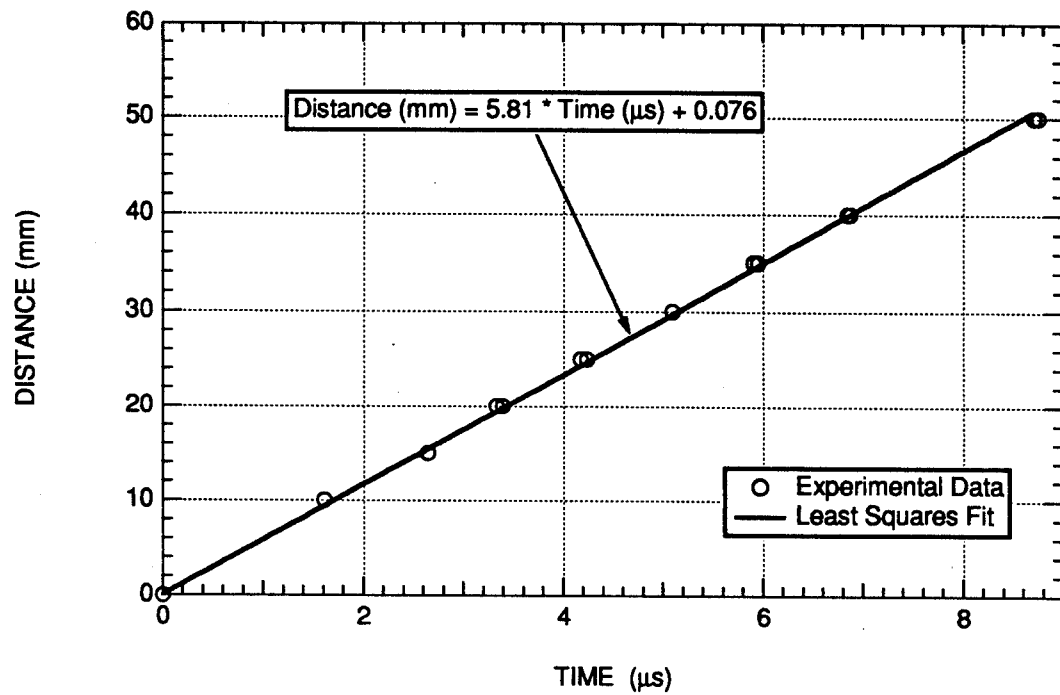


Figure 4-13 Distance-time of arrival data for determining the wave velocity in the spherical wave experiment.

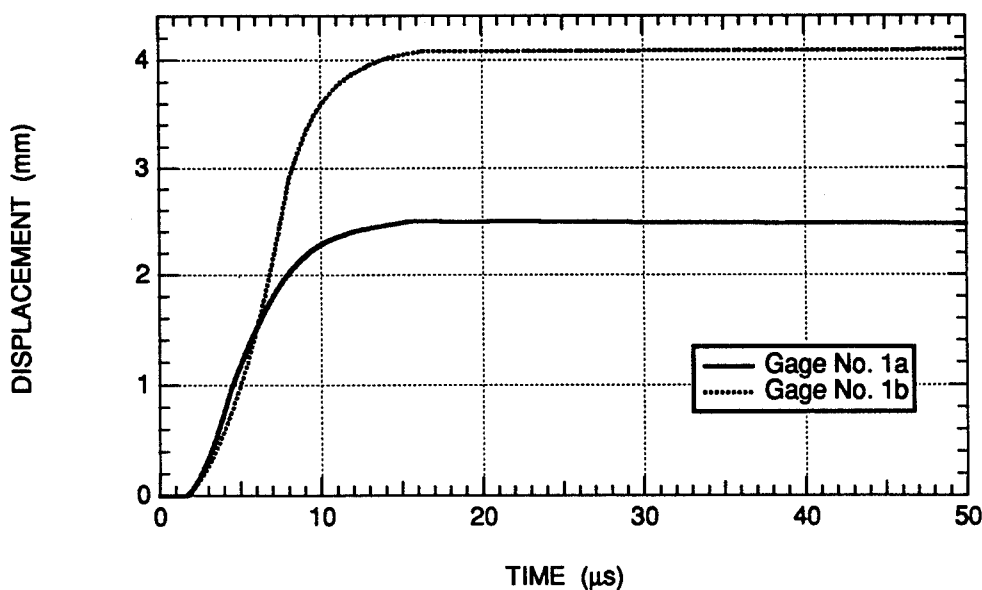


Figure 4-14. Displacement histories at the 1.0-cm range in the spherical wave experiment in Danby marble.

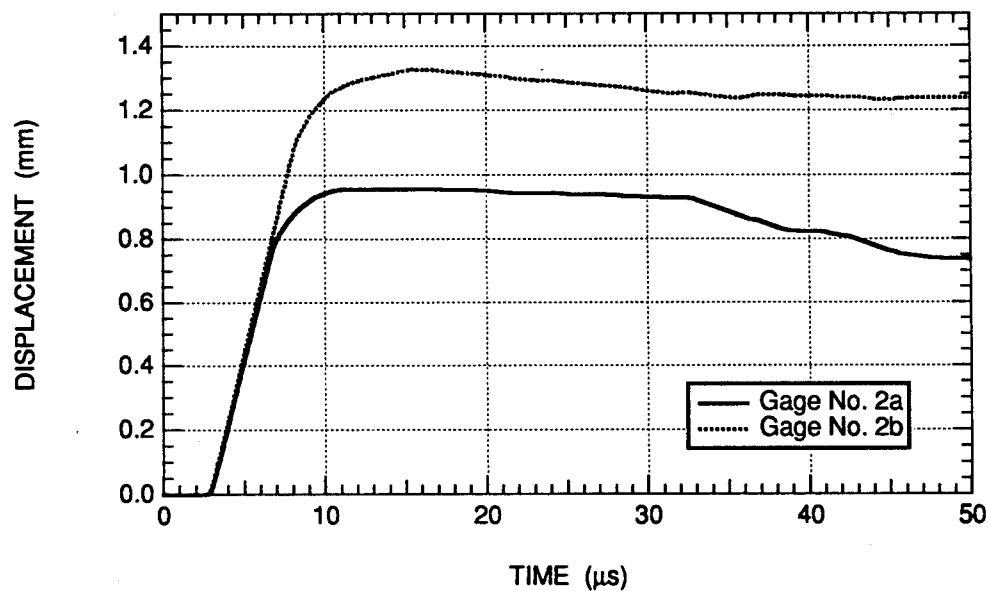


Figure 4-15. Displacement histories at the 1.5-cm range in the spherical wave experiment in Danby marble.

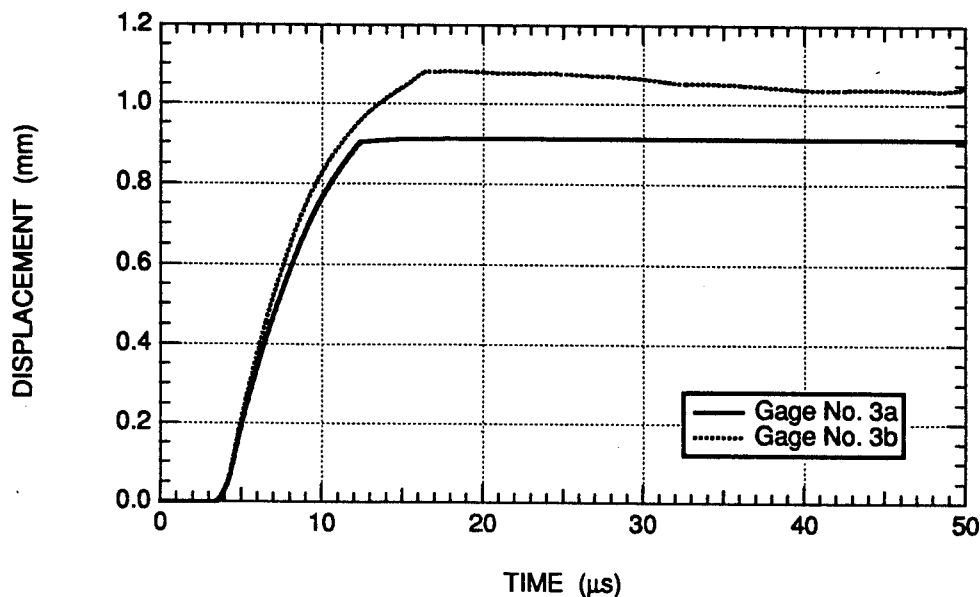


Figure 4-16. Displacement histories at the 2.0-cm range in the spherical wave experiment in Danby marble.

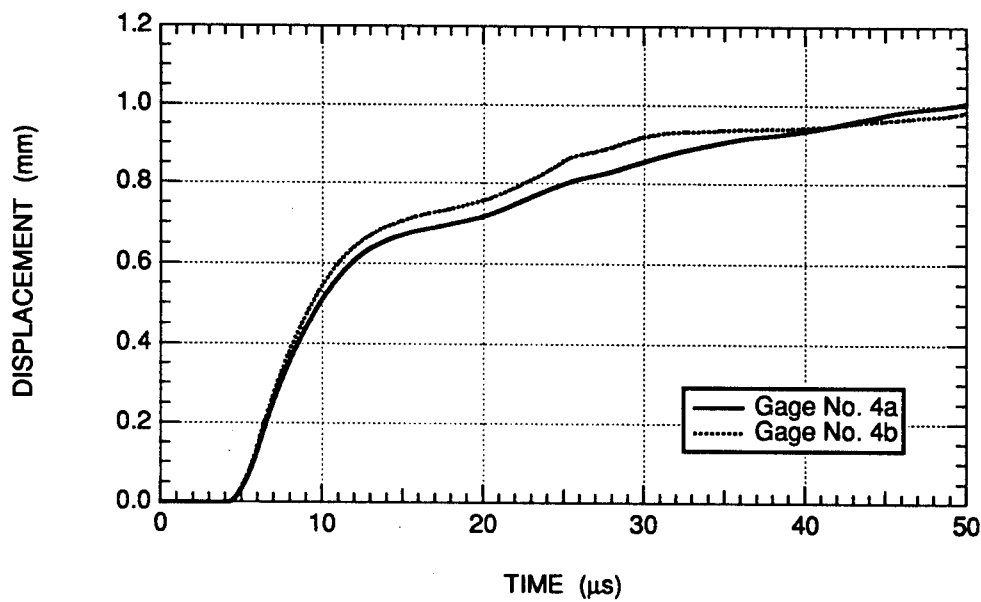


Figure 4-17. Displacement histories at the 2.5-cm range in the spherical wave experiment in Danby marble.

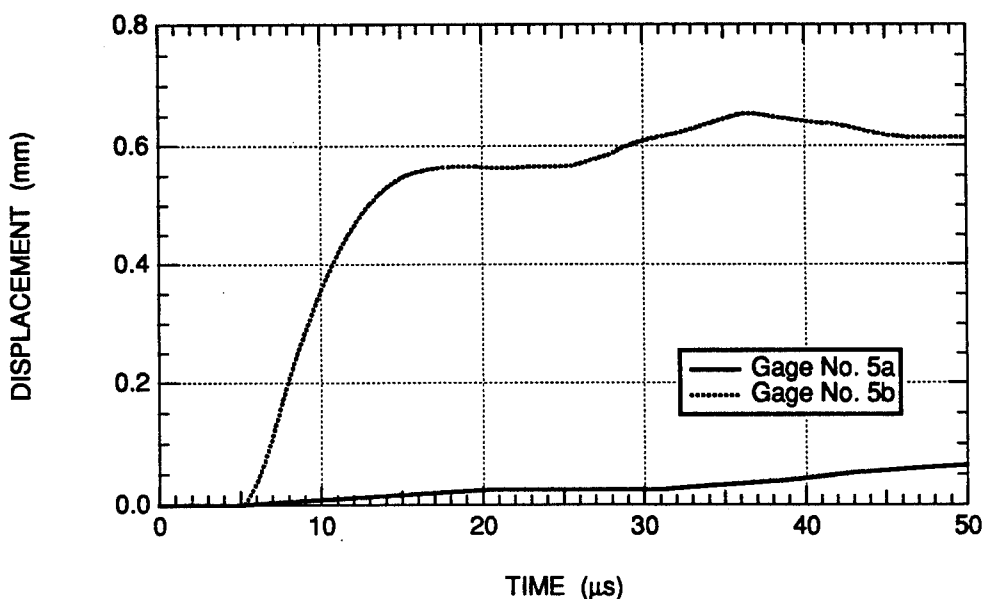


Figure 4-18. Displacement histories at the 3.0-cm range in the spherical wave experiment in Danby marble.

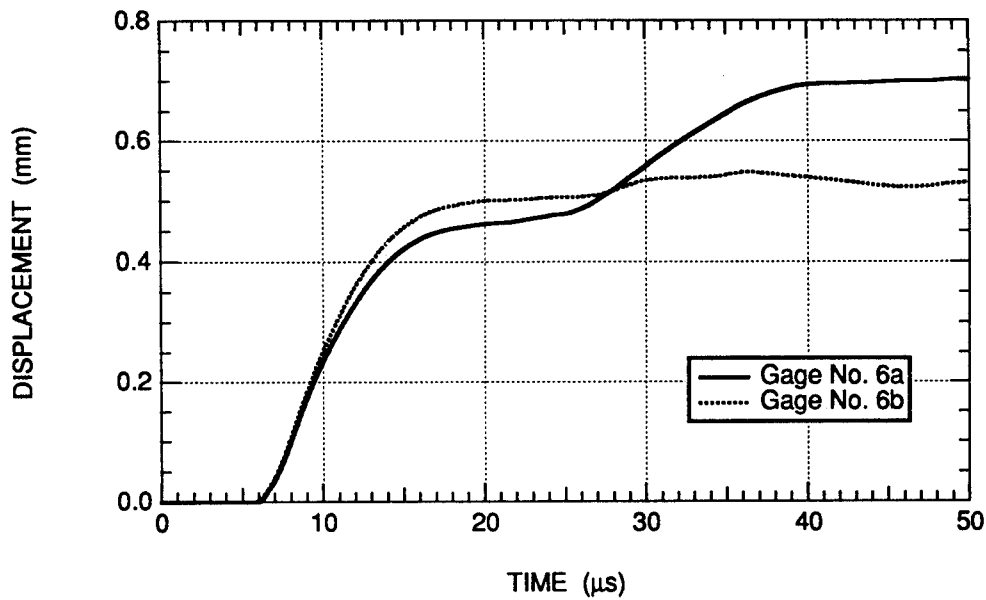
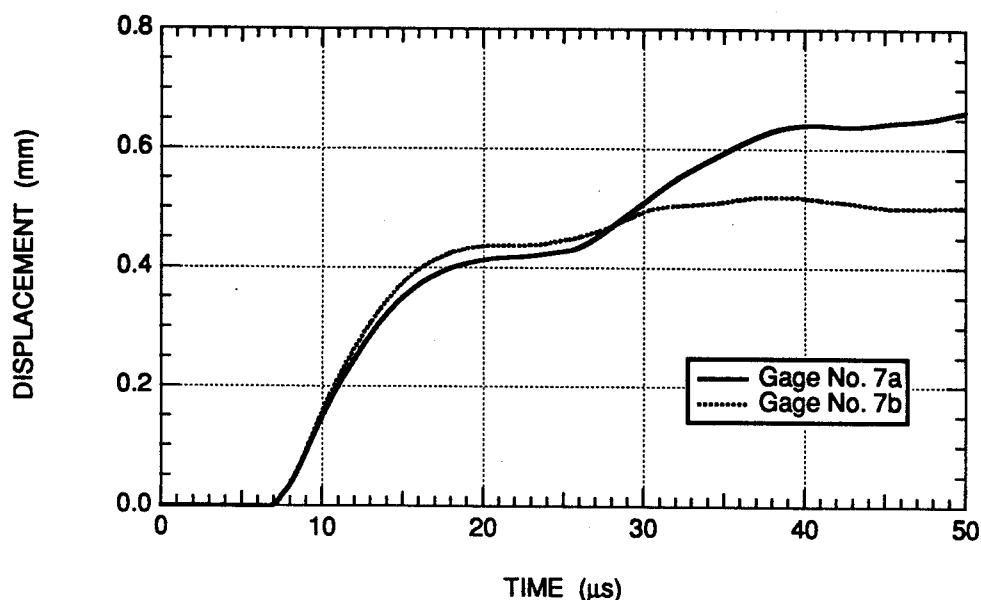
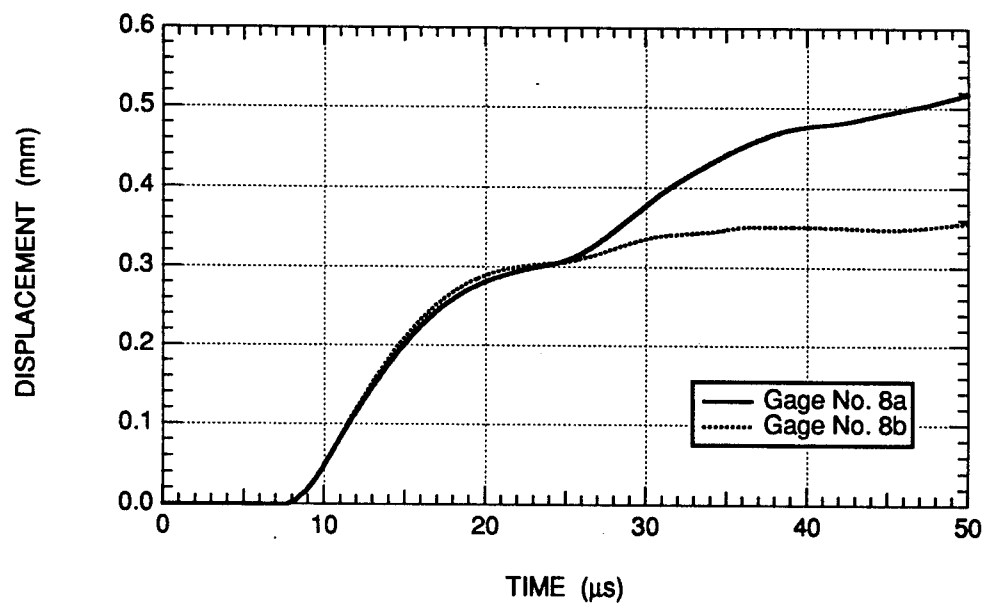


Figure 4-19. Displacement histories at the 3.5-cm range in the spherical wave experiment in Danby marble.



**Figure 4-20.** Displacement histories at the 4.0-cm range in the spherical wave experiment in Danby marble.



**Figure 4-21.** Displacement histories at the 5.0-cm range in the spherical wave experiment in Danby marble.

## **4.4 CODE SIMULATIONS.**

Code simulations were performed to aid in the interpretation of the results of the spherical wave experiment. The simulations were performed in DYNA2D (Whirley and Engelmann, 1992) using a newly developed, computationally oriented constitutive model based on the evolution of damage by crack propagation (Simons et al., 1995). This section briefly describes the main features of the constitutive model and presents the simulation results.

### **4.4.1 Description of the Model.**

The model used in this study is based on the activation and subsequent propagation of pre-existing penny-shaped flaws. In the model, we assume that the heterogeneity of geologic materials leads to local stresses which, in general, are different from the externally applied stresses. The local stresses are given by a statistical distribution centered about the externally applied stress. These local stresses, combined with a fracture-mechanics-based stress intensity factor formulation, are used to monitor the activation of cracks. Once a crack is activated, its propagation is governed by a stress- and crack-size-dependent viscous growth law, and a limiting crack velocity equal to a fraction of the shear wave velocity.

Crack propagation leads to damage and stiffness degradation of the rock. These effects are accounted for in the model by tracking the cracking strain tensor and a scalar damage parameter. The cracking strain is a function of the crack size and the elastic properties of the rock; its separation from the stress-producing elastic strain allows the model to take into account such important phenomena as stiffness degradation, softening, and volume dilatancy (i.e., bulking). The damage parameter, which represents the overall damage on all the crack planes, is a function of the volume of cracked material.

It is used in the model as a relative measure of material degradation and as a failure criterion. After failure, the ability of the material to support tensile loads in the direction normal to the crack plane is diminished.

The model is a multiplane model that allows cracks to propagate on several planes with different spatial orientations. This feature of the model makes it possible to account for crack-induced anisotropy, a well-documented aspect of brittle material behavior. Even when the initial crack distribution is random and the elastic response of the material is isotropic, cracks that begin to propagate do so only on preferential planes along which the projection of the applied stress tensor satisfies the fracture-mechanics-based crack activation criterion. This inherent dependence of crack propagation on the orientation of applied load, combined with the multiplane approach, induces a directional property into the model that, in general, renders an initially isotropic response anisotropic. An advantage of the

multiplane approach is that it affords a realistic representation of jointed rock media where the initial flaws are preferentially oriented in one or more directions.

#### 4.4.2 Simulation Results.

After choosing reasonable values for the material parameters in the model on the basis of published data for marble and similar geologic materials, we attempted to simulate the spherical wave experiment. However, with the cracking model alone, we were unable to obtain good qualitative agreement between the measured and calculated particle velocity histories near the charge cavity. The calculated particle velocity histories had a higher peak and a shorter duration than the measured histories, an indication that the simulated response of the specimen was more elastic than the real response. To obtain good agreement between the simulated and measured results, we found it necessary to use a porous compaction model to represent the material behavior in the vicinity of the charge cavity (within a diameter of 3.5 cm).

The simulated crack patterns in the spherical wave experiment are shown in Figure 4-22 along with the experimentally observed crack patterns. The model reproduced the radial and circumferential crack networks observed in the experiment. The crack visible along the path of the *in situ* joint in the rock was not reproduced in the simulation because the joint itself was not modeled (i.e., initially isotropic behavior was assumed in the calculations).

The model was not quantitatively calibrated to reproduce all the details of the experimental data. The objective of the simulations was to try to provide a better understanding of the mechanisms that contributed to the observed response. To this end, our results indicate that close to the charge cavity the behavior of the rock is dominated by porous compaction, whereas away from the charge the behavior is dominated by crack propagation.

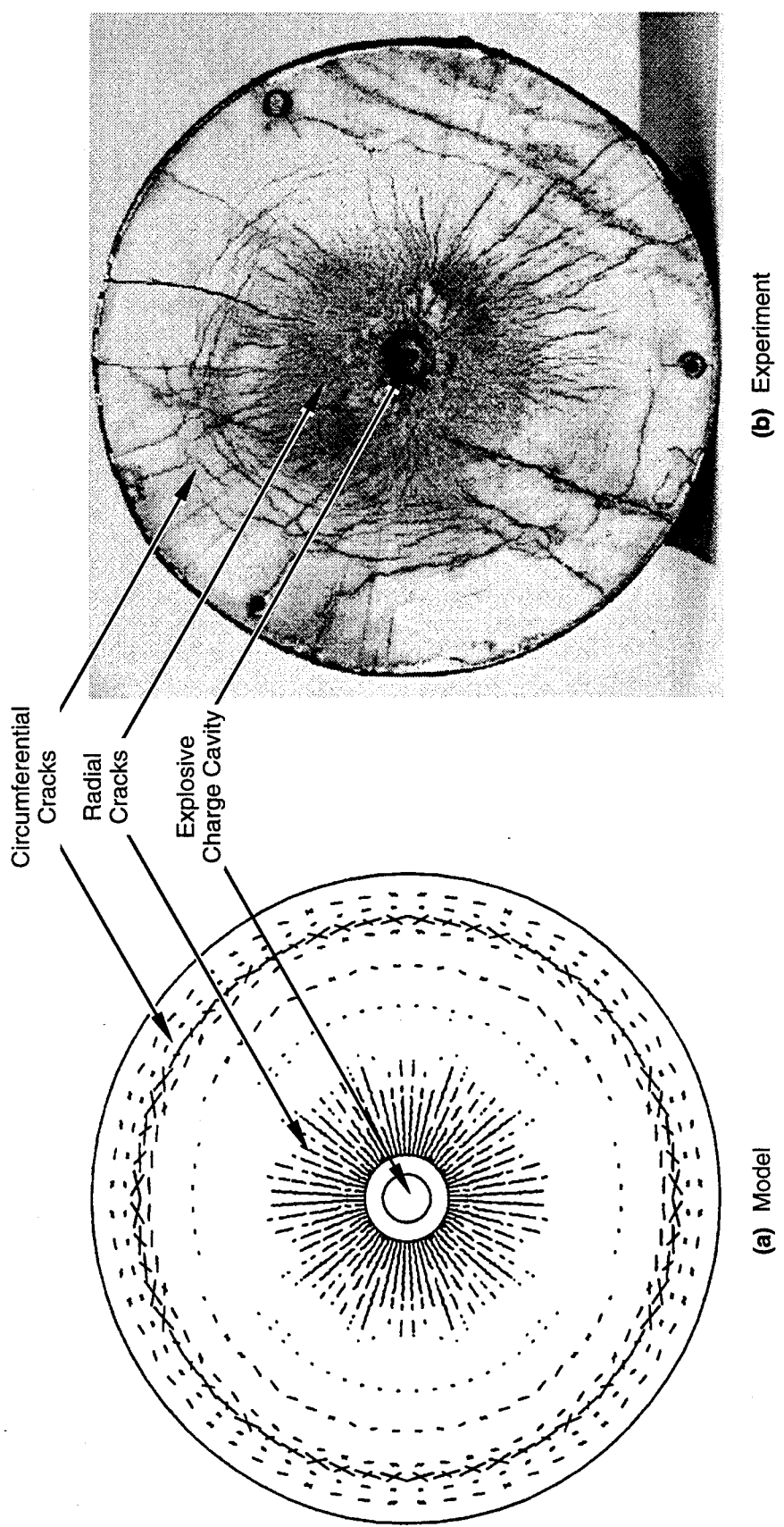


Figure 4-22. Comparison between simulated and experimentally observed crack patterns in the spherical wave experiment on Danby marble.

## SECTION 6

### REFERENCES

Adadurov, G. A., D. B. Balashov, and A. N. Dremin, "A Study of the Volumetric Compressibility of Marble at High Pressure (U)," *Izv. Geophys. Sev.*, 712-716 (1960). (UNCLASSIFIED)

Adams, L. H. and E. D. Williamson, "Compressibility of Minerals and Rocks at High Pressure (U)," *J. Franklin Institute* **195**, 475-529 (1923). (UNCLASSIFIED)

Ahrens, T. J., and V. G. Gregson, "Shock Compression of Crustal Rocks: Data for Quartz, Calcite, and Plagioclase Rocks (U)," *J. Geophys. Res.* **69**(22), 4839-4874 (1964). (UNCLASSIFIED)

Bridgman, P. W., "The High Pressure Behavior of Miscellaneous Minerals (U)," *Amer. J. Sci.* **237**, 7-18 (1939). (UNCLASSIFIED)

Bridgman, P. W., "Rough Compression of 177 Substances to 40,000 kg/cm<sup>2</sup> (U)," *Proc. Am. Acad. Arts Sci.* **76**, 71-87 (1948). (UNCLASSIFIED)

Cowperthwaite, M., "Model Solutions for the Interaction of Steady-State Compression Waves with a Boundary (U)," to be published in the *Proceedings of the 4th International Symposium on Behavior of Dense Media Under Dynamic Pressures*, to be held in Tours, France, 5-9 June (1995). (UNCLASSIFIED)

Cowperthwaite, M., and R. F. Williams, "Determination of Constitutive Relationships with Multiple Gauges in Nondivergent Waves (U)," *J. Appl. Phys.* **42**(1), 456-462 (1971). (UNCLASSIFIED)

DeCarli, P.S., "Stress-Gage System for the Megabar (100 GPa) Range (U)," Final Report to the Defense Nuclear Agency, Contract No. DNA-75-C-0029, Stanford Research Institute, Menlo Park, CA (1976). (UNCLASSIFIED)

DeCarli, P. S., "HYDRO PLUS Procedures Manual No. 5: Flatpack Operations (U)," Draft Technical Report to Defense Nuclear Agency, SRI Project 2667, Contract No. DNA 001-91-C-0112 (November 1993). (UNCLASSIFIED)

Florence, A. L., S. A. Miller, and C. E. Keller, "Decoupling of Underground Explosions by Rubble-Filled Cavities (U)," *J. Geophys. Res.* **98**(B8), 14197-14209 (1993). (UNCLASSIFIED)

Forest, C. A., "Lagrangian Analysis, Data Covariance, and the Impulse Time Integral (U)," Technical Report LA-UR 91-3135, Los Alamos National Laboratory, Los Alamos, NM (1991). (UNCLASSIFIED)

Fowles, R., and R. F. Williams, "Plane Stress Wave Propagation in Solids (U)," *J. Appl. Phys.* **41**(1), 360-363 (1970). (UNCLASSIFIED)

Furnish, M. D., "Dynamic Properties of Indiana, Fort Knox, and Utah Test Range Limestones and Danby Marble Over the Stress Range 1 to 20 GPa (U)," Technical Report SAND92-0983 • UC-703, Sandia National Laboratory, Albuquerque, NM (1994). (UNCLASSIFIED)

Gaffney, E. S., "Artificial Joint Results (U)," Proceedings of the Defense Nuclear Agency Material Properties and High Pressure Equation-of-State Working Group Meeting, held in Albuquerque, NM, August 11-12 (1992). (UNCLASSIFIED)

Gaffney, E. S., and E. A. Smith, "HYDROPLUS Experimental Study of Dry, Saturated and Frozen Geological Materials (U)," Technical Report DNA-TR-93-74, Defense Nuclear Agency, Alexandria, VA (1994). (UNCLASSIFIED)

Gefken P. R., and A. L. Florence, "Spherical Waves in Jointed Limestone (U)," Technical Report DNA-TR-92-122, Defense Nuclear Agency, Alexandria, VA (1993). (UNCLASSIFIED)

Gefken, P. R., and A. L. Florence, "Spherical Wave Experiments With Frozen Limestone (U)," Technical Report, Project No. 3340, SRI International, Menlo Park, CA (1992). (UNCLASSIFIED)

Grady, D.E., "Experimental Analysis of Spherical Wave Propagation (U)," *J.Geophys. Res.* **78**(8), 1299-1307 (1973). (UNCLASSIFIED)

Grady, D. E., "High-Pressure Release-Wave Measurements and Phase Transformation in CaCO<sub>3</sub> (U)," in *Proceedings of the Fourth American Physical Society Topical Conference on Shock Waves in Condensed Matter*, edited by Y.M. Gupta, Plenum Press, 1986, pp. 589-593. (UNCLASSIFIED)

Grady, D. E., R. E. Hollenbach, and K. W. Schuler, "Compression Wave Studies on Calcite Rock (U)," *J. Geophys. Res.* **83**(B6), 2839-2849 (1978). (UNCLASSIFIED)

Keough, D. D., P. S. DeCarli, and T. Cooper, "DISTANT MOUNTAIN Test Series (Test Bed Designs and Flatpack Stress Gage Measurements) (U)," Technical Report DNA-TR-93-103, Defense Nuclear Agency, Alexandria, VA (1993). (UNCLASSIFIED)

Kerley, G. I., "Equations of State for Calcite Minerals. Vol. I: Theoretical Model for Dry Calcium Carbonate (U)," *High Pressure Research* **2**, 29-47 (1989). (UNCLASSIFIED)

Larson, D. B., and G. D. Anderson, "Plane Shock Studies of Porous Geologic Media (U)," *J. Geophys. Res.* **84**(B9), 4592-4600 (1979). (UNCLASSIFIED)

Martin, J. W., and C. Felice, "Characterization of Material from Vertical Drill Hole MP4 (U)," Technical Report TR93-08, Terra Tek, Inc., Salt Lake City, UT (1992). (UNCLASSIFIED)

Miller, S. A., and A. L. Florence, "Laboratory Particle Velocity Experiments on (JVE) Analog Rock (U)," Technical Report GL-TR-90-0279(I), Geophysics Laboratory, Air Force Systems Command, Hanscom Air Force base, MA (1990). (UNCLASSIFIED)

Murri, W. J., D. E. Grady and K. D. Mahrer, "Equation of State of Rocks (U)," Technical Report (SRI Project PYU-1883), Stanford Research Institute, Menlo Park, CA (1975). (UNCLASSIFIED)

Ringwood, A. E., "Mineralogical Constitution of the Deep Mantle (U)," *J.Geophys. Res.* **67**, 4839-4874 (1962). Phillips, B. R., "Mechanical Response of Dry Reid-Bedford Model Sand and Saturated Misers Bluff Sand," Technical Report SL-86-27, Department of the Army, Waterways Experiment Station, Corps of Engineers (1986a). (UNCLASSIFIED)

Phillips, B. R., "Mechanical Properties of Dry Reid-Bedford Model Sand (U)," Technical Report SL-86-29, Department of the Army, Waterways Experiment Station, Corps of Engineers (1986b). (UNCLASSIFIED)

Seaman, L., "Analysis of Dynamic *In Situ* Backfill Property Tests, Report 2: an Improved Lagrangian Analysis for Stress and Particle Velocity Gage Arrays (U)," Technical Report SL-87-11, Department of the Army, U.S. Army Corps of Engineers, Washington, DC (1987). (UNCLASSIFIED)

Seaman, L. and D. R. Curran, "SRI PUFF 8 Computer Program for One-Dimensional Stress Wave Propagation (U)," SRI International Final Report (Volume II), prepared for the U.S. Army Ballistics Research Laboratory, Contract No. DAAC11-77-C-0083 (1978). (UNCLASSIFIED)

Simons, J.W., Curran, D. R., and Antoun, T. H., "A Computer Model for Explosively-Induced Rock Fragmentation During Mining Operations (U)," in *Proceedings of the 56<sup>th</sup> Annual University of Minnesota Mining Symposium*, Duluth, MN, January 24-26 (1995). (UNCLASSIFIED)

Singh, A. K., and G. C. Kennedy, "Compression of Calcite to 40 kbar (U)," *J.Geophys. Res.* 79, 2615-2622 (1974). (UNCLASSIFIED)

Stapleton, B. S., and Y. M. Gupta, "Response of Single Crystal Calcite Shocked to 40 kbar Along the C-Axis (U)," in *Proceedings of the American Physical Society Topical Conference on Shock Compression of Condensed Matter*, Williamsburg, VA, June 17-20, 1992, S. C. Schmidt, R. D. Dick, J. W. Forbes, and D. G. Tasker, Elsevier Science Publishers, Amsterdam, 1992, pp. 199-202. (UNCLASSIFIED)

Wang, C. Y., "Velocity of Compressional Waves in Limestones, Marbles, and a Single Crystal of Calcite to 20 Kilobars (U)," *J.Geophys.Res.* 71(14), 3543-3547 (1966). (UNCLASSIFIED)

Wang, C. Y., "Ultrasonic Study of Phase Transition in Calcite to 20 Kilobars and 180°C (U)," *J. Geophys. Res.* 73(12), 3937-3944 (1968). (UNCLASSIFIED)

Wang, C. Y., and M. Meltzer, "Propagation of Sound Waves in a Rock Undergoing Phase Transformations (U)," *J.Geophys. Res.* 78(8), 1293-1298 (1973). (UNCLASSIFIED)

Whirley, R. G., and B. E. Engelmann, "DYNA2D a Nonlinear, Explicit, Two-Dimensional Finite Element Code for Solid Mechanics, User Manual (U)," Technical Report UCRL-MA-110630, Lawrence Livermore National Laboratory, Livermore, CA (1992). (UNCLASSIFIED)

## APPENDIX A

### RISE TIME OF IN-MATERIAL GAGES

Solids cannot sustain discontinuities in pressure or particle velocity. If a discontinuity is introduced, the material produces waves to carry the discontinuity away so as to leave the material in such a state that both pressure and particle velocity are continuous.\* When a gage package that has finite thickness and a shock impedance different from that of the test medium is embedded between two slabs of material, the impedance mismatch between the gage package and the sample causes discontinuity in the flow field. The perturbed flow gives rise to stress waves that originate at the gage package/specimen interfaces to carry away the discontinuity. Several stress wave reverberations occur within the gage package before the gage comes to pressure and particle velocity equilibrium with the surrounding medium.

The rise time of the gage (i.e., the time required to achieve pressure and particle velocity equilibrium) varies depending on the gage plane thickness and the mismatch in material properties between the gage package and the test medium. A good estimate of the rise time of the gage is important especially to help in the interpretation of experimental records when time-resolved details of the wave structure are of primary importance. This Appendix presents a method for calculating the rise time of the gage.

#### A.1 ANALYTICAL SOLUTION.

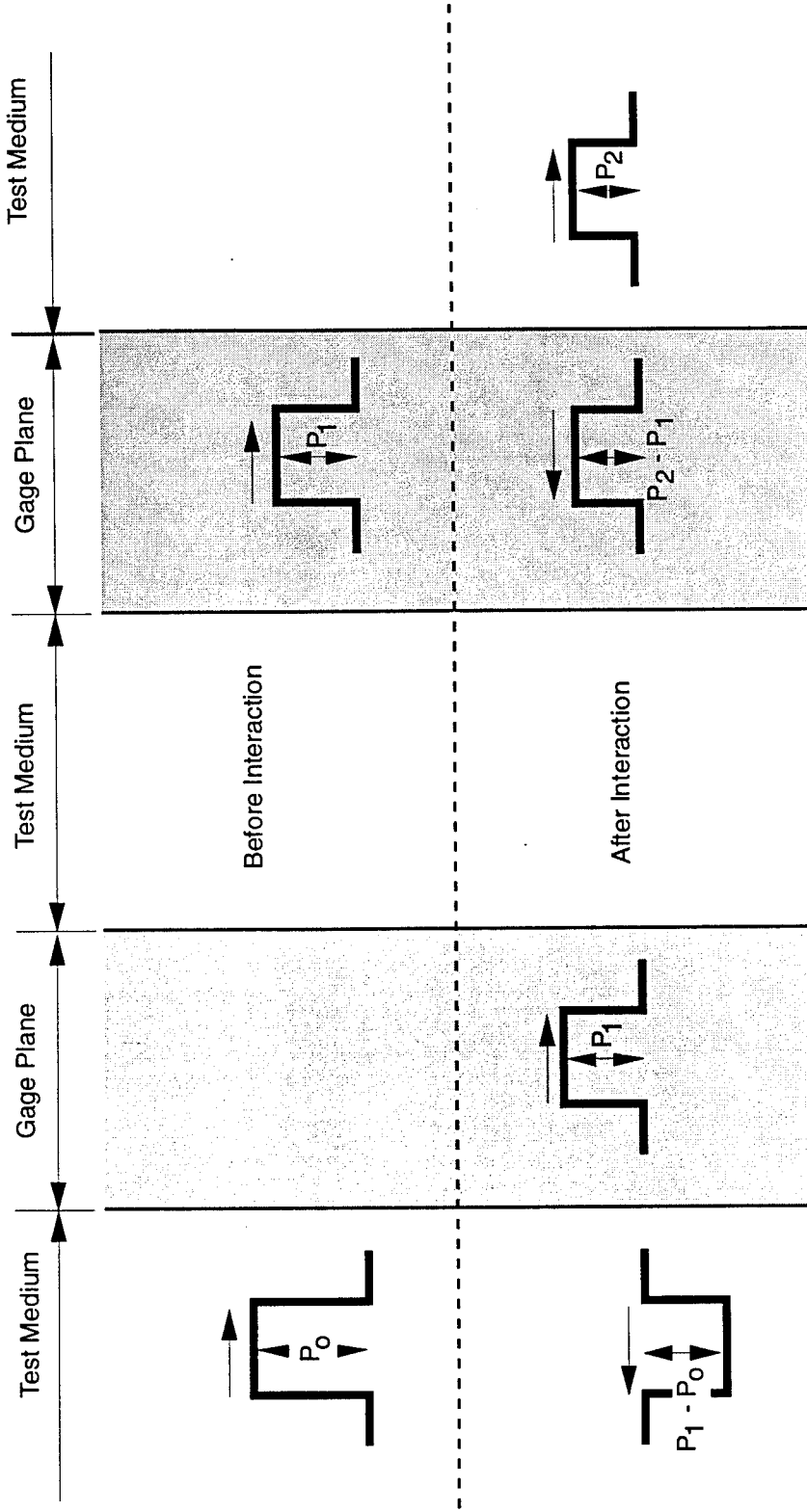
Consider an in-material, Lagrangian gage embedded between two blocks of a material sample. For the purposes of the present analysis, the sample blocks can be considered semi-infinite. Consistent with the experiments conducted during this investigation, we assume that the average impedance of the gage package,  $Z_g$ , is smaller than that of the sample,  $Z_s$ . We further assume a linear acoustic response.

If a square pressure pulse of magnitude  $P_0$  impinges on the gage plane, it will be partially transmitted into the gage package and partially reflected back into the sample block, as shown in Figure A-1(a). The transmission and reflection coefficients,  $T_{sg}$  and  $R_{sg}$ , may be defined as follows:

$$T_{sg} = \frac{P_1}{P_0} = \frac{2Z_g}{Z_g + Z_s} \quad (\text{A-1})$$

---

\*Haynes, D.B., "Introduction to Stress Wave Phenomena," Sandia National Laboratory Report SLA-73-0801, August 1973.



(a) Wave interactions at leftmost interface      (b) Wave interactions at rightmost interface

Figure A-1. Wave interactions between the test medium and the gage package (compressive waves are shown positive).

and

$$R_{sg} = \frac{P_0 - P_1}{P_0} = \frac{Z_s - Z_g}{Z_s + Z_g} \quad (A-2)$$

where  $P_1$  is the equilibrium pressure after wave interaction.

The next interaction of interest occurs as the pressure pulse of magnitude  $P_1$  impinges on the rightmost interface between the gage package and the sample, as shown in Figure A-1(b). As before, the wave is partially transmitted and partially reflected. The transmission and reflection coefficients,  $T_{gs}$  and  $R_{gs}$ , are given by the following relations,

$$T_{gs} = \frac{P_2}{P_1} = \frac{2 Z_s}{Z_s + Z_g} \quad (A-3)$$

and

$$R_{gs} = \frac{P_1 - P_2}{P_1} = \frac{Z_g - Z_s}{Z_s + Z_g} \quad (A-4)$$

where  $P_2$  is the equilibrium pressure after wave interaction.

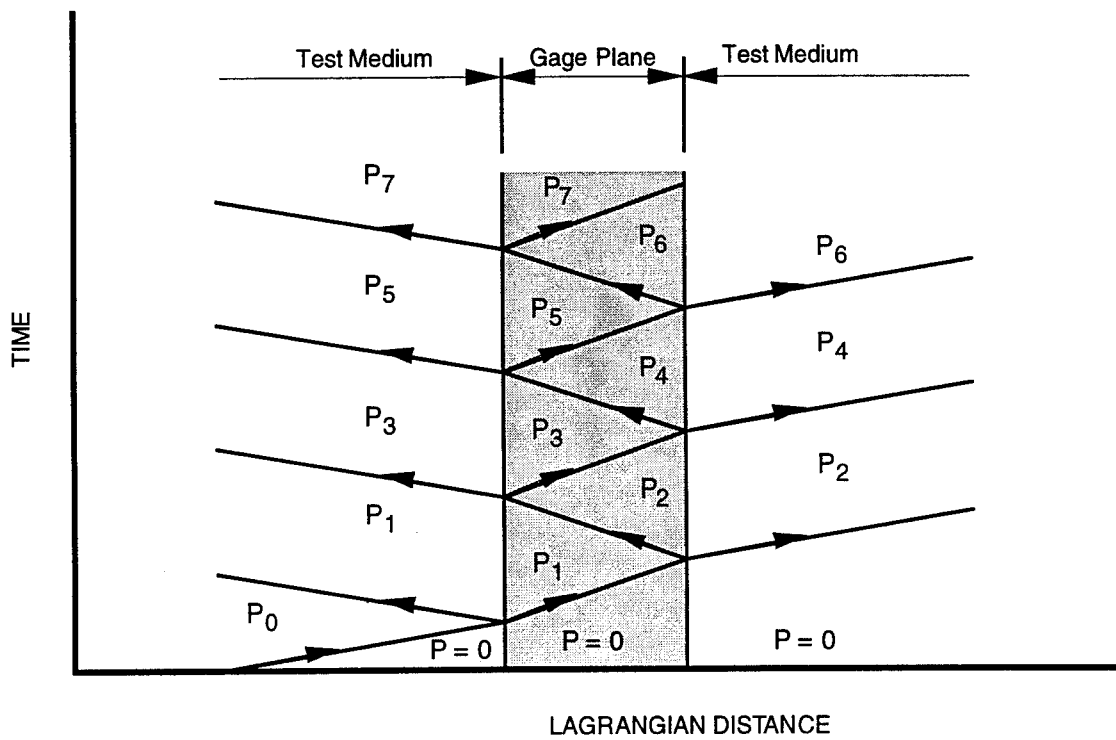
It is important to note the differences between Equations (A-1) and (A-2) and Equations (A-3) and (A-4). These differences stem from the fact that Equations (A-1) and (A-2) pertain to shock waves traveling from a high impedance material into a low impedance material, while Equations (A-3) and (A-4) pertain to shock waves traveling from a low impedance material into a high impedance material. These differences are further illustrated in Figure A-1 (i.e., the reflected pulse is a release wave in one case and a compressive wave in the other case).

Figure A-2 shows an x-t diagram and a P-u diagram for several wave reverberations within the gage package. The pressure in the gage package increases with each reverberation. After several wave reflections, the pressure in the gage approaches the equilibrium pressure ( $P_0$ ). These observations can be formalized with the aid of Equations (A-1) through (A-4) into a general equation relating the relative pressure in the gage,  $\frac{P_n}{P_0}$ , to the impedance of the gage package and test medium,  $Z_g$  and  $Z_s$ , and to the number of reverberations within the gage package,  $n$ . This equation takes the form

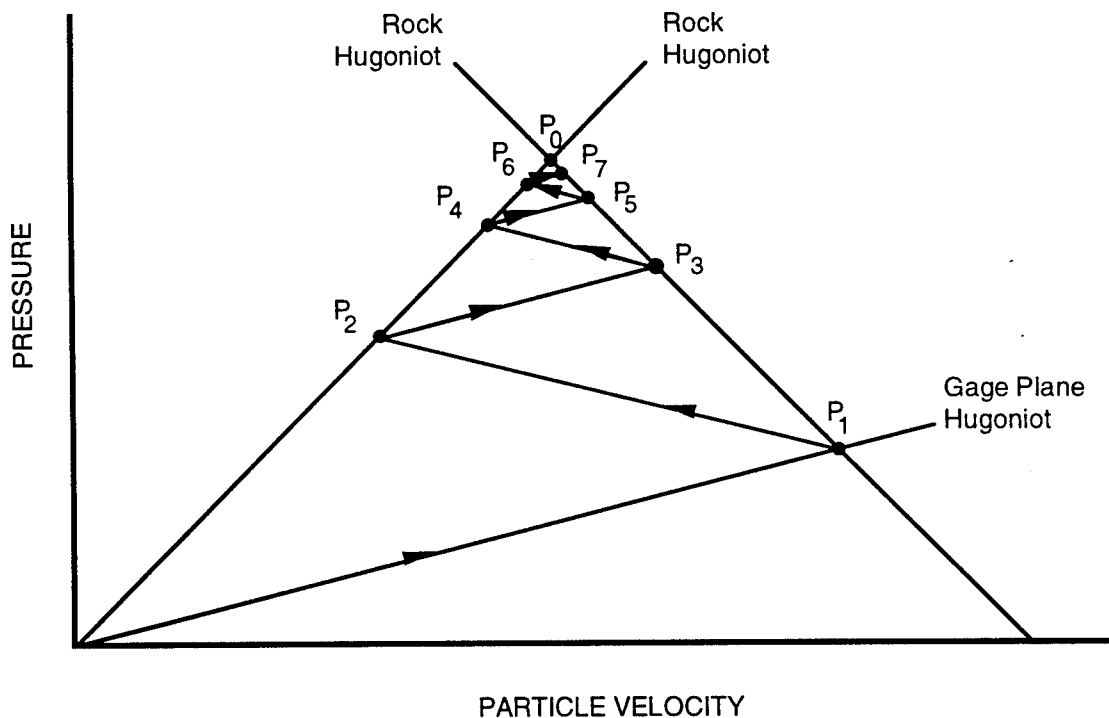
$$\frac{P_n}{P_0} = T_{sg} \sum_{i=0}^{n-1} R_{sg}^i \quad (A-5)$$

The power series in Equation (A-5) is a convergent series and possesses the following unique solution as  $n \rightarrow \infty$ :

$$\frac{P_\infty}{P_0} = \frac{T_{sg}}{1 - R_{sg}} \quad (A-6)$$



(a) x-t diagram showing wave reverberations in gage plane



(b) P-u diagram showing the gage plane equilibrium process

Figure A-2. Wave reverberations due to impedance mismatch between the test medium and the gage plane.

and since

$$T_{sg} + R_{sg} = 1 \quad (\text{A-7})$$

Equation (A-6) simply reduces to

$$\frac{P_\infty}{P_0} = 1 \quad (\text{A-8})$$

as one would expect.

### RISE TIME ESTIMATE.

The rise time of the gage is directly proportional to the number of stress wave reflections within the gage package required to bring the gage to pressure and particle velocity equilibrium with the surrounding medium. If  $n$  reflections are required to achieve equilibrium, the rise time can be obtained from the relation

$$t = \frac{n \ell}{C} \quad (\text{A-9})$$

where  $\ell$  is the thickness and  $C$  is the average wave speed of the gage package. The relative pressure in the gage plane at time  $t$  (or after  $n$  reverberations) is given by Equation (A-5).

In the rock equation of state experiments of the present study, a typical gage package is about 0.0762 mm-thick and consists mainly of epoxy. In the stress range of interest, the average mechanical impedance of the gage package,  $Z_g$ , is approximately 750 kbar- $\mu\text{s}/\text{cm}$  and the shock velocity,  $C$ , is approximately 0.6 cm/ $\mu\text{s}$ .\* The mechanical impedance of the rock sample,  $Z_s$ , is approximately 1500 kbar- $\mu\text{s}/\text{cm}$ .\*\*

The equilibrium pressures and corresponding rise times for the first 12 wave reflections within a typical gage plane are summarized in Table A-1, and the results are plotted in Figure A-3. As these results indicate, three reverberations are required to reach about 95% of the equilibrium pressure in a time span of about 38 ns.

---

\*Keough, D., "Procedure for Fabrication and Operation of Manganin Shock Pressure Gages," AFWL-TR-68-57, Air Force Weapons Laboratory, Kirtland AFB, NM, 1968.

\*\*Murri, W. J., D. E. Grady, and K. D. Mahrer, "Equation of State of Rocks" Stanford Research Institute Technical Report (SRI Project PYU-1883), July 1975.

**Table A-1. Computed relative pressures and equilibrium times for an epoxy gage plane embedded in limestone.**

<i>n</i>	$\frac{P_n}{P_0}$	t (ns)
1	0.6364	12.70
2	0.8678	25.40
3	0.9519	38.10
4	0.9825	50.80
5	0.9936	63.50
6	0.9977	76.20
7	0.9991	88.88
8	0.9997	101.63
9	0.9999	114.30
10	0.9999	126.98
11	0.9999	139.73
12	0.9999	152.4

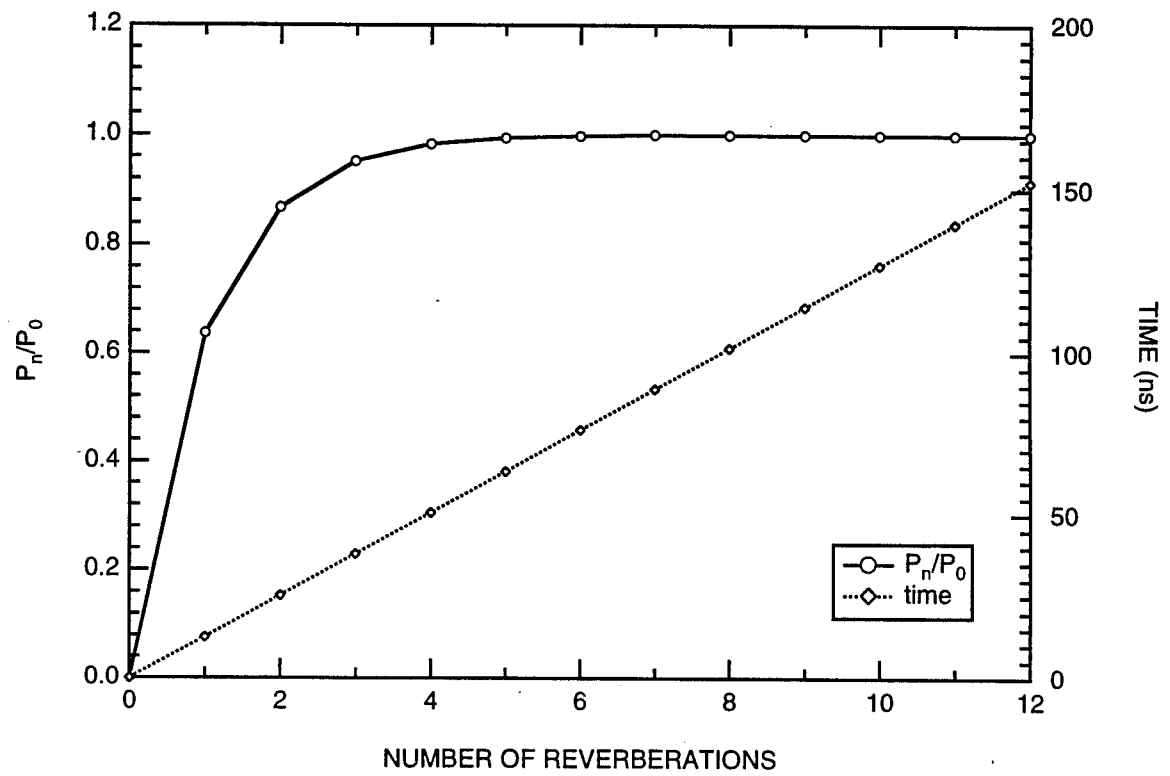


Figure A-3. Relative pressure and corresponding rise time for a typical gage plane.

## APPENDIX B

### SUMMARY OF THE EXPERIMENTAL RESULTS OF THE UNIAXIAL STRAIN, IN-CONTACT EXPLOSIVE EXPERIMENTS

This Appendix summarizes the raw data and reduced experimental results of all the uniaxial strain, in-contact explosive experiments conducted during the present investigation. Some of the results presented here have been presented elsewhere in this report. These results are included here for the sake of providing a complete set of results that encompass all the uniaxial strain experiments conducted during the course of the study.

Table B-1 summarizes the experimental conditions (explosive system, joint type) of all the uniaxial strain experiments and provides the thickness of each rock slab used in constructing the specimens as well as the overall thicknesses of the specimens. For each of the experiments listed in Table B-1, the experimental results are displayed graphically in the following order:

- (1) Specimen configuration and dimensions (e.g., Figure B-4).
- (2) Summary of the output of all the stress or particle velocity gages in a given experiment (e.g., Figure B-5).
- (3) One figure for each gage plane displaying the output of the particle velocity gages (stress gage in the case of HPEOS Experiment 1) as a function of time (e.g., Figures B-6 through B-10).
- (4) Particle velocity histories (stress history in the case of HPEOS Experiment 1) that correspond to the gage output described in (3) above (e.g., Figures B-11 through B-15).

**Table B-1. Summary of the configurations and dimensions of the uniaxial strain experiments.**

Experiment No.	Explosive System	Joint Type Orientation	Specimen dimensions (mm)								
			Layer 1 <sup>1</sup>	Layer 2	Layer 3	Layer 4	Layer 5	Layer 6	Layer 7	Layer 8	Thickness <sup>2</sup>
HPEOS1-L <sup>3</sup>	P-40 + 2-in. PBX	<i>In situ</i>	5.00	6.10	--	--	--	--	--	--	11.18
HPEOS2-M	P-60 + 6-in. Baratol	No joint	3.20	28.65	3.15	3.33	3.28	--	--	--	41.94
HPEOS3-M	P-60 + 2-in. Baratol	No joint	3.33	19.30	3.35	3.35	3.38	--	--	--	33.27
HPEOS4-M	P-60 + 2-in. Baratol	R S S <sup>4</sup>	N <sup>5</sup>	3.40	9.63	9.60	3.35	3.28	3.33	--	35.15
HPEOS5-M	P-60 + 2-in. Baratol	R S M	N	3.20	3.33	3.35	3.33	3.30	3.35	3.10	3.23
HPEOS6-M	P-60 + 2-in. Baratol	No joint	3.31	19.29	3.06	3.05	3.19	--	--	--	32.42
HPEOS7-M	P-60 + 2-in. Baratol	No joint	2.85	19.28 <sup>6</sup>	3.37	3.32	3.96	--	--	--	33.30
HPEOS8-M	P-60 + 2-in. Baratol	S C S	-	3.37	3.39	12.80	3.31	3.30	3.33	3.30	--
HPEOS9-M	P-60 + 2-in. Baratol	R S S	-	3.31	3.40	12.77	3.39	3.39	3.35	3.37	--
HPEOS10-M	P-60 + 2-in. Baratol	R S S	N	3.34	9.57	9.59	3.30	3.37	3.26	--	34.94
HPEOS11-M	P-60 + 2-in. Baratol	S S S	N	3.17	12.81	12.78	3.31	3.31	3.23	--	41.12
HPEOS12-M	P-60 + 2-in. Baratol	R S M	N	3.30	3.23	3.22	3.24	3.23	3.34	3.36	32.93
HPEOS13-M	P-60 + 2-in. Baratol	S S M	N	3.32	3.20	3.29	3.36	3.22	3.38	3.41	33.12
HPEOS14-M	P-60 + 2-in. Baratol	S S S	-	3.35	3.33	12.80	3.35	3.37	3.33	3.34	--
HPEOS15-L	P-60 + 2-in. Baratol	<i>In situ</i>		3.30	9.58	9.56	2.66	2.82	3.21	--	31.79
HPEOS16-L	P-60 + 2-in. Baratol	<i>In situ</i>		3.20	9.37	9.54	3.20	3.13	4.09	--	33.49

<sup>1</sup> This represents the actual thickness of the rock layer. It does not include gage plane and/or joint thickness.

<sup>2</sup> This represents the overall thickness of the specimen, including any joints and/or gage planes.

<sup>3</sup> The letter that follows the shot number indicates the material used in the experiment (L indicates limestone and M indicates marble).

<sup>4</sup> The first letter indicates whether the joint was smooth (S) or rough (R), the second letter indicates whether the joint was closed (C) or sand-filled (S); and the third letter indicates whether it was a single (S) or a multiple (M) joint.

<sup>5</sup> N = normal with respect to the direction of wave propagation,

I = inclined (45°) with respect to the direction of wave propagation.

<sup>6</sup> This layer was made up of two 9.53-mm-thick (3/8-in) slabs bonded together using EPON epoxy. Glue line thickness was 0.025-mm (0.001 in.)

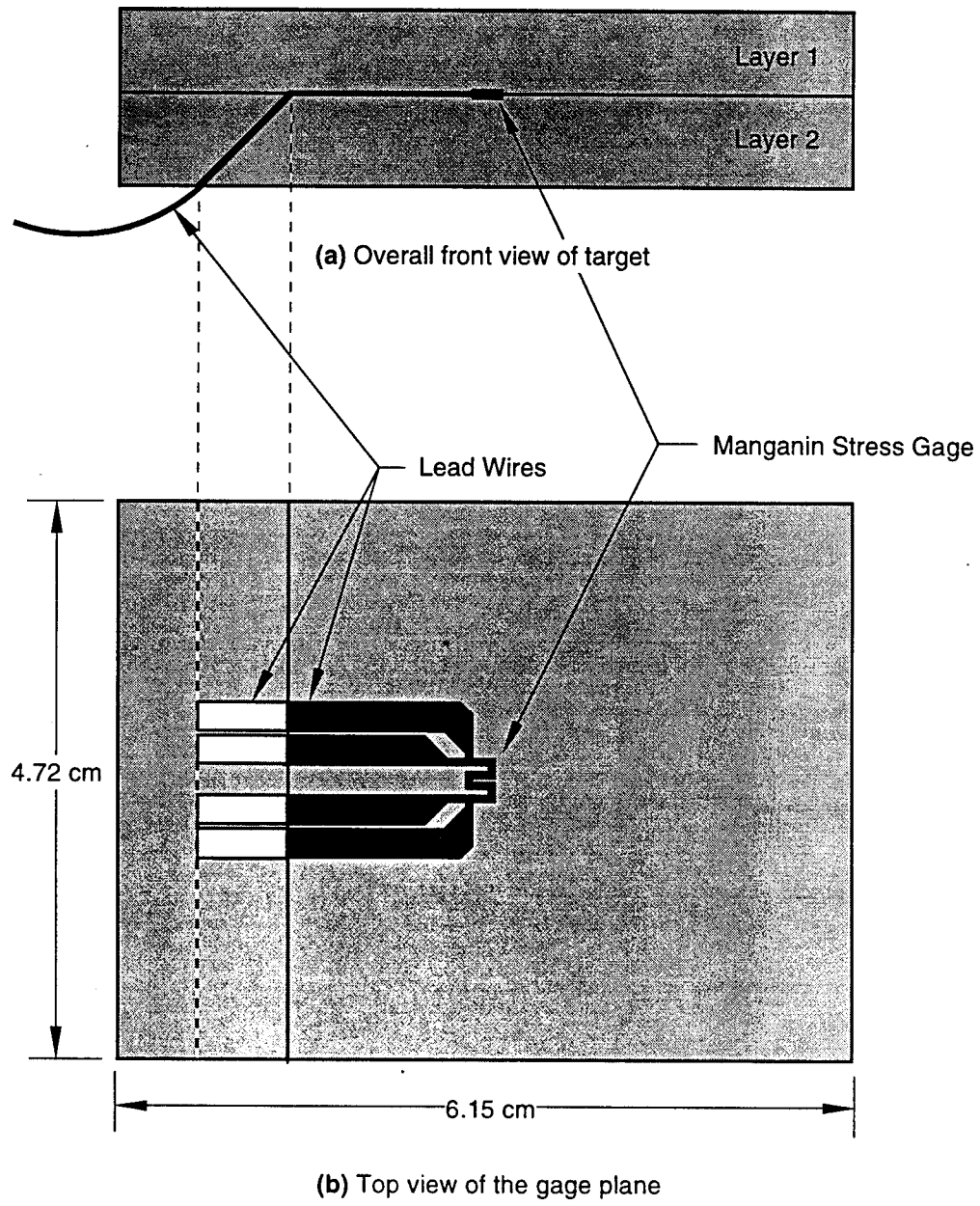


Figure B-1. Specimen configuration and dimensions for HPEOS Experiment 1 (UTTR limestone).

Note: The explosive system used in the experiment and the thicknesses of the rock layers can be obtained from Table B-1.

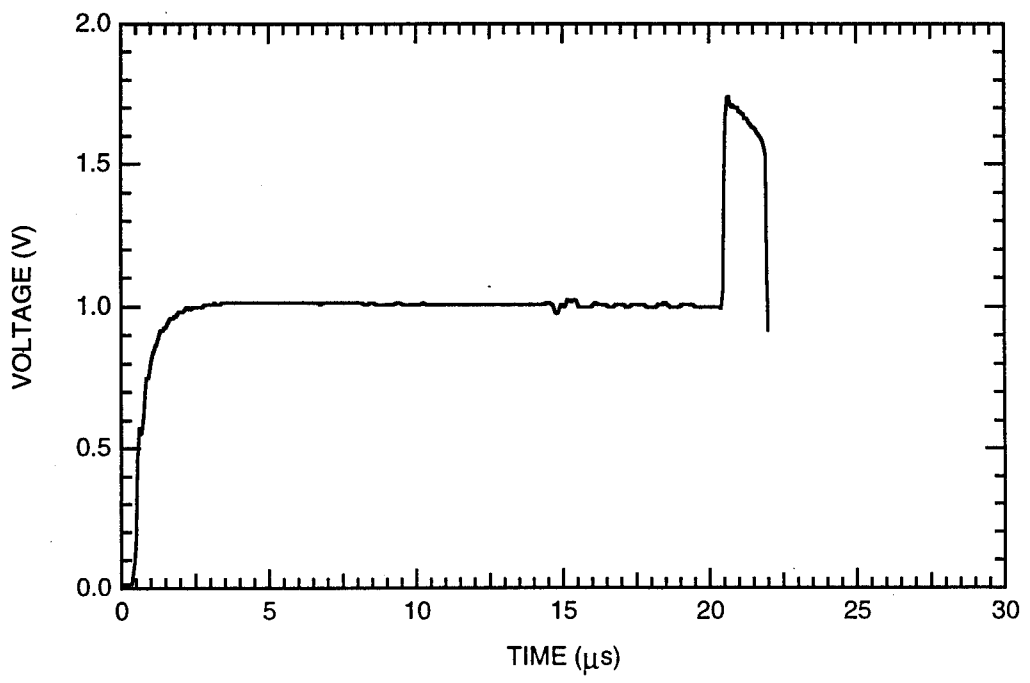


Figure B-2. Manganin gage record in HPEOS Experiment 1.

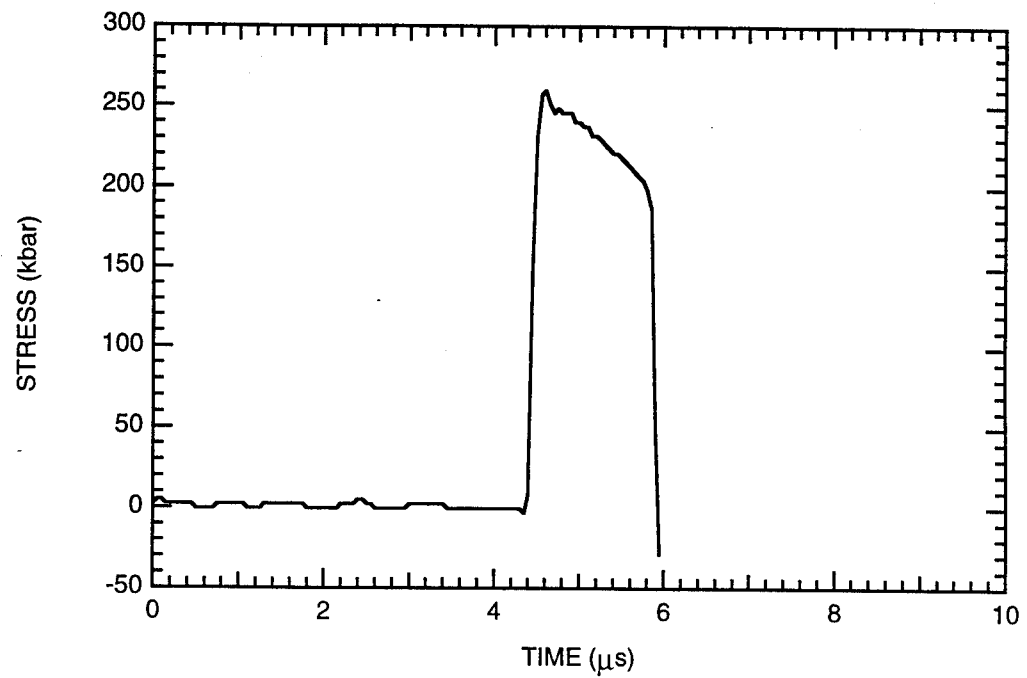


Figure B-3. Stress history at the gage plane in HPEOS Experiment 1.

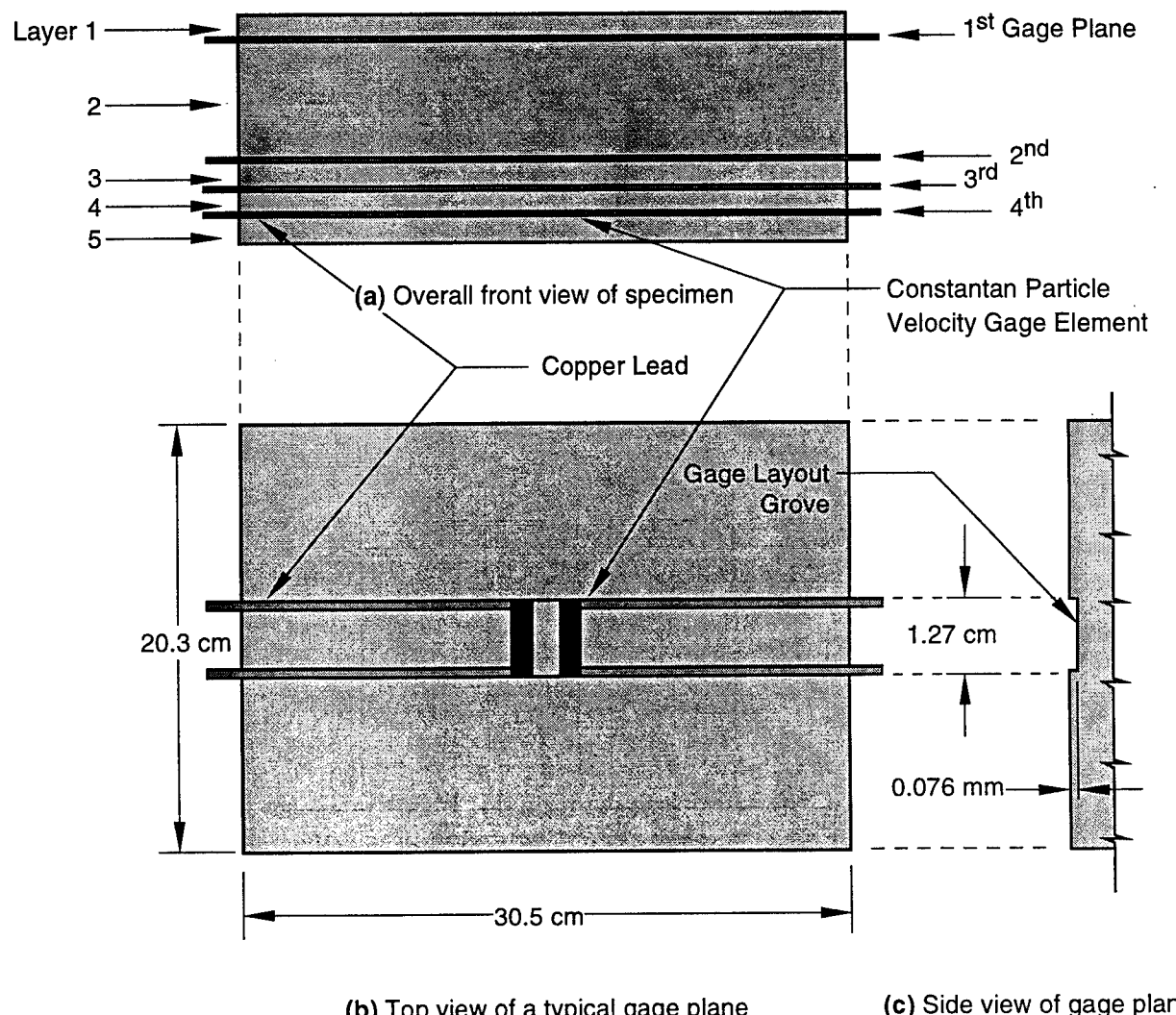


Figure B-4. Specimen configuration and dimensions for HPEOS Experiment 2 (marble).

Note: The explosive system used in the experiment and the thicknesses of the rock layers can be obtained from Table B-1.

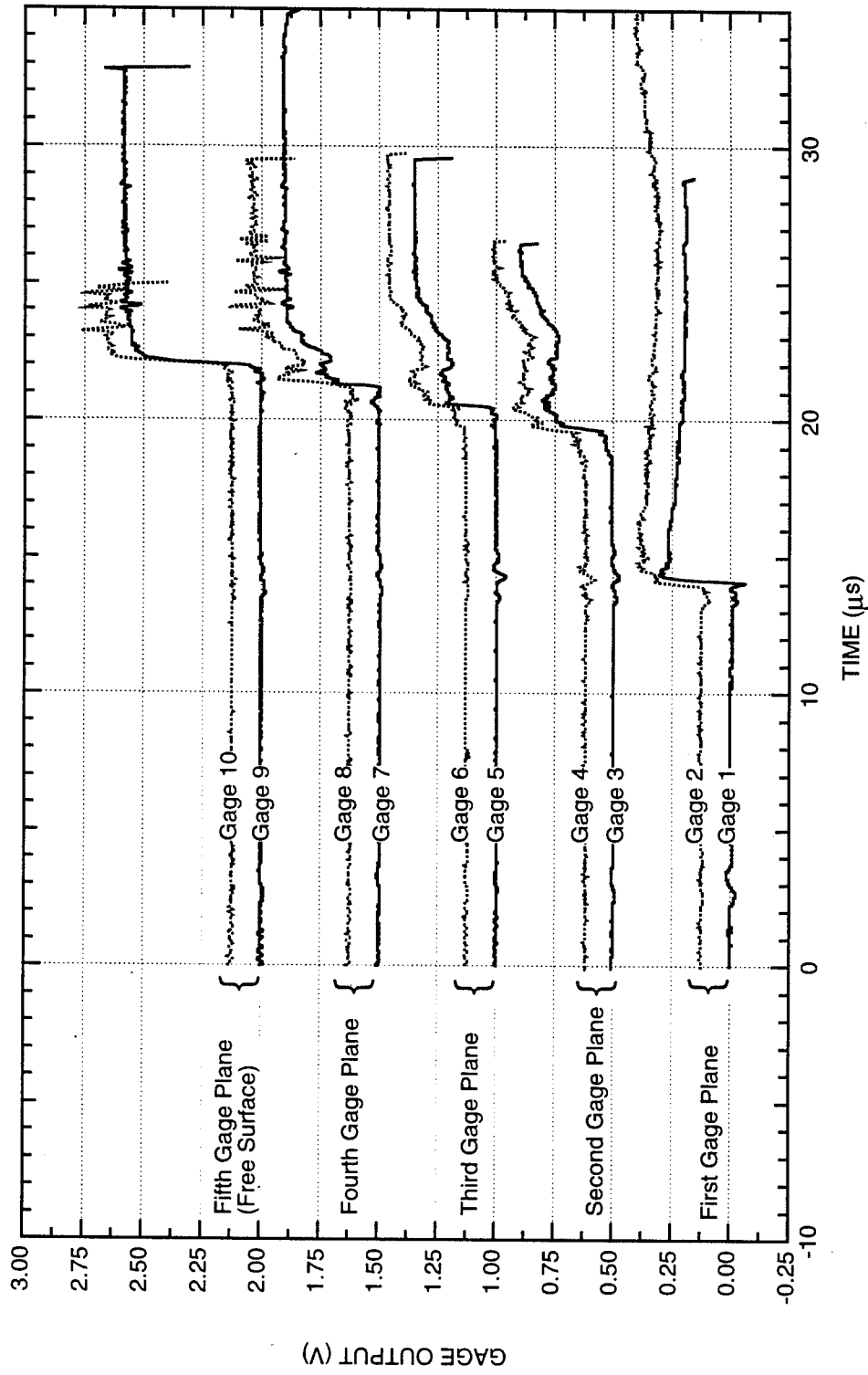


Figure B-5. Summary of the output of all particle velocity gages in HPEOS Experiment 2.

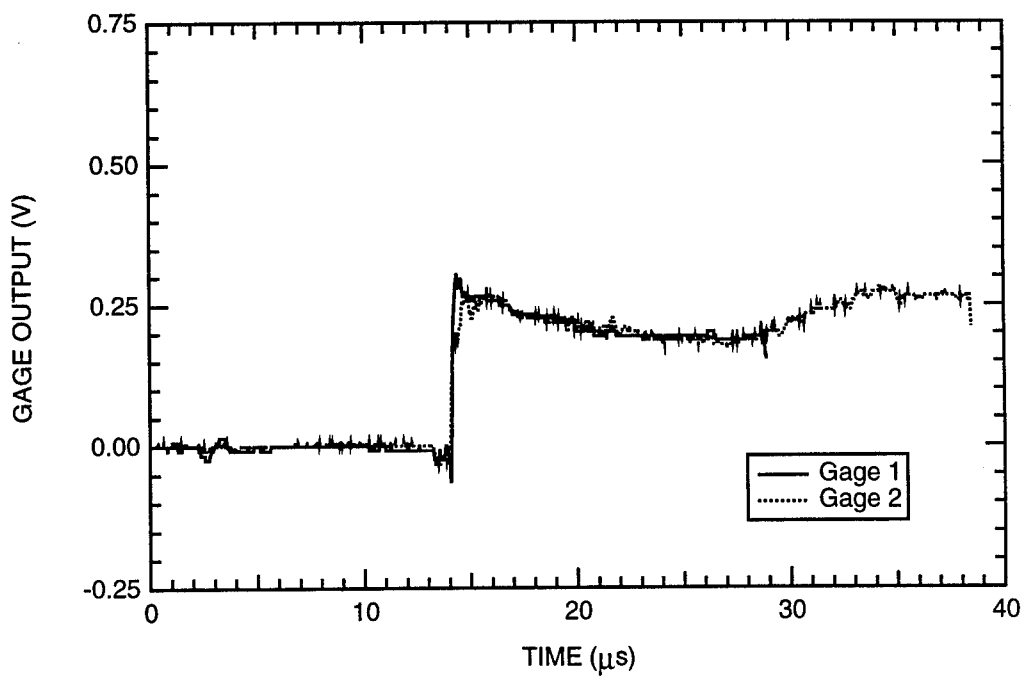


Figure B-6. Output of particle velocity gages at the first gage plane of HPEOS Experiment 2.

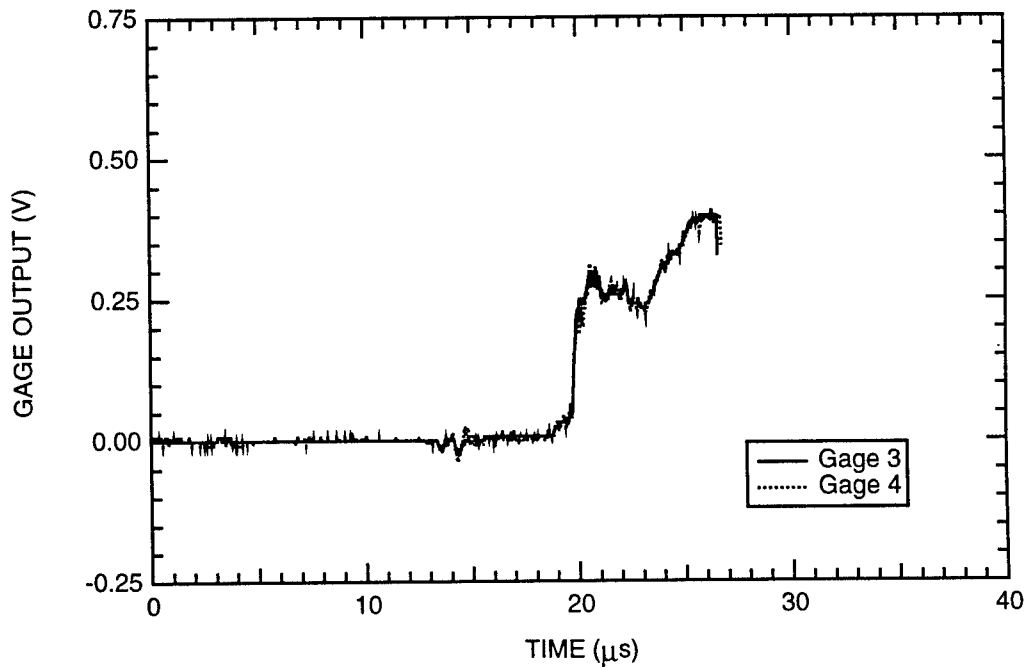


Figure B-7. Output of particle velocity gages at the second gage plane of HPEOS Experiment 2.

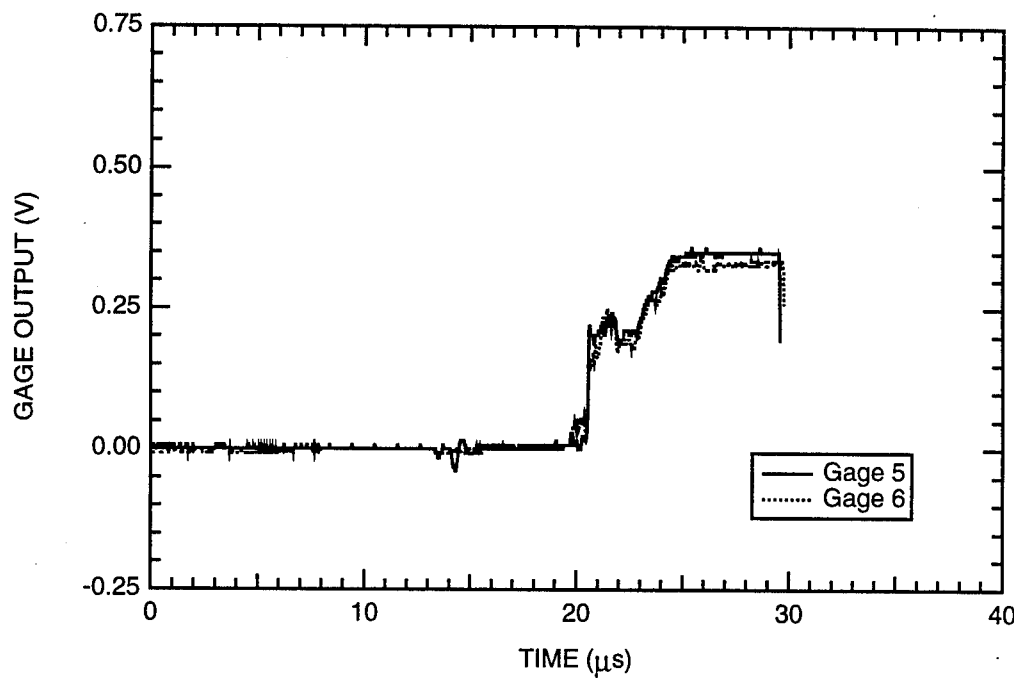


Figure B-8. Output of particle velocity gages at the third gage plane of HPEOS Experiment 2.

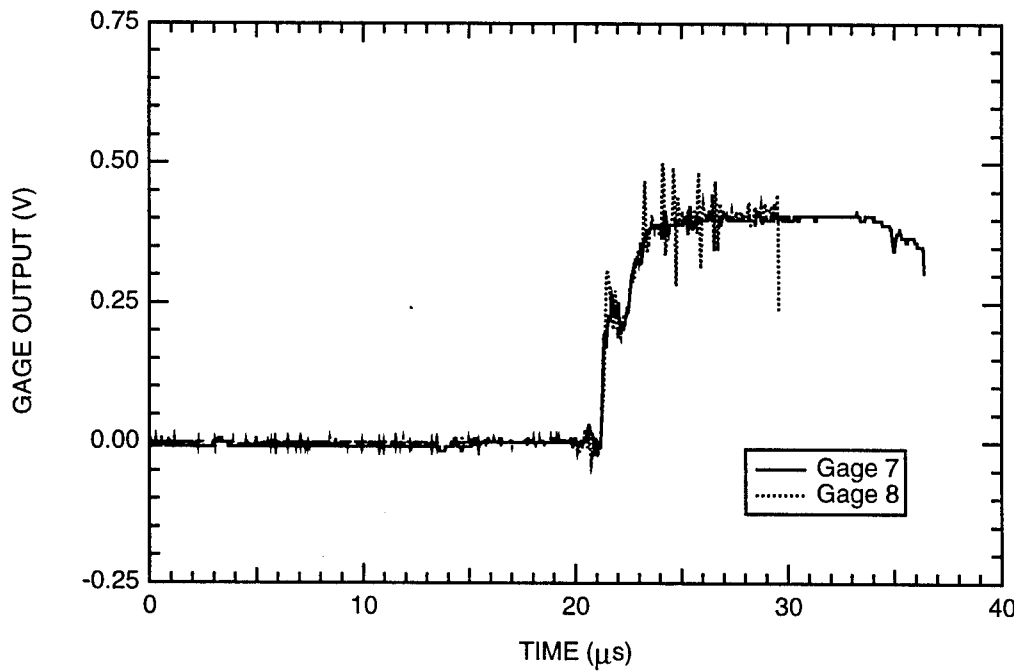


Figure B-9. Output of particle velocity gages at the fourth gage plane of HPEOS Experiment 2.

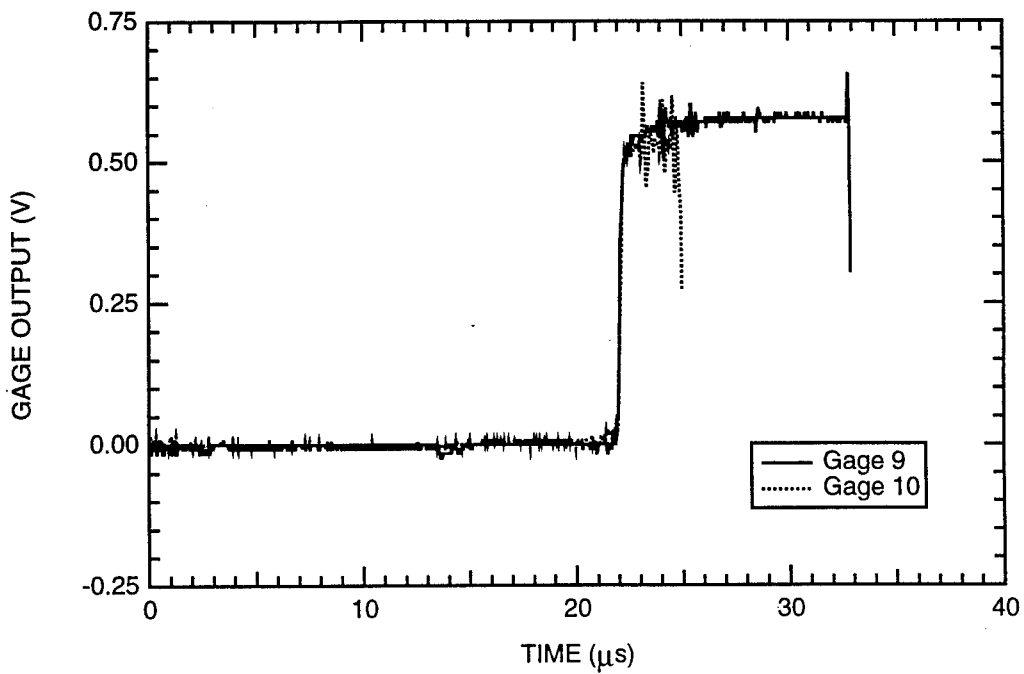


Figure B-10. Output of particle velocity gages at the fifth gage plane (free surface) of HPEOS Experiment 2.

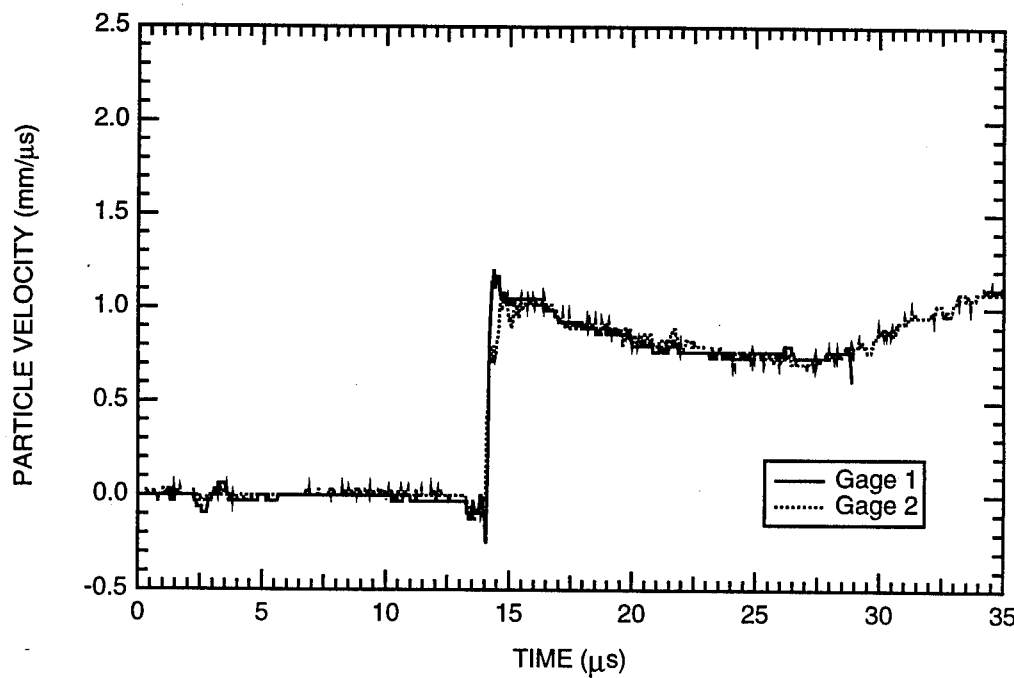


Figure B-11. Particle velocity histories at the first gage plane of HPEOS Experiment 2.

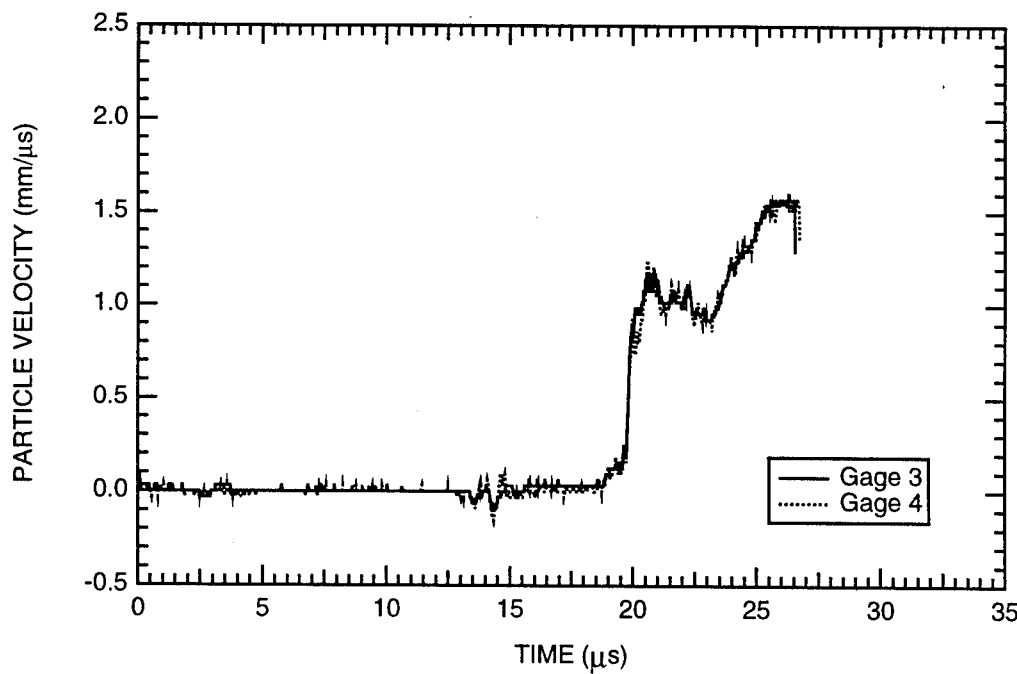


Figure B-12. Particle velocity histories at the second gage plane of HPEOS Experiment 2.

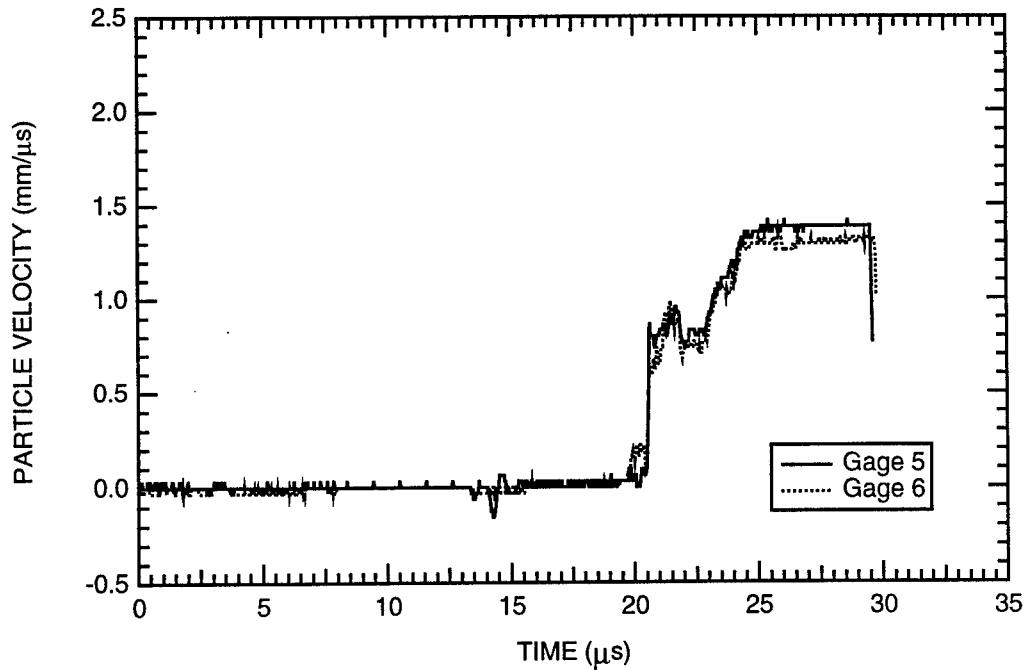


Figure B-13. Particle velocity histories at the third gage plane of HPEOS Experiment 2.

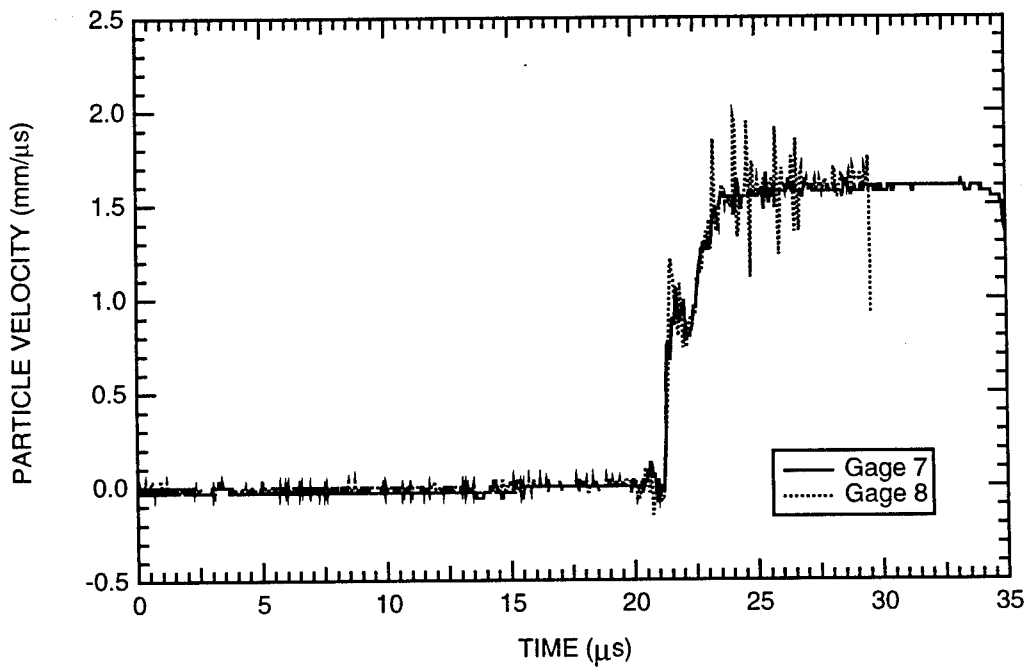


Figure B-14. Particle velocity histories at the fourth gage plane of HPEOS Experiment 2.

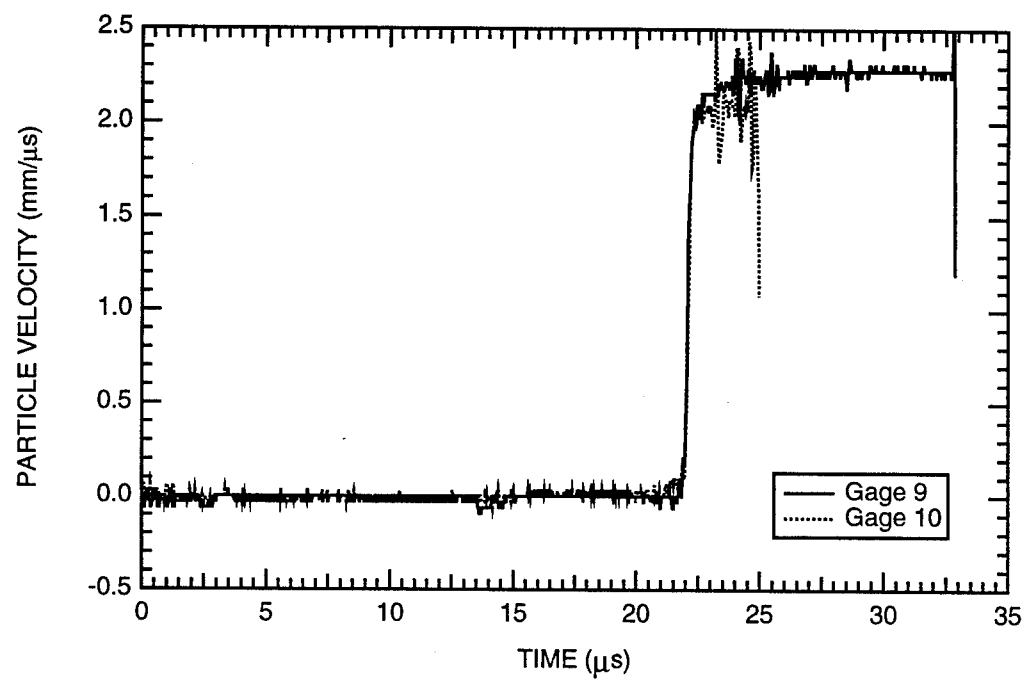


Figure B-15. Particle velocity histories at the fifth gage plane (free surface) of HPEOS Experiment 2.

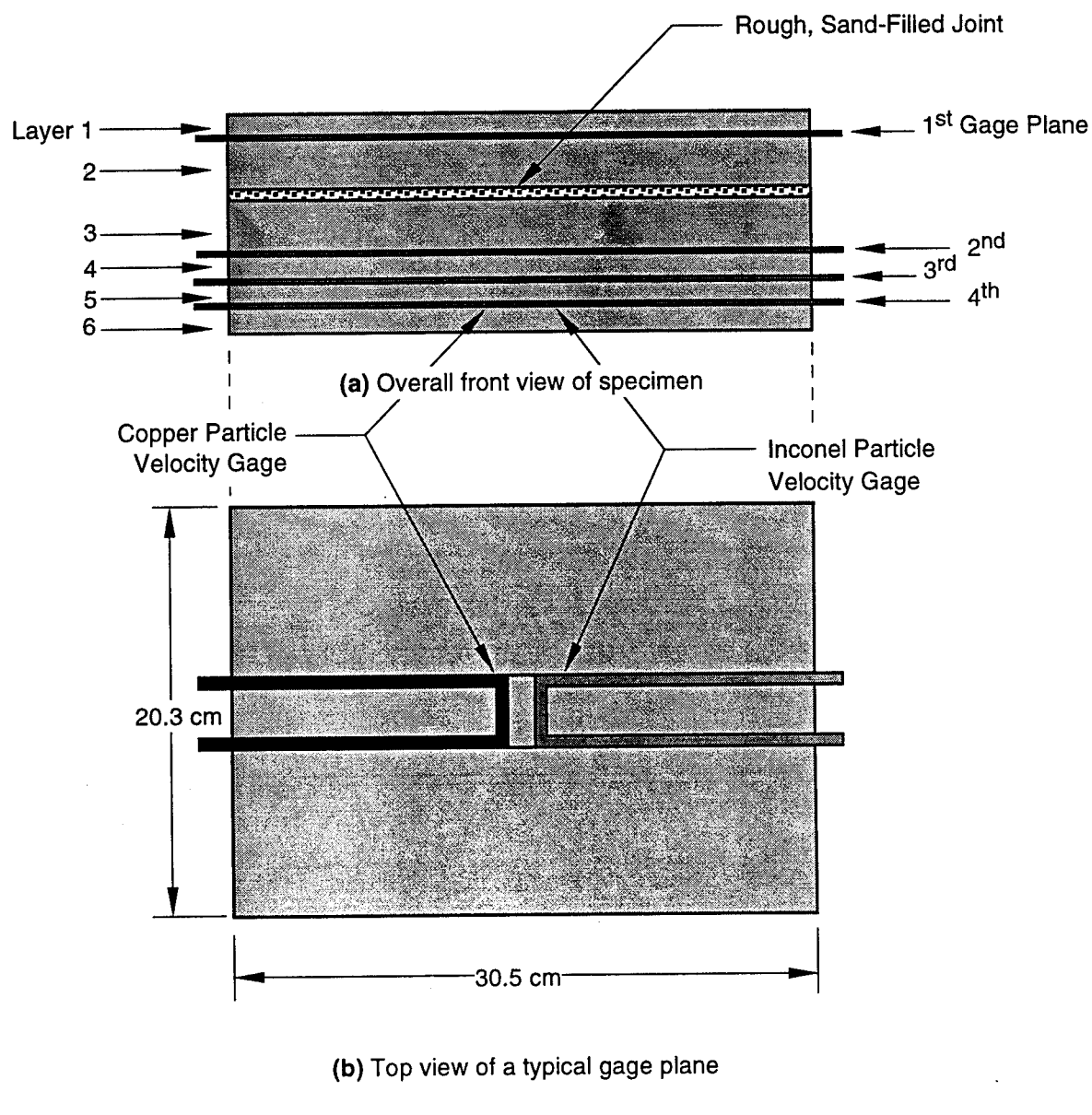


Figure B-16. Specimen configuration and dimensions for HPEOS Experiment 4 (marble).

Note: The explosive system used in the experiment and the thicknesses of the rock layers can be obtained from Table B-1.

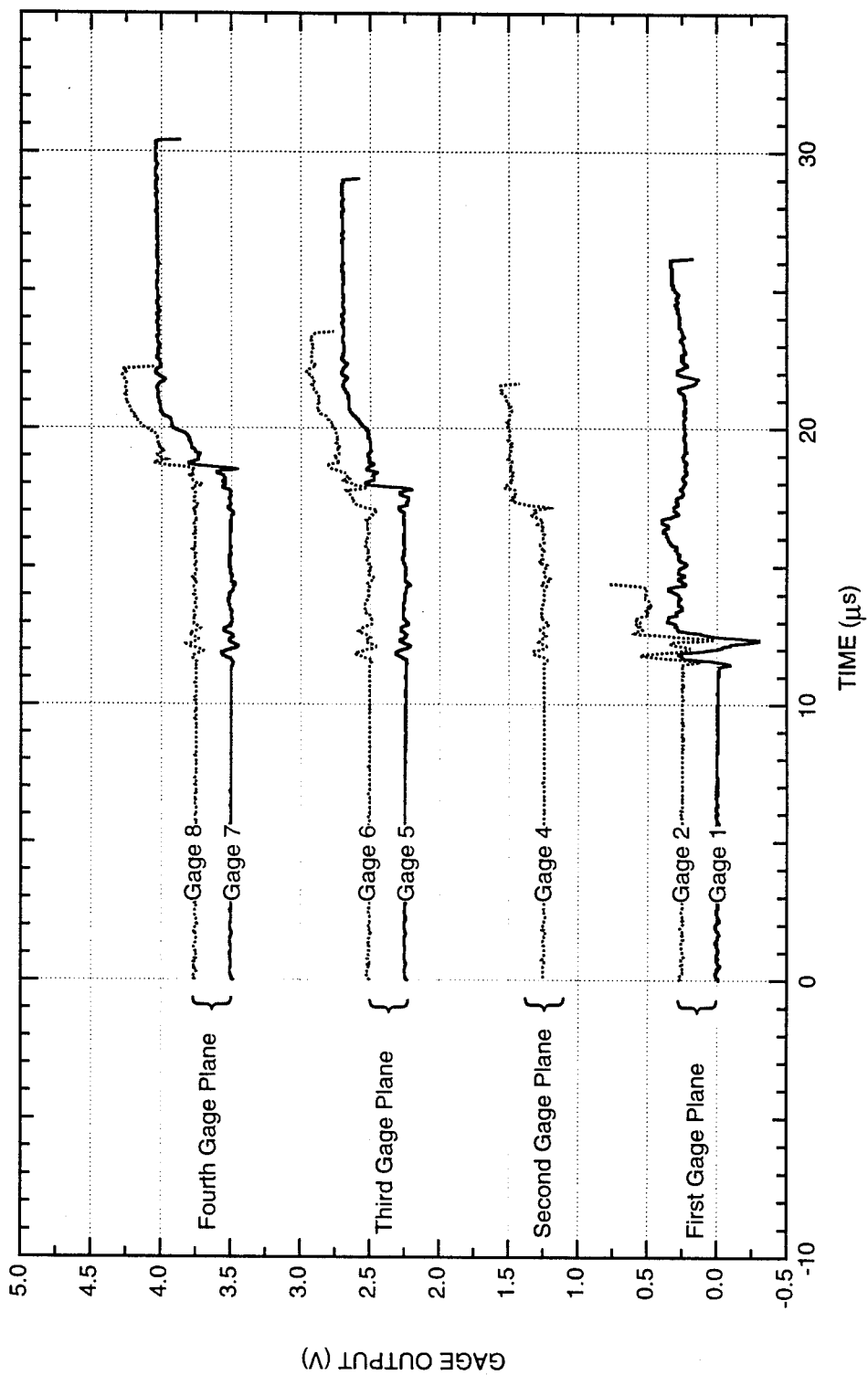


Figure B-17. Summary of the output of all particle velocity gages in HPEOS Experiment 4.

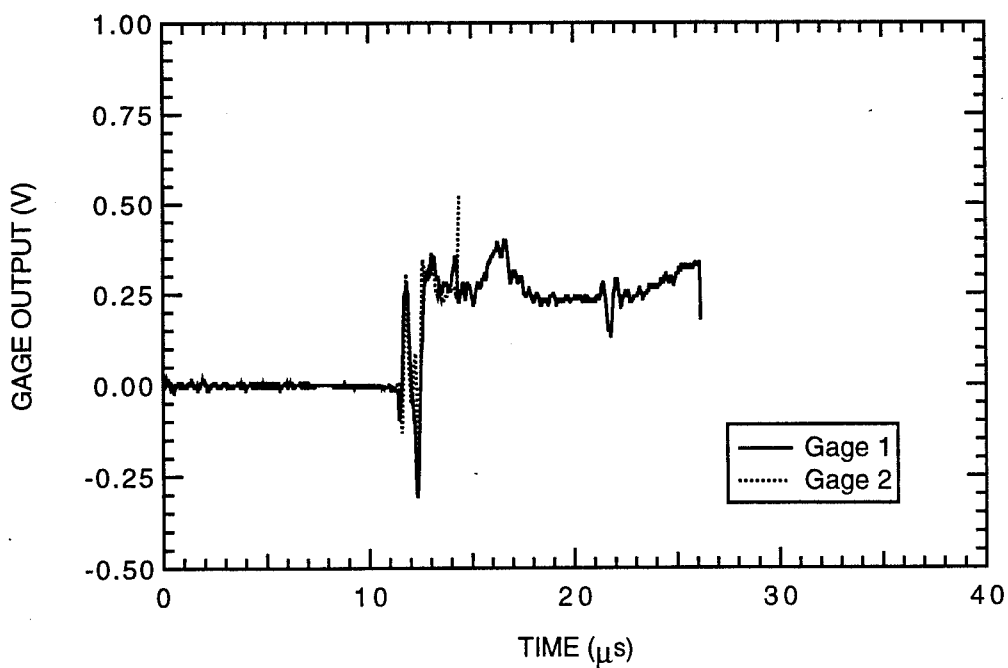


Figure B-18. Output of particle velocity gages at the first gage plane of HPEOS Experiment 4.

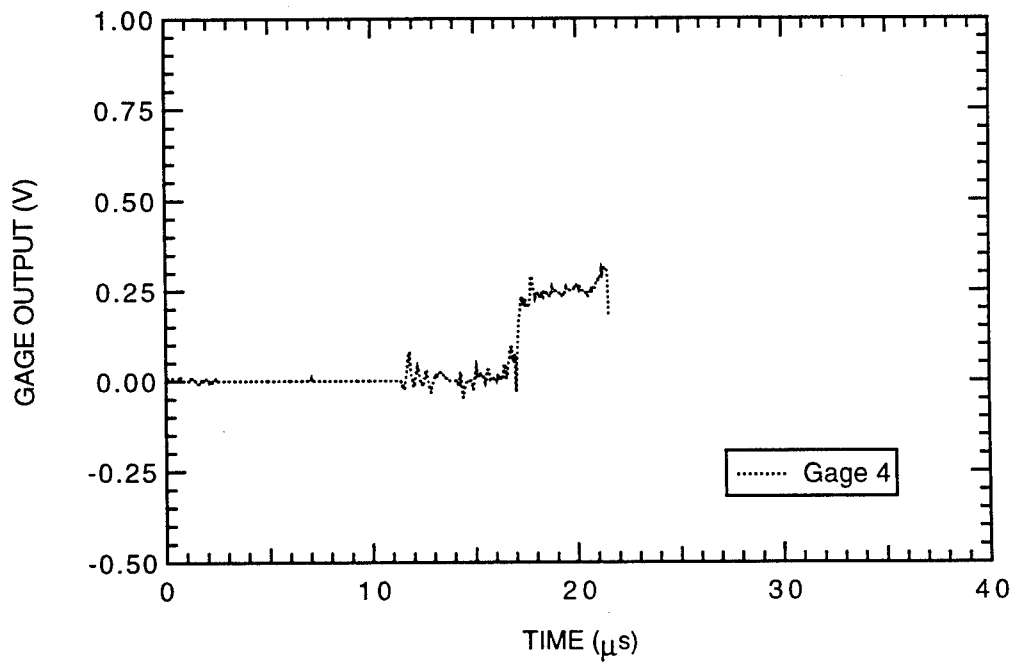


Figure B-19. Output of particle velocity gages at the second gage plane of HPEOS Experiment 4.

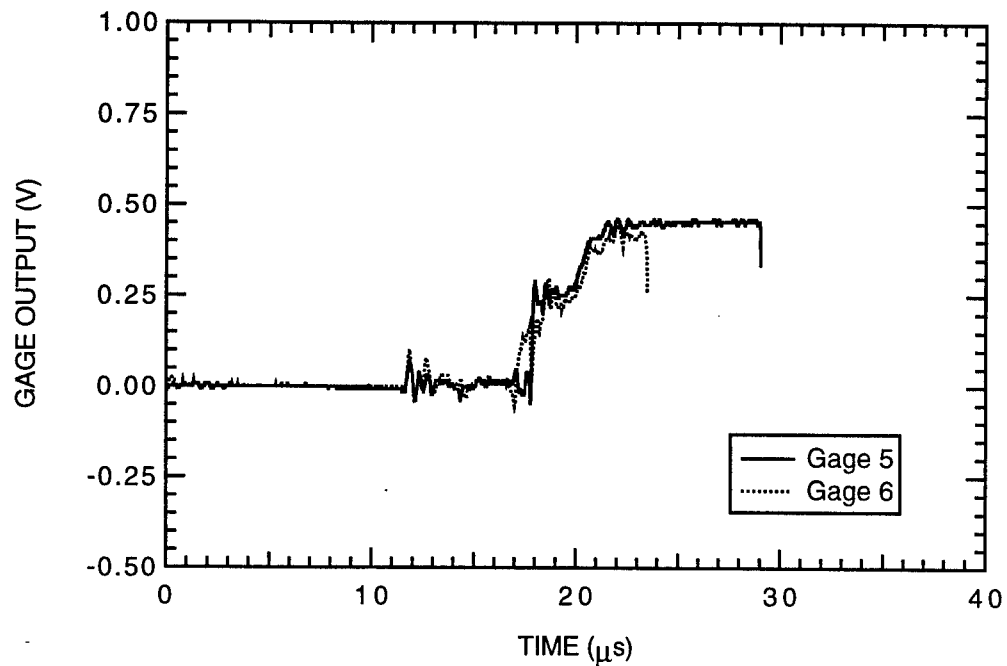


Figure B-20. Output of particle velocity gages at the third gage plane of HPEOS Experiment 4.

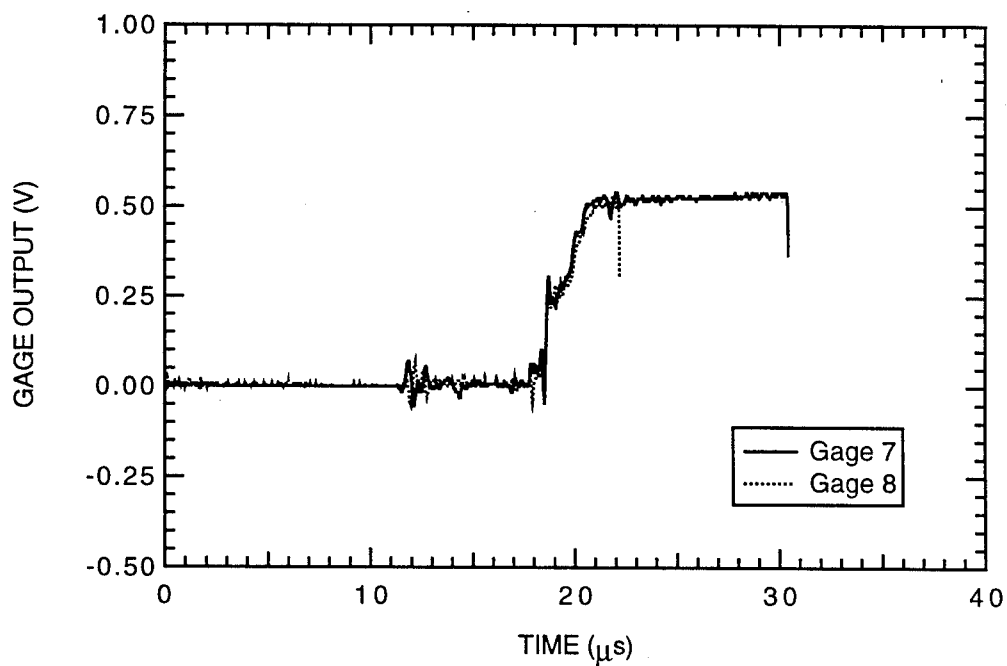


Figure B-21. Output of particle velocity gages at the fourth gage plane of HPEOS Experiment 4.

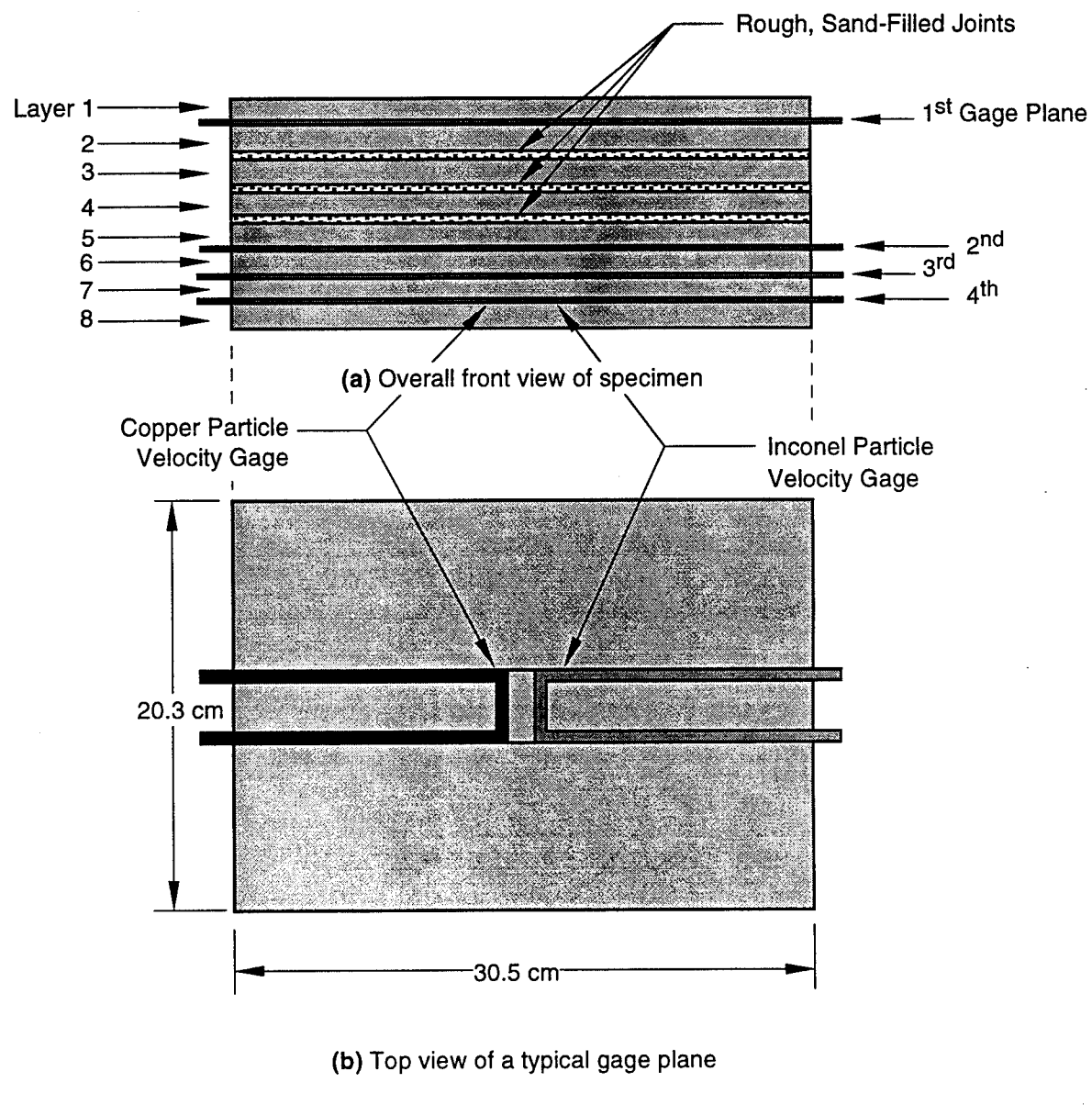


Figure B-22. Specimen configuration and dimensions for HPEOS Experiment 5 (marble).

Note: The explosive system used in the experiment and the thicknesses of the rock layers can be obtained from Table B-1.

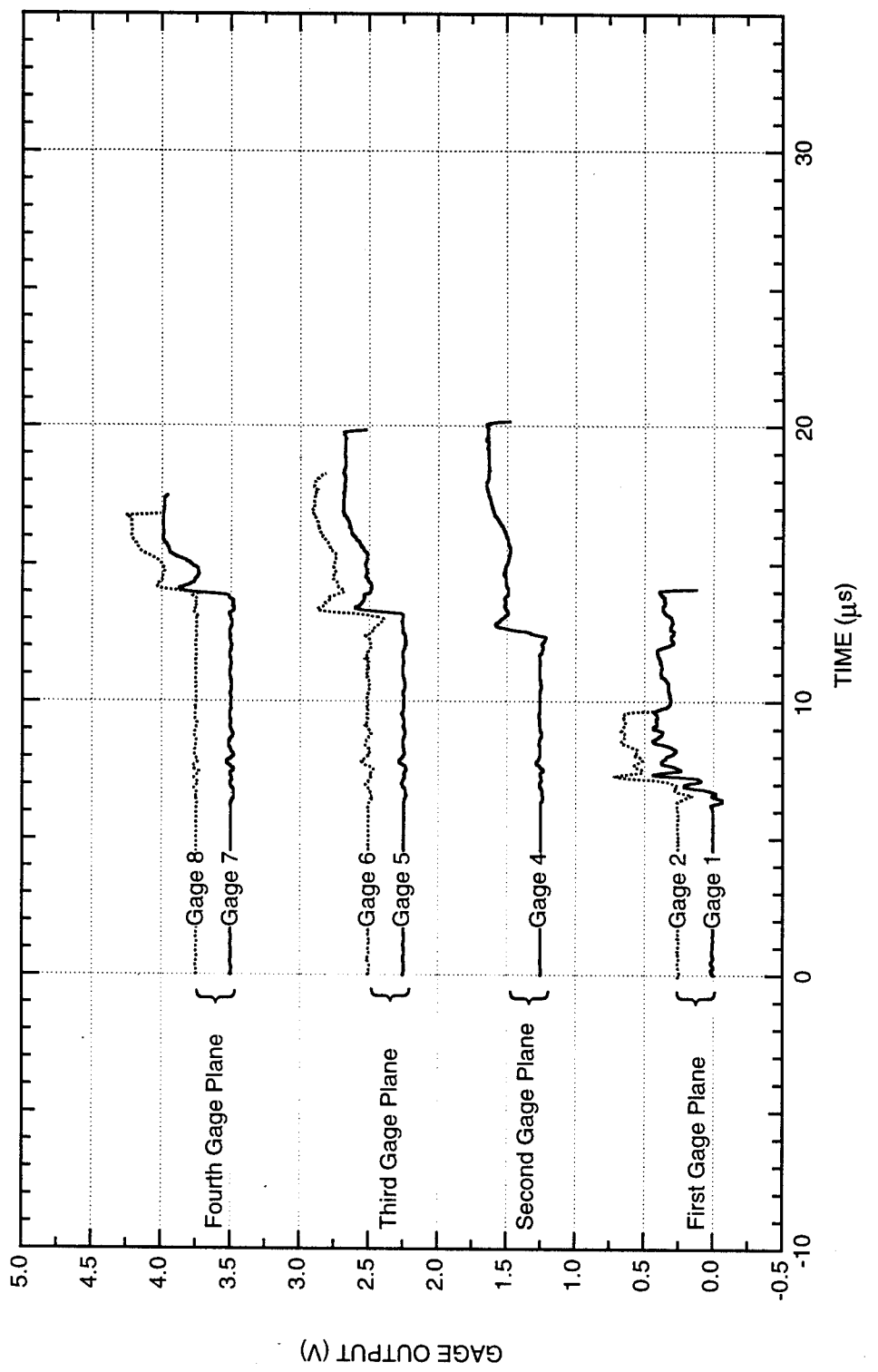


Figure B-23. Summary of the output of all particle velocity gages in HPEOS Experiment 5.

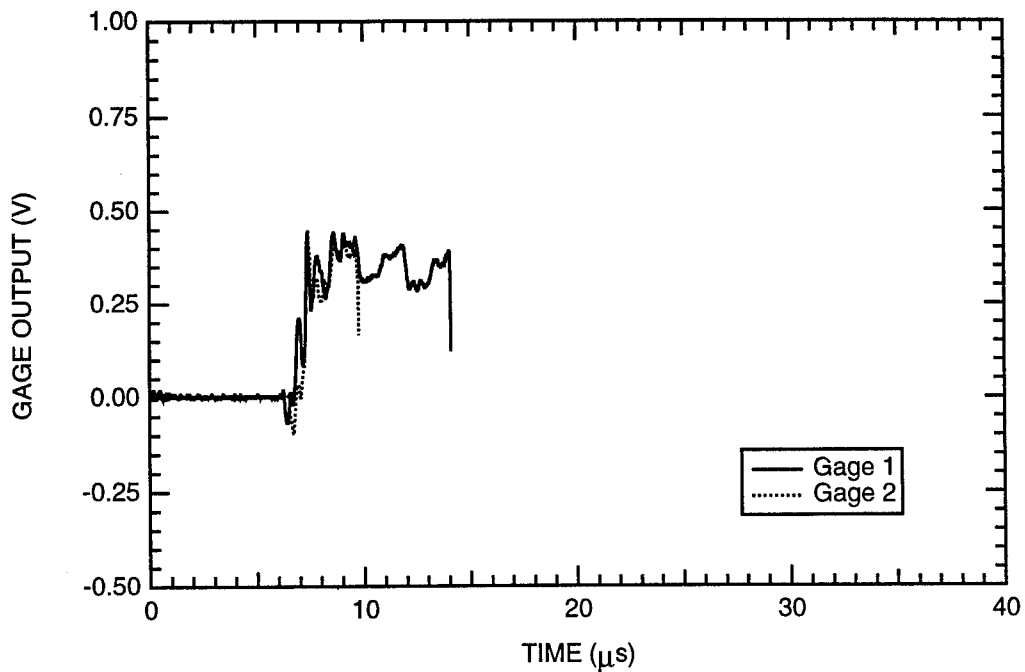


Figure B-24. Output of particle velocity gages at the first gage plane of HPEOS Experiment 5.

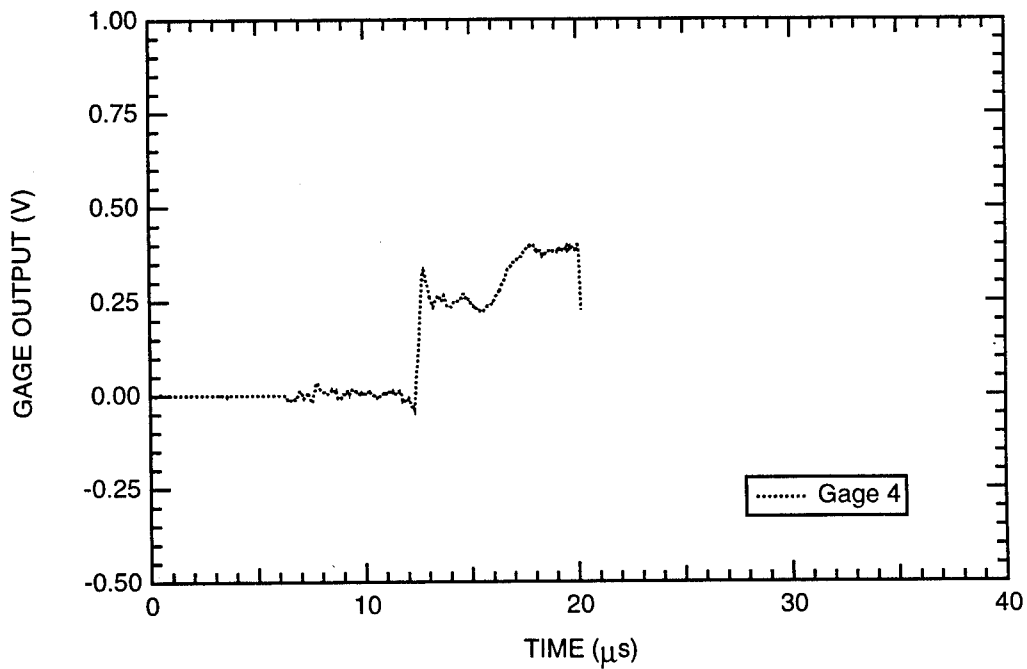


Figure B-25. Output of particle velocity gages at the second gage plane of HPEOS Experiment 5.

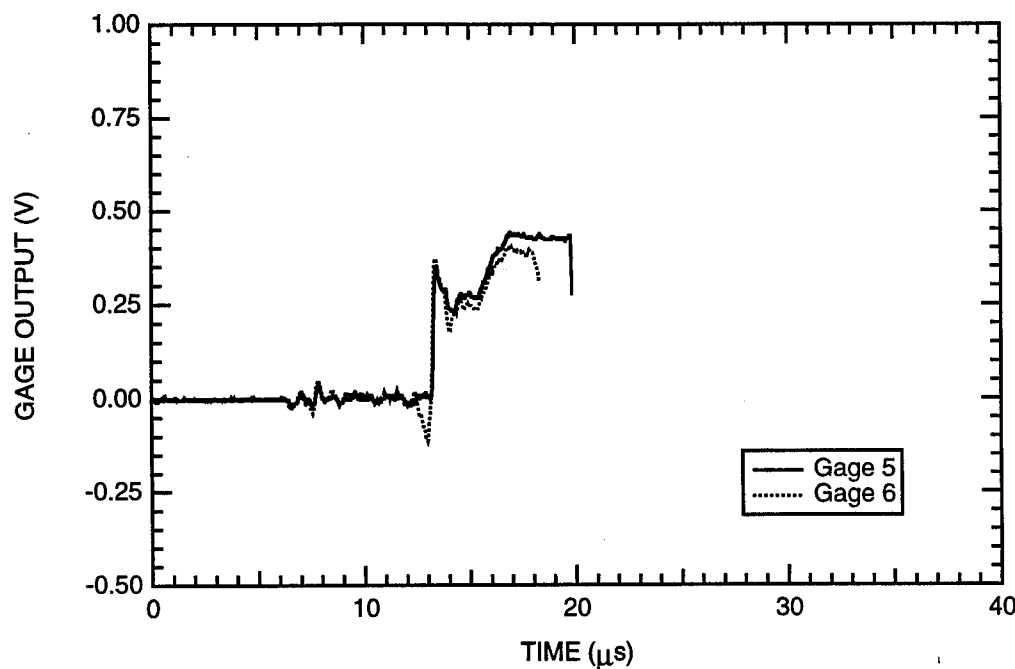


Figure B-26. Output of particle velocity gages at the third gage plane of HPEOS Experiment 5.

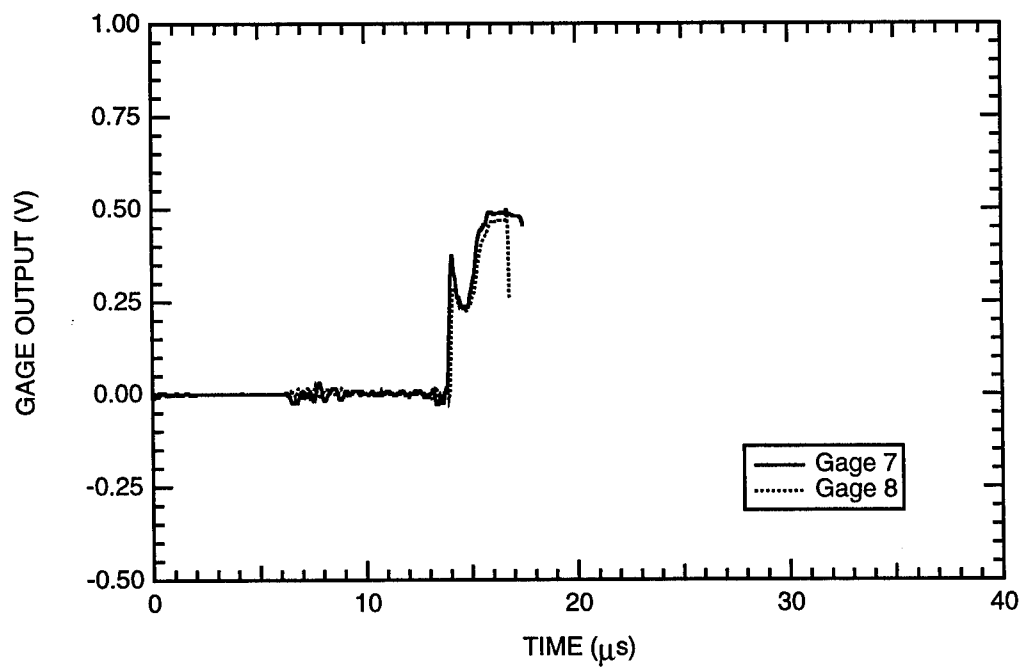


Figure B-27. Output of particle velocity gages at the fourth gage plane of HPEOS Experiment 5.

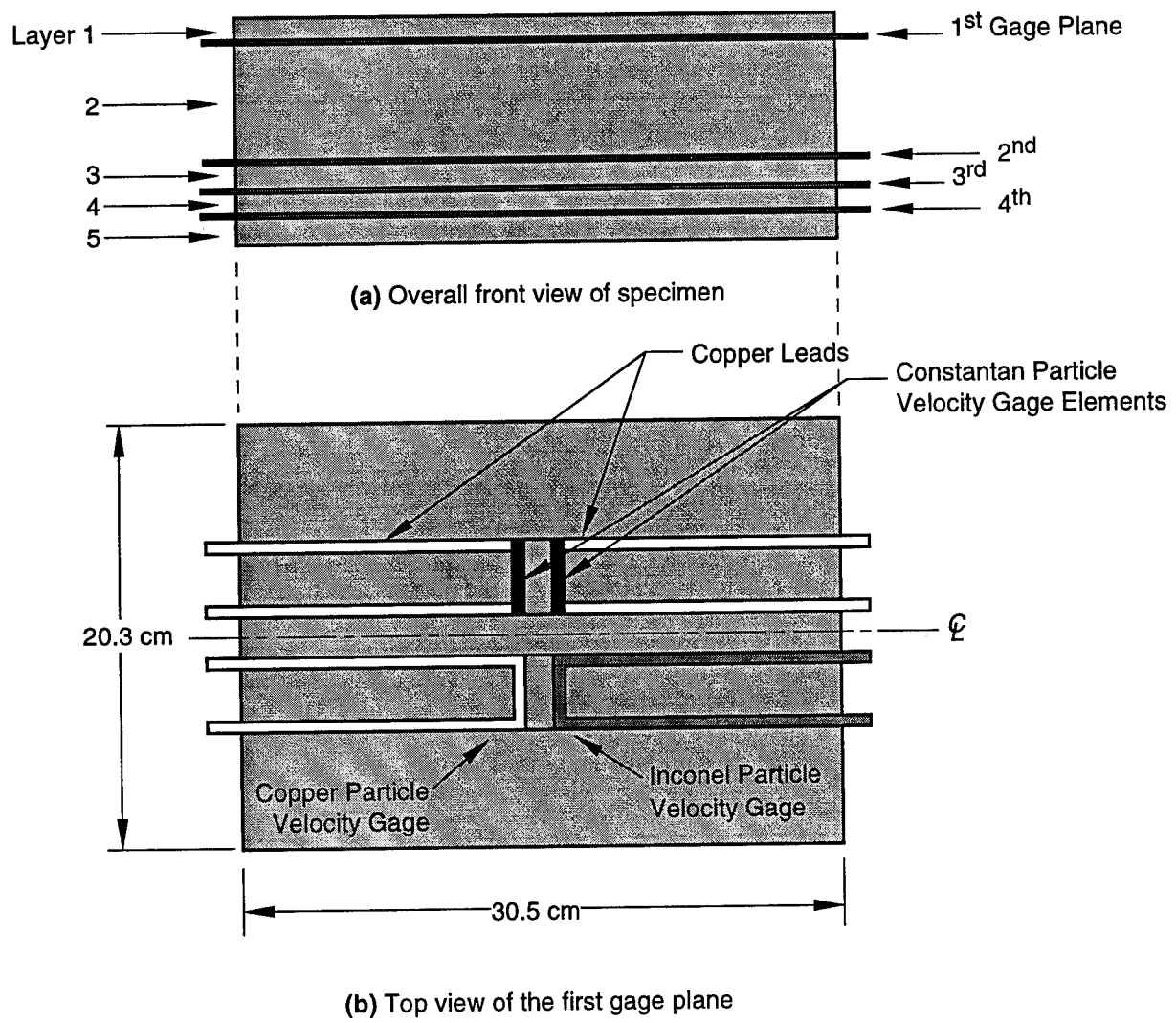


Figure B-28. Specimen configuration and dimensions for HPEOS Experiment 6 (marble).

Note: The explosive system used in the experiment and the thicknesses of the rock layers can be obtained from Table B-1.

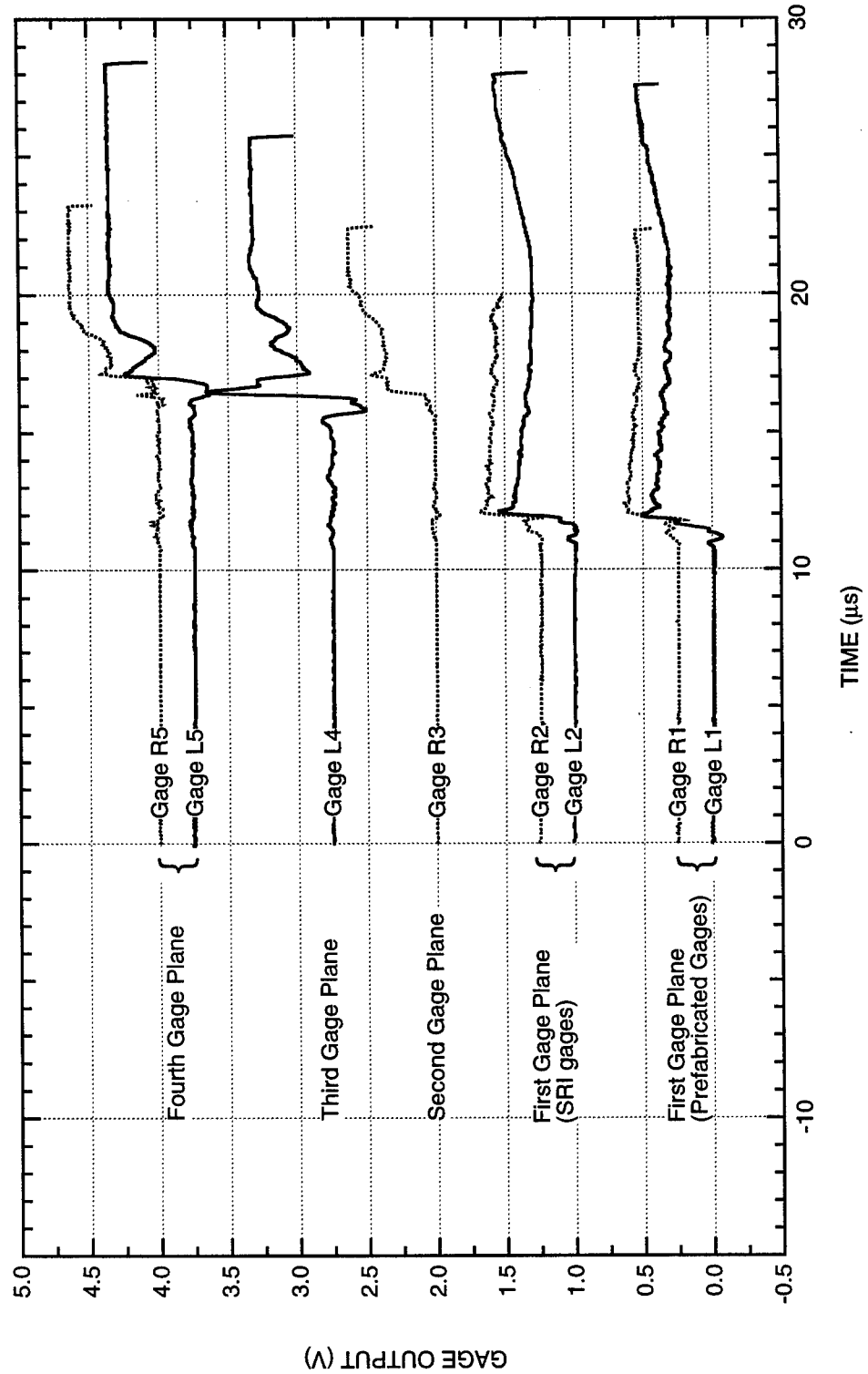


Figure B-29. Summary of the output of all particle velocity gages in HPEOS Experiment 6.

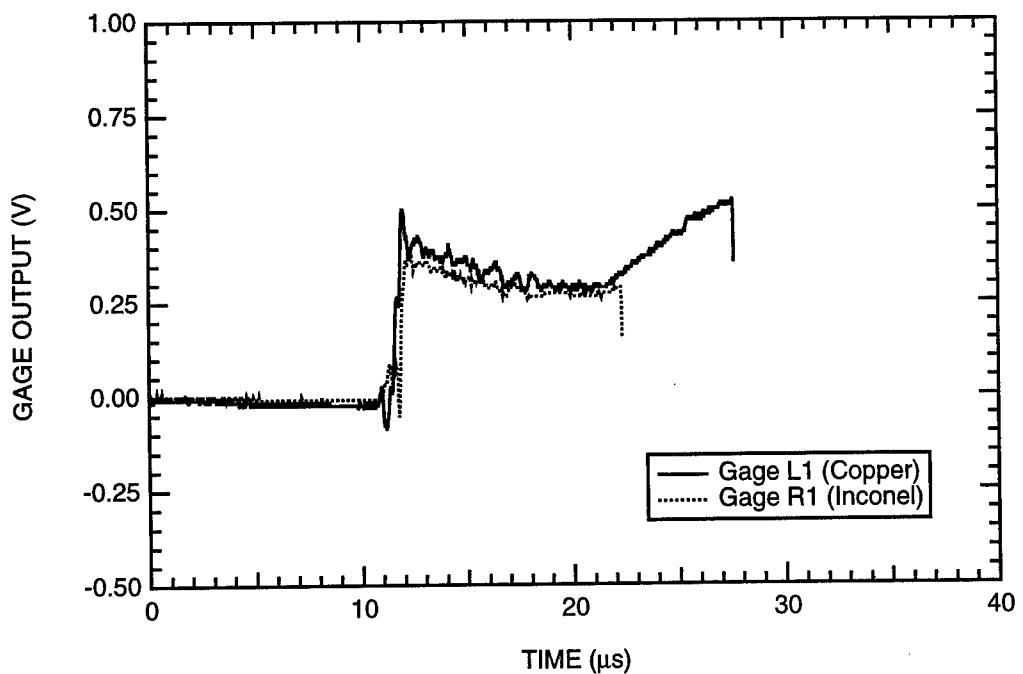


Figure B-30. Output of prefabricated particle velocity gages at the first gage plane of HPEOS Experiment 6.

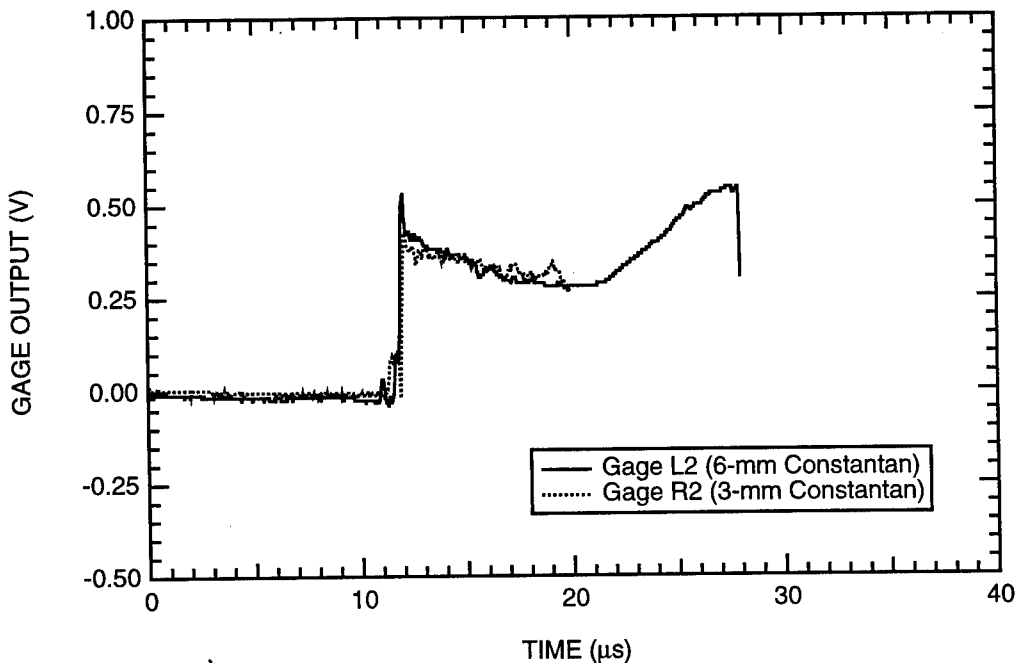


Figure B-31. Output of SRI-manufactured particle velocity gages at the first gage plane of HPEOS Experiment 6.

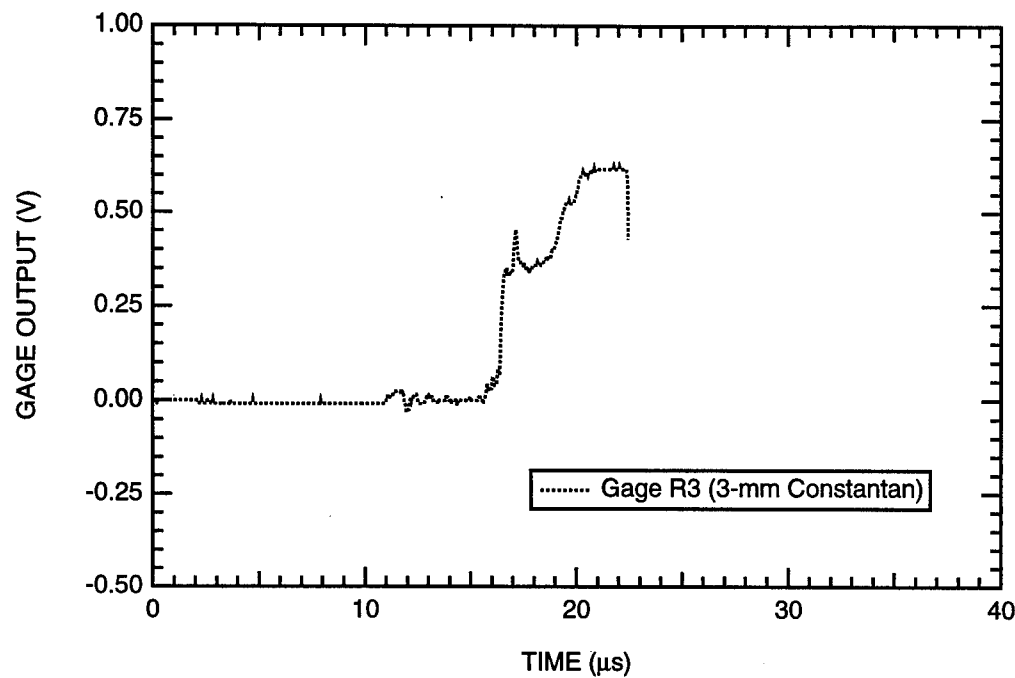


Figure B-32. Output of SRI-manufactured particle velocity gages at the second gage plane of HPEOS Experiment 6.

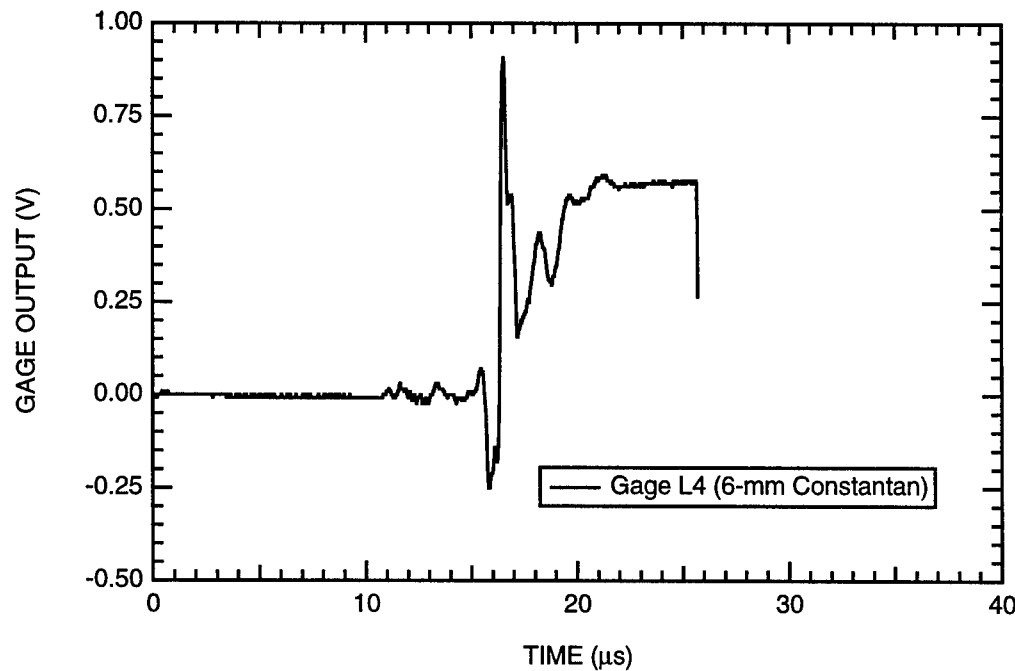


Figure B-33. Output of SRI-manufactured particle velocity gages at the third gage plane of HPEOS Experiment 6.

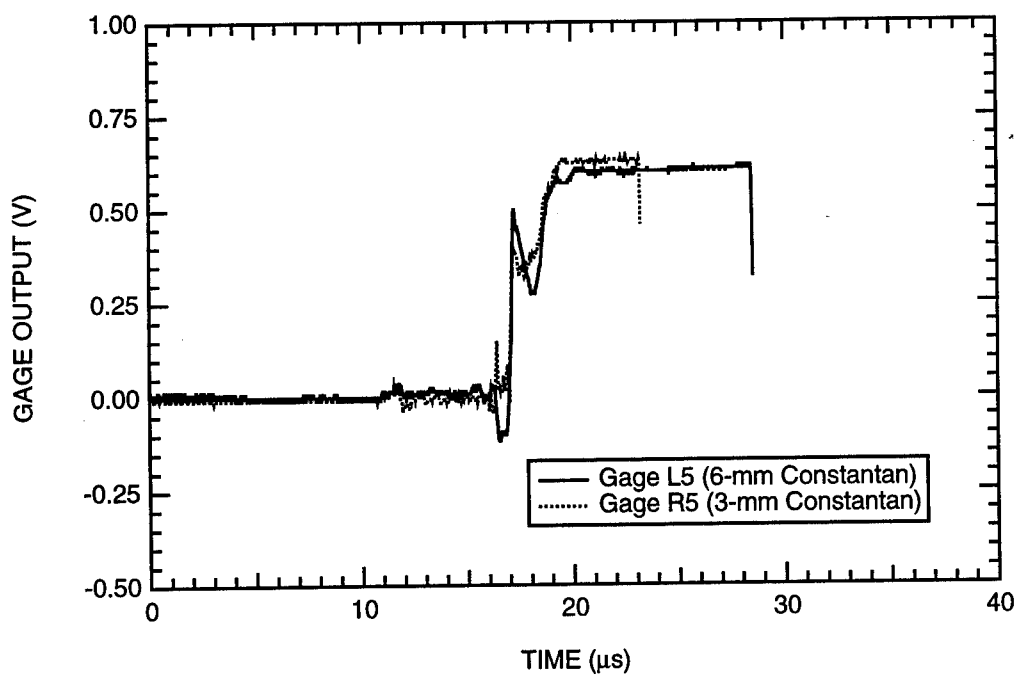


Figure B-34. Output of SRI-manufactured particle velocity gages at the fourth gage plane of HPEOS Experiment 6.

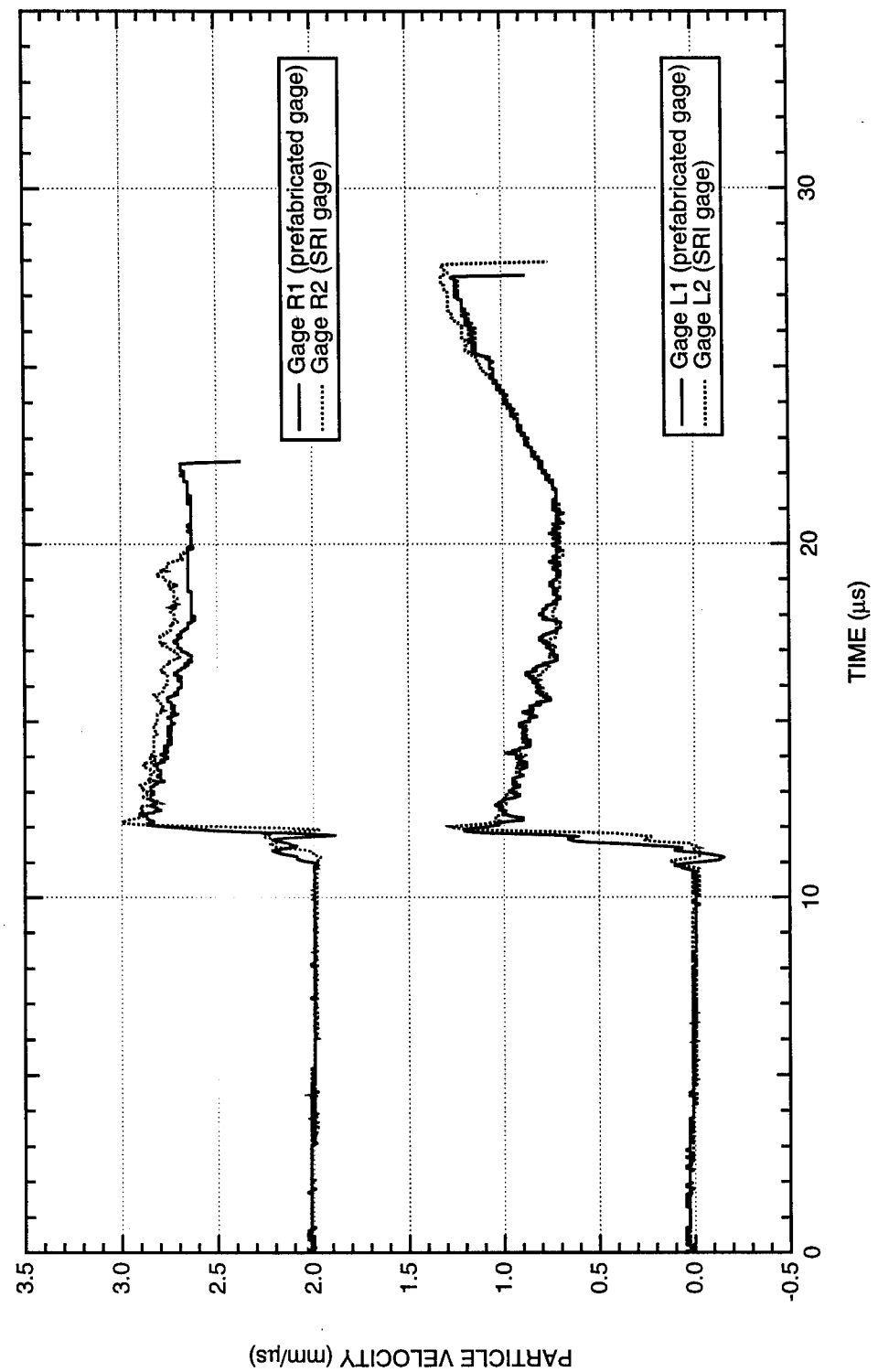


Figure B-35. Comparison of the output of prefabricated and SRI-manufactured particle velocity gages in HPEOS Experiment 6 (data for the first gage plane).

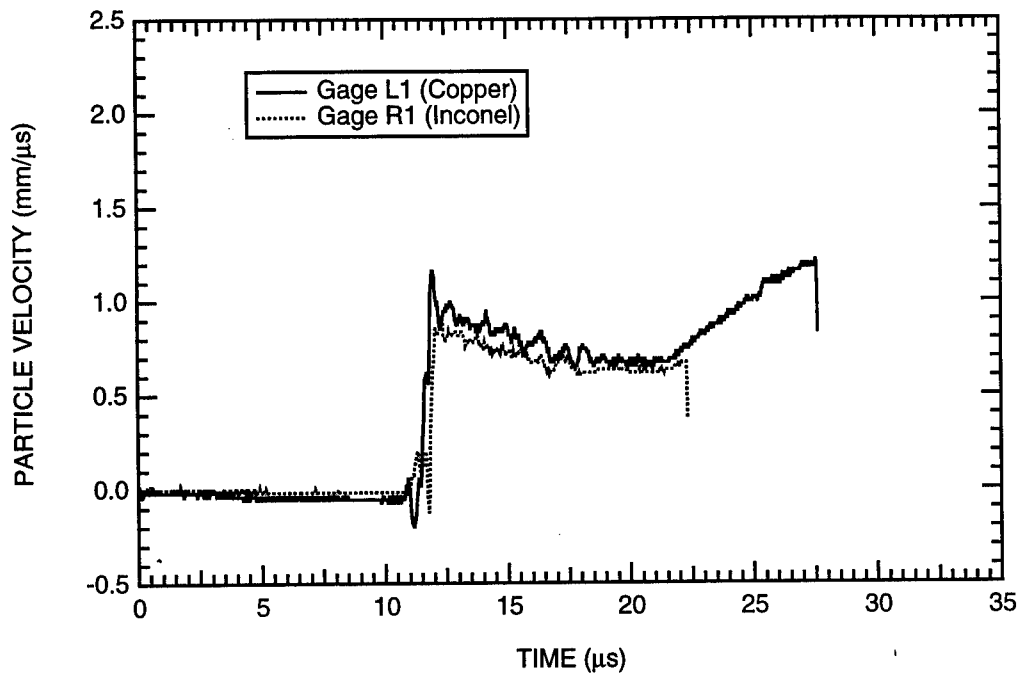


Figure B-36. Particle velocity histories at the first gage plane of HPEOS Experiment 6 (prefabricated gages).

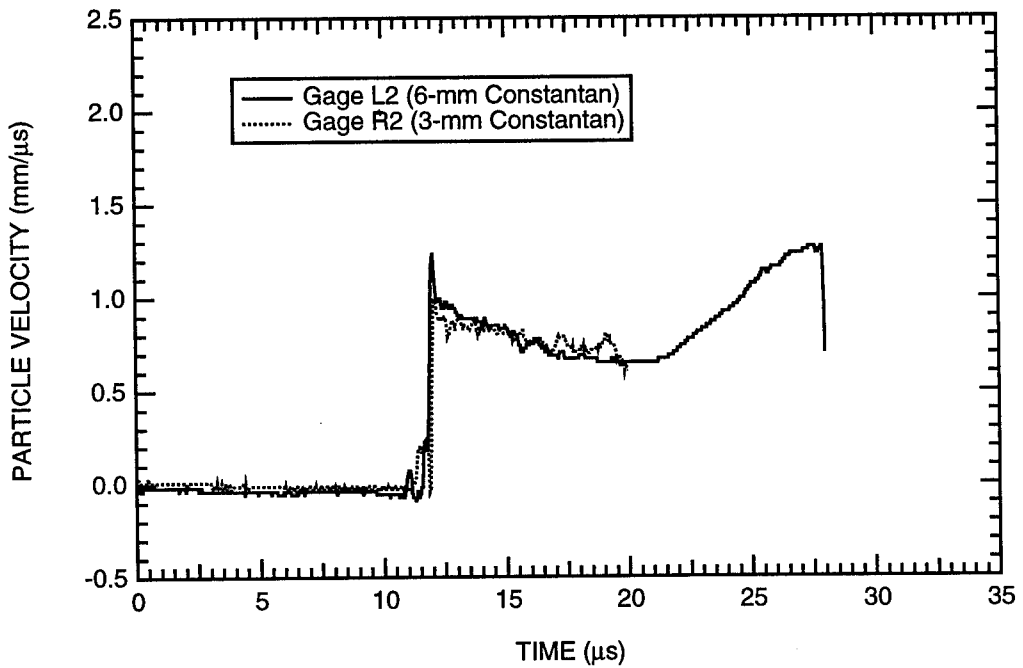


Figure B-37. Particle velocity histories at the first gage plane of HPEOS Experiment 6 (SRI-manufactured gages).

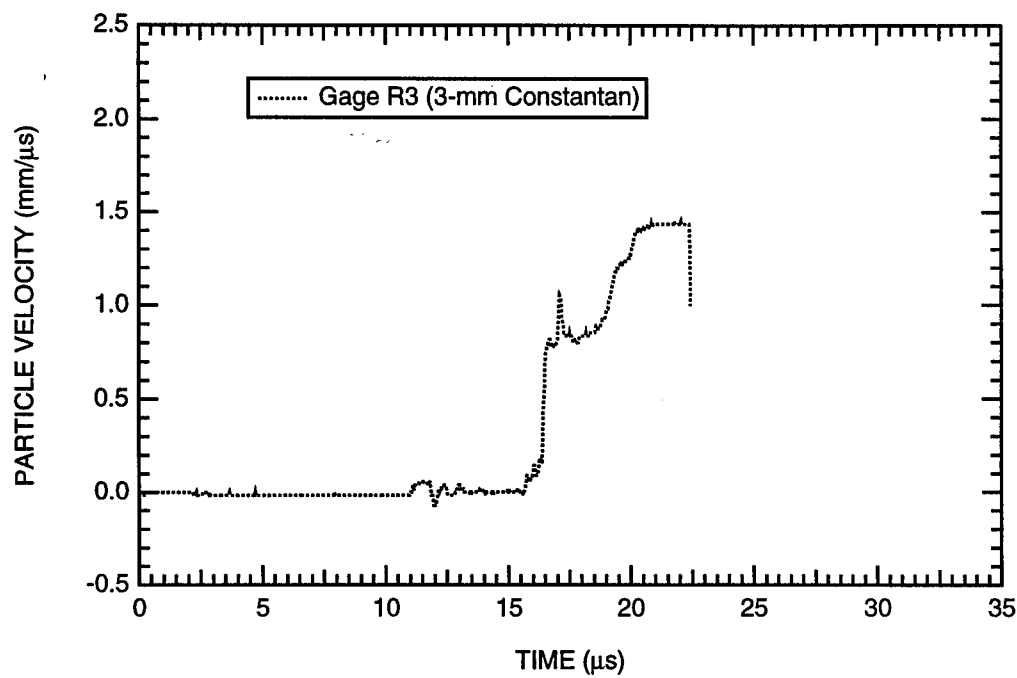


Figure B-38. Particle velocity histories at the second gage plane of HPEOS Experiment 6 (SRI-manufactured gages).

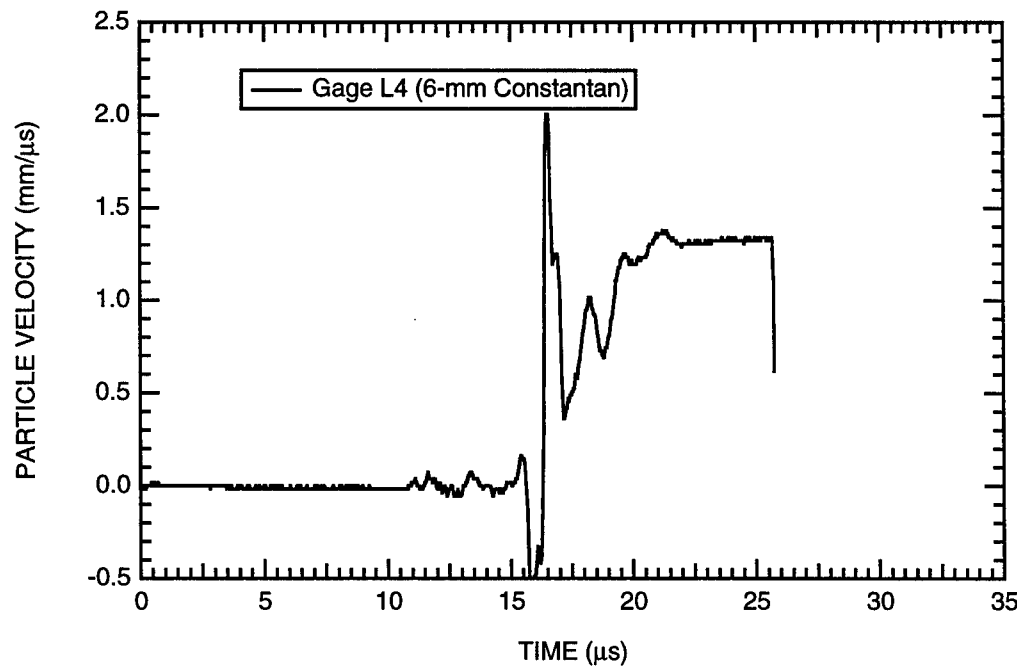


Figure B-39. Particle velocity histories at the third gage plane of HPEOS Experiment 6 (SRI-manufactured gages).

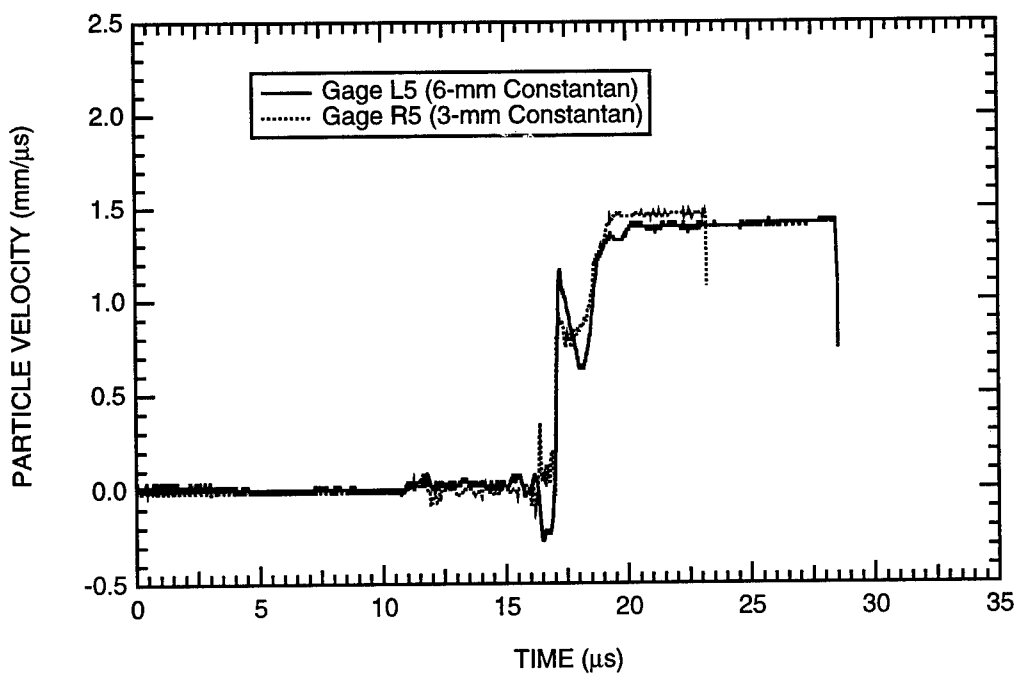


Figure B-40. Particle velocity histories at the fourth gage plane of HPEOS Experiment 6 (SRI-manufactured gages).

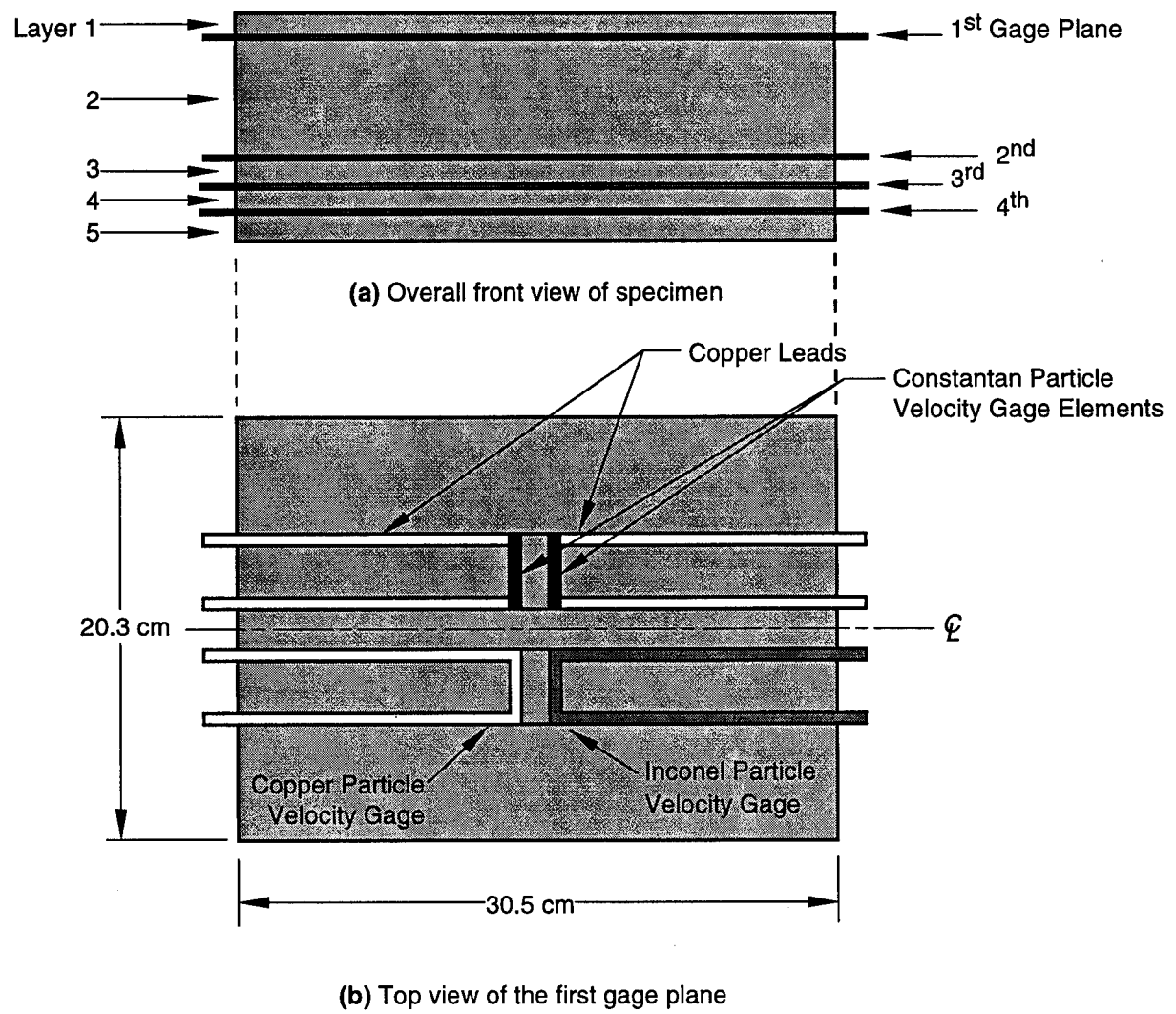


Figure B-41. Specimen configuration and dimensions for HPEOS Experiment 7 (marble).

Note: The explosive system used in the experiment and the thicknesses of the rock layers can be obtained from Table B-1.

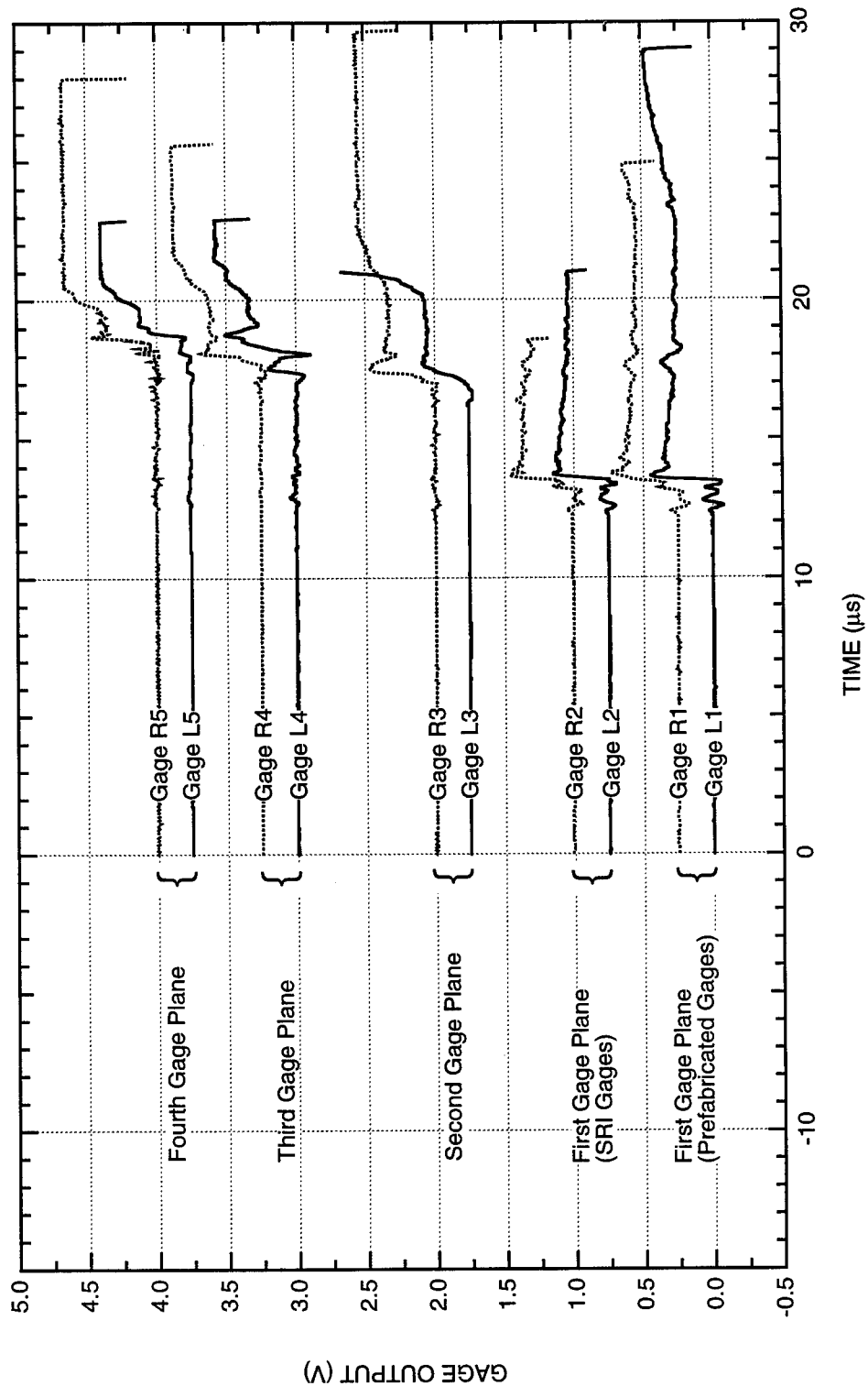


Figure B-42. Summary of the output of all particle velocity gages in HPEOS Experiment 7.

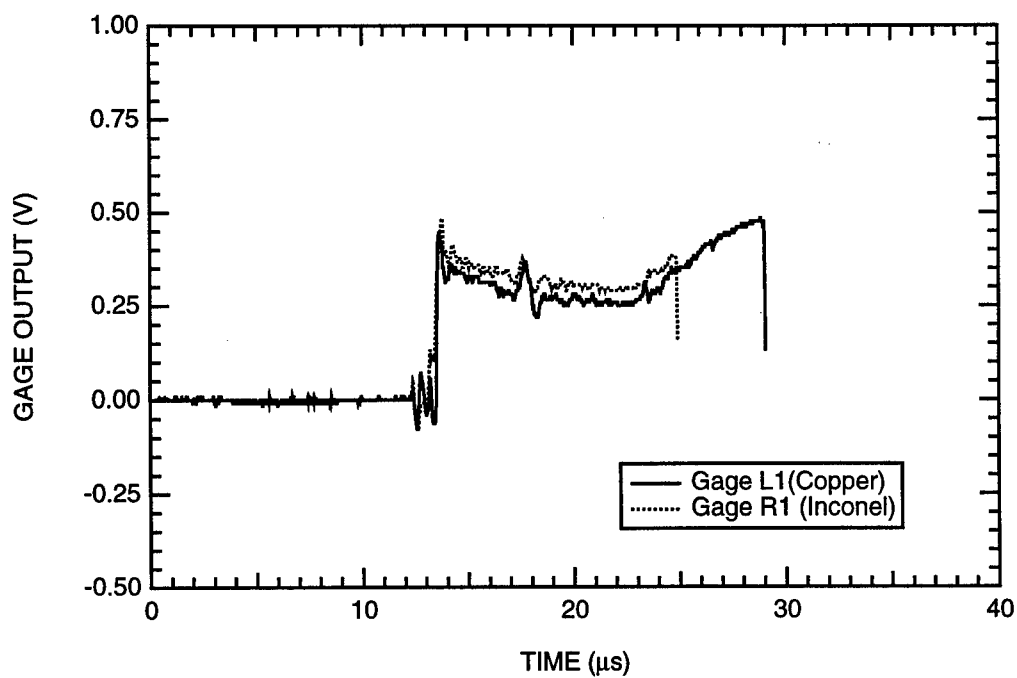


Figure B-43. Output of prefabricated particle velocity gages at the first gage plane of HPEOS Experiment 7.

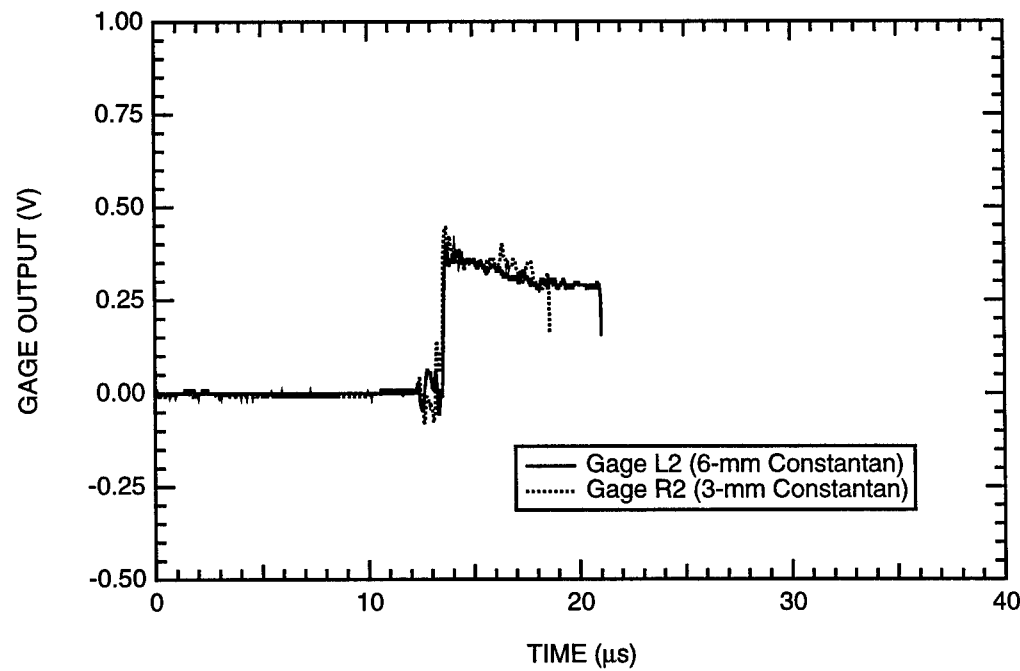


Figure B-44. Output of SRI-manufactured particle velocity gages at the first gage plane of HPEOS Experiment 7.

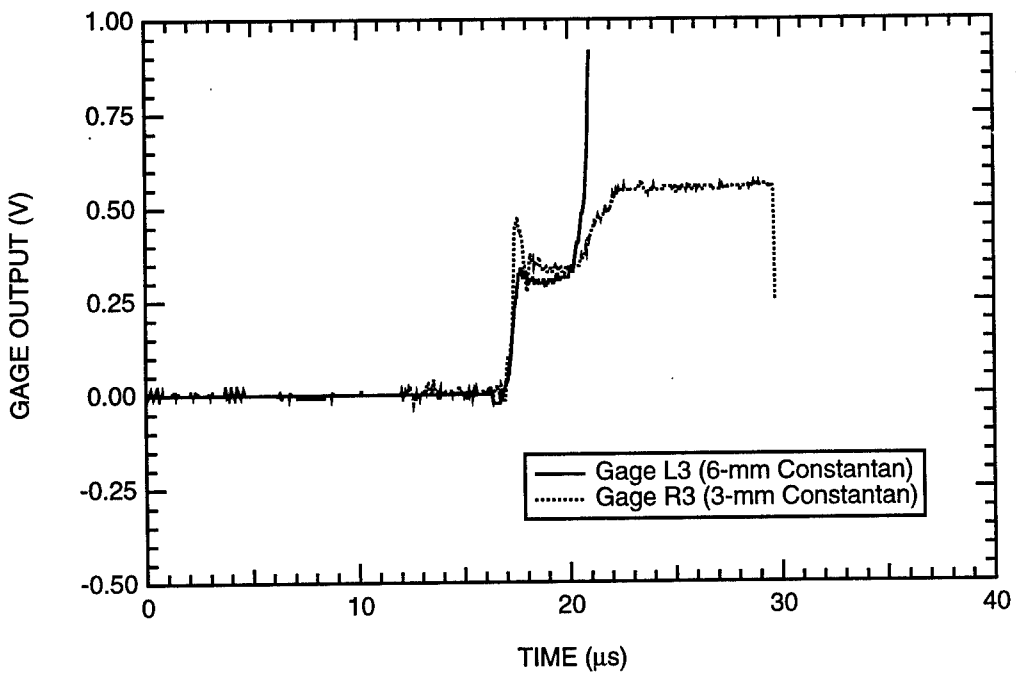


Figure B-45. Output of SRI-manufactured particle velocity gages at the second gage plane of HPEOS Experiment 7.

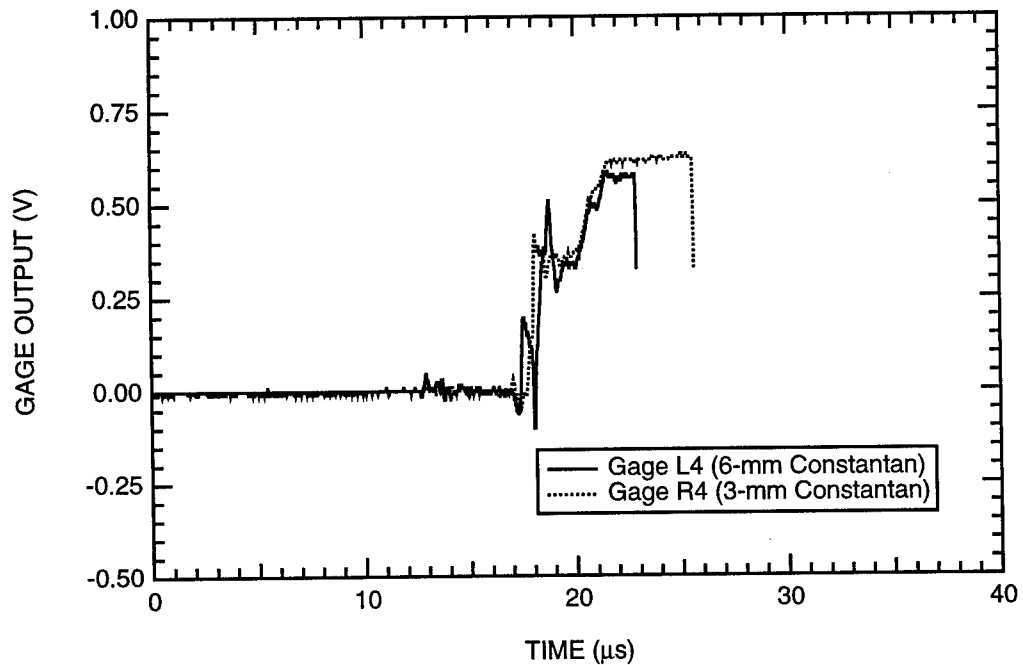


Figure B-46. Output of SRI-manufactured particle velocity gages at the third gage plane of HPEOS Experiment 7.

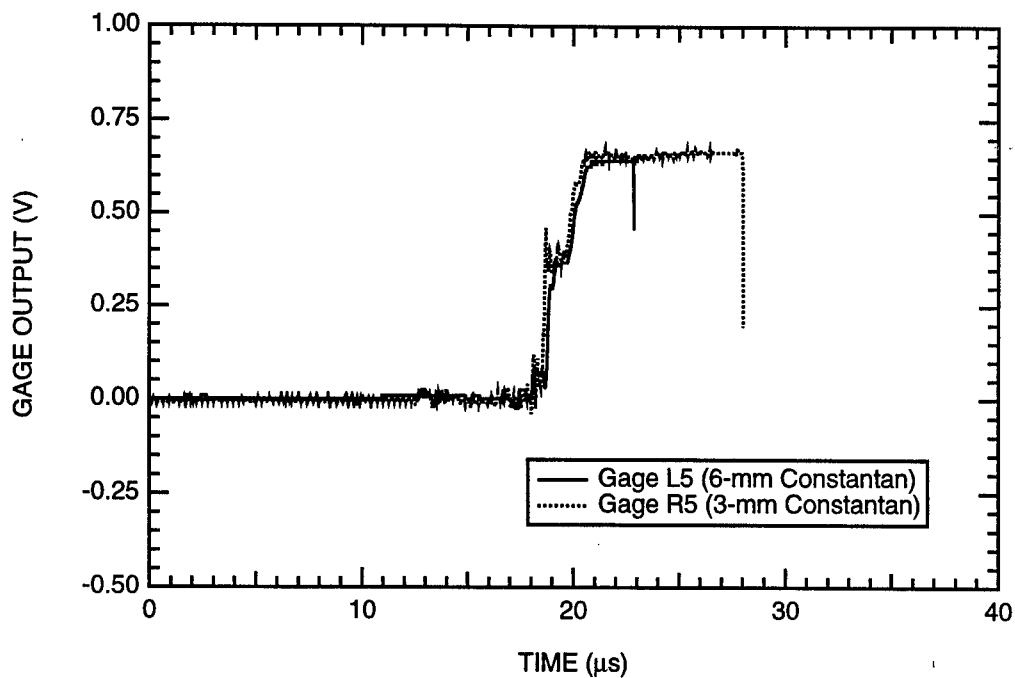


Figure B-47. Output of SRI-manufactured particle velocity gages at the fourth gage plane of HPEOS Experiment 7.

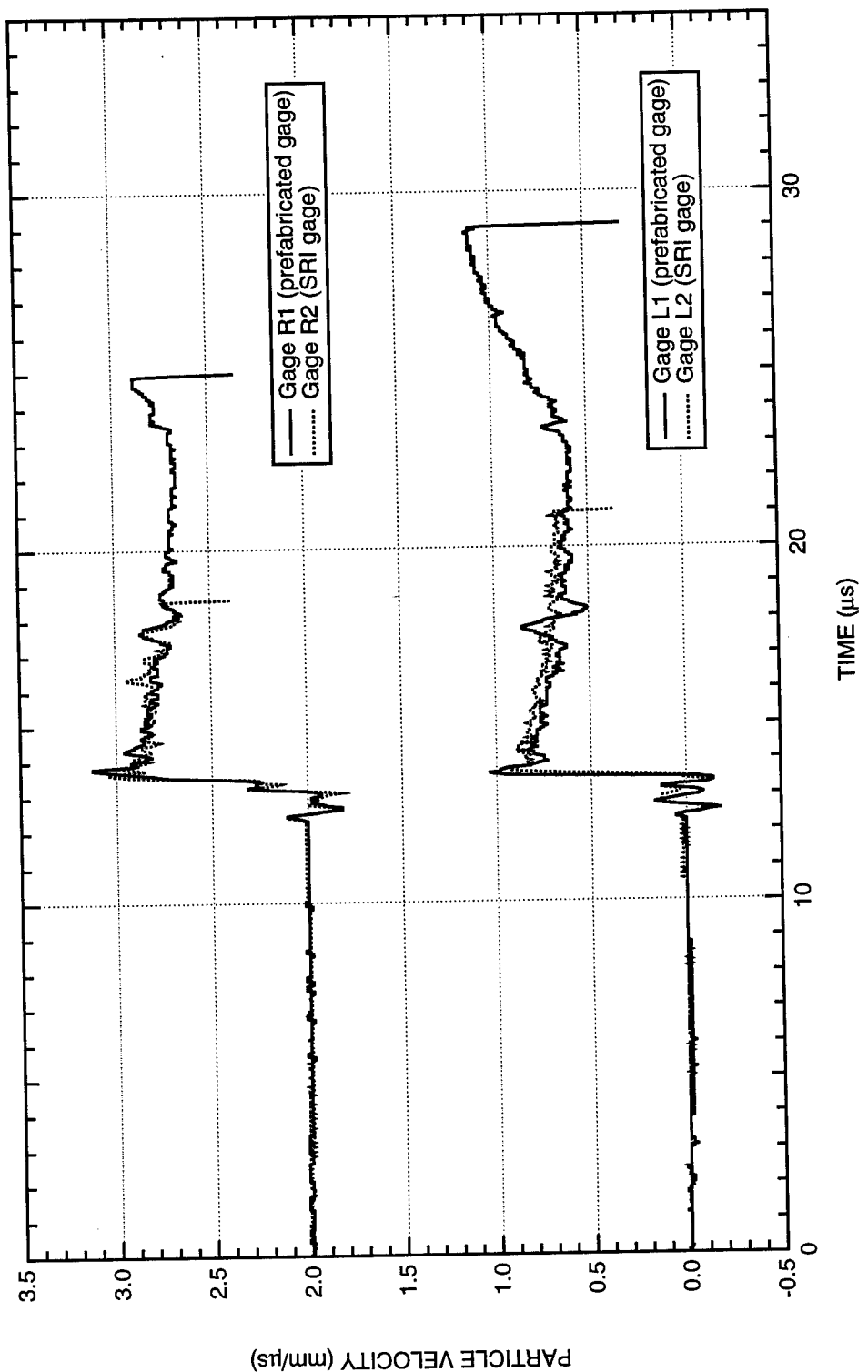


Figure B-48. Comparison of the output of prefabricated and SRI-manufactured particle velocity gages in HPEOS Experiment 7  
(data for the first gage plane).

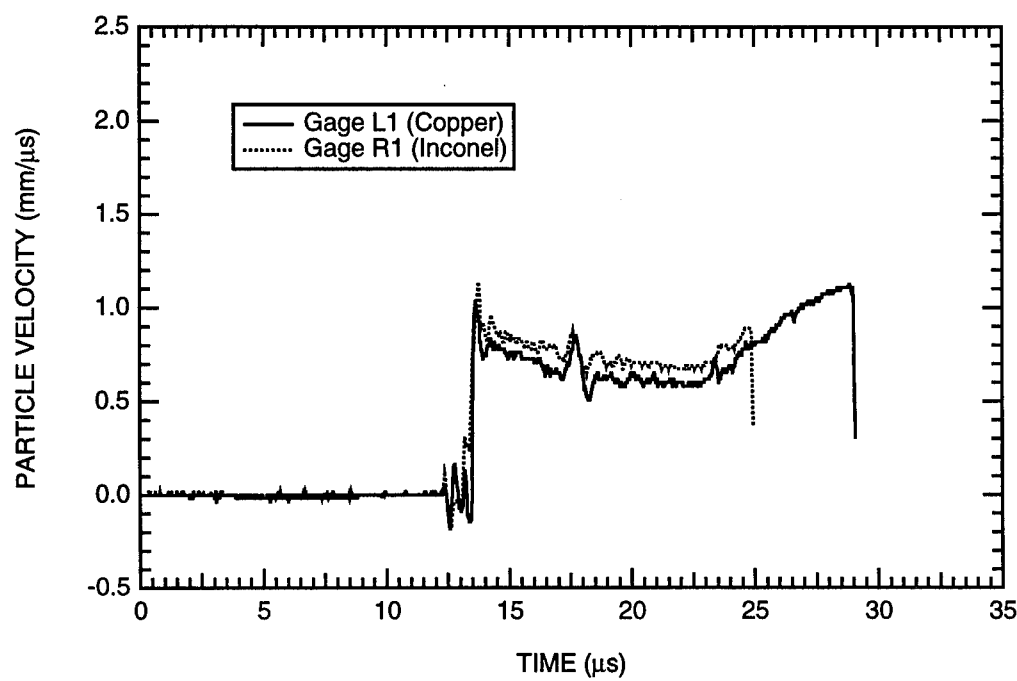


Figure B-49. Particle velocity histories at the first gage plane of HPEOS Experiment 7 (prefabricated gages).

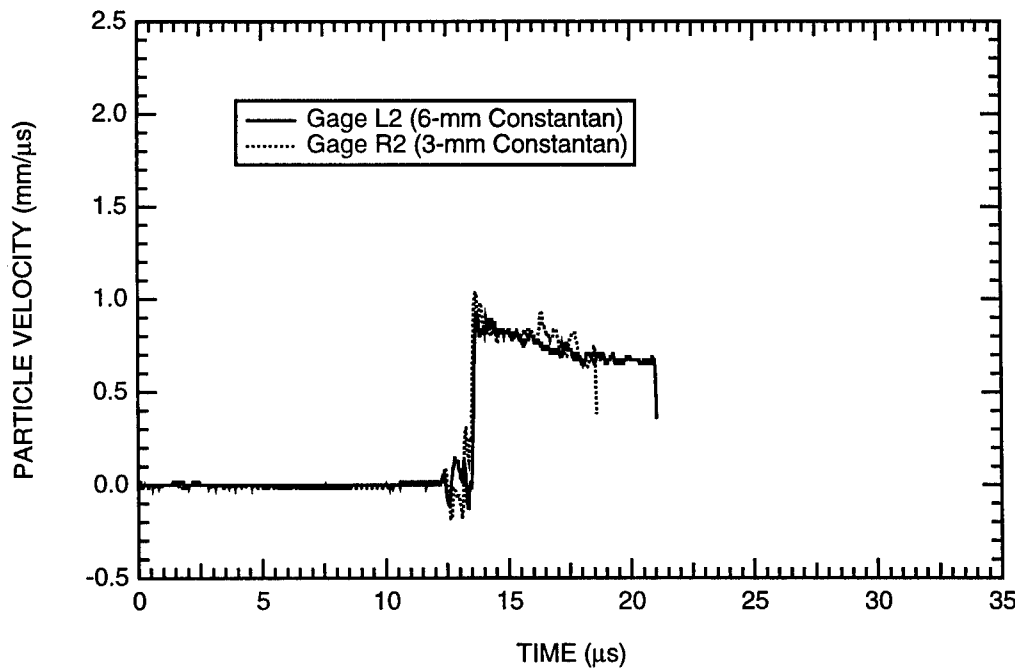


Figure B-50. Particle velocity histories at the first gage plane of HPEOS Experiment 7 (SRI-manufactured gages).

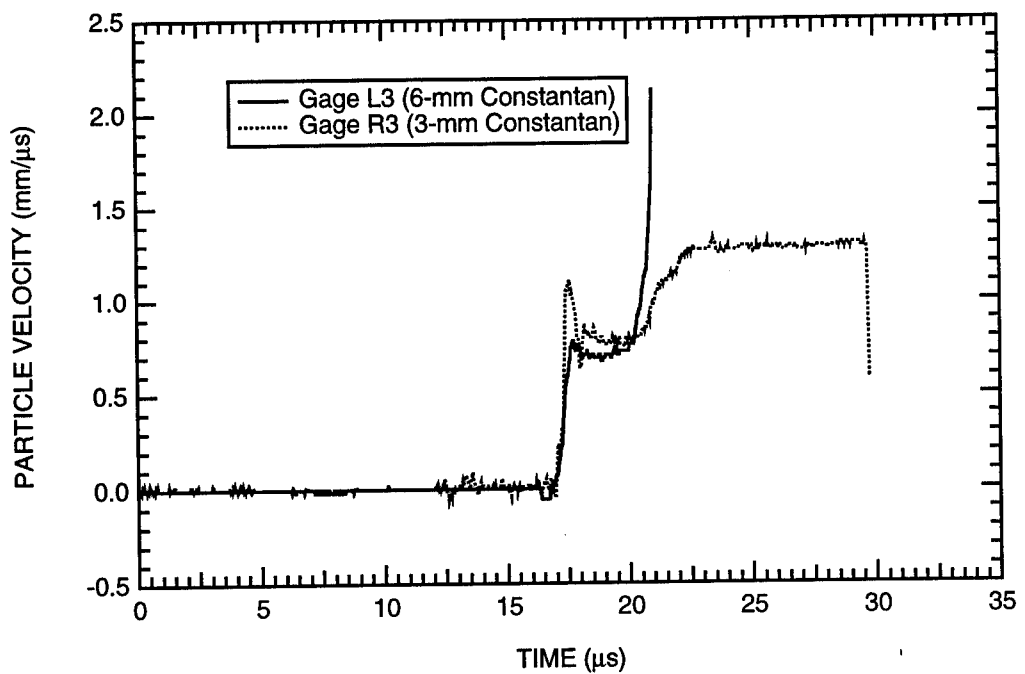


Figure B-51. Particle velocity histories at the second gage plane of HPEOS Experiment 7 (SRI-manufactured gages).

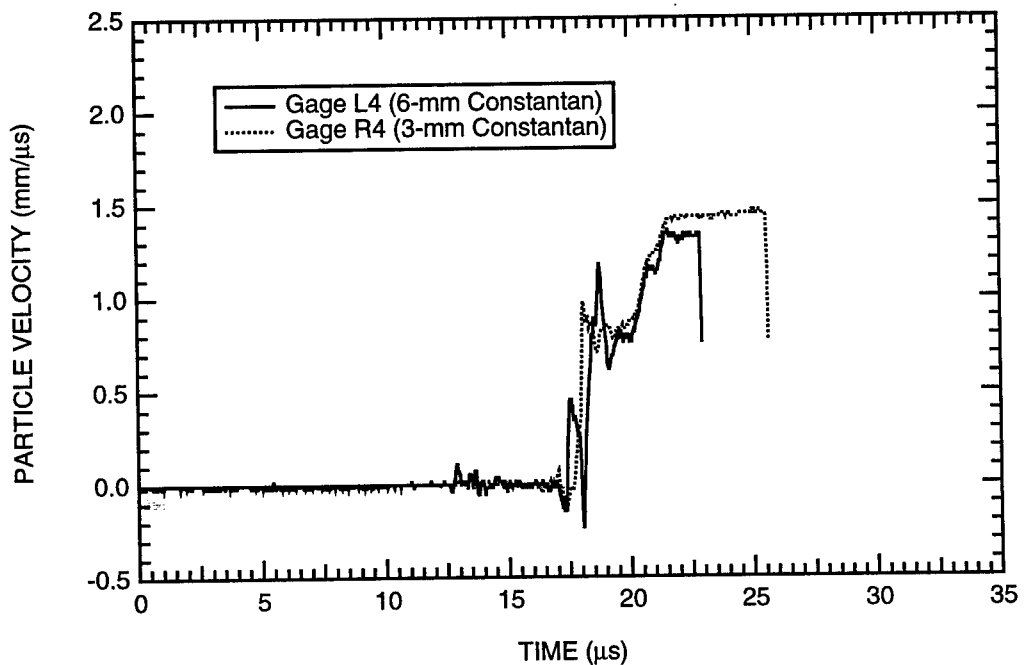


Figure B-52. Particle velocity histories at the third gage plane of HPEOS Experiment 7 (SRI-manufactured gages).

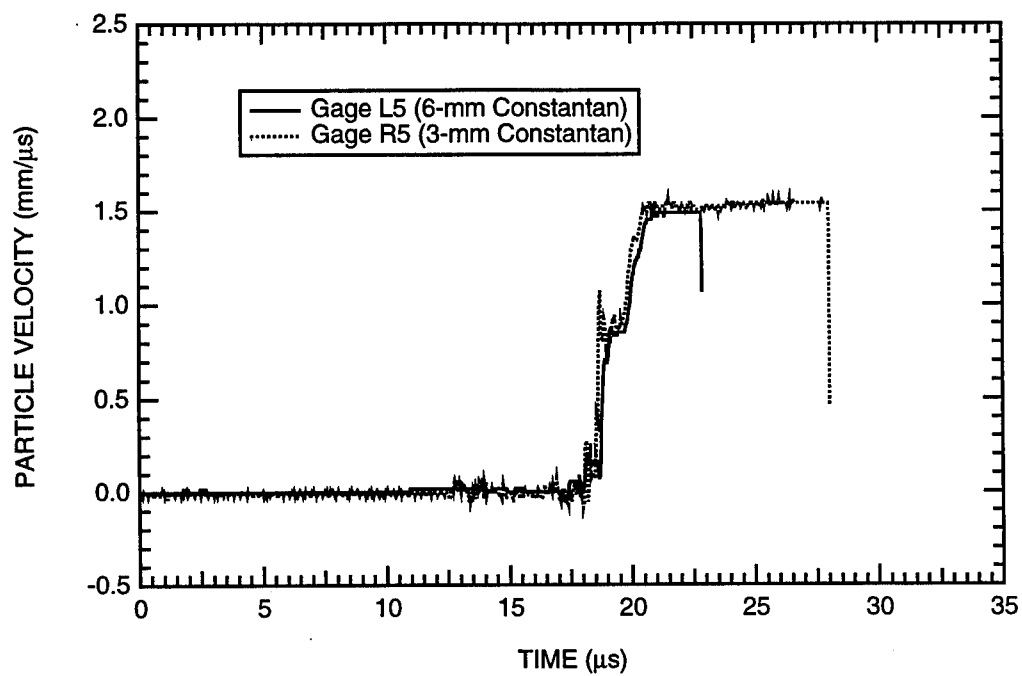


Figure B-53. Particle velocity histories at the fourth gage plane of HPEOS Experiment 7 (SRI-manufactured gages).

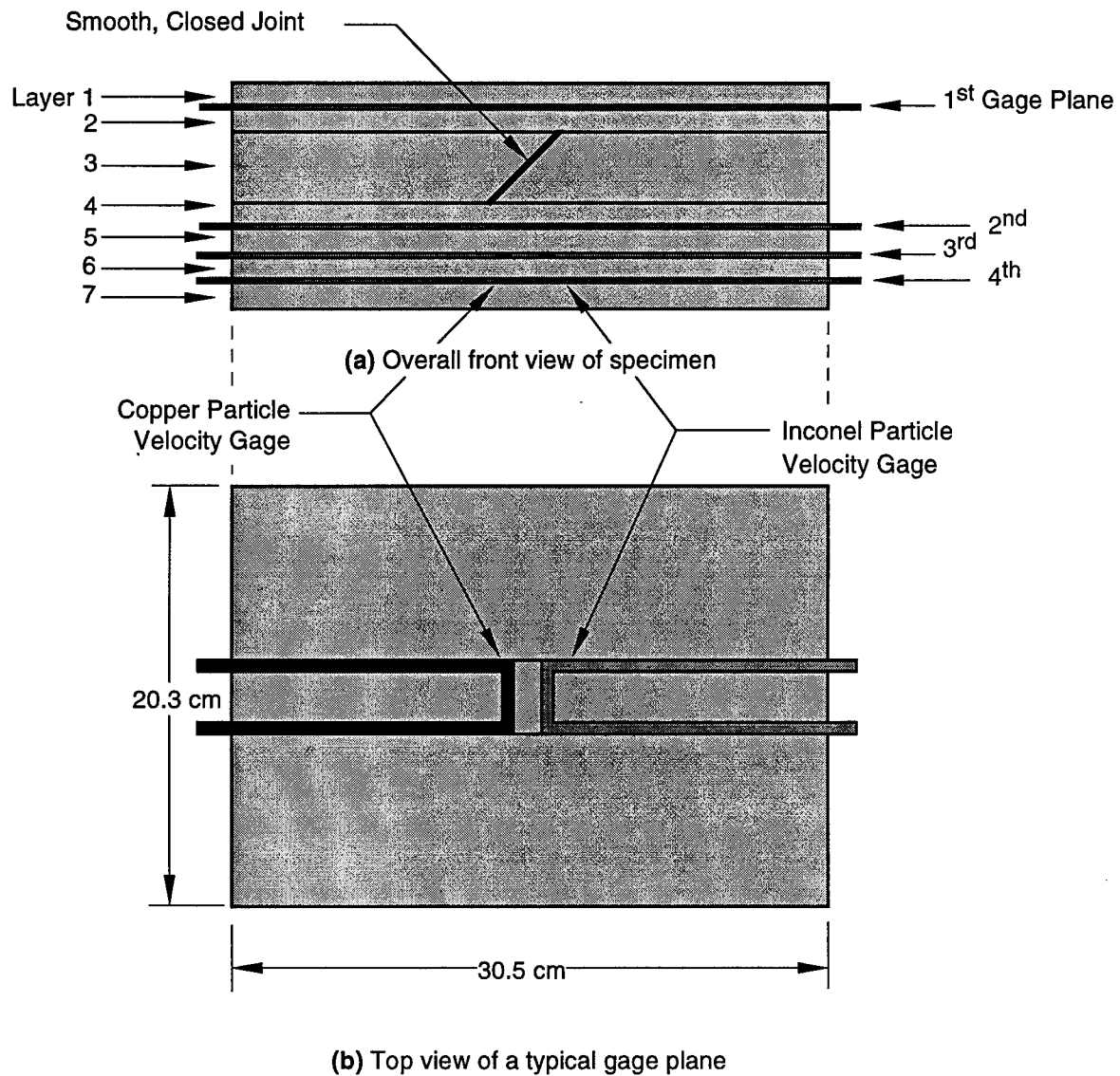


Figure B-54. Specimen configuration and dimensions for HPEOS Experiment 8 (marble).

Note: The explosive system used in the experiment and the thicknesses of the rock layers can be obtained from Table B-1.

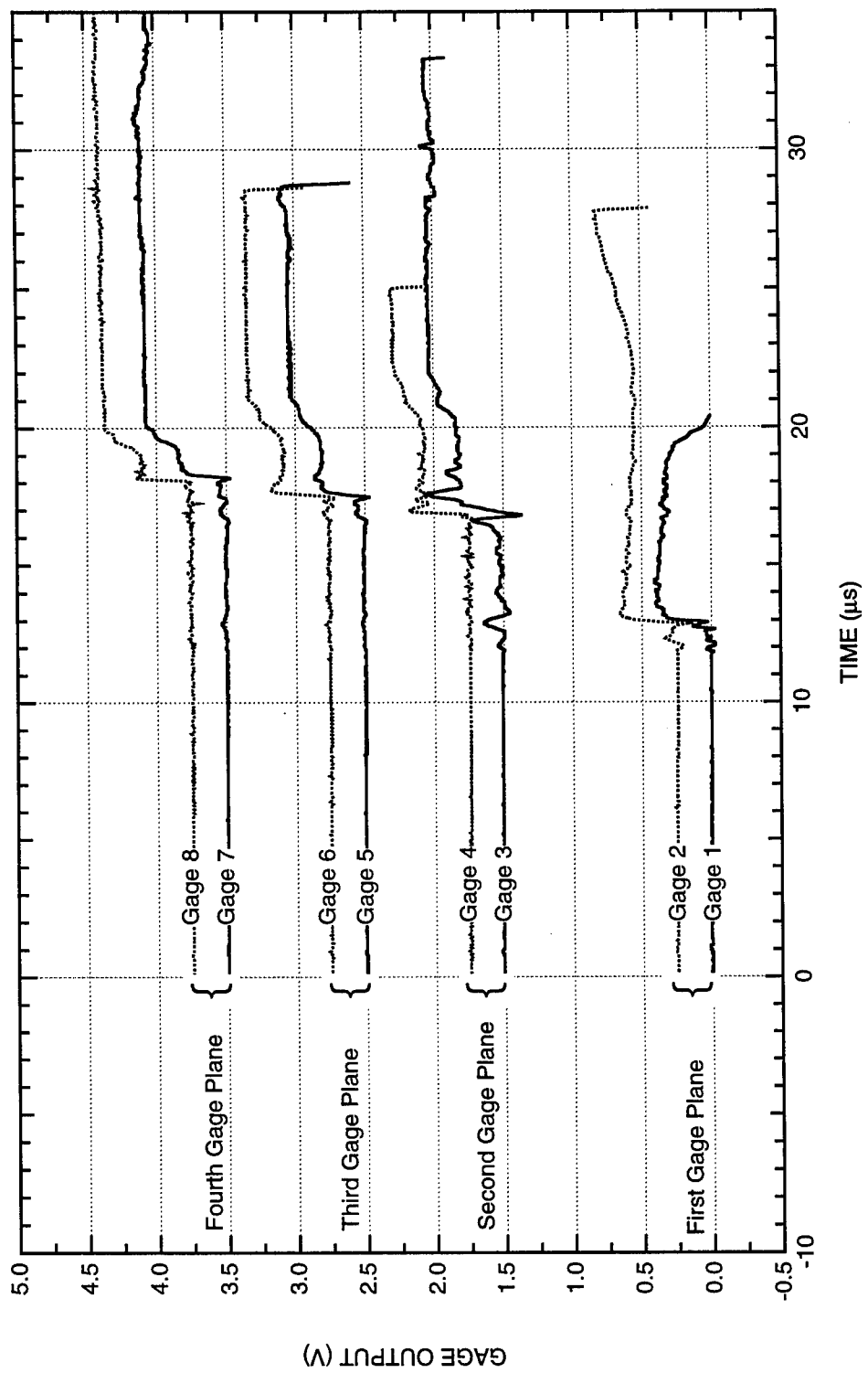


Figure B-55. Summary of the output of all particle velocity gages in HPEOS Experiment 8.

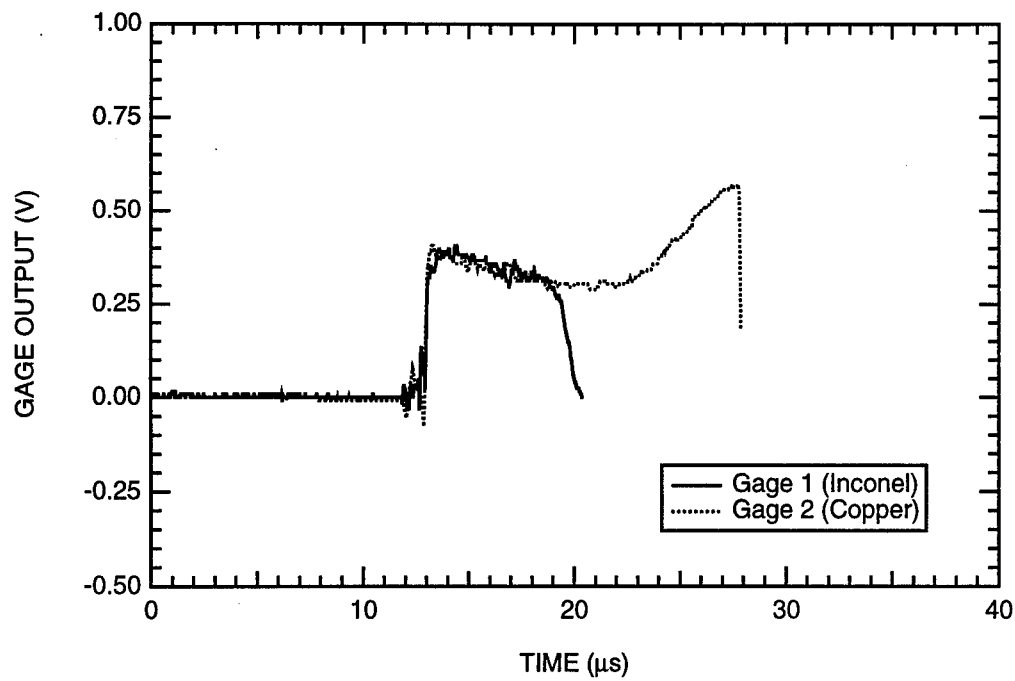


Figure B-56. Output of particle velocity gages at the first gage plane of HPEOS Experiment 8.

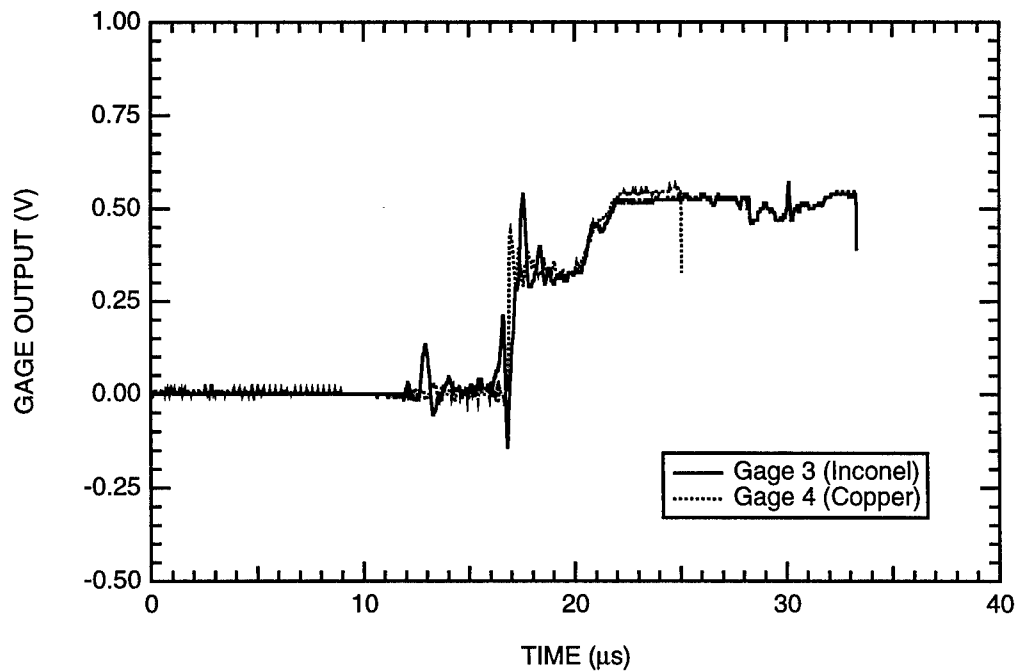


Figure B-57. Output of particle velocity gages at the second gage plane of HPEOS Experiment 8.

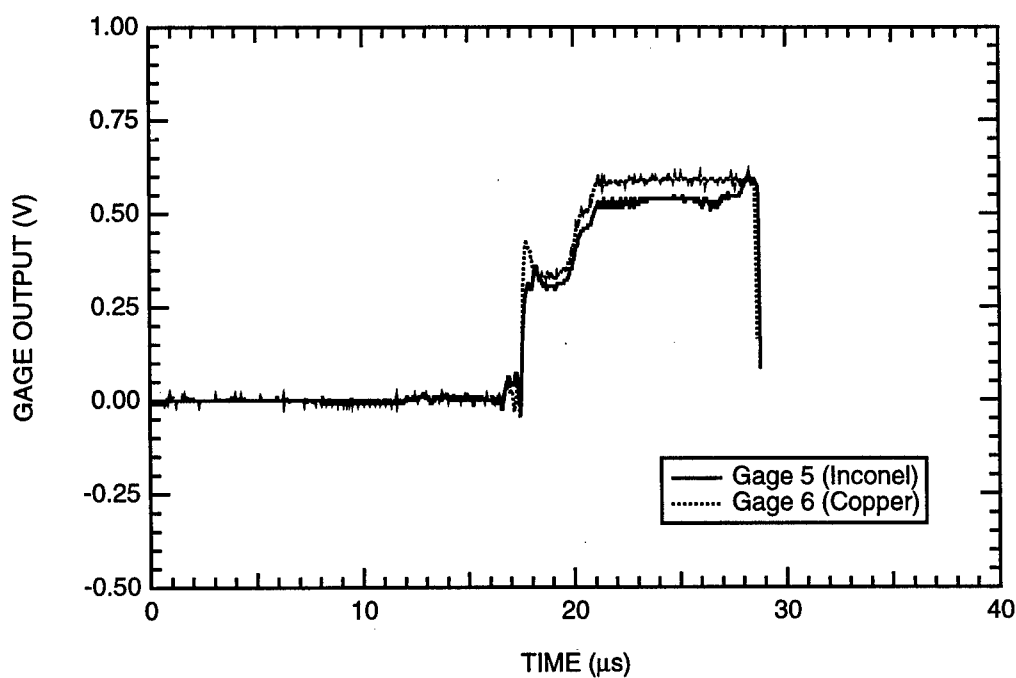


Figure B-58. Output of particle velocity gages at the third gage plane of HPEOS Experiment 8.

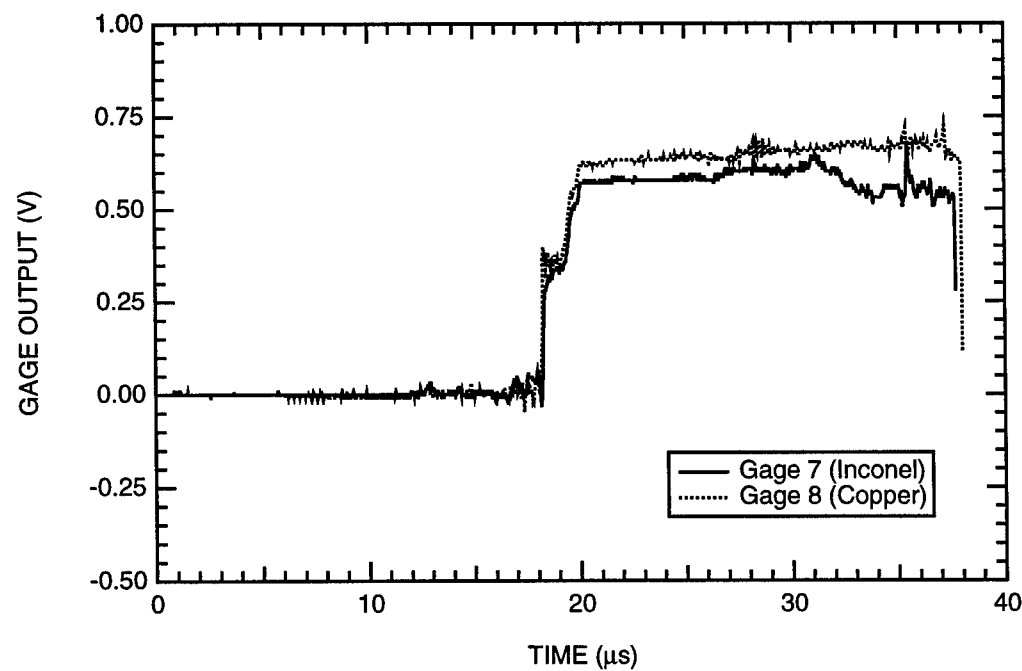


Figure B-59. Output of particle velocity gages at the fourth gage plane of HPEOS Experiment 8.

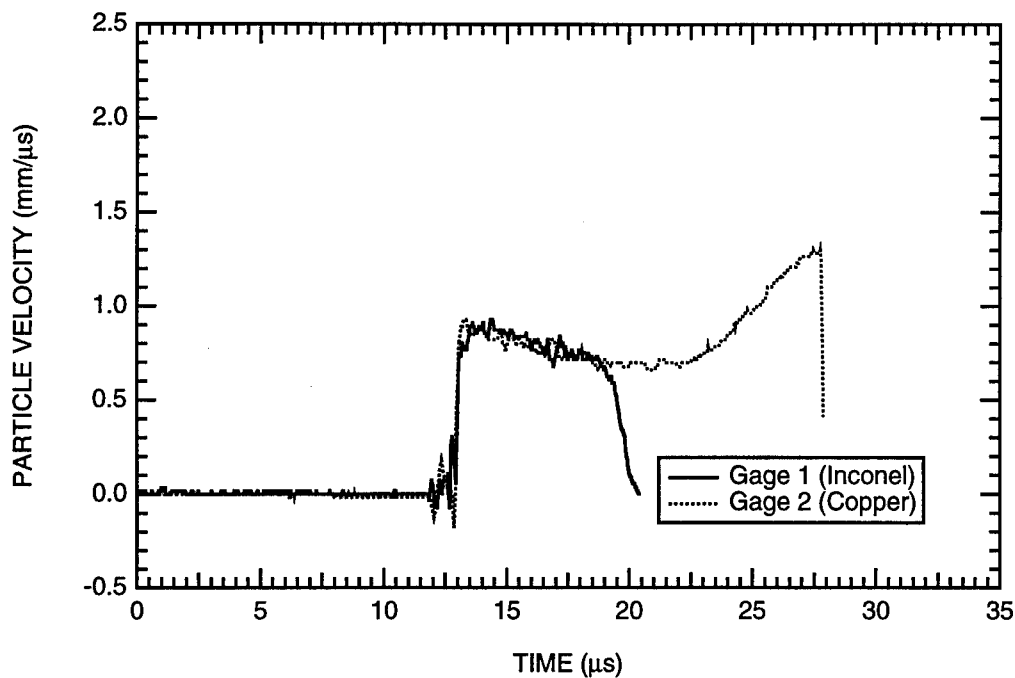


Figure B-60. Particle velocity histories at the first gage plane of HPEOS Experiment 8.

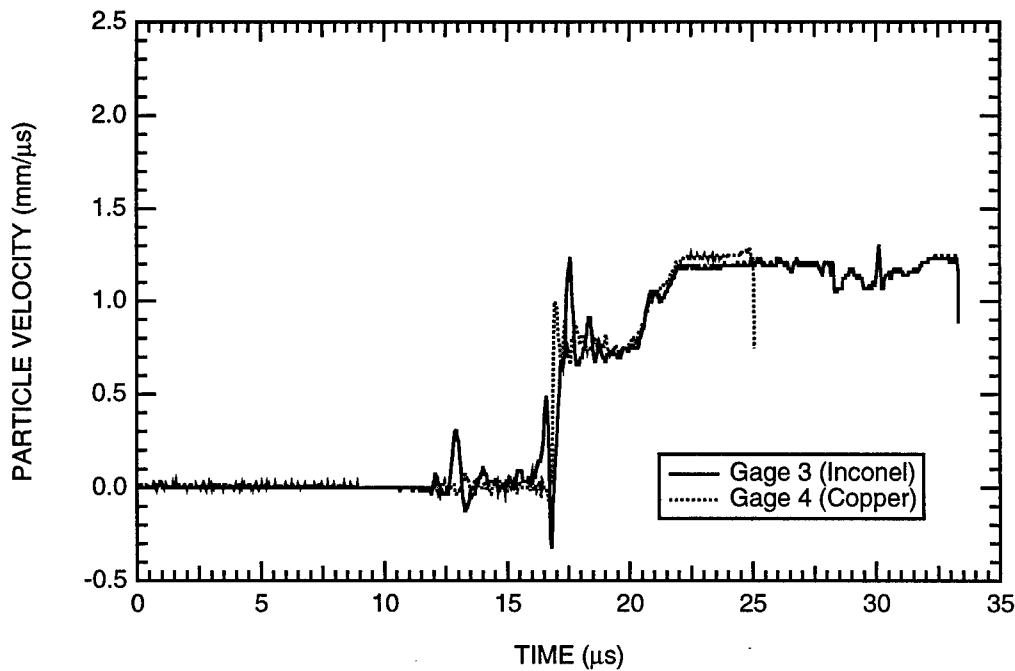


Figure B-61. Particle velocity histories at the second gage plane of HPEOS Experiment 8.

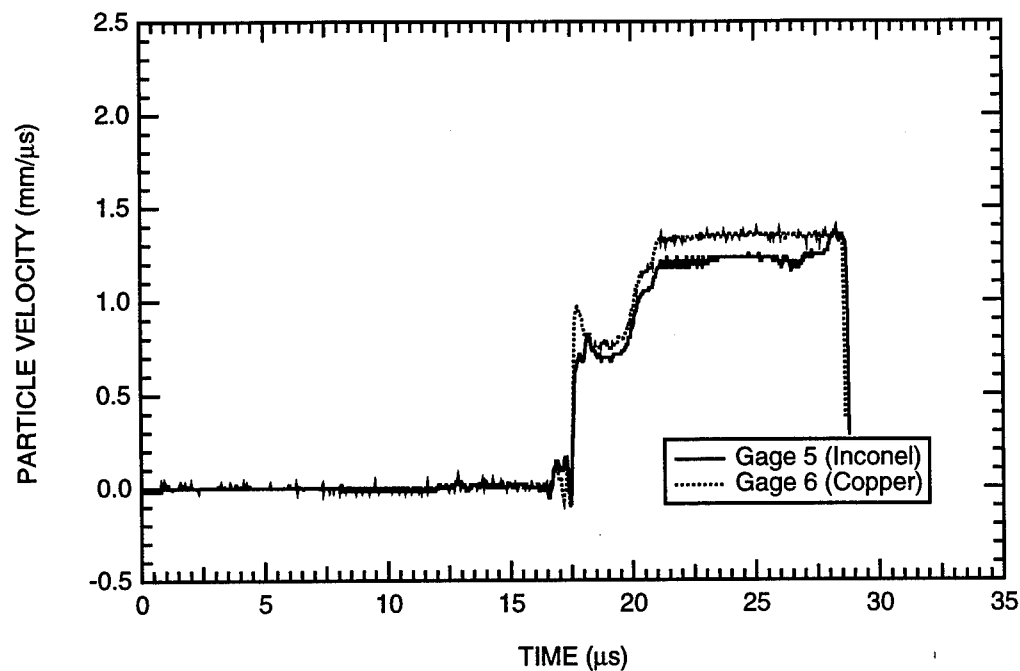


Figure B-62. Particle velocity histories at the third gage plane of HPEOS Experiment 8.

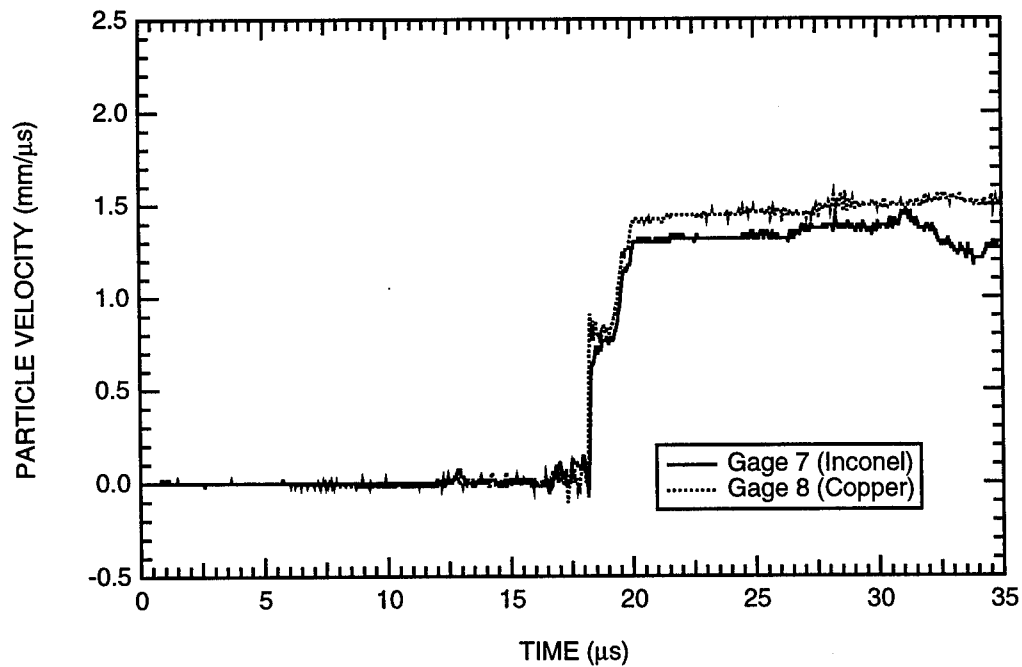


Figure B-63. Particle velocity histories at the fourth gage plane of HPEOS Experiment 8.

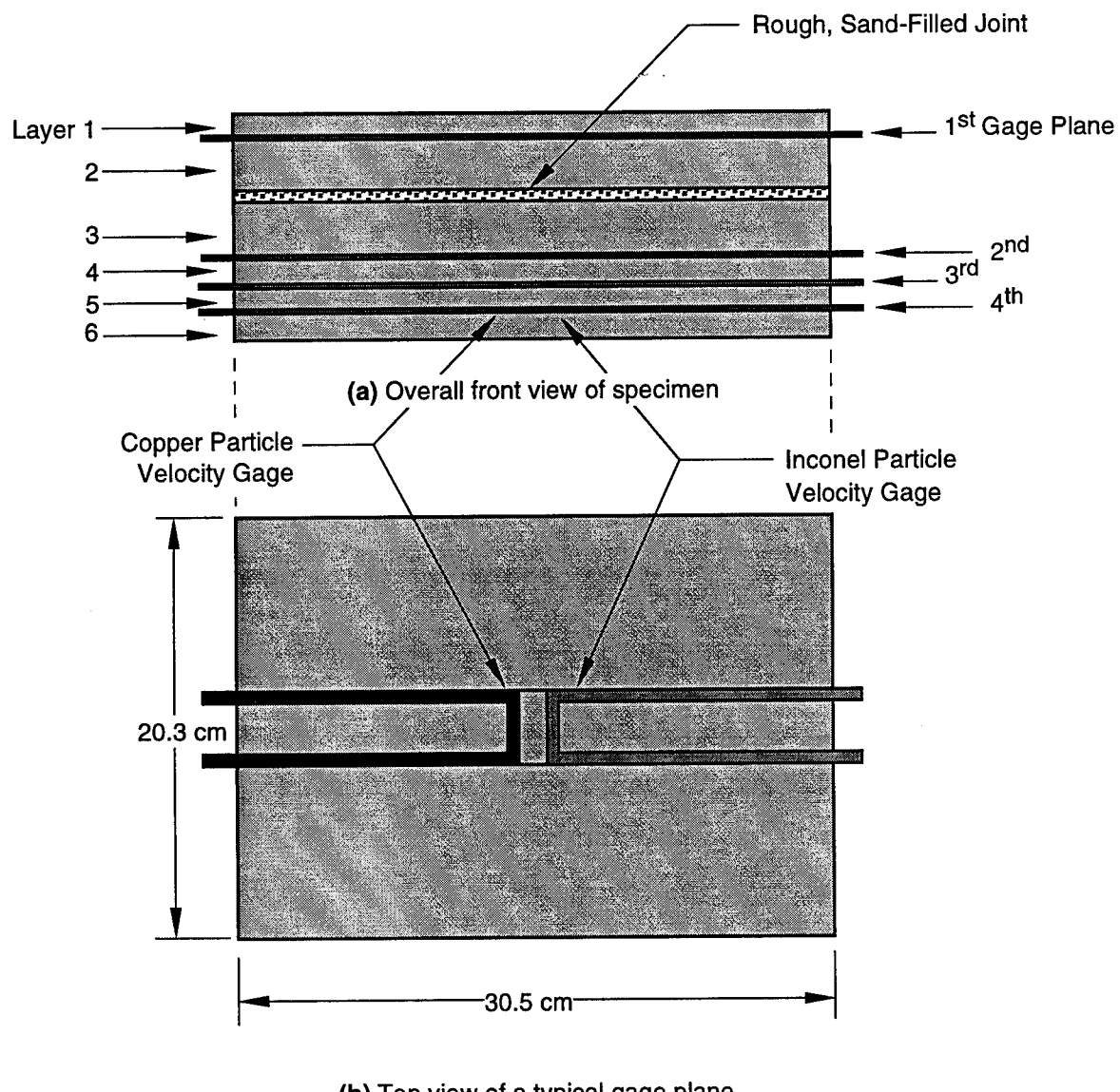


Figure B-64. Specimen configuration and dimensions for HPEOS Experiment 10 (marble).

Note: The explosive system used in the experiment and the thicknesses of the rock layers can be obtained from Table B-1.

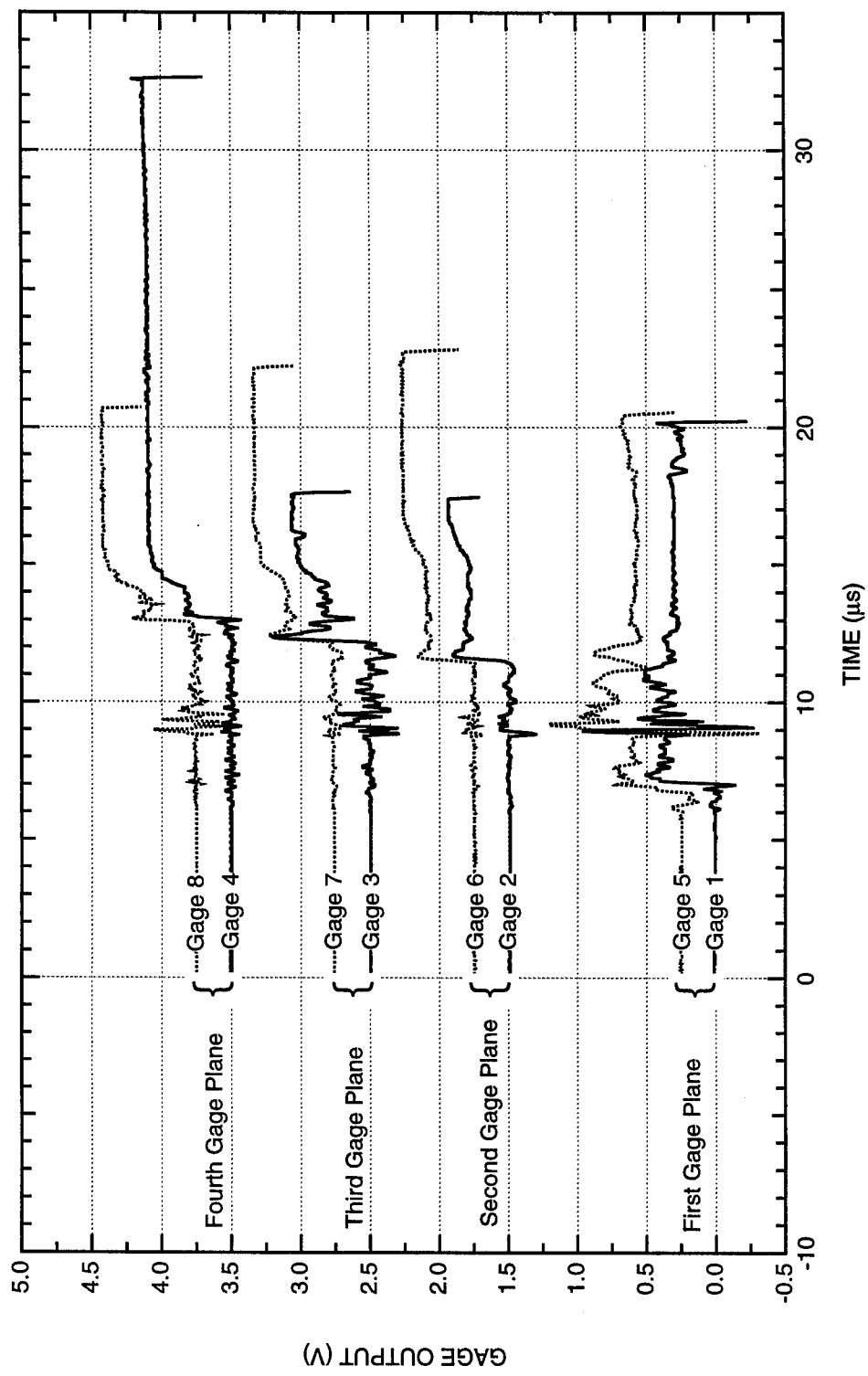


Figure B-65. Summary of the output of all particle velocity gages in HPEOS Experiment 10.

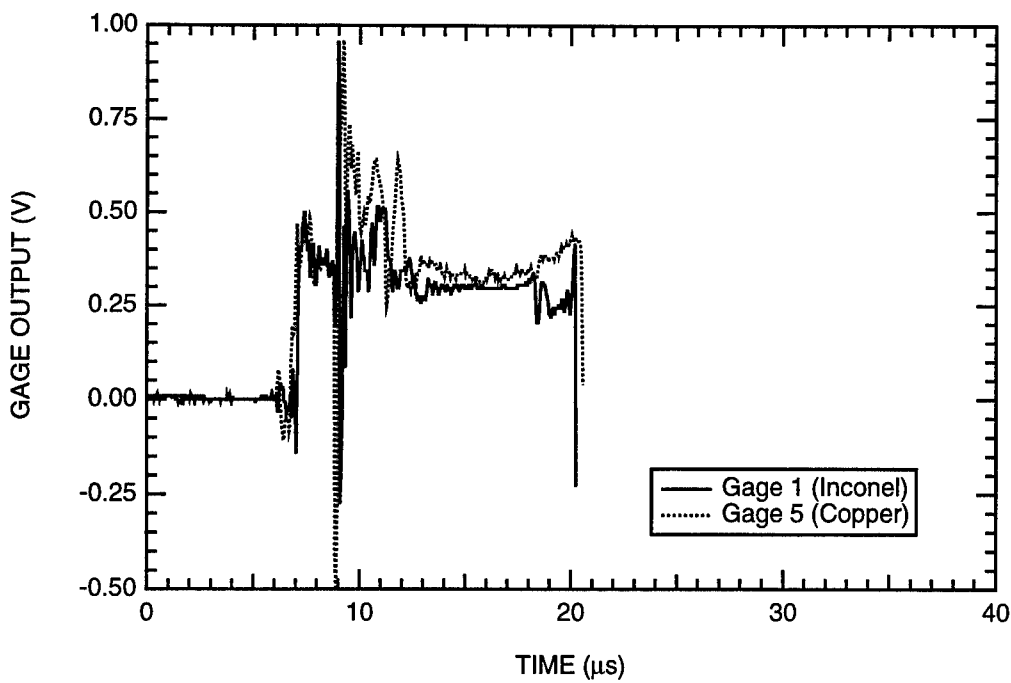


Figure B-66. Output of particle velocity gages at the first gage plane of HPEOS Experiment 10.

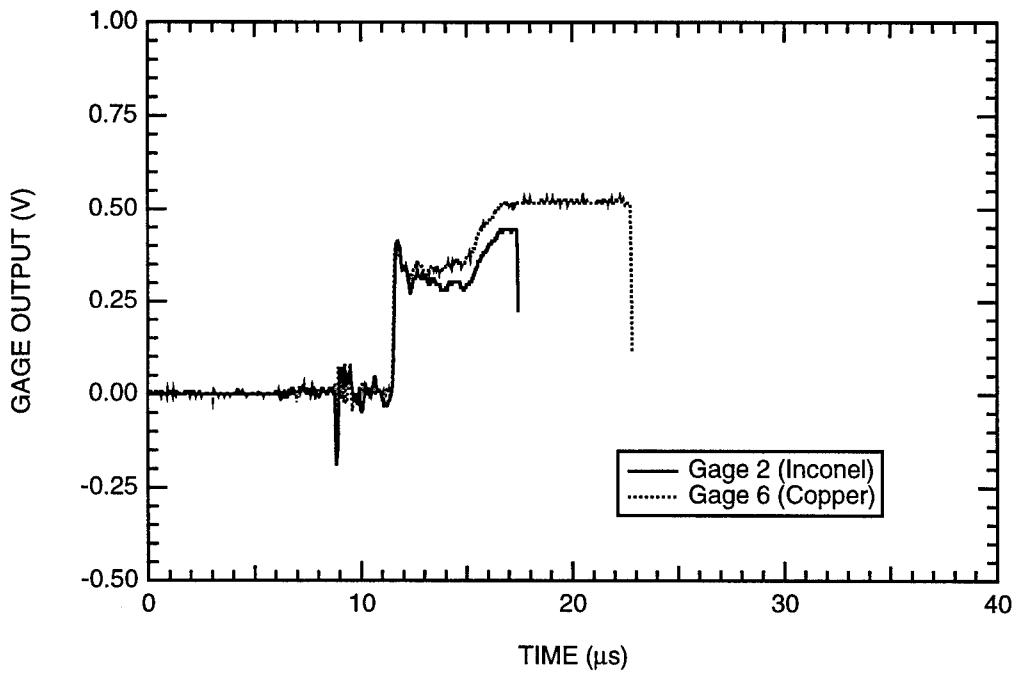


Figure B-67. Output of particle velocity gages at the second gage plane of HPEOS Experiment 10.

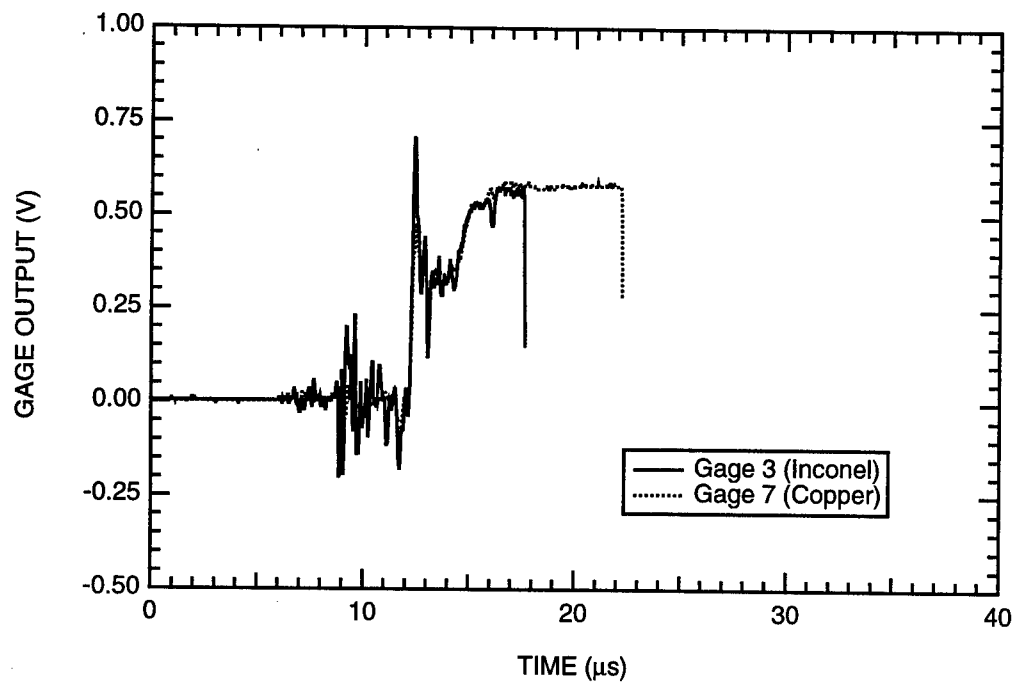


Figure B-68. Output of particle velocity gages at the third gage plane of HPEOS Experiment 10.

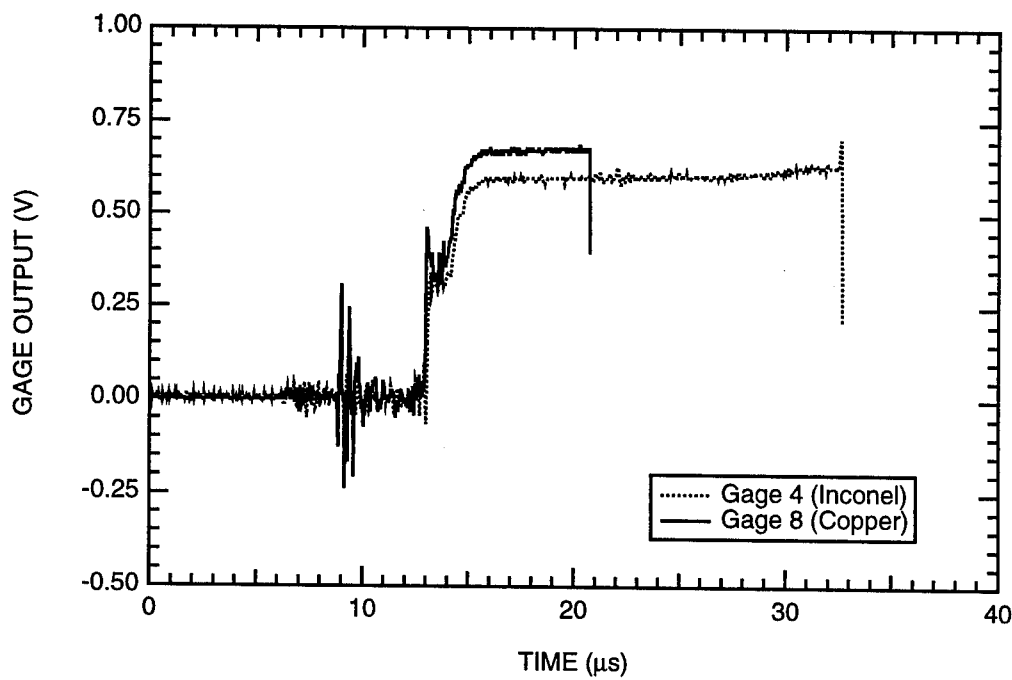


Figure B-69. Output of particle velocity gages at the fourth gage plane of HPEOS Experiment 10.

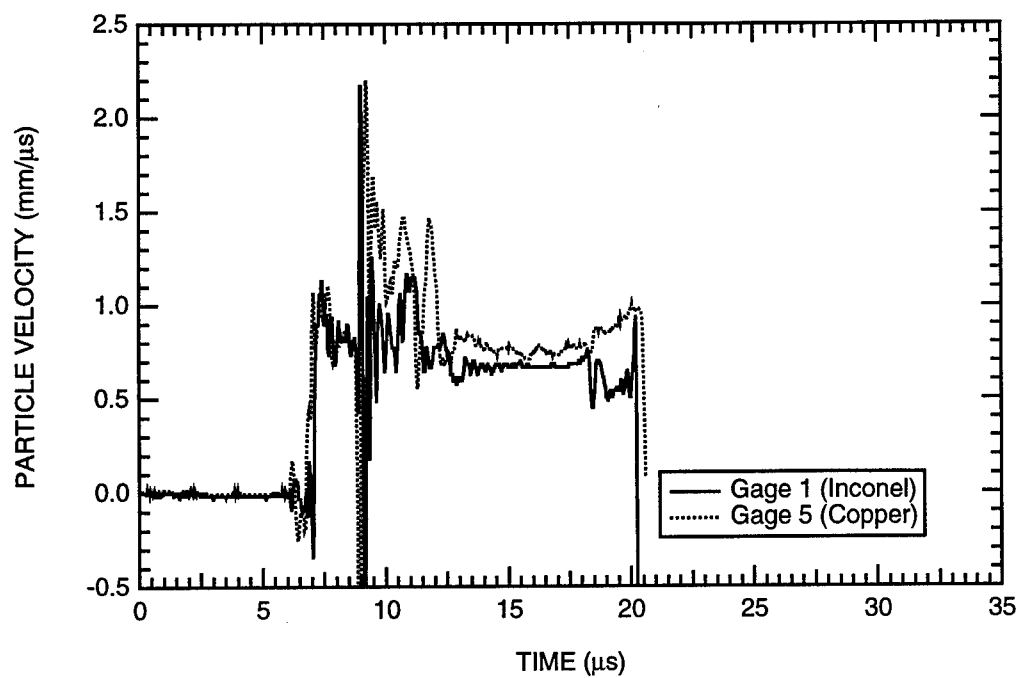


Figure B-70. Particle velocity histories at the first gage plane of HPEOS Experiment 10.

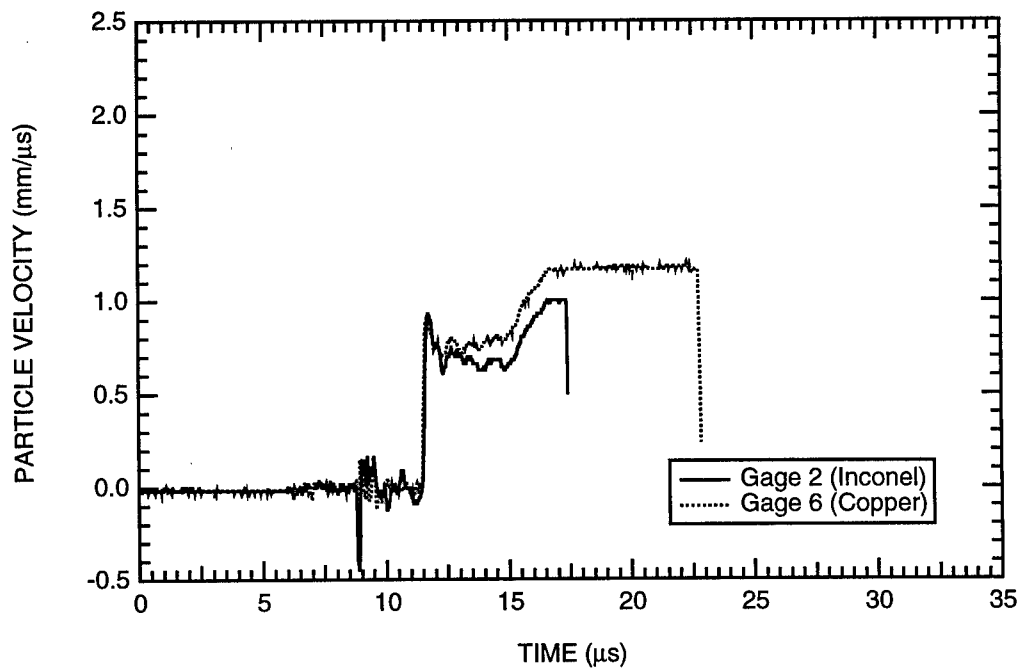


Figure B-71. Particle velocity histories at the second gage plane of HPEOS Experiment 10.

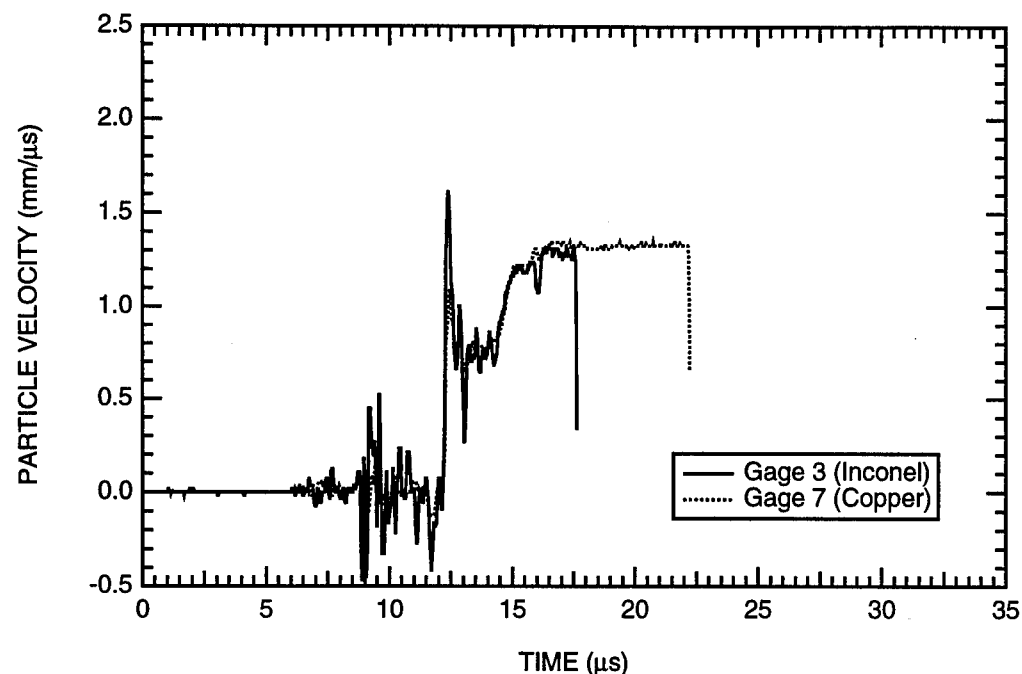


Figure B-72. Particle velocity histories at the third gage plane of HPEOS Experiment 10.

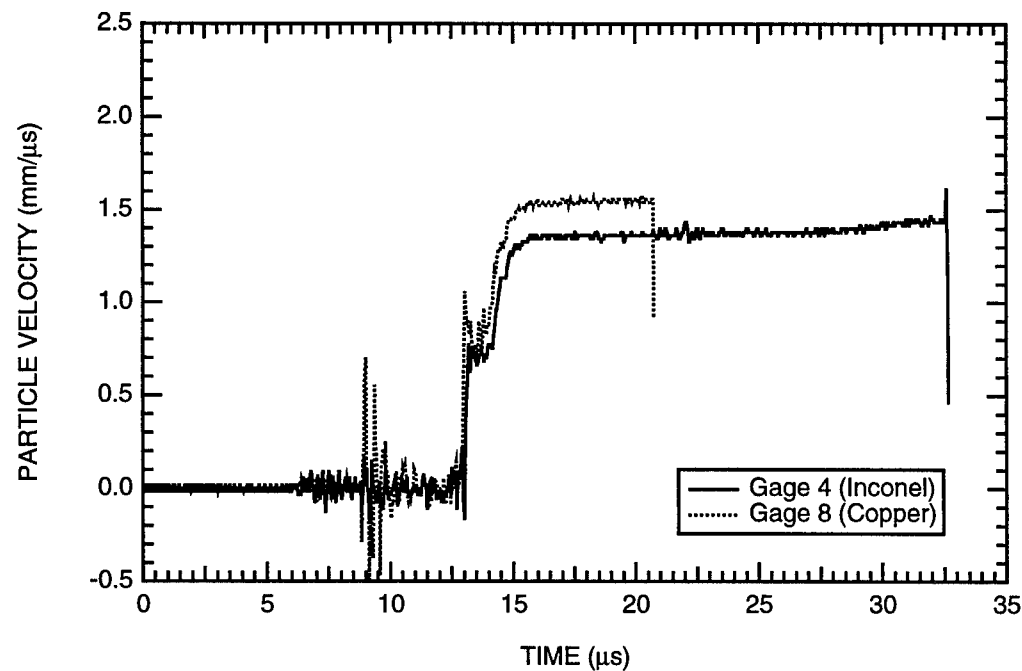


Figure B-73. Particle velocity histories at the fourth gage plane of HPEOS Experiment 10.

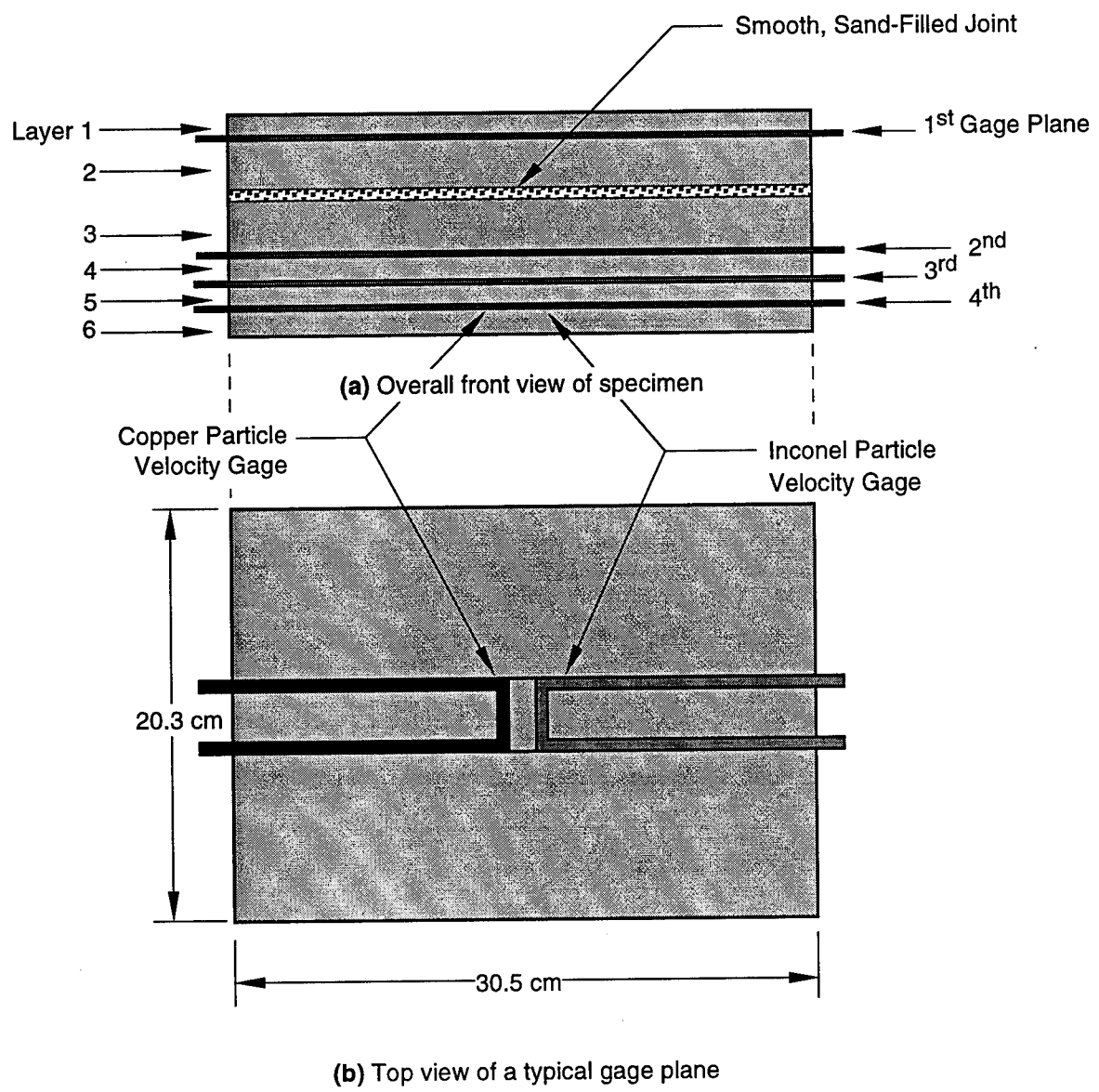


Figure B-74. Specimen configuration and dimensions for HPEOS Experiment 11 (marble).

Note: The explosive system used in the experiment and the thicknesses of the rock layers can be obtained from Table B-1.

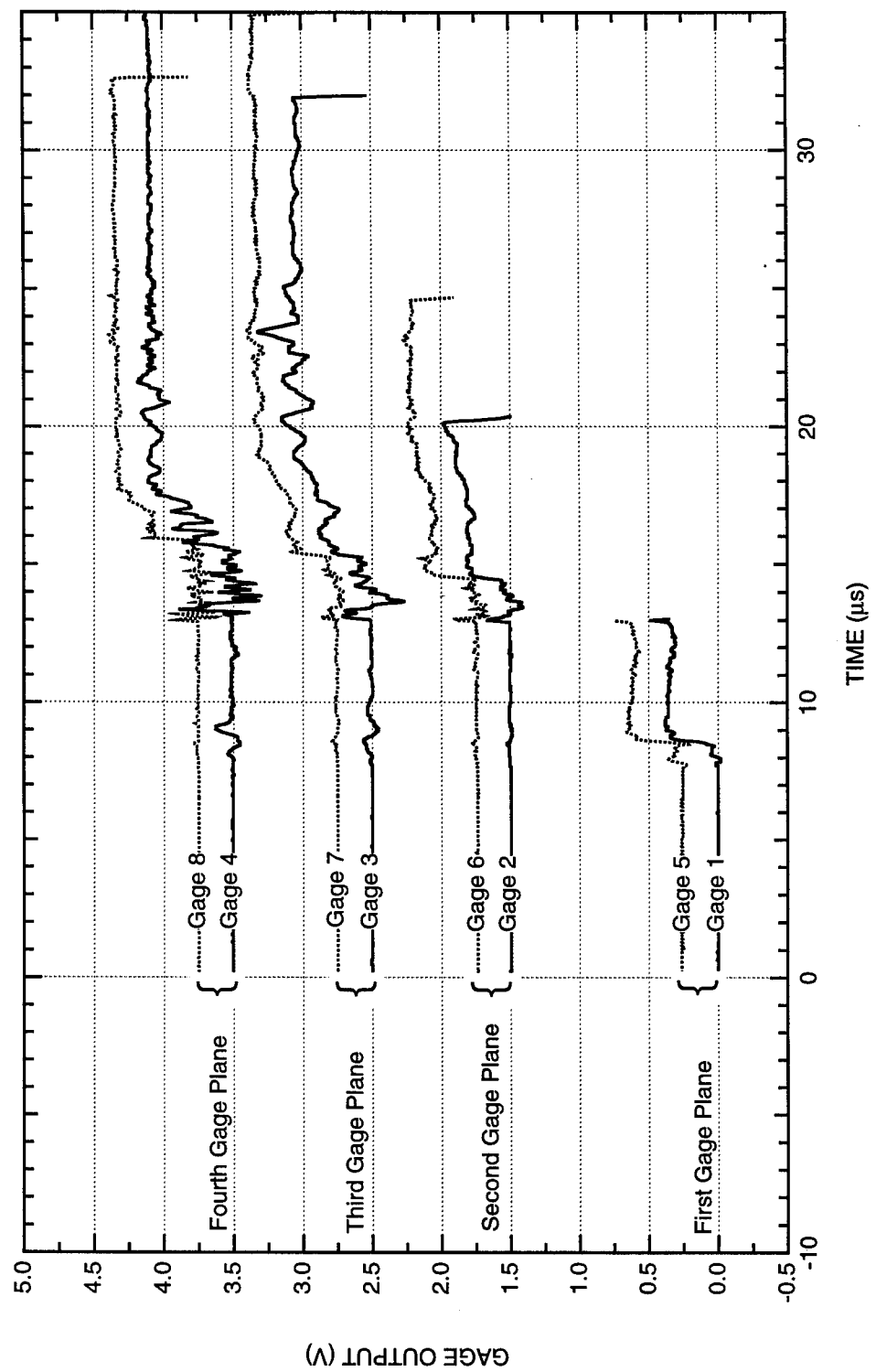


Figure B-75 Summary of the output of all particle velocity gages in HPEOS Experiment 11.

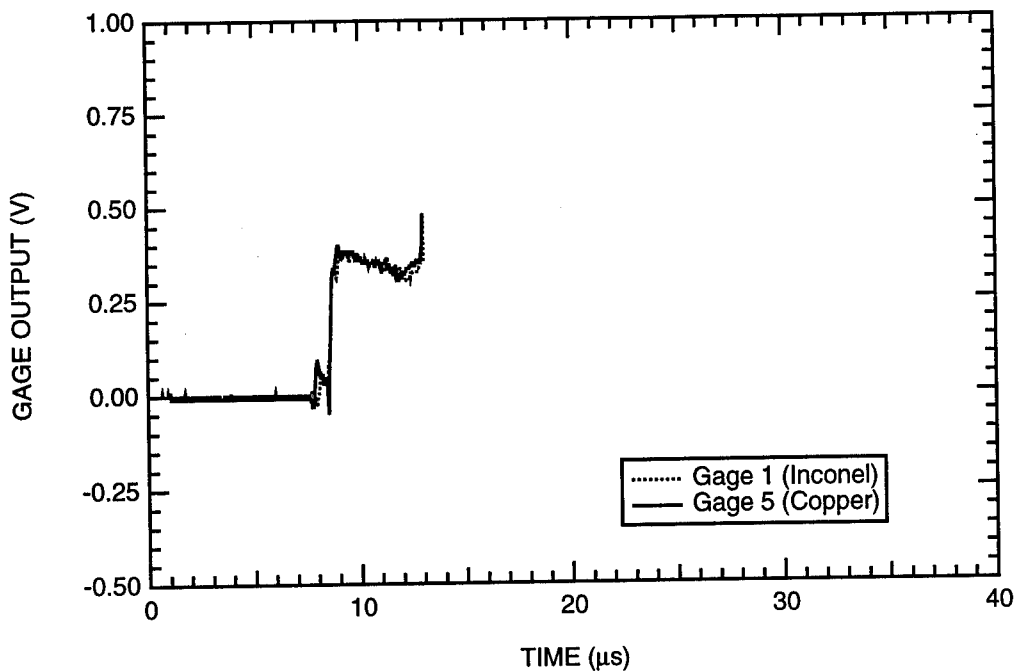


Figure B-76. Output of particle velocity gages at the first gage plane of HPEOS Experiment 11.

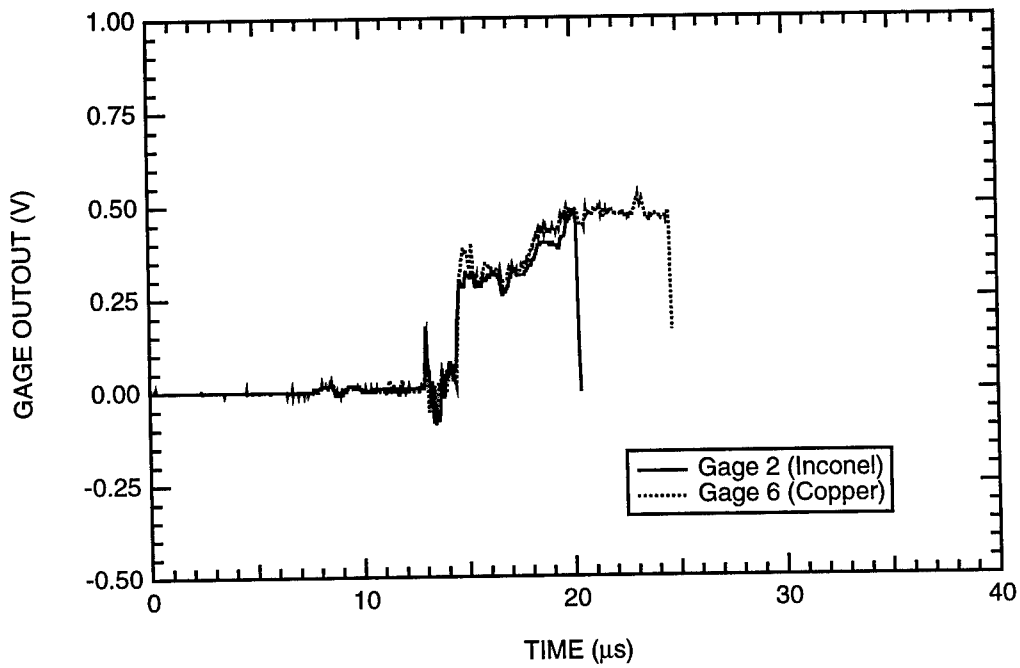


Figure B-77. Output of particle velocity gages at the second gage plane of HPEOS Experiment 11.

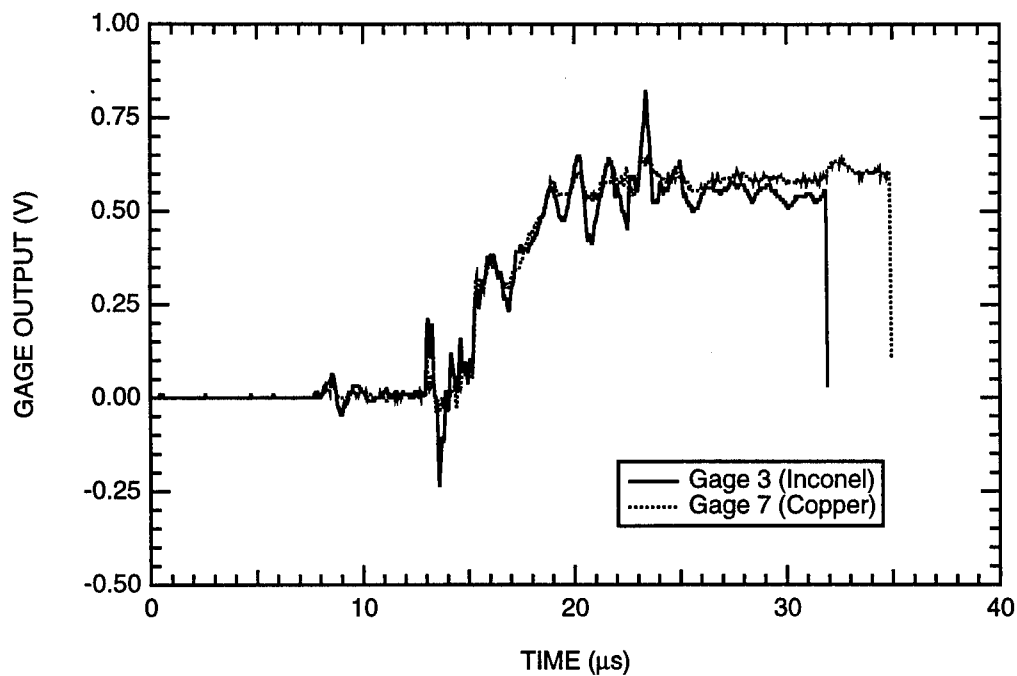


Figure B-78. Output of particle velocity gages at the third gage plane of HPEOS Experiment 11.

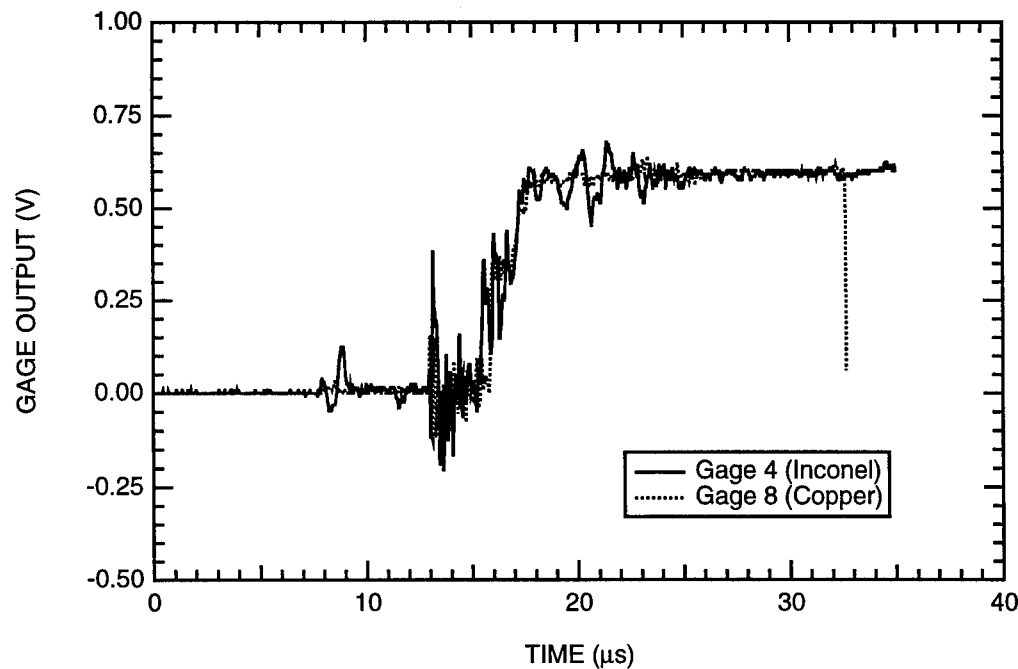


Figure B-79. Output of particle velocity gages at the fourth gage plane of HPEOS Experiment 11.

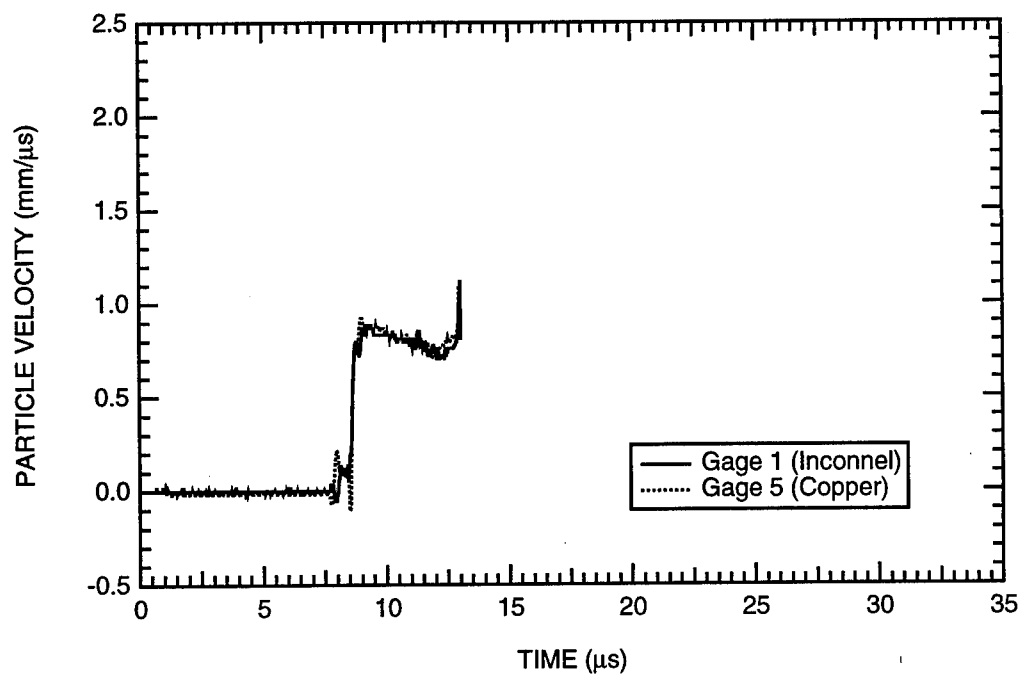


Figure B-80. Particle velocity histories at the first gage plane of HPEOS Experiment 11.

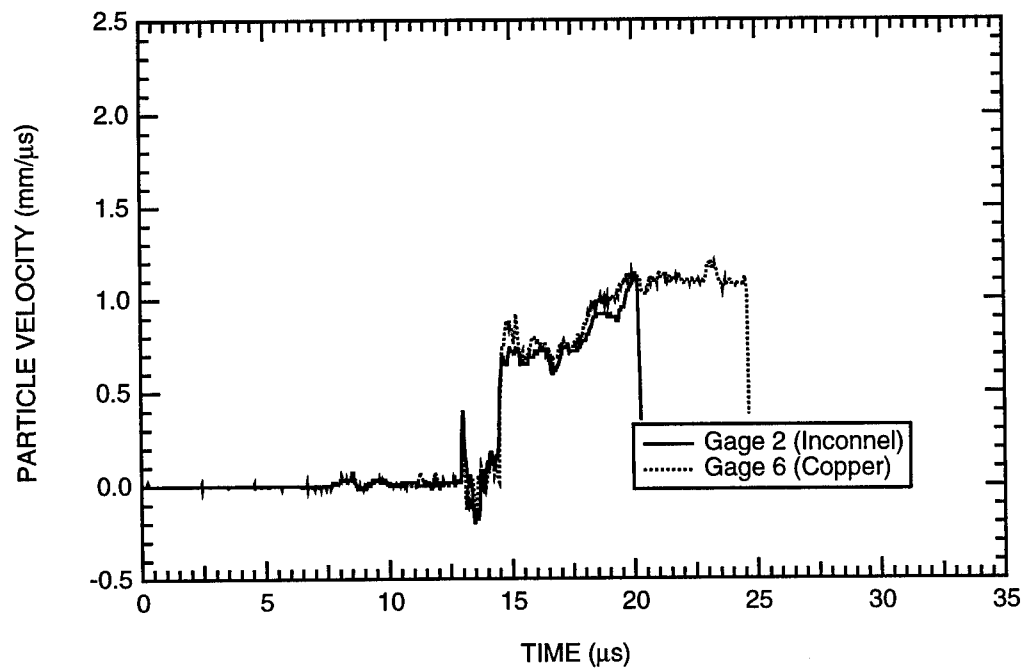


Figure B-81. Particle velocity histories at the second gage plane of HPEOS Experiment 11.

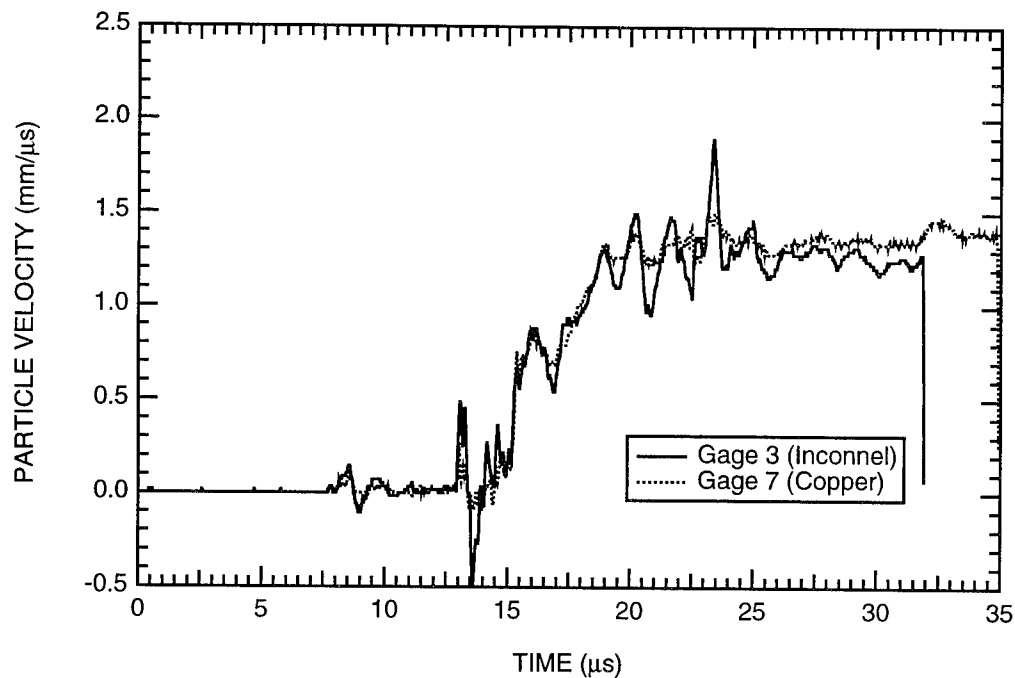


Figure B-82. Particle velocity histories at the third gage plane of HPEOS Experiment 11.

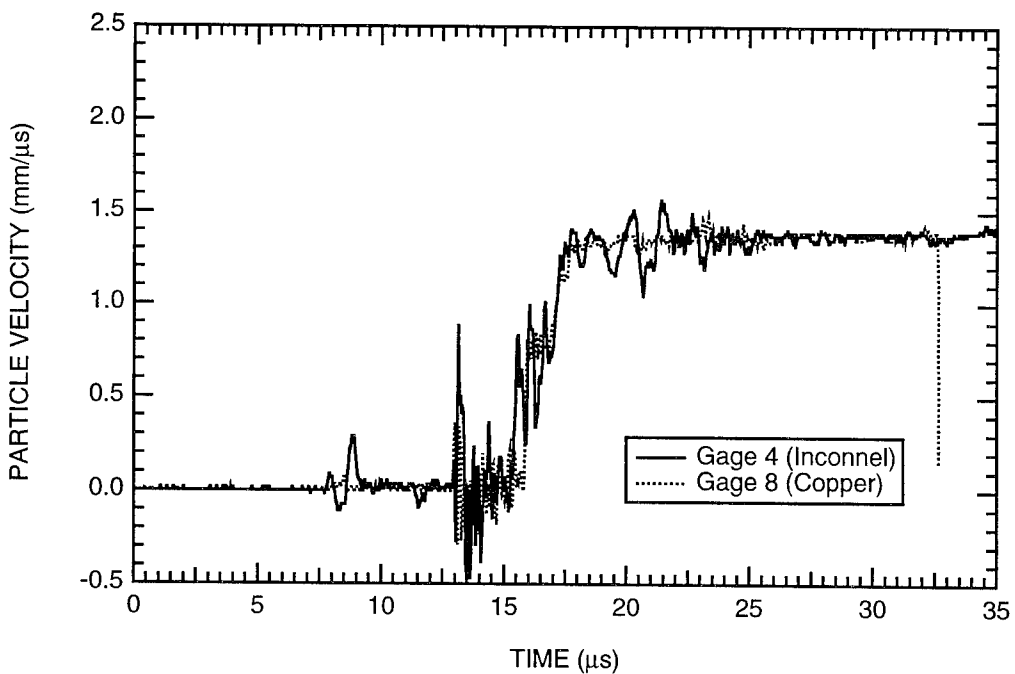


Figure B-83. Particle velocity histories at the fourth gage plane of HPEOS Experiment 11.

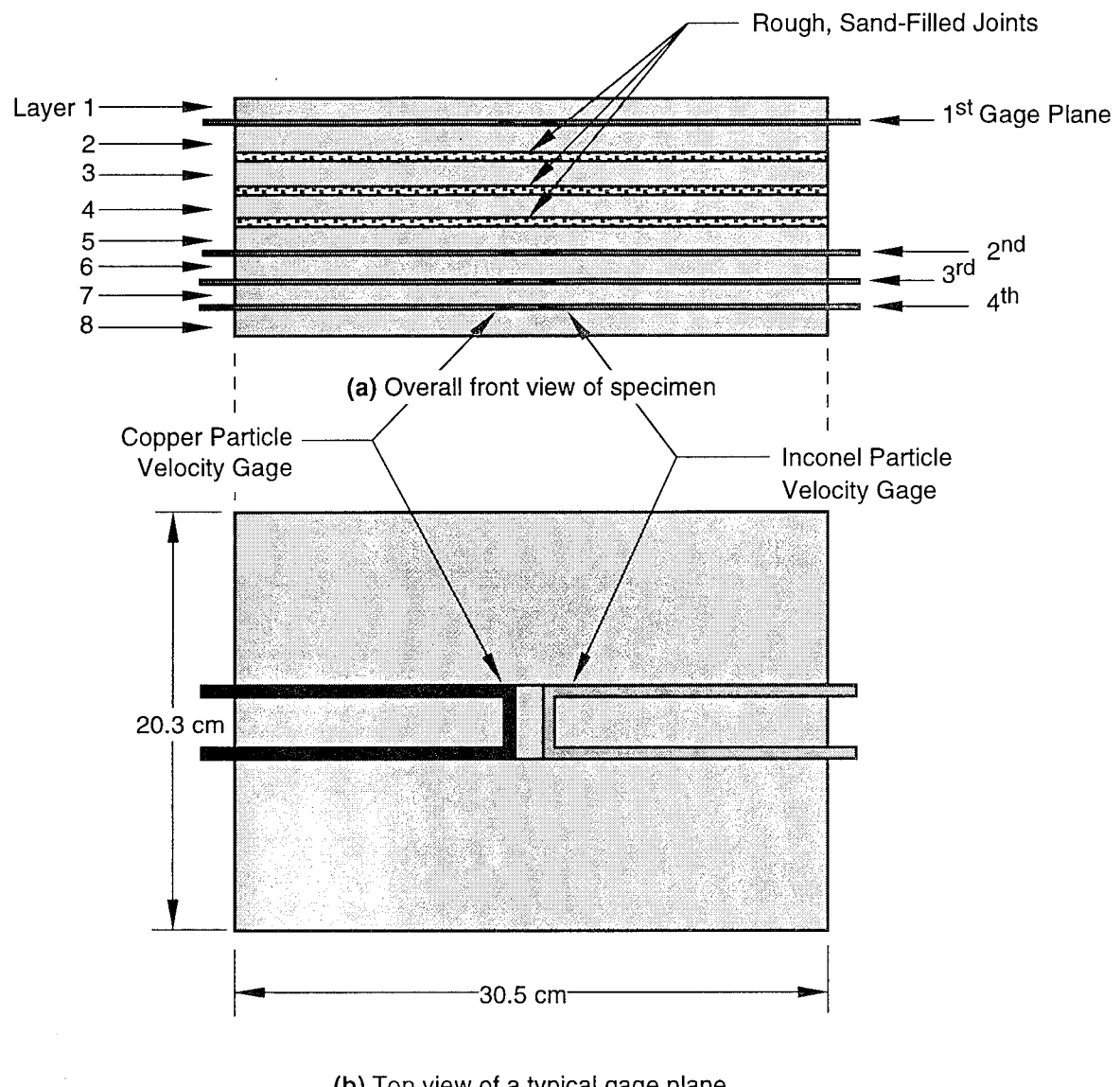


Figure B-84. Specimen configuration and dimensions for HPEOS Experiment 12 (marble).

Note: The explosive system used in the experiment and the thicknesses of the rock layers can be obtained from Table B-1.

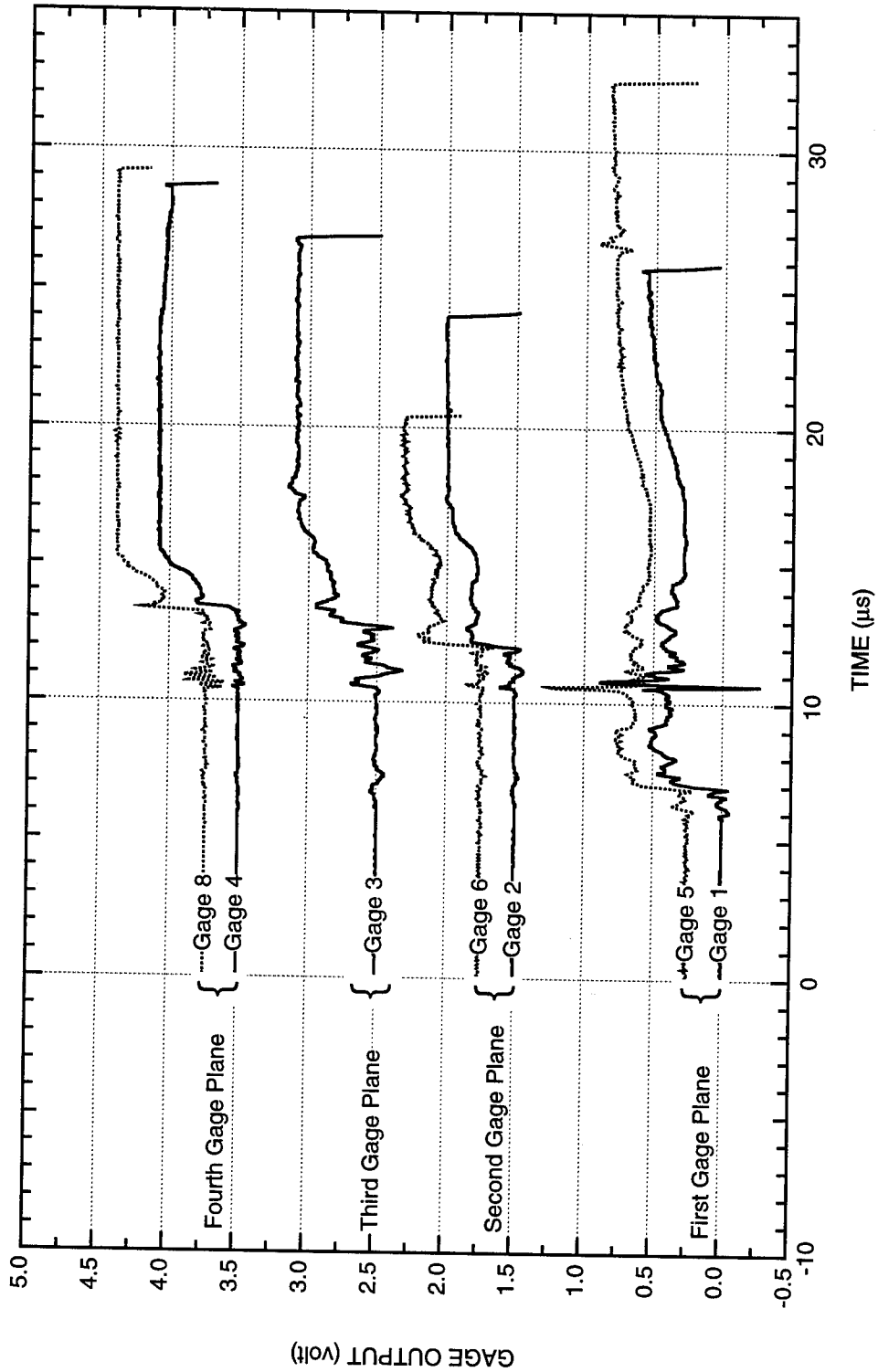


Figure B-85. Summary of the output of all particle velocity gages in HPEOS Experiment 12.

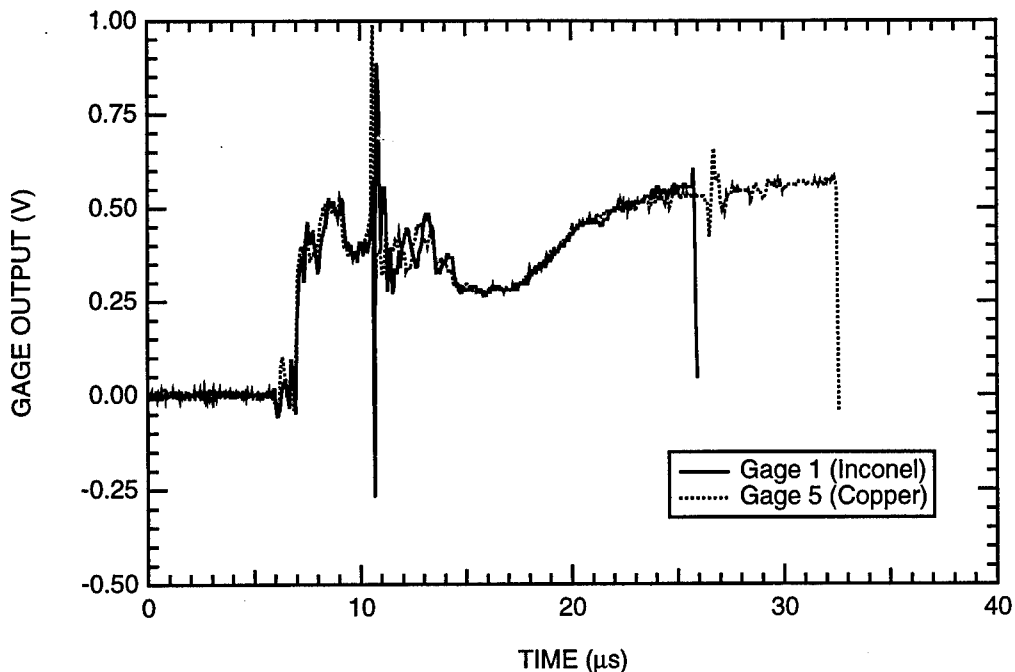


Figure B-86. Output of particle velocity gages at the first gage plane of HPEOS Experiment 12.

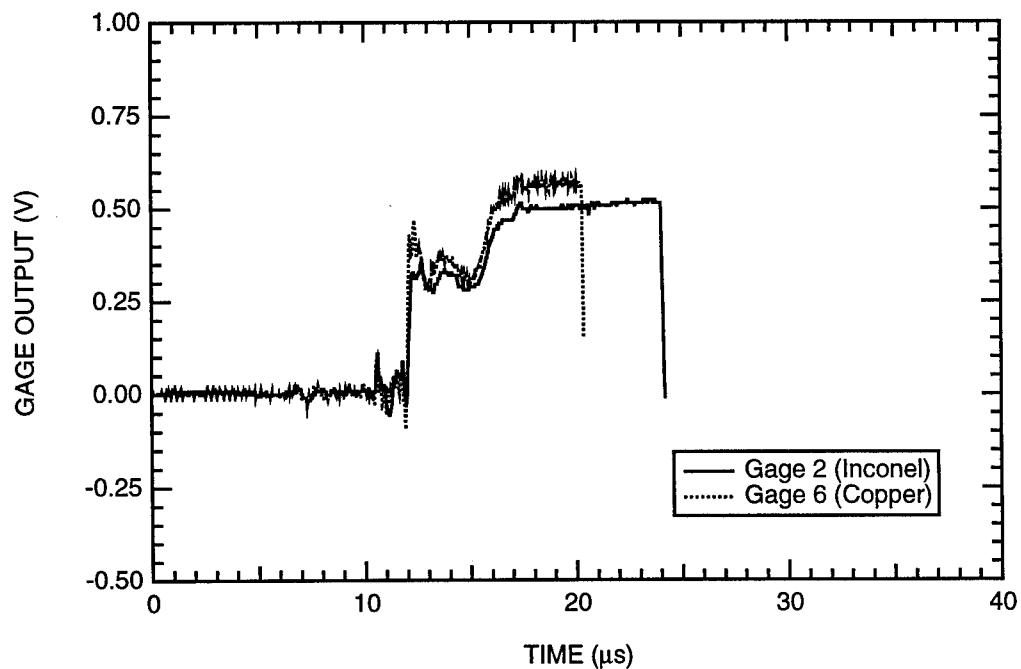


Figure B-87. Output of particle velocity gages at the second gage plane of HPEOS Experiment 12.

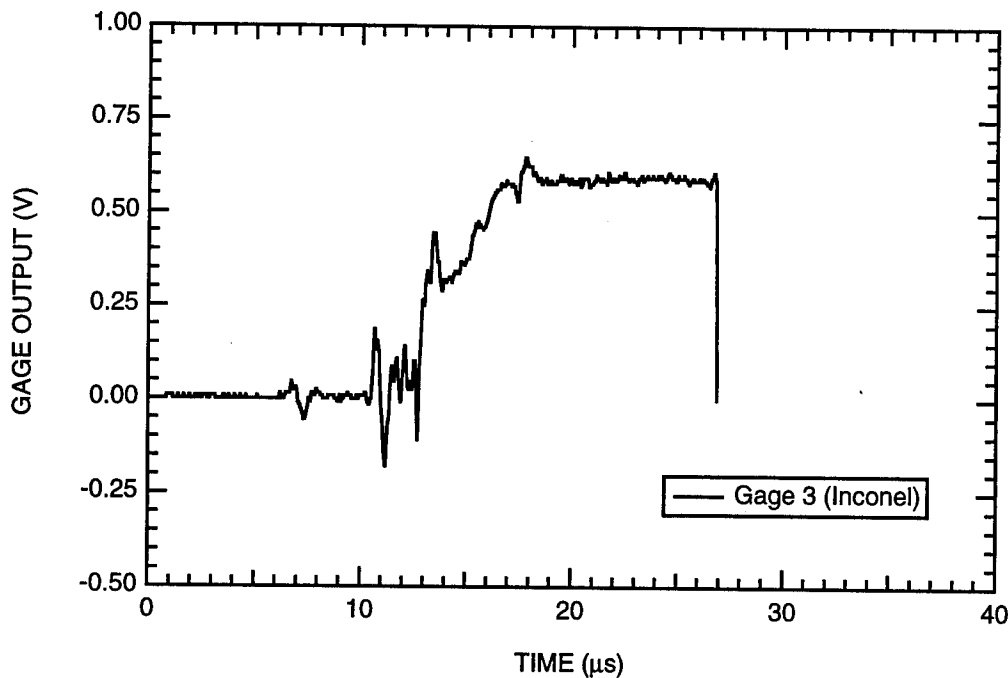


Figure B-88. Output of particle velocity gages at the third gage plane of HPEOS Experiment 12.

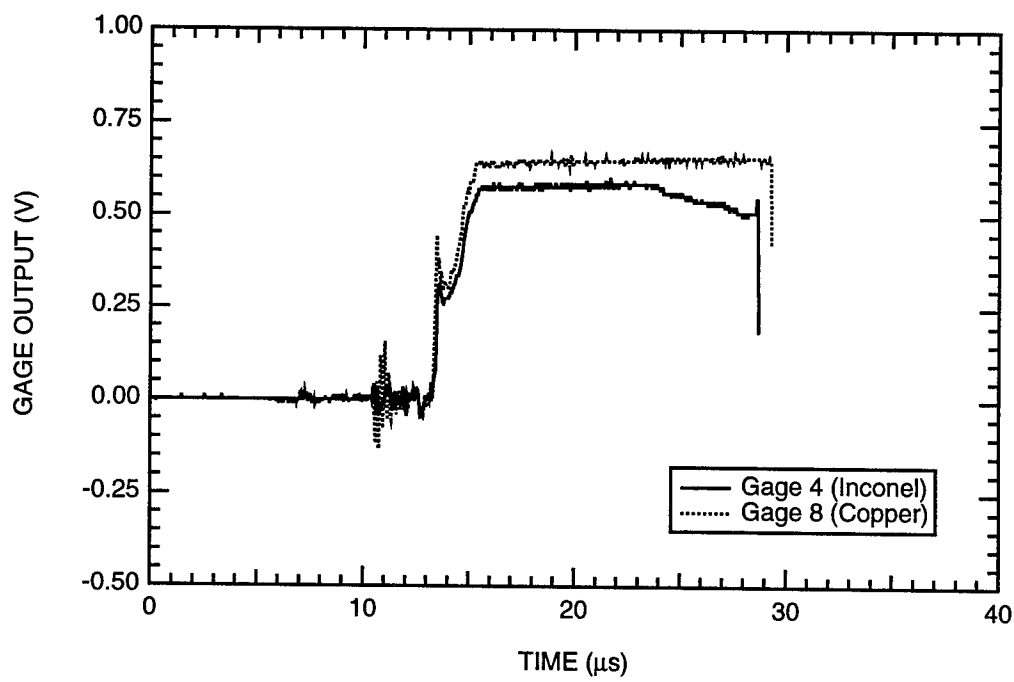


Figure B-89. Output of particle velocity gages at the fourth gage plane of HPEOS Experiment 12.

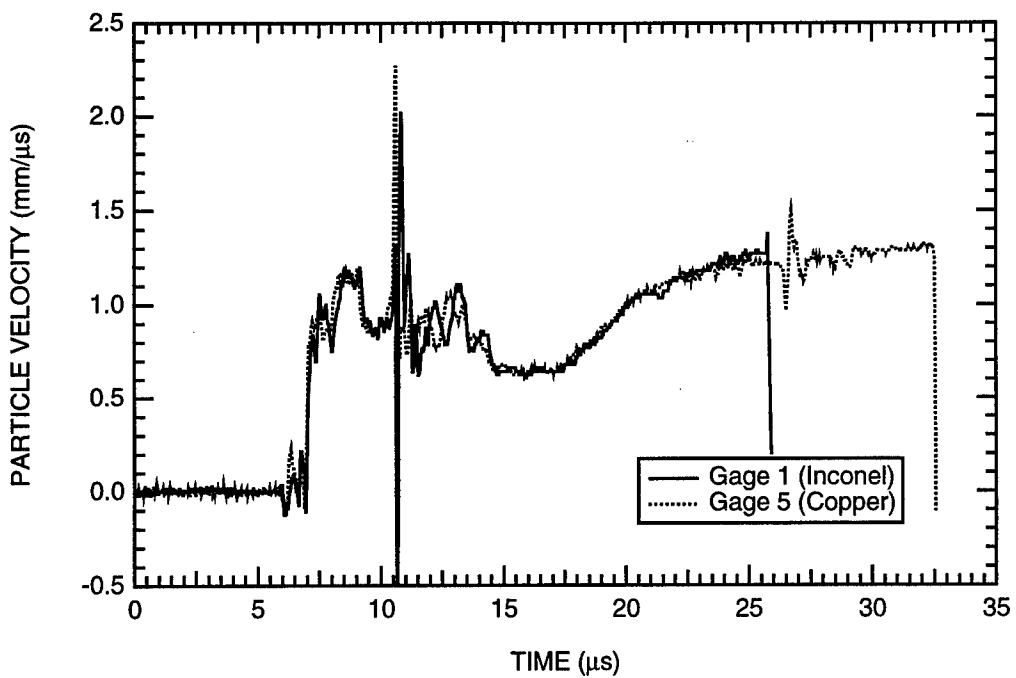


Figure B-90. Particle velocity histories at the first gage plane of HPEOS Experiment 12.

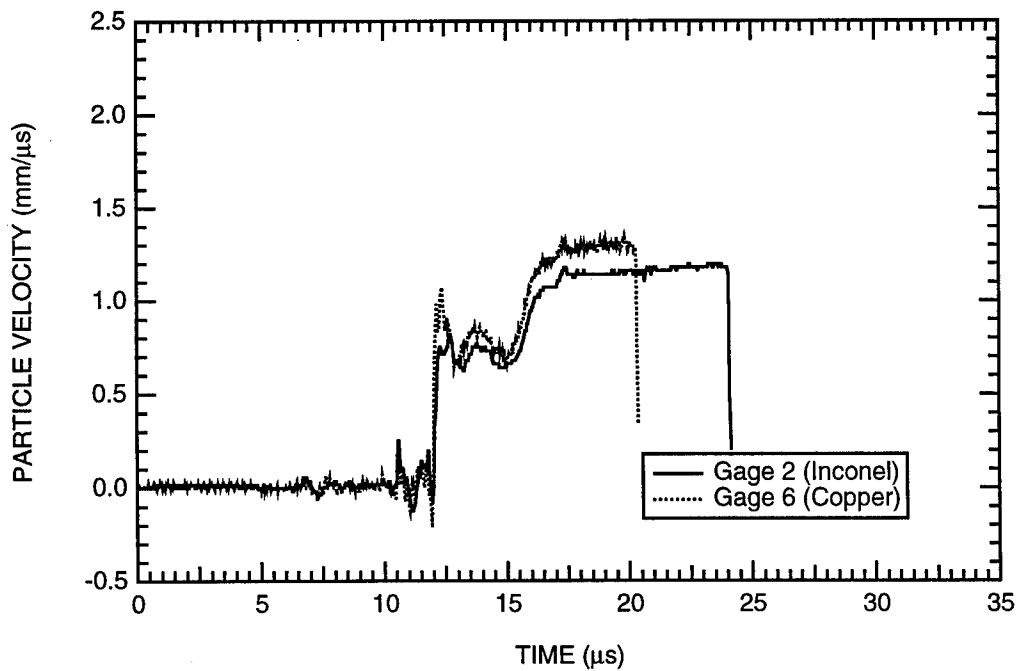


Figure B-91. Particle velocity histories at the second gage plane of HPEOS Experiment 12.

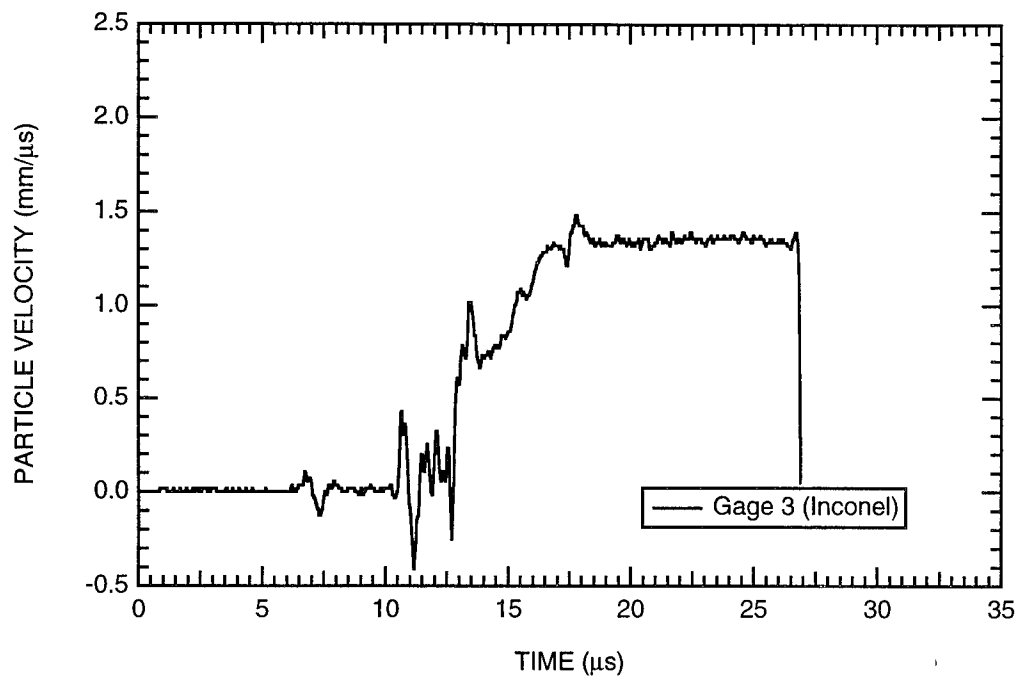


Figure B-92. Particle velocity histories at the third gage plane of HPEOS Experiment 12.

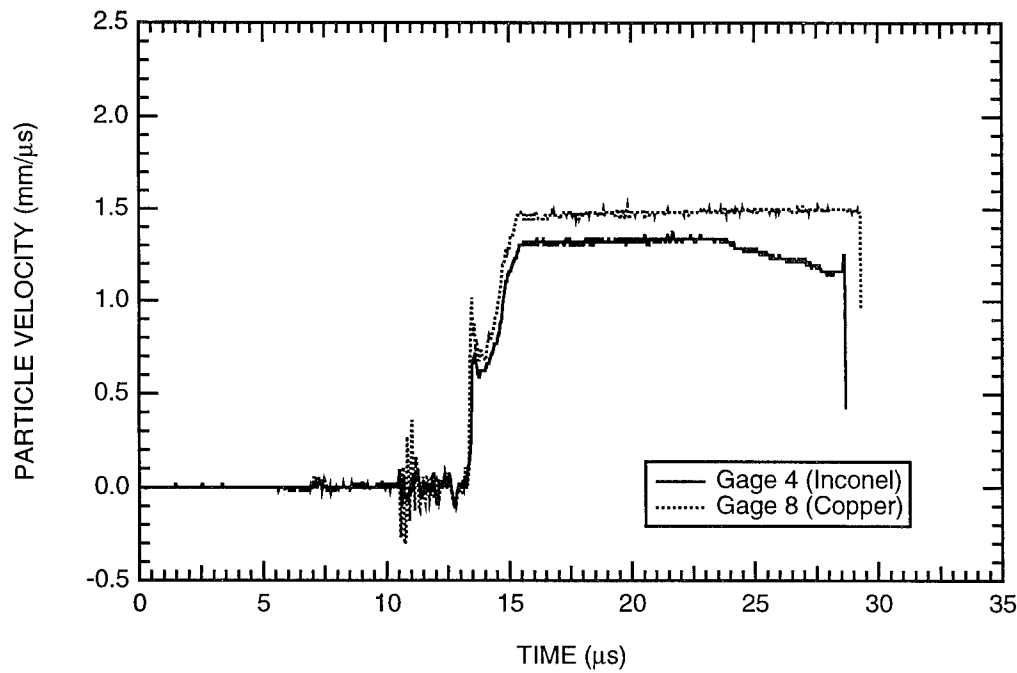


Figure B-93. Particle velocity histories at the fourth gage plane of HPEOS Experiment 12.

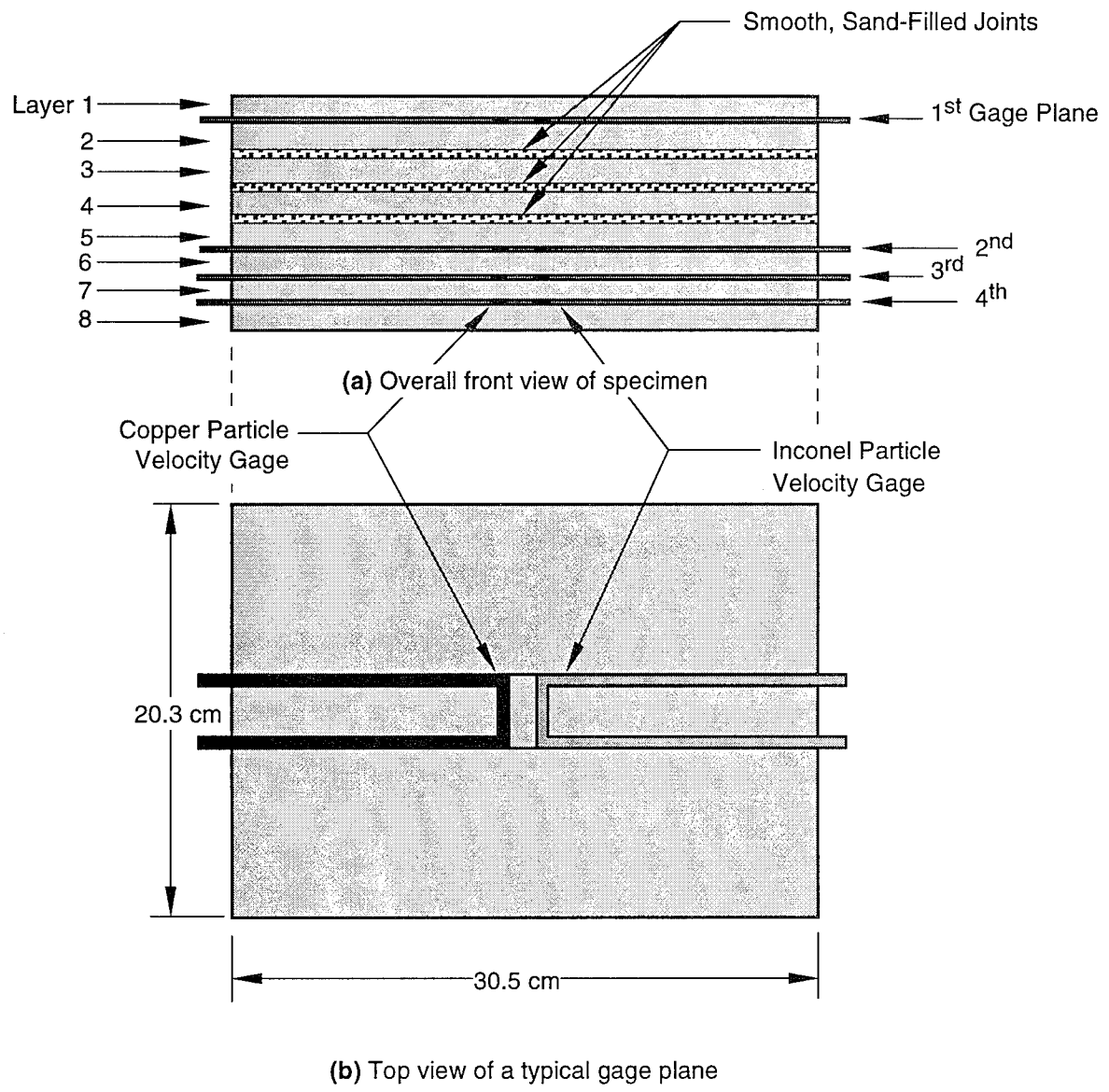


Figure B-94. Specimen configuration and dimensions for HPEOS Experiment 13 (marble).

Note: The explosive system used in the experiment and the thicknesses of the rock layers can be obtained from Table B-1.

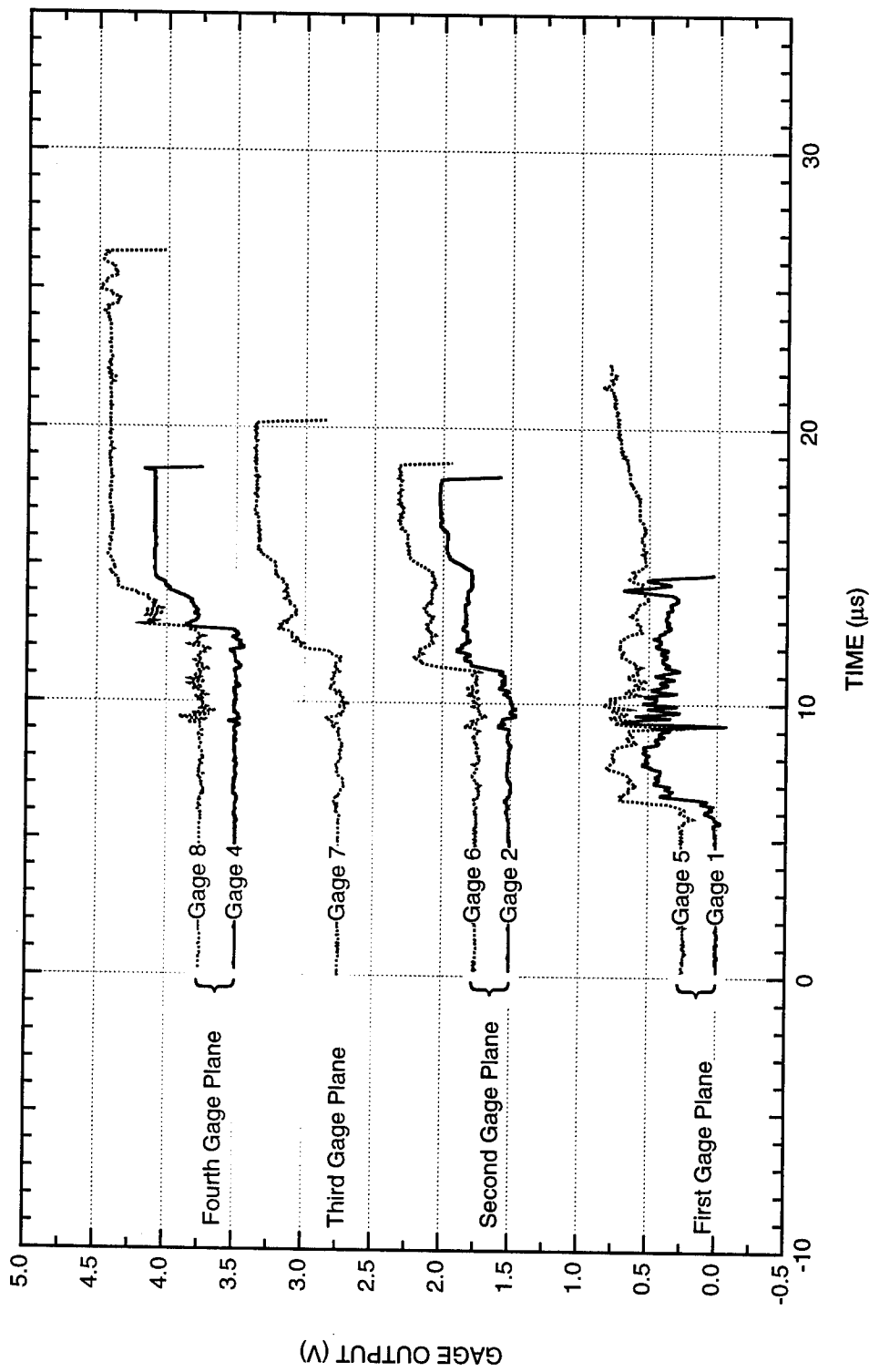


Figure B-95. Summary of the output of all particle velocity gages in HPEOS Experiment 13.

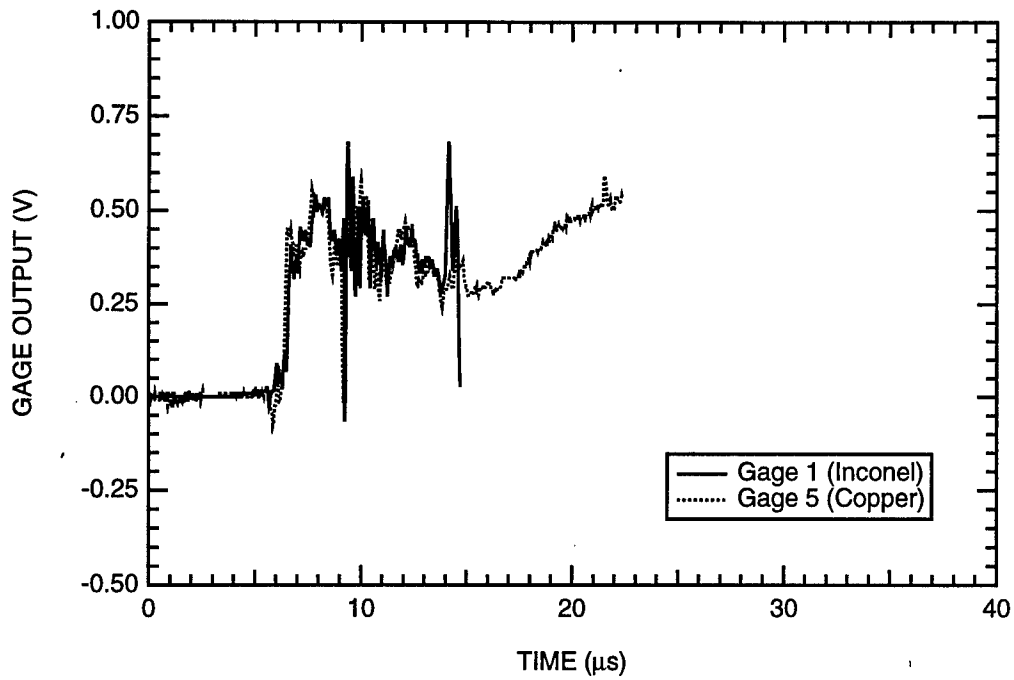


Figure B-96. Output of the particle velocity gages at the first gage plane of HPEOS Experiment 13.

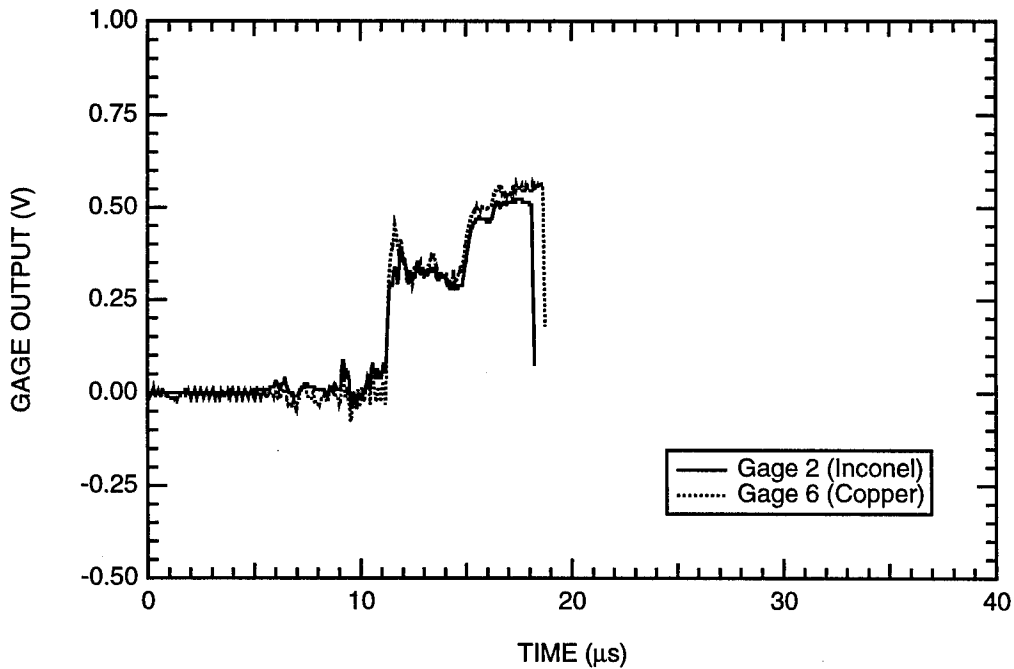


Figure B-97. Output of the particle velocity gages at the second gage plane of HPEOS Experiment 13.

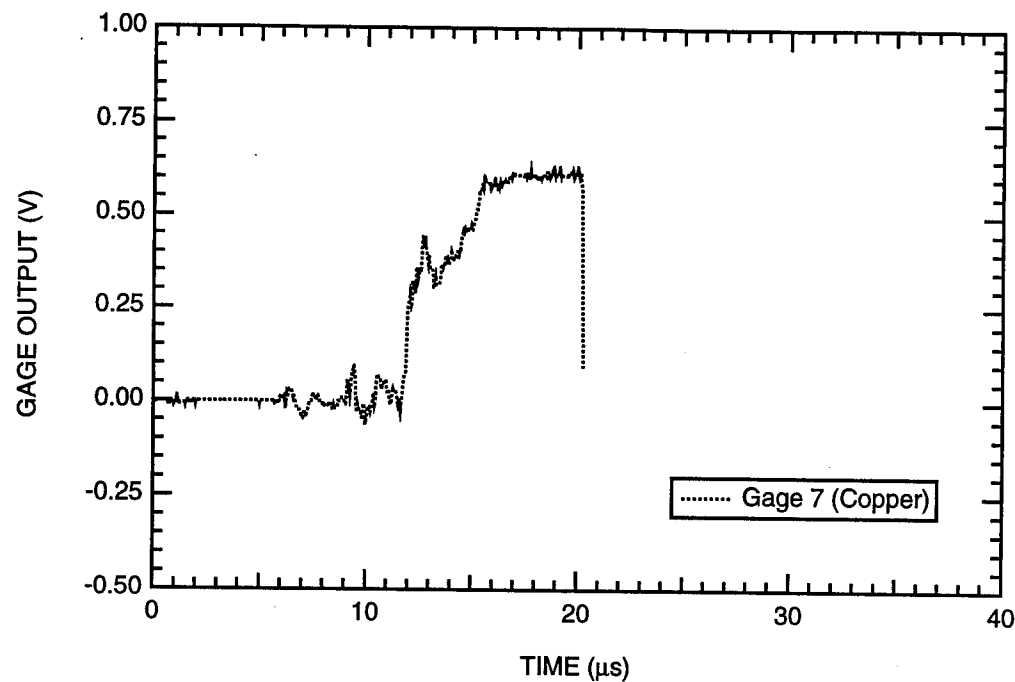


Figure B-98. Output of the particle velocity gages at the third gage plane of HPEOS Experiment 13.

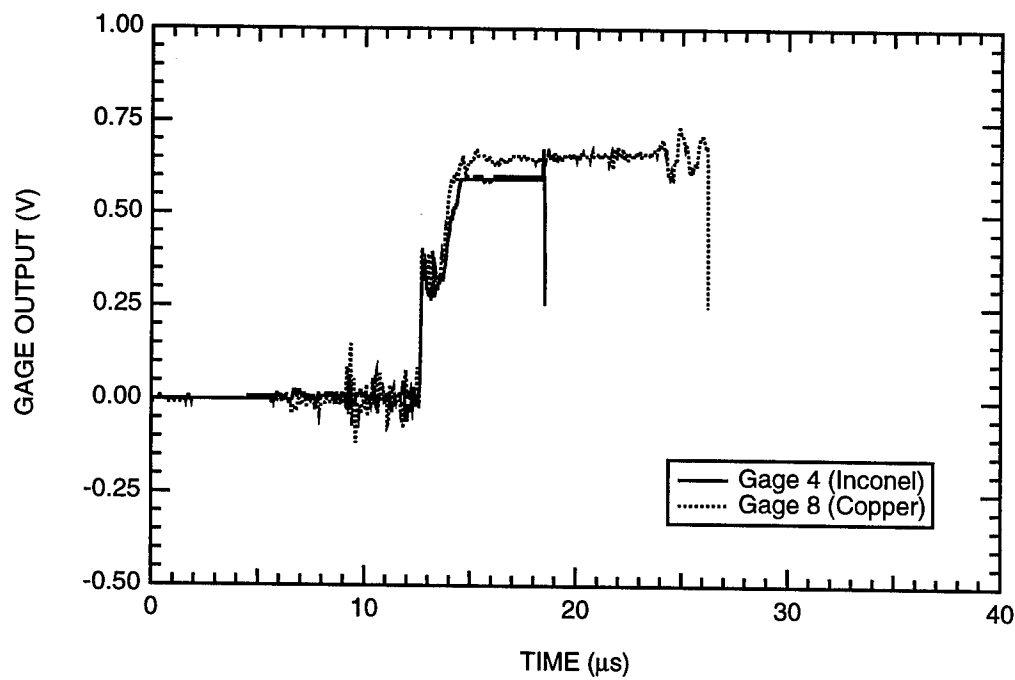


Figure B-99. Output of the particle velocity gages at the fourth gage plane of HPEOS Experiment 13.

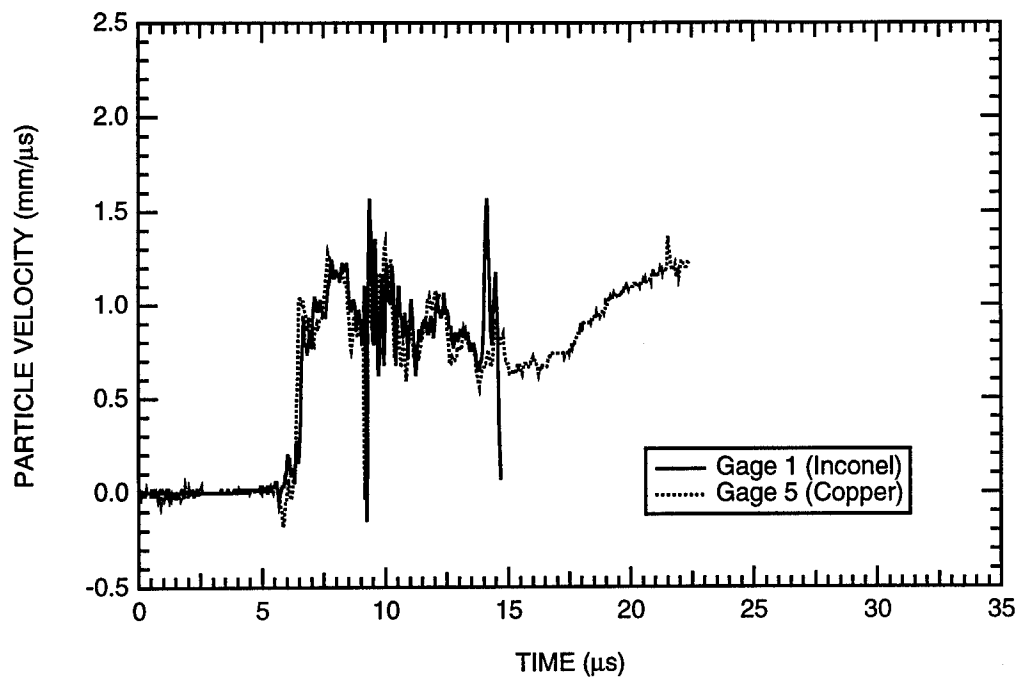


Figure B-100. Particle velocity histories at the first gage plane of HPEOS Experiment 13.

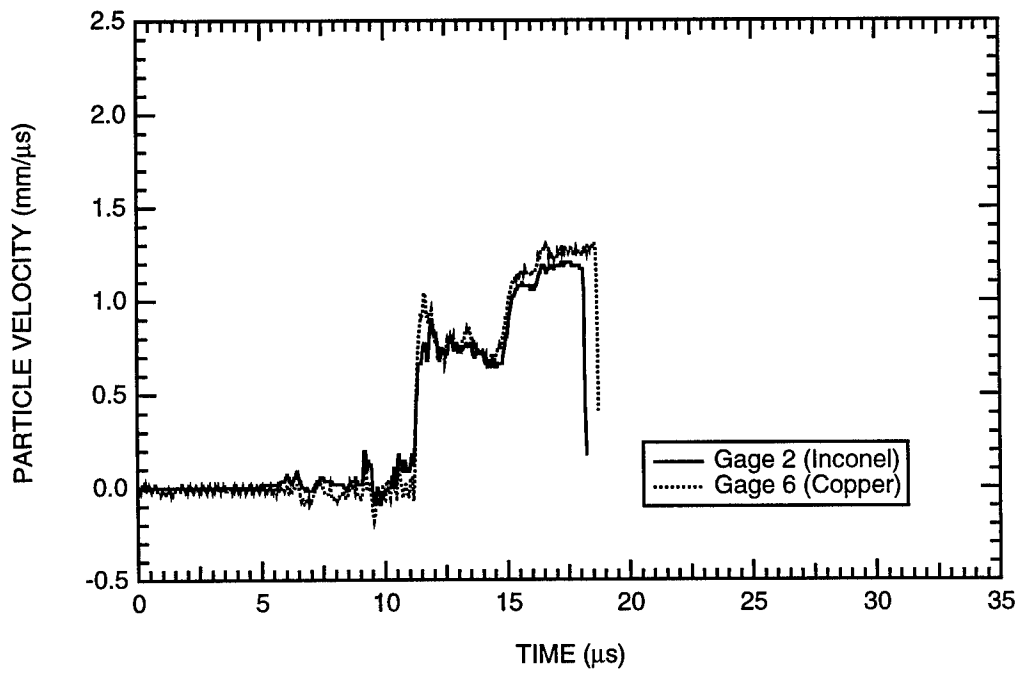


Figure B-101. Particle velocity histories at the second gage plane of HPEOS Experiment 13.

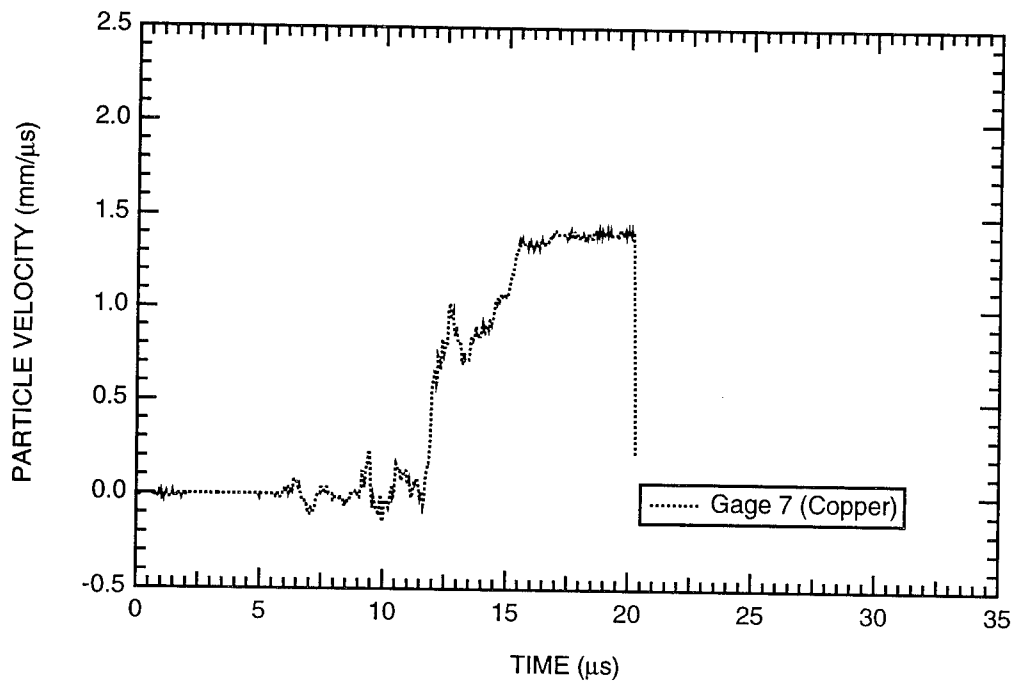


Figure B-102. Particle velocity histories at the third gage plane of HPEOS Experiment 13.

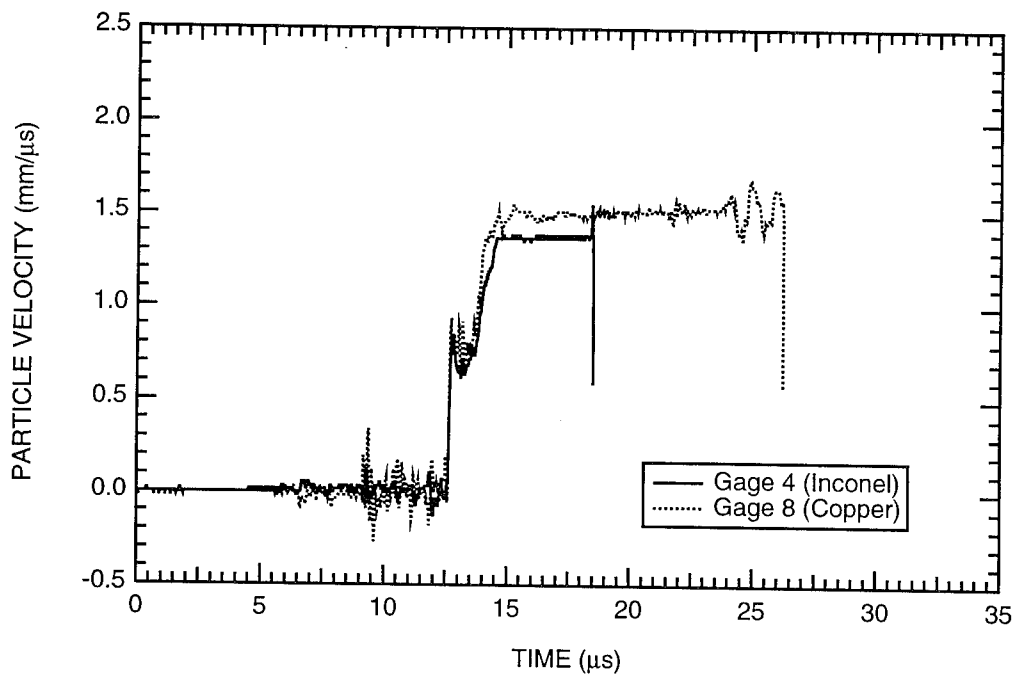


Figure B-103. Particle velocity histories at the fourth gage plane of HPEOS Experiment 13.

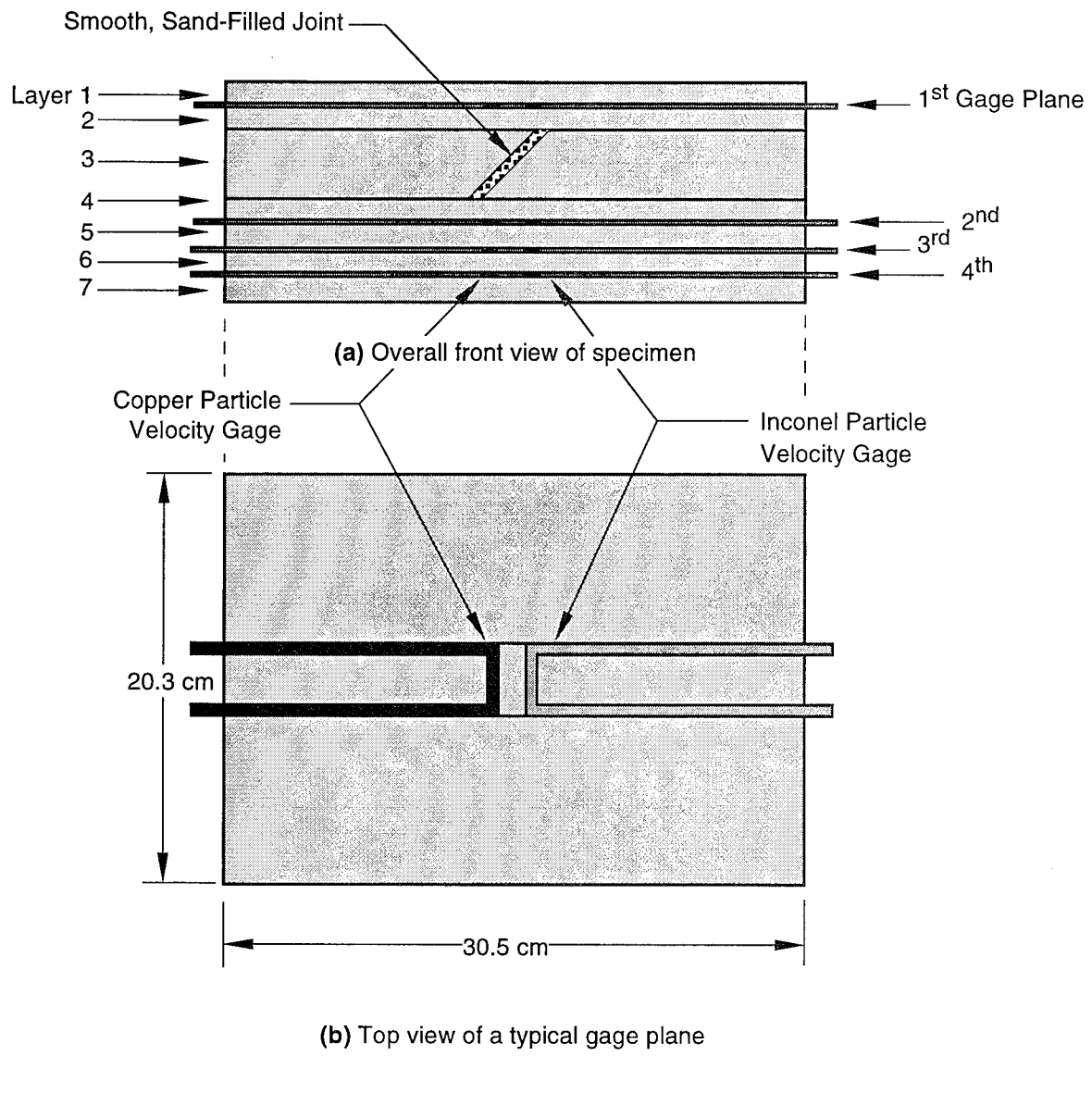


Figure B-104. Specimen configuration and dimensions for HPEOS Experiment 14 (marble).

Note: The explosive system used in the experiment and the thicknesses of the rock layers can be obtained from Table B-1.

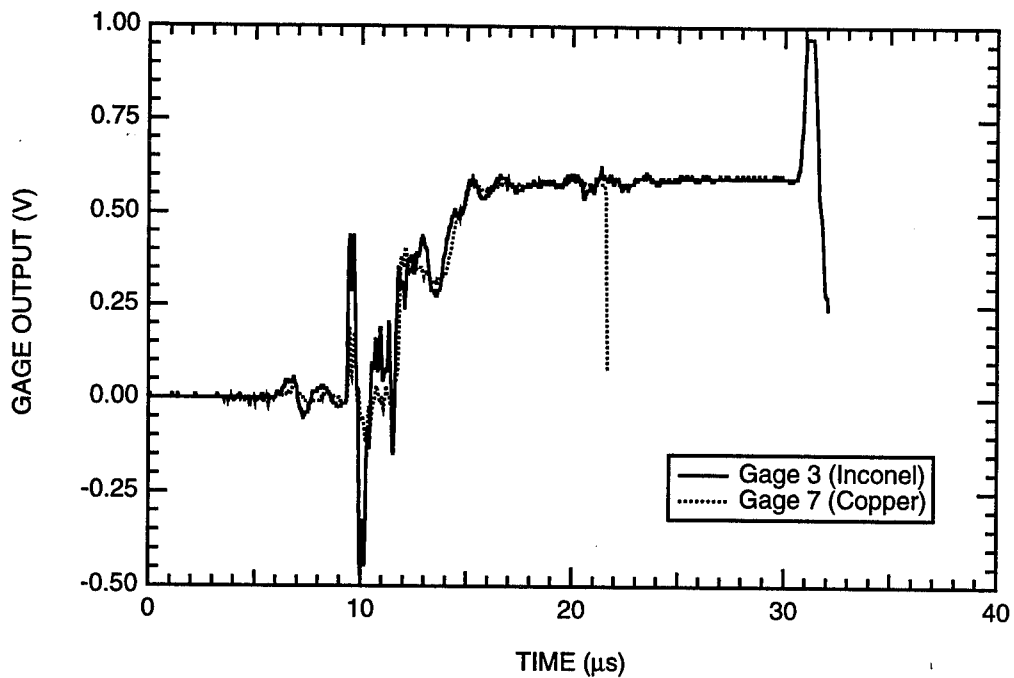


Figure B-108. Output of particle velocity gages at the third gage plane of HPEOS Experiment 14.

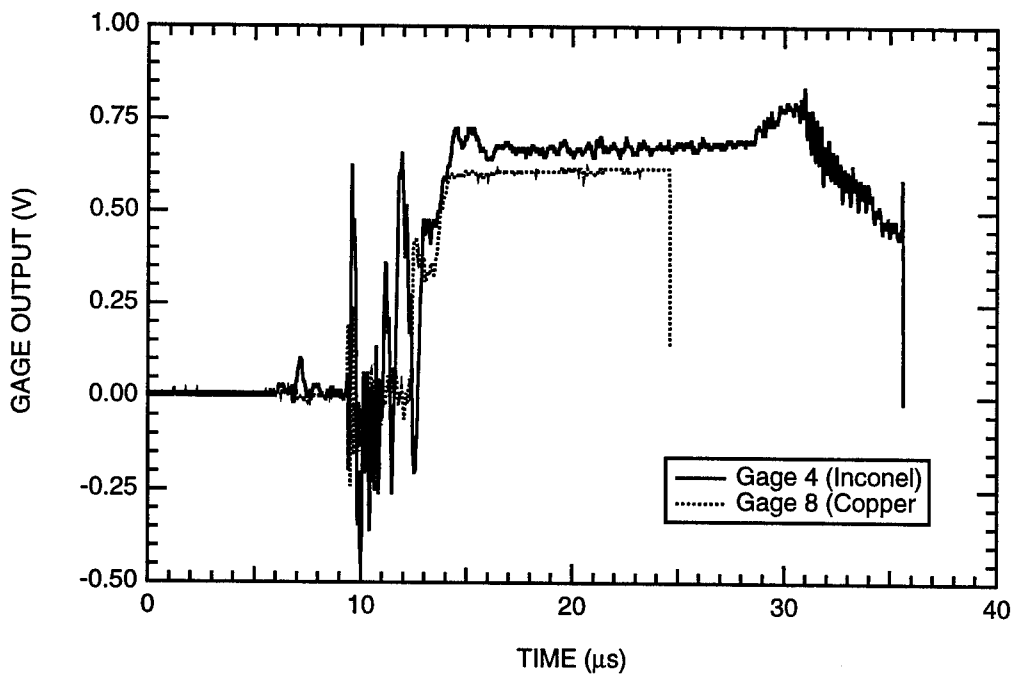


Figure B-109. Output of particle velocity gages at the fourth gage plane of HPEOS Experiment 14.

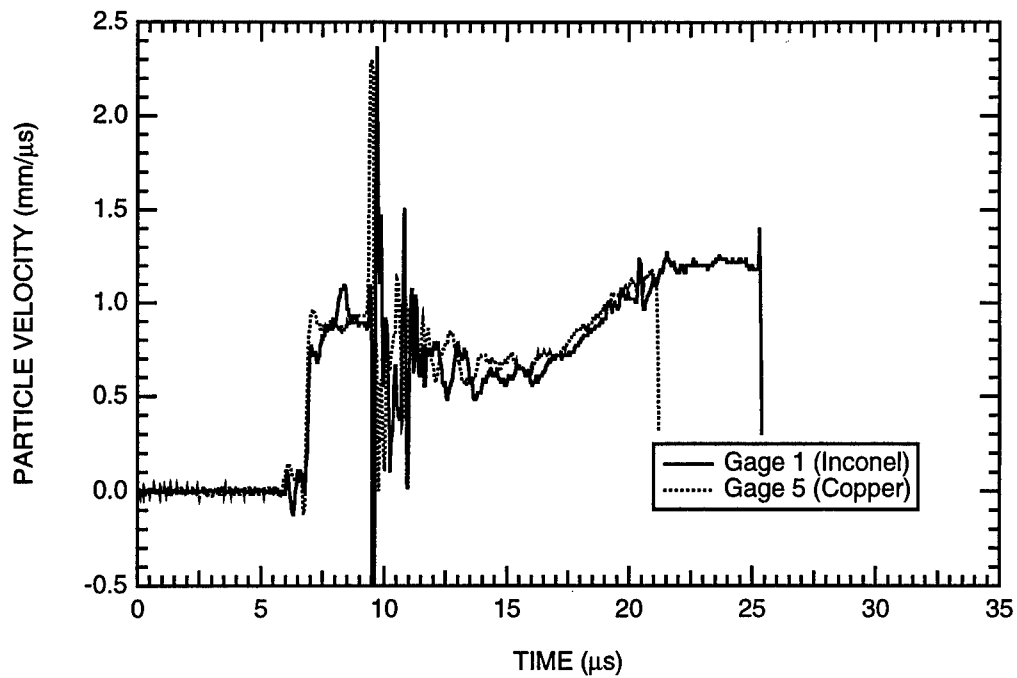


Figure B-110. Particle velocity histories at the first gage plane of HPEOS Experiment 14.

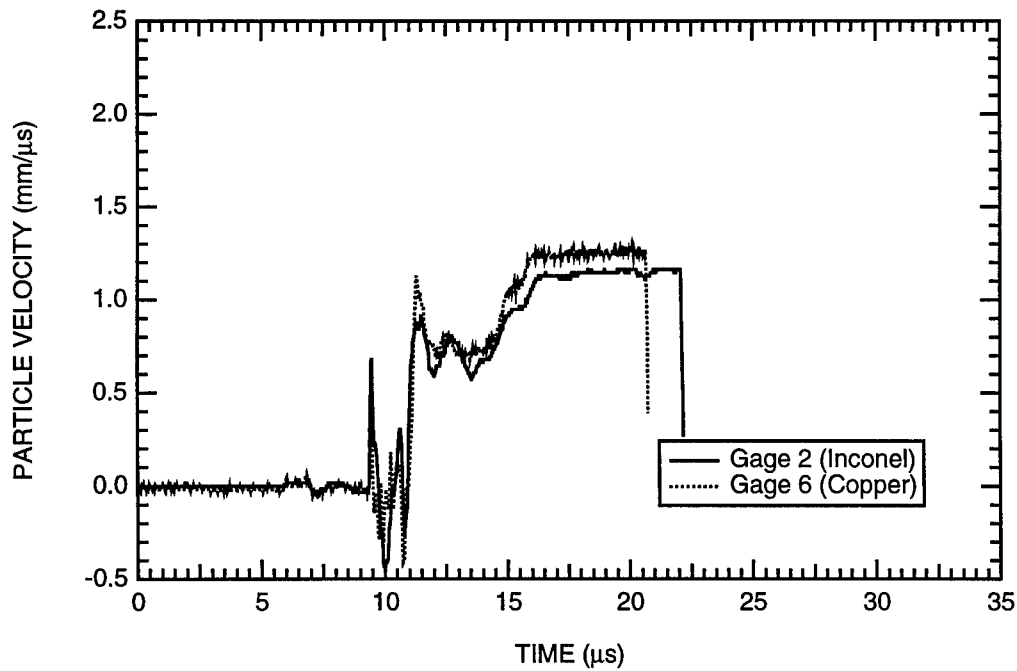


Figure B-111. Particle velocity histories at the second gage plane of HPEOS Experiment 14.

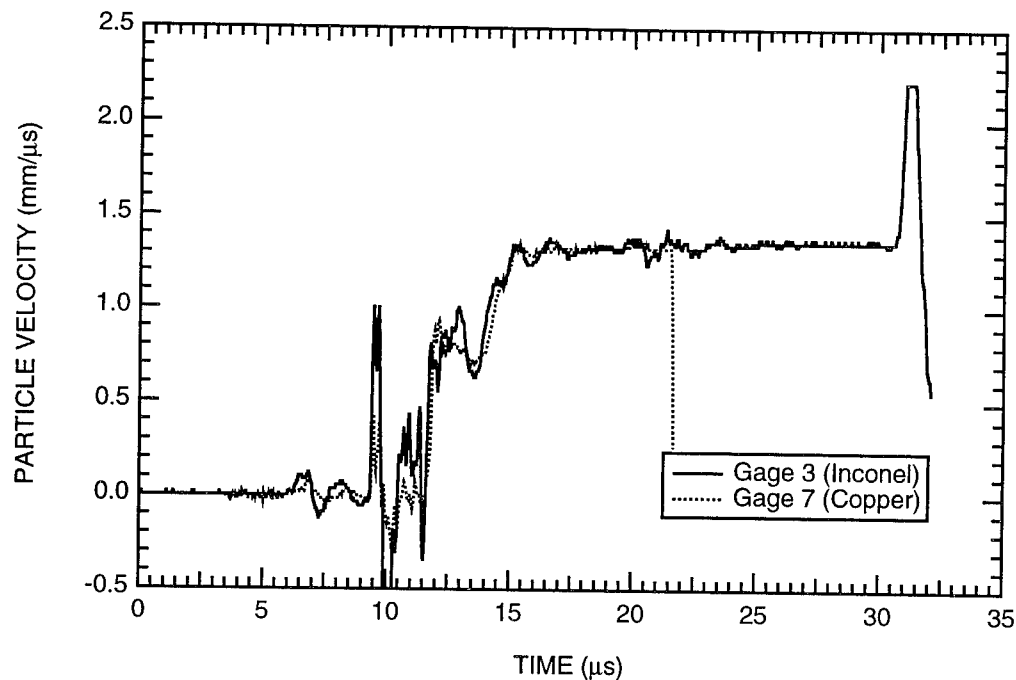


Figure B-112. Particle velocity histories at the third gage plane of

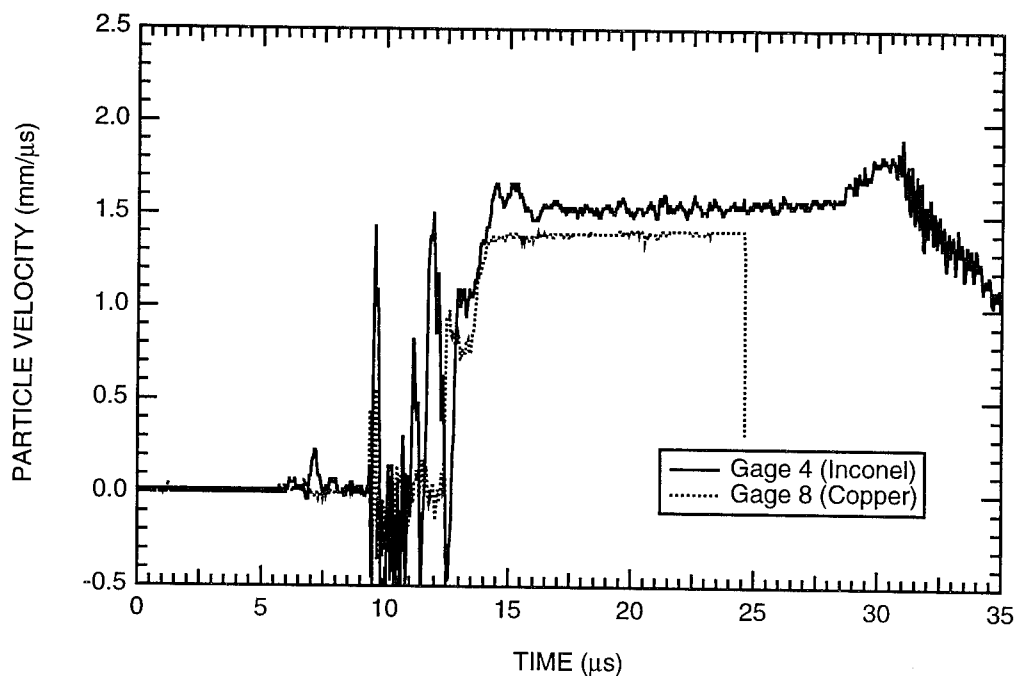
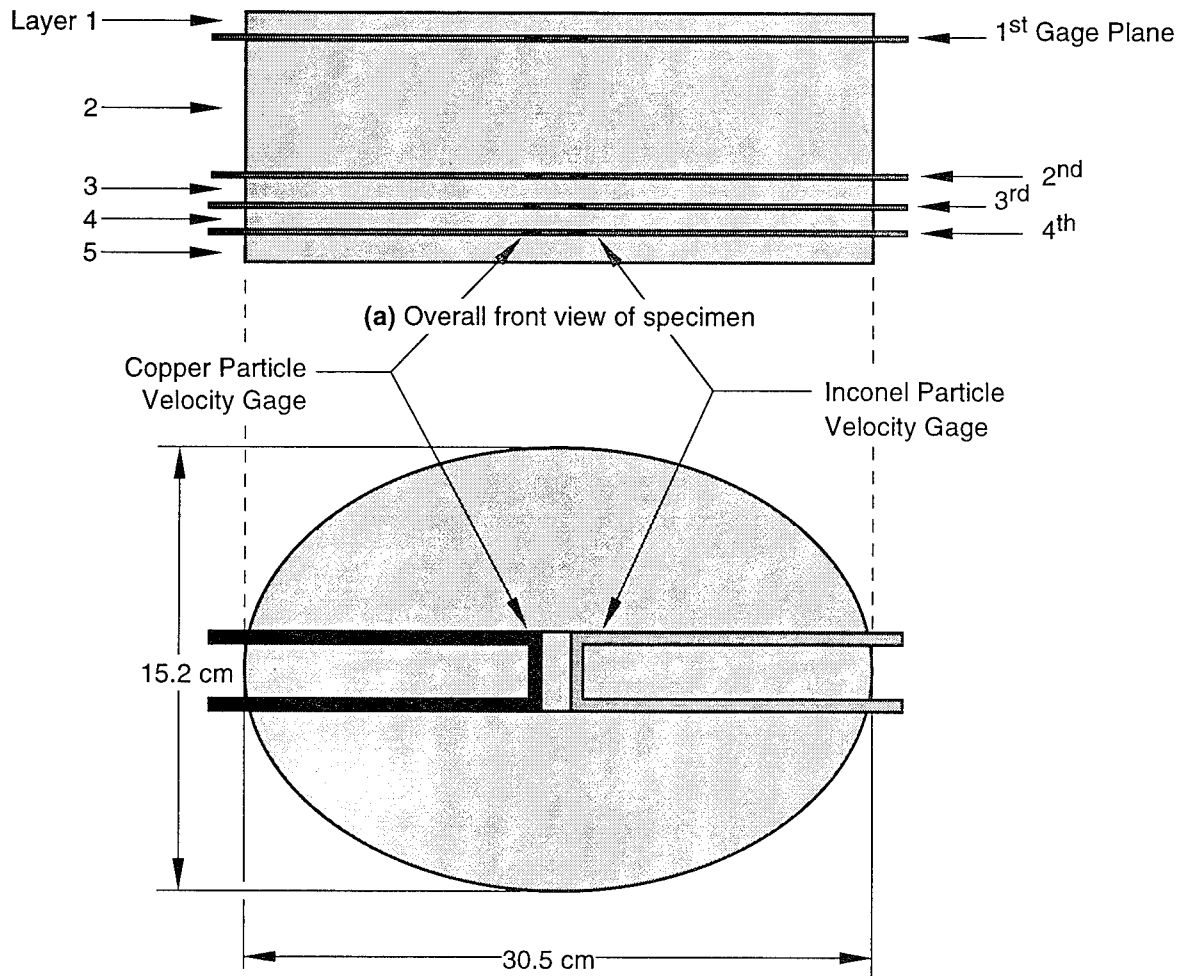


Figure B-113. Particle velocity histories at the fourth gage plane of HPEOS Experiment 14.



(b) Top view of a typical gage plane

Figure B-114. Specimen configuration and dimensions for HPEOS Experiment 16 (marble).

Note: The explosive system used in the experiment and the thicknesses of the rock layers can be obtained from Table B-1.

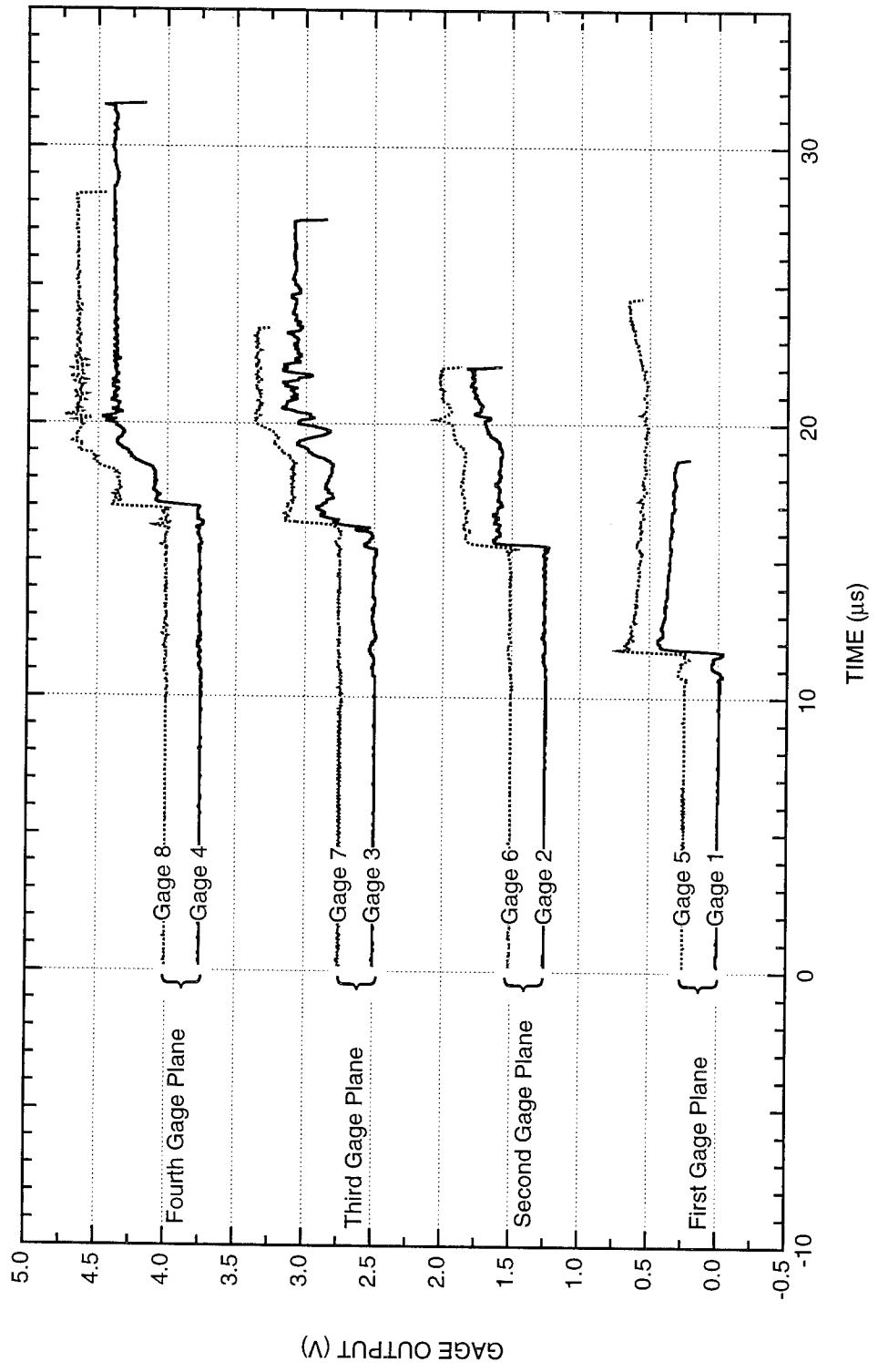


Figure B-115. Summary of the output of all particle velocity gages in HPEOS Experiment 16.

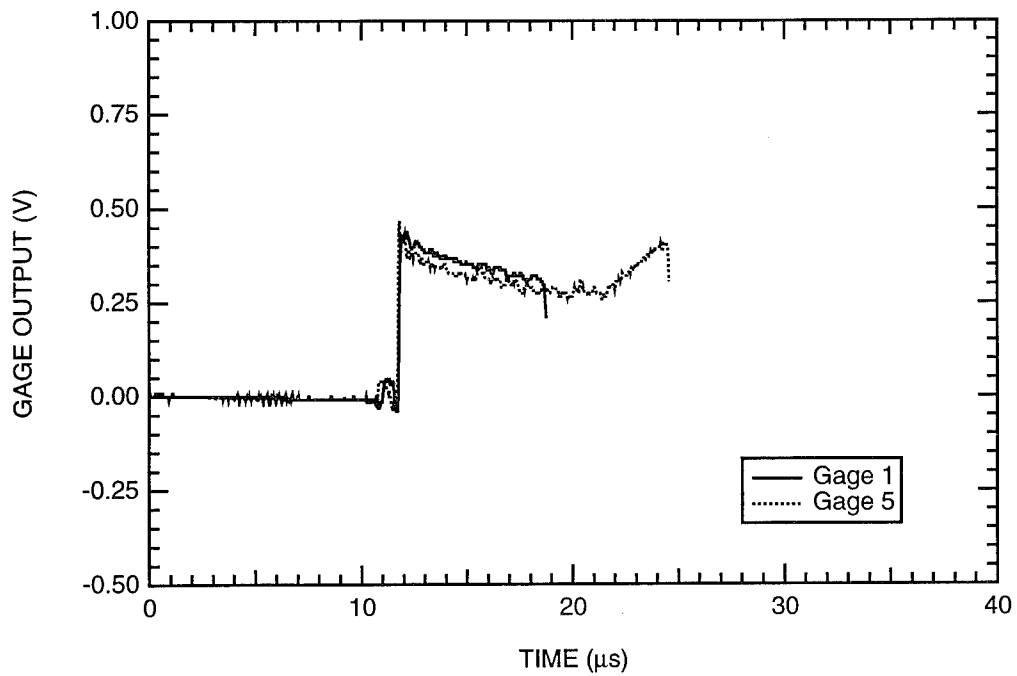


Figure B-116. Output of particle velocity gages at the first gage plane of HPEOS Experiment 16.

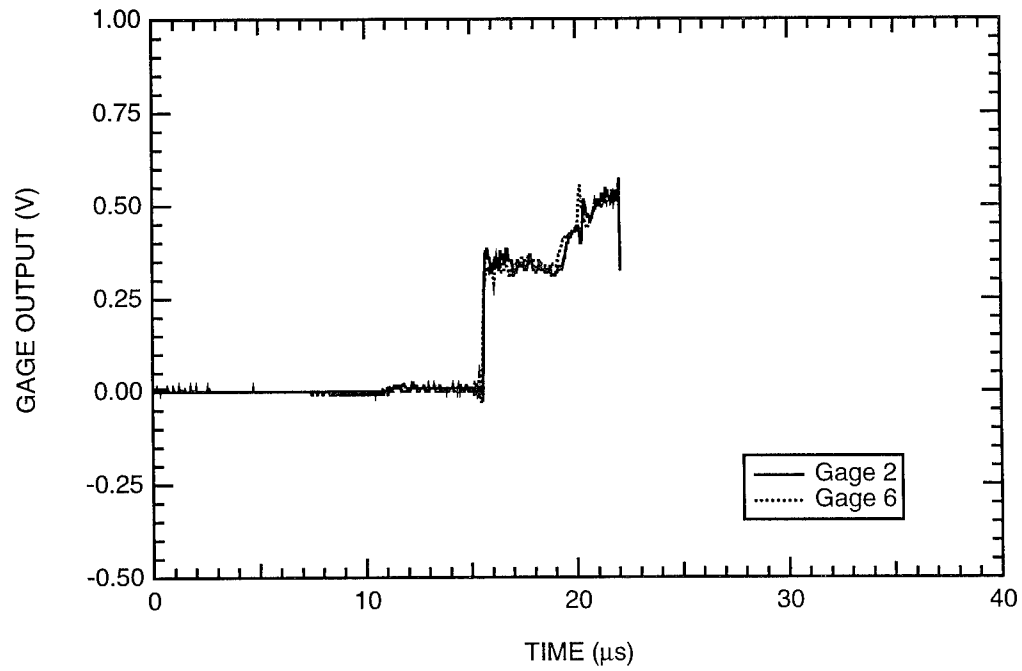


Figure B-117. Output of particle velocity gages at the second gage plane of HPEOS Experiment 16.

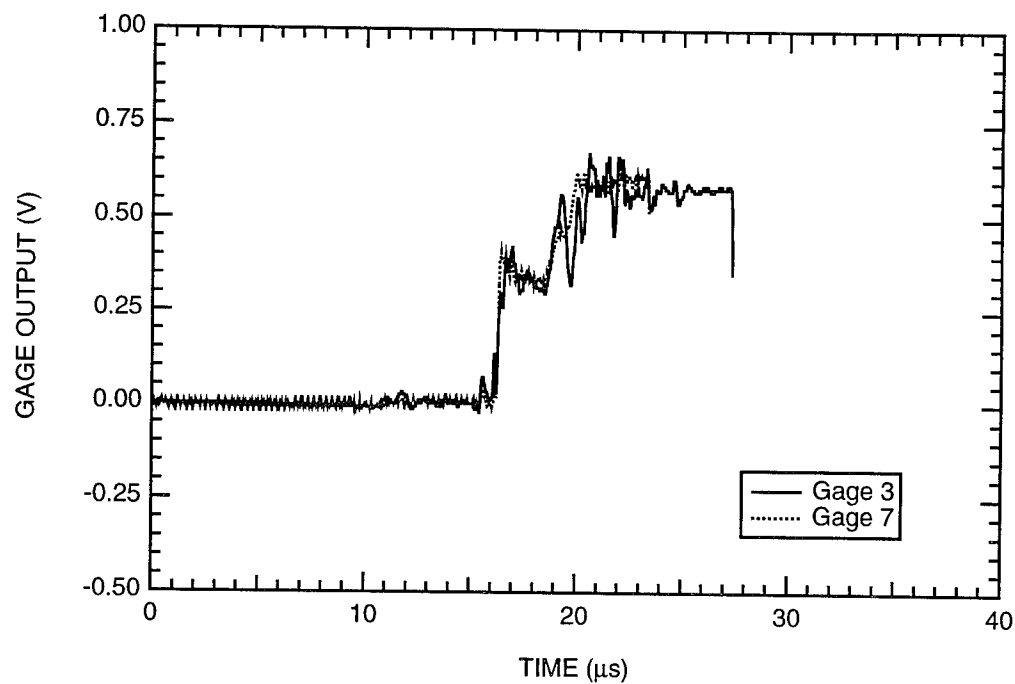


Figure B-118. Output of particle velocity gages at the third gage plane of HPEOS Experiment 16.

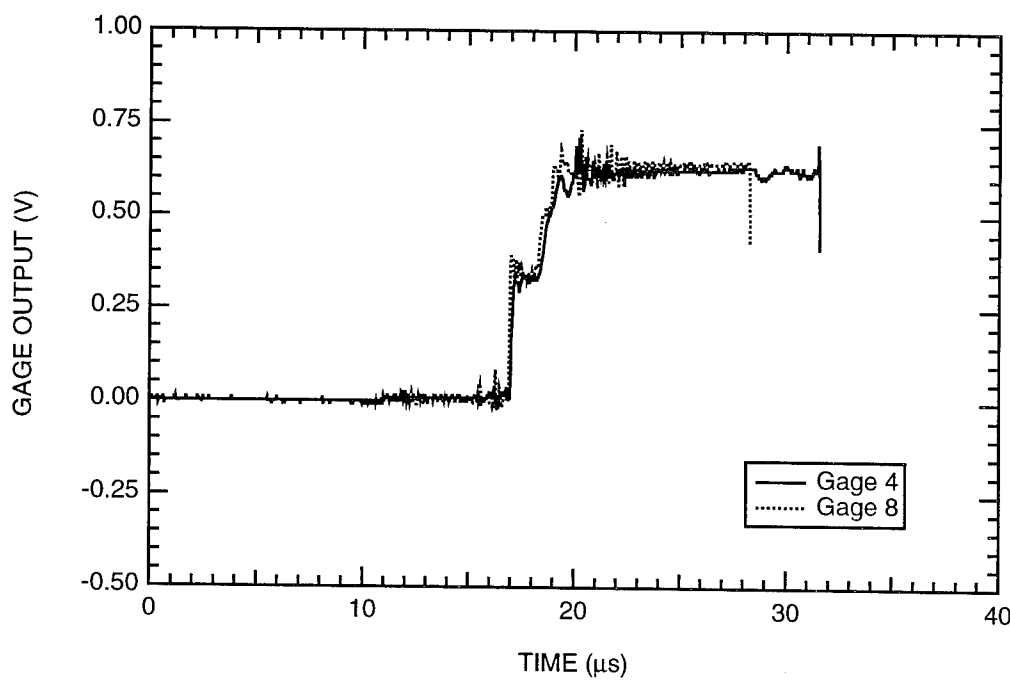


Figure B-119. Output of particle velocity gages at the fourth gage plane of HPEOS Experiment 16.

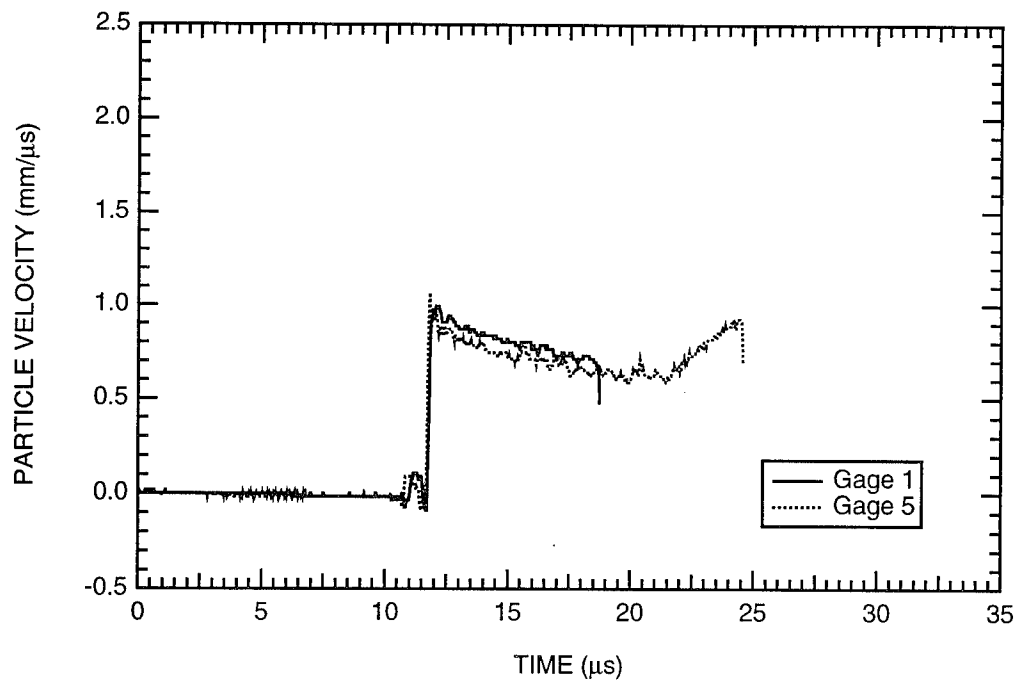


Figure B-120. Particle velocity histories at the first gage plane of HPEOS Experiment 16.

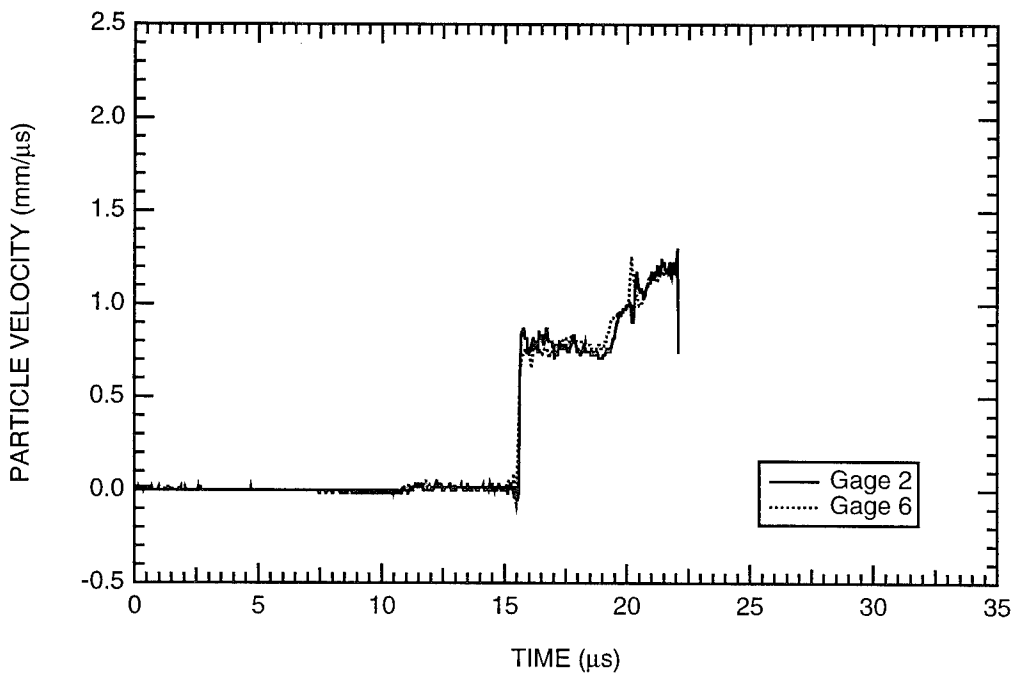


Figure B-121. Particle velocity histories at the second gage plane of HPEOS Experiment 16.

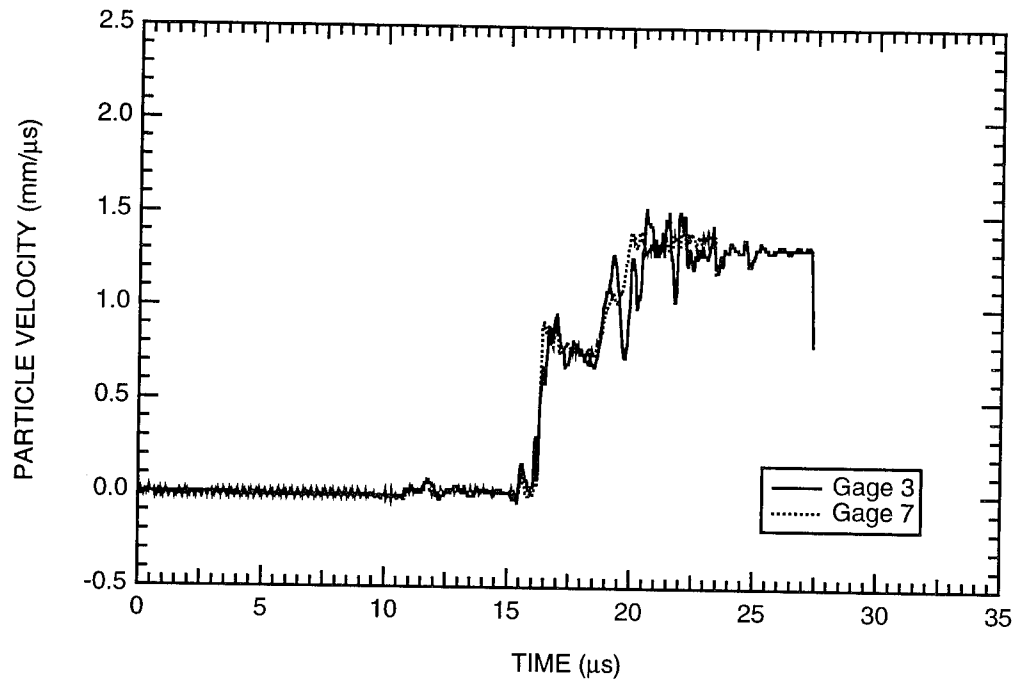


Figure B-122. Particle velocity histories at the third gage plane of

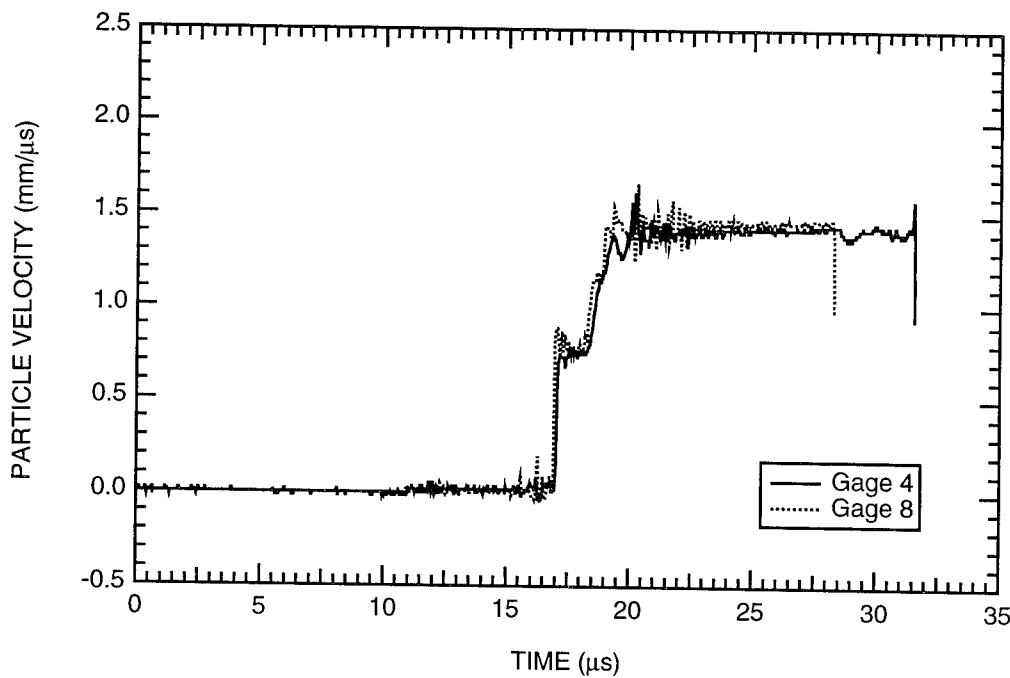


Figure B-123. Particle velocity histories at the fourth gage plane of HPEOS Experiment 16.

## **APPENDIX C**

### **MODEL SOLUTIONS FOR THE INTERACTION OF STEADY-STATE COMPRESSION WAVES WITH A BOUNDARY**

This appendix contains a copy of the technical paper entitled "Model Solutions for the Interaction of Steady-State Compression Waves with a Boundary." This paper was written by M. Cowperthwaite and will be published in the proceedings of the 4<sup>th</sup> International Symposium on Behavior of Dense Media Under Dynamic Pressures, to be held in Tours, France, 5-9 June 1995.

# MODEL SOLUTIONS FOR THE INTERACTION OF STEADY-STATE COMPRESSION WAVES WITH A BOUNDARY

M. Cowperthwaite

SRI International  
333 Ravenswood Avenue  
Menlo Park, CA 94025

## C.1 ABSTRACT.

Model solutions for the flows produced by the reflection of steady-state compression waves from boundaries with different shock impedances are presented to exemplify flow features that are ignored when the incident wave is treated as a shock discontinuity.

## C.2 INTRODUCTION.

Advances in measuring particle velocity histories in shock wave experiments lead to an interest in flow features that are associated with the structure of the shock. This paper is concerned with such flow features produced when a steady-state compression wave (SSCW) with a finite rise time is reflected from a boundary. Model solutions for such flows, produced when SSCWs with different shapes are reflected from boundaries with different shock impedances, are constructed by the method of characteristics. Particular solutions are presented to demonstrate the explicit dependence of these flows on the shape of the SSCW and exemplify flow features that are ignored when the compression wave is treated as a shock discontinuity.

## C.3 MATERIAL MODEL AND CHARACTERISTIC EQUATIONS.

For tractability in constructing our model solutions, we assume that the material supporting an incident SSCW has a linear constitutive relationship, and a constant propagation velocity C. Then the stress ( $\sigma$ ), particle velocity (u), and specific volume (v) in the SSCW are related by the equations,

$$\sigma = \rho_0 Cu \quad (C-1) \quad \sigma = \rho_0 C^2 \left( 1 - \frac{v}{v_0} \right) \quad (C-2)$$

where the density  $\rho = v^{-1}$ , the subscript o denotes the material's initial state and  $u_0 = \sigma_0 = 0$ .

We let t and h denote time and Lagrange distance, and write the flow equations expressing the balance of mass and momentum as

$$\frac{\partial v}{\partial t} = v_0 \frac{\partial u}{\partial h} \quad (C-3) \quad \frac{\partial u}{\partial t} = -v_0 \frac{\partial \sigma}{\partial h} \quad (C-4)$$

For our linear material, Equations (C-2), (C-3), and (C-4) can be combined to obtain its characteristic equations<sup>[1]</sup> as,

$$\frac{\partial h}{\partial \alpha} = C \frac{\partial t}{\partial \alpha} \quad , \quad \frac{\partial u}{\partial \alpha} = -\frac{v_0}{C} \frac{\partial \sigma}{\partial \alpha} \quad \text{along} \quad C_+ \quad (C-5)$$

$$\frac{\partial h}{\partial \beta} = -C \frac{\partial t}{\partial \beta} , \quad \frac{\partial u}{\partial \beta} = \frac{v_0}{C} \frac{\partial \sigma}{\partial \beta} \quad \text{along } C_- \quad (C-6)$$

where  $C_+$  and  $C_-$  are used, respectively, to denote the forward facing and backward facing characteristics.

Integrating Equations (C-5) and (C-6), and introducing the Riemann invariants  $r$  and  $s^{[1]}$  leads to the equations,

$$t = \frac{h}{C} + R(\beta) , \quad u + \frac{\sigma}{\rho_0 C} = 2r(\beta) \text{ along } C_+ \quad (C-7)$$

$$t = -\frac{h}{C} + S(\alpha) , \quad u - \frac{\sigma}{\rho_0 C} = 2s(\alpha) \text{ along } C_- \quad (C-8)$$

It follows from Equations (C-7) and (C-8) that the  $C_+$  and  $C_-$  characteristics in the  $(h-t)$  plane are straight lines, and that  $u$  and  $\sigma$  are related to  $r$  and  $s$  by the equations,

$$u = r - s \quad (C-9) \quad \sigma = \rho_0 C (r + s) \quad (C-10)$$

When  $r$  and  $s$  are known functions of  $\alpha$  and  $\beta$ , the equations  $\beta = R^{-1}(t-h/C)$ ,  $\alpha = S^{-1}(t+h/C)$ , Equations (C-9) and (C-10) define  $u$  and  $\sigma$  as functions of  $h$  and  $t$ , and the equation for  $v$  in terms of  $h$  and  $t$  follows from Equation (C-2).

#### C.4 THE REFLECTED FLOW PROBLEM.

We will consider the flows produced when a SSCW propagates to the right and impacts another material with a different shock impedance. The SSCW has a finite rise time ( $T$ ) and the impact surface has a Lagrange position  $h = L$ . For convenience, we also assume that the bounding material (BM) has a linear constitutive relationship, and we denote its properties by the subscript  $b$ . The equations governing the flow in BM can then be obtained by writing a subscript  $b$  on the parameters,  $C$ ,  $R(\beta)$ ,  $S(\alpha)$ ,  $r(\beta)$ ,  $s(\alpha)$ , and  $(\rho_0 C)$  in Equations (C-7) and (C-8). Figure C-1 shows a typical  $(t/T - h/CL)$  diagram for such a flow produced by the reflection of a SSCW from a material BM with a higher propagation velocity  $C_b > C$ , when the interface  $BB'$  is situated at  $L/CT = 1.5$ .

To be more definitive when considering Figure C-1, we note that  $OI2C$  represents the incident SSCW,  $2I'R3$  represents the steady state reflected wave (SSRW),  $II'2$  represents the region of penetration produced by the interaction of the reflected and incident waves, and  $II''TW$  represents the SSCW transmitted into BM. The parallel straight lines emanating from  $OC$  are the  $C_+$  characteristics in the incident SSCW. The parallel straight lines emanating from  $II'$  with a negative slope are the  $C_-$  characteristics in the SSRW and those emanating from  $II'$  with a positive slope are the  $C_+$  characteristics in the transmitted SSCW.

Figure C-1 shows clearly two significant features of the flow produced by the reflection of our incident SSCW from  $BB'$ . The first, that the penetration region  $II'2$  occurs because  $OI2C$  has a finite rise time. The second, that for linear materials, the flows in the steady-state transmitted and reflected waves have the same rise time as  $OI2C$  and are determined, respectively, by the flow conditions along  $II'$  and  $2I'$ . Moreover, in the limit as the rise time in the incident SSCW approaches zero and

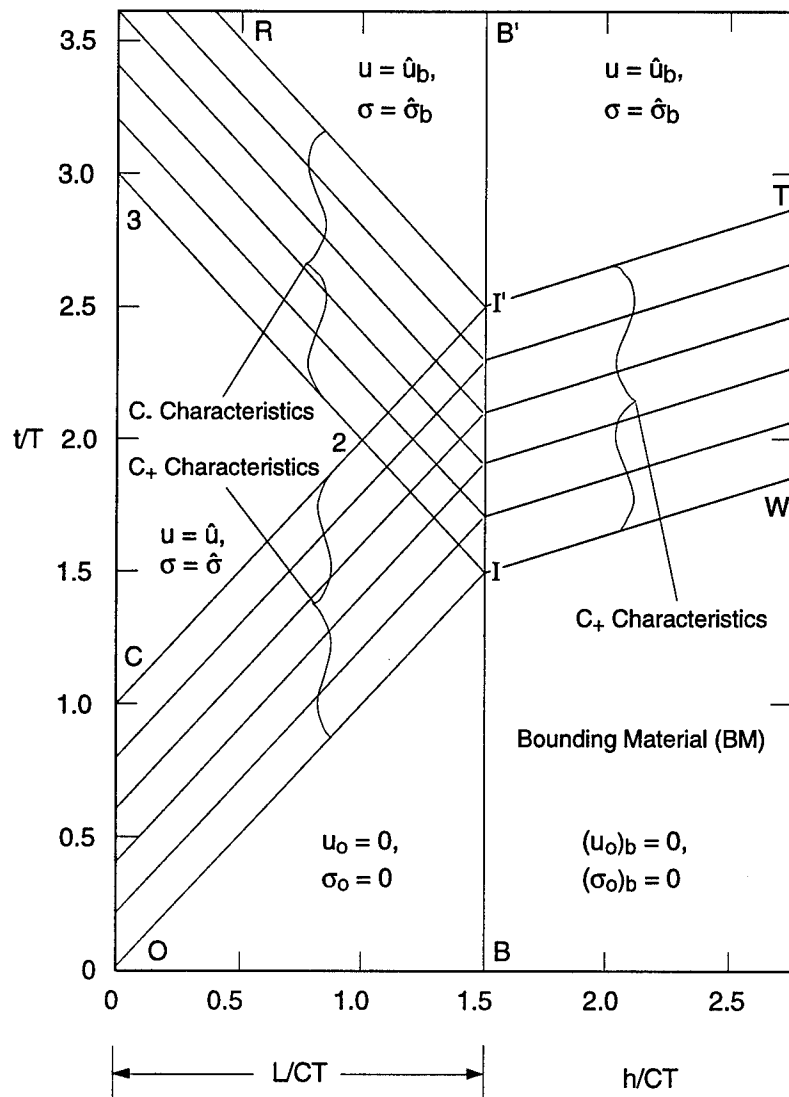


Figure C-1. A nondimensional Lagrange distance-time diagram for the flow produced by the reflection of a steady-state compression wave from a boundary with a higher shock impedance when the material supporting the incident wave and the bounding material (BM) have linear stress ( $\sigma$ ) - particle velocity ( $u$ ) relationships.

$C_1'$  approaches  $OI$ , it is clear that the penetration region  $II'2$  will disappear, the incident wave will become a step discontinuity represented by  $OI$ , and the reflected and transmitted waves will also become step discontinuities, represented respectively, by  $I3$  and  $IW$ . For these reasons, we are particularly interested in the penetration region and how its flow is governed by the shape of the incident SSCW.

After consider these qualitative flow features, it is convenient to define our reflected flow problem as that of calculating the flow in the penetration region when the flow in the incident SSCW is prescribed. Because we will refer to Figure C-1 when making such calculations by the method of characteristics, we first derive the equations for the  $C_+$  characteristics in  $OI'C$  and  $II'TW$  and the  $C_-$  characteristics in  $II'R3$ .

### C.5 THE EQUATIONS FOR THE CHARACTERISTICS IN THE $(t/T - h/CT)$ PLANE.

First, we divide the first equation in Equation (C-7) by  $T$  and set  $R(\beta)/T = \beta$  to obtain the equation for the  $C_+$  characteristics in  $OI2C$  as

$$\frac{t}{T} = \frac{h}{CT} + \beta \quad , \quad 0 \leq \beta \leq 1 \quad (C-11)$$

Next, we use  $t^B$  to denote the time along the interface  $BB'$  and write the equations for the  $C_+$  characteristics in  $BM$  emanating from  $II'$  as

$$\frac{t-t^B}{T} = \frac{h-L}{C_b T} \quad , \quad t_I^B \leq t^B \leq t_T^B \quad (C-12)$$

Combining Equation (C-12) with the equation obtained by setting  $t = t^B$ ,  $h = L$ , and  $\beta = \beta_b$ , in Equation (C-11), then gives the equation for the  $C_+$  characteristics in  $II'TW$  as

$$\frac{t}{T} = \frac{C}{C_b} \left( \frac{h}{CT} \right) + \frac{L}{CT} \left( 1 - \frac{C}{C_b} \right) + \beta_b \quad , \quad 0 \leq \beta_b \leq 1 \quad (C-13)$$

A procedure, similar to that used to derive Equation (C-13), gives the equation for the  $C_-$  characteristics emanating from  $II'$  as

$$\frac{t}{T} = -\frac{h}{CT} + \frac{2L}{CT} + \alpha \quad , \quad 0 \leq \alpha \leq 1 \quad (C-14)$$

These equations for the  $C_+$  and  $C_-$  characteristics will be used to construct solutions to our reflected flow problem for incident SSCWs with different shapes. The flows produced by a linear ramp wave will be constructed before those produced by a nonlinear wave.

### C.6 INTERACTION OF A RAMP WAVE WITH A BOUNDARY.

Before writing the equations for the ramp wave, it is convenient to derive the equations for  $r$  and  $s$  and  $r_b$  and  $s_b$  in an incident and transmitted SSCW. Combining Equations (C-1), (C-9), and (C-10) gives the equation,  $r-s = r+s$ , which shows that,  $s=0$  and  $r=u$ , in an incident SSCW. Similarly, it can be shown that,  $s_b=0$  and  $r_b=u_b$ , in the transmitted SSCW.

#### C.6.1 Flow in the Ramp Wave.

We use  $\hat{u}$  and  $\hat{\sigma}$  to denote the peak particle velocity and peak stress in our incident ramp wave, and write its equations for  $u$  and  $\sigma$  as

$$\frac{u}{\hat{u}} = \frac{\sigma}{\hat{\sigma}} = \frac{1}{T} \left( t - \frac{h}{C} \right) \quad (C-15)$$

Equations (C-11) and (C-15) then allow us to write the equations for  $r$  and  $s$  in the ramp wave as

$$r = \hat{u}\beta \quad , \quad s = 0 \quad \text{for } 0 \leq \beta \leq 1 \quad (C-16)$$

We can now use the equations relating  $u$  and  $\sigma$  to  $r$  and  $s$ , and the boundary conditions along  $\Pi'$  at the interface,  $u^B = u_b$  and  $\sigma^B = \sigma_b$ , to derive the equations governing the flows produced by the reflection of the ramp wave at the boundary.

### C.6.2 Conditions Along $\Pi'$ .

Remembering, that  $r = \hat{u}\beta$  in OI2C and that  $s_b = 0$  in  $\Pi' TW$ , Equations (C-9) and (C-10) allow us to write the boundary conditions along  $\Pi'$  as

$$u^B = \hat{u}\beta - s^B = r_b \quad (C-17)$$

$$\sigma^B = \rho_0 C (\hat{u}\beta + s^B) = (\rho_0 C)_b r_b \quad (C-18)$$

Combining Equations (C-17) and (C-18) gives the following equations for  $s^B$  and  $r_b$

$$s^B = \hat{u} \left( \frac{1-Z}{1+Z} \right) \beta \quad (C-19) \quad r_b = \frac{2Z}{(1+Z)} \hat{u} \beta_b \quad (C-20)$$

where  $Z = \rho_0 C / (\rho_0 C)_b$ .

We can now calculate the flow in the penetration region  $\Pi'2$ , the SSRW 2IR3 and the transmitted wave  $\Pi' TW$ .

### C.6.3 The Flow in the Penetration Region $\Pi'2$ .

To obtain the equations for the flow in  $\Pi'2$ , we first use the condition that  $\alpha = \beta$  along  $\Pi'$  and set  $\alpha = \beta$  in Equation (C-19) to obtain the equation for  $s$  in the reflected wave as

$$s = \hat{u} \left( \frac{1-Z}{1+Z} \right) \alpha \quad , \quad 0 \leq \alpha \leq 1 \quad (C-21)$$

We then use Equations (C-9), (C-10), (C-16), and (C-21) to obtain the equations for  $u$  and  $\sigma$  in  $\Pi'2$  as

$$u = \hat{u} \left( \beta - \frac{(1-Z)}{(1+Z)} \alpha \right) \quad (C-22) \quad \sigma = \hat{\sigma} \left( \beta + \frac{(1-Z)}{(1+Z)} \alpha \right) \quad (C-23)$$

and use Equation (C-11) and (C-14) to rewrite these equations in terms of  $h$  and  $t$  as

$$u = \frac{2\hat{u}Z}{(1+Z)} \left[ \frac{t}{T} - \frac{L}{CT} + \frac{1}{Z} \left( \frac{L-h}{CT} \right) \right] \quad (C-24)$$

$$\sigma = \frac{2\hat{\sigma}Z}{(1+Z)} \left[ \frac{L-h}{CT} + \frac{1}{Z} \left( \frac{t}{T} - \frac{L}{CT} \right) \right] \quad (C-25)$$

for  $0 \leq t/T - L/CT \leq 1$  and  $0 \leq (L-h)/CT \leq 1/2$ .

#### C.6.4 The Flows in the II' TW and 2I'R3.

The condition that  $u_b = r_b$  in a steady-state transmitted wave, together with Equations (C-20), (C-1), and (C-13) give the equations for  $u_b$  and  $\sigma_b$  in II' TW as,

$$\frac{u_b}{\hat{u}} = \frac{2Z}{(1+Z)} \left[ \frac{t}{T} - \frac{C}{C_b} \left( \frac{h}{CT} \right) - \frac{L}{CT} \left( 1 - \frac{C}{C_b} \right) \right] \quad (C-26)$$

$$\frac{\sigma_b}{\hat{\sigma}} = \frac{2}{(1+Z)} \left[ \frac{t}{T} - \frac{C}{C_b} \left( \frac{h}{CT} \right) - \frac{L}{CT} \left( 1 - \frac{C}{C_b} \right) \right] \quad (C-27)$$

The condition that  $\beta = 1$  in a SSRW, together with Equations (C-22), (C-23), and (C-14) give the equations for  $u$  and  $\sigma$  in 2I'R3 as

$$\frac{u}{\hat{u}} = \left[ 1 - \frac{(1-Z)}{(1+Z)} \left( \frac{t}{T} + \frac{h}{CT} - \frac{2L}{CT} \right) \right] \quad (C-28)$$

$$\frac{\sigma}{\hat{\sigma}} = \left[ 1 + \frac{(1-Z)}{(1+Z)} \left( \frac{t}{T} + \frac{h}{CT} - \frac{2L}{CT} \right) \right] \quad (C-29)$$

#### C.6.5 Flows Produced by the Reflection of the Ramp Wave from a Boundary.

We first consider the steady-state transmitted and reflected waves produced by the reflection of our ramp wave from the boundary. Subjecting Equations (C-26) and (C-27) and Equations (C-28) and (C-29), respectively, to the conditions that  $\beta_b = 1$  and  $\alpha = 1$  give the equations for the particle velocity ( $u_b$ ) and the stress ( $\sigma_b$ ) along I'T and I'R as

$$\frac{\hat{u}_b}{\hat{u}} = Z \frac{\hat{\sigma}_b}{\hat{\sigma}} = \frac{2Z}{1+Z} \quad (C-30)$$

It follows from these equations, that  $\hat{u}_b > \hat{u}$  and  $\hat{\sigma}_b < \hat{\sigma}$  when  $Z > 1$ , but that  $\hat{u}_b < \hat{u}$  and  $\hat{\sigma}_b > \hat{\sigma}$  when  $Z < 1$ . Consequently, the impact of the ramp wave produces a reflected rarefaction wave when  $\rho_0 C > (\rho_0 C)_b$ , but produces a reflected compression wave when  $\rho_0 C < (\rho_0 C)_b$ . Clearly, the equalities in Equation (C-30) can also be obtained from an impedance mismatch calculation for such linear materials in the ( $u-\sigma$ ) plane, when the incident, transmitted and reflected waves are treated as step discontinuities.

We now consider the flow in the penetration region II'2. For a SSCW with a finite rise time T as shown in Figure C-1, only the particles lying in the range,  $L/CT - 1/2 \leq h/CT \leq L/CT$ , enter the penetration region along I2, pass through it, and then leave along 2I'. Across I2 and 2I' the flow derivatives of these particles have jump discontinuities, but within II'2 they are constant. For this case, the values for the flow derivatives of  $u$  and  $\sigma$  in II'2 follow from Equations (C-24) and (C-25) as,  $\partial(u/\hat{u})/\partial(t/T) = 2Z/(1+Z)$ ,  $\partial(u/\hat{u})/\partial(h/CT) = -2/(1+Z)$ ,  $\partial(\sigma/\hat{\sigma})/\partial(t/T) = 2/(1+Z)$ , and

$\partial(\sigma/\hat{\sigma})/\partial(h/CT) = -2Z/(1+Z)$ . It is clear from our derivation of Equations (C-24) and (C-25) that these flow derivatives are constant because the incident SSCW is a ramp wave.

We next consider the curves of constant  $u$  and  $\sigma$  in  $\Pi'2$ . Differentiating Equations (C-24) and (C-25) gives the equations for the slopes of these  $u$  and  $\sigma$  contours, respectively, as

$$\left( \frac{\partial(t/T)}{\partial(h/CT)} \right)_u = \frac{1}{Z} \quad (C-31) \quad \left( \frac{\partial(t/T)}{\partial(h/CT)} \right)_\sigma = Z \quad (C-32)$$

It follows from Equations (C-31) and (C-32) that the  $u$  and  $\sigma$  contours in  $\Pi'2$  are parallel straight lines, and that the sum of the angles they make with the  $(h/CT)$  direction is  $\pi/4$ . When  $Z < 1$ , the  $u$  contours in  $\Pi'2$  are steeper than  $2I'$  but the  $\sigma$  contours are not, and consequently  $u$  decreases along  $2I'$  as  $\sigma$  increases. Thus, while  $\Pi'2$  is covered by the  $u$  contours that emanate from  $I2$ , it is covered by the  $\sigma$  contours that emanate from  $I2$  and  $2I'$ . Alternatively, when  $Z > 1$ , the  $\sigma$  contours are steeper than  $2I'$  but the  $u$  contours are not, and  $\sigma$  decreases along  $2I'$  as  $u$  increases.  $\Pi'2$  is then covered by the  $\sigma$  contours emanating from  $I2$  and by the  $u$  contours emanating from  $I2$  and  $2I'$ .

We continue this treatment of our reflected flow problem by considering the two limiting cases for the boundary, namely, a rigid wall and a free surface. However, because of space limitations, we will only consider the reflection of a ramp wave from a rigid wall and that of a nonlinear wave from a free surface.

## C.7 REFLECTION OF A RAMP WAVE FROM A RIGID WALL.

### C.7.1 Conditions Along $\Pi'$ .

Conditions at a rigid wall are obtained by letting  $Z \rightarrow 0$  and  $C_b \rightarrow \infty$  in pertinent equations presented here earlier. The boundary conditions for  $u$  and  $\sigma$  along  $BB'$  are obtained as,  $u^B = 0$  and  $\sigma^B = 2\hat{\sigma}\beta$ , by combining Equations (C-17) and (C-18) with the equations,  $s^B = \hat{u}\beta$  and  $r_b = 0$ , obtained respectively by setting  $Z = 0$  in Equations (C-19) and (C-20). The condition that  $t \rightarrow t^B$  as  $C_b \rightarrow \infty$  from Equation (7), shows that the  $C_+$  characteristics emanating from  $\Pi'$  become parallel to the  $h/CT$  axis when  $BM$  is treated as a rigid wall.

### C.7.2 The Reflected Flow.

The equations for  $u$  and  $\sigma$  in the penetration region  $\Pi'2$  are obtained by letting  $Z \rightarrow 0$  in Equations (C-24) and (C-25) as

$$\frac{u}{\hat{u}} = 2 \left( \frac{L-h}{CT} \right) \quad (C-33) \quad \frac{\sigma}{\hat{\sigma}} = 2 \left( \frac{t}{T} - \frac{L}{CT} \right) \quad (C-34)$$

Consequently,  $u$  is constant along particle paths and  $\sigma$  is constant along isochrones, and as shown by Equations (C-31) and (C-32), the slopes of the  $u$  and  $\sigma$  contours in the penetration regions are, respectively, infinite and zero when the boundary is a rigid wall.

Setting  $\beta = 1$  and  $Z = 0$  in Equations (C-22) and (C-23) gives the following equations for  $2I'R3$ ,  $u = \hat{u}(1-\alpha)$  and  $\sigma = \hat{\sigma}(1+\alpha)$ , which show that  $u/\hat{u}$  decreases from one to zero while  $\sigma/\hat{\sigma}$  increases from zero to two as  $\alpha$  increases from zero to one in the SSCW reflected from a rigid wall.

## C.8 THE REFLECTION OF A NONLINEAR WAVE FROM A FREE SURFACE.

### C.8.1 Flow in an Incident Nonlinear Wave.

To provide a more realistic description of an incident SSCW, we assume that it has a point of inflection, and for the sake of tractability prescribe its equations for  $u$  and  $\sigma$  as

$$\frac{u}{\hat{u}} = \frac{\sigma}{\hat{\sigma}} = 3 \left( \frac{t}{T} - \frac{h}{CT} \right)^2 - 2 \left( \frac{t}{T} - \frac{h}{CT} \right)^3 \quad (\text{C-35})$$

The temporal and spatial derivatives of  $(u/\hat{u})$  and  $(\sigma/\hat{\sigma})$  in this wave are zero when  $\beta = 0$  and 1, its point of inflection is located at  $\beta = 1/2$ , and its equations for  $r$  and  $s$  are

$$r = \hat{u} (3\beta^2 - 2\beta^3), \quad s = 0 \quad \text{for} \quad 0 \leq \beta \leq 1 \quad (\text{C-36})$$

### C.8.2 Conditions Along II'.

Conditions at a free surface are obtained by letting  $Z \rightarrow \infty$  and  $C_b \rightarrow 0$  in pertinent equations presented here earlier. The boundary conditions for  $u$  and  $\sigma$  along BB' are obtained as  $\sigma^B = 0$  and  $u = 2\hat{u}\beta$ , by combining Equations (C-17) and (C-18) with the equations,  $s^B = -\hat{u}\beta$  and  $r_B = 0$ ; obtained, respectively, by letting  $Z \rightarrow \infty$  in Equations (C-19) and (C-20). The condition that  $h \rightarrow L$  as  $C_b \rightarrow 0$  from Equation (7), shows that the  $C_+$  characteristics emanating from II' collapse onto IB' when the boundary is treated as a free surface.

### C.8.3 The Reflected Flow.

We use the boundary condition  $\sigma^B = 0$  and Equation (C-9) to show that  $r^B = -s^B$  along BB', and then the condition that  $\alpha = \beta$  along II' to obtain the following equation for  $s$  in the reflected wave,

$$s = \hat{u} (3\alpha^2 - 2\alpha^3) \quad (\text{C-37})$$

Equations (C-9), (C-10), (C-36), and (C-37) then give the equations for  $u$  and  $\sigma$  in II'2 as

$$\frac{u}{\hat{u}} = 3(\beta^2 + \alpha^2) - 2(\beta^3 + \alpha^3) \quad (\text{C-38})$$

$$\frac{\sigma}{\hat{\sigma}} = 3(\beta^2 - \alpha^2) - 2(\beta^3 - \alpha^3) \quad (\text{C-39})$$

for  $0 \leq \beta \leq 1$  and  $0 \leq \alpha \leq 1$ . Setting  $\beta = 1$  in these equations gives the following equations for  $u$  and  $\sigma$  in the 2I'R3,

$$\frac{u}{\hat{u}} = 1 + \alpha^2 (3-2\alpha) \quad (\text{C-40}) \quad \frac{\sigma}{\hat{\sigma}} = 1 - \alpha^2 (3-2\alpha) \quad (\text{C-41})$$

which show that  $u/\hat{u}$  increases from one to two while  $\sigma/\hat{\sigma}$  decreases from one to zero as  $\alpha$  increases from zero to one in the SS rarefaction wave reflected from a free surface. Combining Equations (C-11) and (C-14) with Equations (C-38) and (C-39), and with Equations (C-40) and (C-41) give the equations for  $u$  and  $\sigma$  in II'2 and 2I'R3 in terms of  $h$  and  $t$  but we will not present these equations here.

Because of an interest in Lagrange gage histories recorded in shock wave experiments, we will now consider the flow produced by the reflection of our nonlinear wave from a free surface in more detail. The equations obtained by differentiating Equations (C-35), (C-38), and (C-39) with respect to  $t/T$  and  $h/CT$  show, in contrast to the flow produced by the reflection of a ramp wave, that the temporal and spatial derivatives of  $u/u$  and  $\sigma/\sigma$  are continuous across  $I2$  and  $2I'$  and depend on both  $t/T$  and  $h/CT$  in  $II'2$ . Other significant features of the flow can be obtained by considering a set of Lagrange particle velocity histories and the shape of the  $u$  and  $\sigma$  contours in  $II'2$ .

Such a set of  $u/u$  versus  $t/T$  records, supposedly obtained from four Lagrange gages, G1, G2, G3, and G4, situated as shown in Figure C-3 at  $h/CT = 0.8, 1.0, 1.3$ , and  $1.5$ , is presented in Figure C-2.

The records from G1 and G2 show clearly that particles at Lagrange positions  $h \leq L/CT - 1/2$  have the same acceleration in both the incident SSCW and the reflected SS rarefaction wave. The records G2, G3, and G4 show that  $u/u = 1$  when  $t/T = 2$  and thus indicate that this condition will be satisfied by all the particles entering  $II'2$ . This is verified in our following treatment of the  $u$  and  $\sigma$  contours in the penetration region.

The derivatives,  $[\partial(t/T)/\partial(h/CT)]_u$  and  $[\partial(t/T)/\partial(h/CT)]_\sigma$ , are convenient for deriving properties of the  $u$  and  $\sigma$  contours in  $II'2$ . Differentiating Equations (C-38) and (C-39) gives the equations for these derivatives in terms of  $\alpha$  and  $\beta$  as

$$\left( \frac{\partial(t/T)}{\partial(h/CT)} \right)_u = \frac{\beta(1-\beta) - \alpha(1-\alpha)}{\beta(1-\beta) + \alpha(1-\alpha)} \quad (C-42)$$

$$\left( \frac{\partial(t/T)}{\partial(h/CT)} \right)_\sigma = \frac{\beta(1-\beta) + \alpha(1-\alpha)}{\beta(1-\beta) - \alpha(1-\alpha)} \quad (C-43)$$

It follows from Equation (C-42), that  $[\partial(t/T)/\partial(h/CT)]_u = 1, 0, -1$ , and  $0$ , respectively, along  $I2$  where  $\alpha = 0$ , along  $II'$  where  $\alpha = \beta$ , along  $2I'$  where  $\beta = 1$ , and along  $22'$  where  $\alpha + \beta = 1$  and  $t/T = 2$ . Thus in  $II'2$ ,  $22'$  separates the  $u$  contours connecting points on  $I2$  to points on  $I2'$  from those connecting points on  $2I'$  to points on  $2I'$ . The  $u$  contours below  $22'$ , that emanate from points on  $I2$  satisfying the condition  $0 < \beta < 1$ , initially have the same slope as these  $C_+$  characteristics in  $OI2C$  and become perpendicular to the free surface along  $I2'$ . The  $u$  contours above  $22'$ , that emanate from points on  $2I'$  satisfying the condition  $0 < \alpha < 1$ , initially have the same slope as these  $C_-$  characteristics in  $2I'R3$  and become perpendicular to the free surface along  $2I'$ . Such a set of  $u$  contours is shown in Figure C-3.

It follows from Equation (C-43), that  $[\partial(t/T)/\partial(h/CT)]_\sigma = 1, \infty, -1$ , and  $\infty$ , respectively, along  $2I$  where  $\alpha = 0$ , along  $II'$  where  $\alpha = \beta$ , along  $2I'$  where  $\beta = 1$ , and along  $22'$  where  $\alpha + \beta = 1$  and  $t/T = 2$ . Thus in  $II'2$  where  $II'$  is the  $\sigma = 0$  isobar, the other isobars connect points on  $I2$  to points on  $2I'$ . The  $\sigma$  contours that emanate from points on  $I2$  satisfying the condition  $0 < \beta < 1$ , have the same slope as these  $C_+$  characteristics in  $OI2C$ , are parallel to  $II'$  along  $22'$ , and at points on  $2I$  satisfying the condition  $0 < \alpha < 1$  have the same slope as the  $C_-$  characteristics in  $2I'R3$ . The fact that the isobars in  $II'2$  are perpendicular to  $22'$ , shows that the  $\sigma/\sigma$  histories at the Lagrange positions in the penetration region have a maximum at  $t/T = 2$  except at  $h = L/CT$ . Such a set of  $\sigma$  contours is also shown in Figure 3.

## C.9 CONCLUSIONS.

Model solutions for the flows produced by the reflection of SSCWs from boundaries with different shock impedances were constructed and used to exemplify flow features that are ignored when an incident SSCW is treated as a shock discontinuity. In constructing these solutions by the method of characteristics, both the material supporting the SSCW and the bounding material were assumed to have linear ( $\sigma-u$ ) relationships, and the incident wave was treated both as a linear ramp

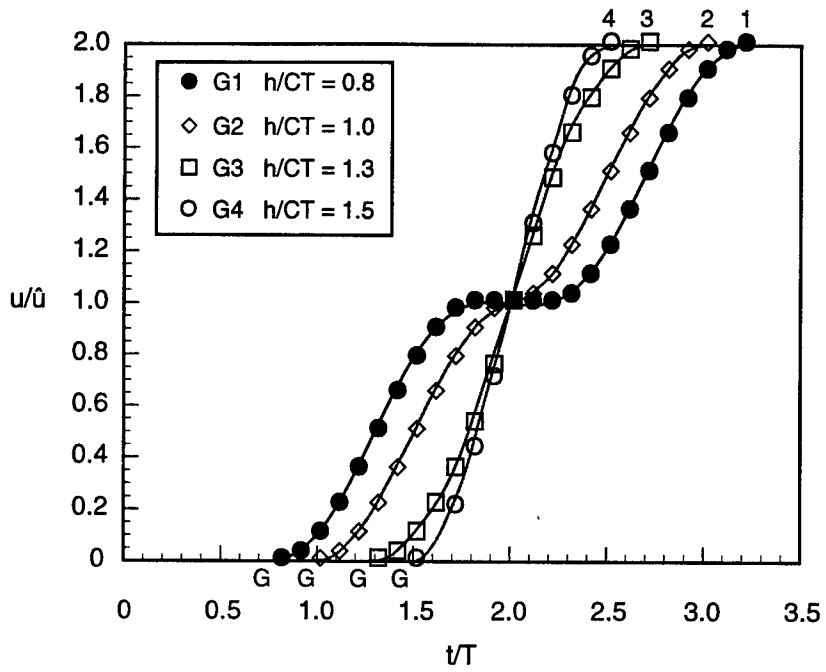


Figure C-2. A set of nondimensional Lagrange particle velocity ( $u/\hat{u}$ ) - time ( $t/T$ ) profiles recorded in the flow produced when a steady-state compression wave propagating in a material with a linear stress ( $\sigma$ ) - particle velocity ( $u$ ) relationship is reflected from a free surface.

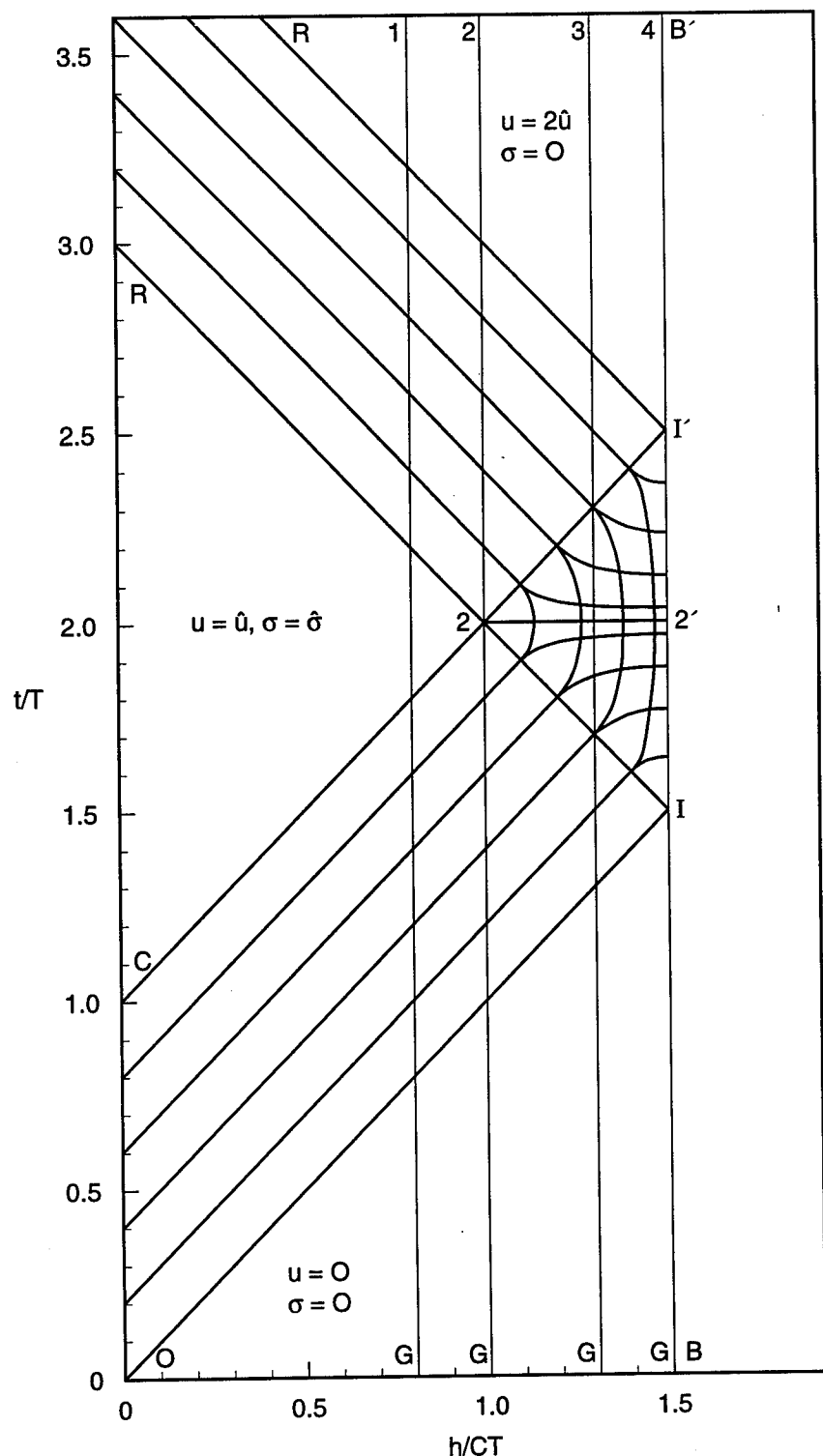


Figure C-3. A nondimensional Lagrange distance-time diagram showing the stress ( $\sigma$ ) and particle velocity ( $u$ ) contours in an incident nonlinear steady-state compression wave and in the flow produced by its reflection from a free surface.

wave and a nonlinear wave with a point of inflection. For such solutions, the steady state flows in the reflected wave and the transmitted compression wave have the same rise time as the incident wave and are separated by a penetration region where the flow is unsteady. As for shock discontinuities, the condition for the steady reflected flow to be, either a compression or rarefaction wave, is that the shock impedance of the bounding material, be either greater or less than, the shock impedance of the material supporting the incident SSCW. Flows in the penetration region produced by (1) the reflection of a ramp wave from a surface with a variable shock impedance and from a rigid wall, and (2) the reflection of the nonlinear wave from a free surface were discussed to provide a better understanding of the dependence of the unsteady flows produced by such reflections on the shape of the incident SSCW and the boundary conditions at the interface.

## REFERENCE

1. R. Courant and K. O. Friedrichs, "Supersonic Flow and Shock Waves," Interscience Publishers, Inc., New York, 1948, Chapter III.

## DISTRIBUTION LIST

DNA-TR-95-47

### DEPARTMENT OF DEFENSE

DEFENSE INTELLIGENCE AGENCY  
ATTN: DT-1

DEFENSE NUCLEAR AGENCY  
2 CY ATTN: ISST  
ATTN: PM D LINGER  
ATTN: PMAS-TV F RENSVOLD  
ATTN: PMT E TREMBA  
ATTN: WE

DEFENSE TECHNICAL INFORMATION CENTER  
ATTN: DTIC/OCP

FIELD COMMAND DEFENSE NUCLEAR AGENCY  
ATTN: FCTN B HARRIS-WEST  
ATTN: NTV

FIELD COMMAND DEFENSE NUCLEAR AGENCY  
ATTN: FCTT-RQ B RISTVET  
ATTN: FCTT-RQ E RINEHART  
ATTN: FCTT DR BALADI  
ATTN: FCTT J HUGHES  
ATTN: FCTTS A MARTINEZ  
ATTN: FCTTS J LEVERETTE  
ATTN: FCTTS LT COL AULETTA  
ATTN: FCTTS DR REINKE  
ATTN: FCTTS P THOMPSON

### DEPARTMENT OF THE ARMY

U S ARMY ENGR WATERWAYS EXPER STATION  
ATTN: E JACKSON CEWES-SD-R  
ATTN: J ZELASKO CEWES-SD-R

### DEPARTMENT OF THE AIR FORCE

PHILLIPS LABORATORY  
ATTN: PL/SUL

### DEPARTMENT OF ENERGY

EG&G, INC  
ATTN: D EILERS

LAWRENCE LIVERMORE NATIONAL LAB  
ATTN: F HEUZE  
ATTN: LEWIS GLENN  
ATTN: J RAMBO  
ATTN: J WHITE  
ATTN: W C MOSS  
ATTN: R WARD  
ATTN: TECH LIBRARY

LOS ALAMOS NATIONAL LABORATORY  
ATTN: DAVID KING  
ATTN: FRED APP  
ATTN: T KUNKLE  
ATTN: T MCKOWN

ATTN: J FRITZ  
ATTN: C MORRIS  
2 CY ATTN: REPORT LIBRARY  
ATTN: J N JOHNSON

ATTN: THOMAS DEY  
ATTN: TOM WEAVER

SANDIA NATIONAL LABORATORIES  
ATTN: DIV 9321 W BOYER  
ATTN: MIKE FURNISH  
2 CY ATTN: TECH LIB 3141

### DEPARTMENT OF DEFENSE CONTRACTORS

DEFENSE GROUP, INC  
ATTN: ROBERT POLL

ENSCO INC  
ATTN: P FISHER  
JAYCOR  
ATTN: CYRUS P KNOWLES

KAMAN SCIENCES CORPORATION  
2 CY ATTN: DASIAC

KTECH CORP  
ATTN: E SMITH  
ATTN: FRANK DAVIES  
ATTN: L LEE

LOGICON R & D ASSOCIATES  
ATTN: J RENICK

MAXWELL LABORATORIES INC  
ATTN: DR E PETERSON  
ATTN: J BAKER  
ATTN: J MORRIS  
ATTN: P COLEMAN  
ATTN: S PEYTON

SCIENCE APPLICATIONS INTL CORP  
ATTN: DAN PATCH  
ATTN: JACK KLUMP  
ATTN: L SCOTT  
ATTN: MARTIN FOGL  
ATTN: MR M MCKAY

SRI INTERNATIONAL  
2 CY ATTN: D R CURRAN  
ATTN: DR JIM GRAN  
ATTN: MARK GROETHE  
ATTN: P DE CARLI  
2 CY ATTN: T H ANTOUN

TECH REPS, INC  
ATTN: F McMULLAN  
ATTN: R NAEGELI

TERRA TEK, INC  
ATTN: W MARTIN  
TITAN CORPORATION (THE)  
ATTN: A FREDERICKSON  
ATTN: S SCHUSTER

### DIRECTORY OF OTHER

MARYLAND UNIVERSITY OF  
ATTN: RICHARD DICK